Proximity measures in topological structure for discrimination

Rafik Abdesselam

COACTIS-ISH Laboratory of Management - Human Sciences Institute,
Faculty of Economic and Management Sciences, University of Lyon, Lumière Lyon 2,
Campus Berges du Rhône, 69635 Lyon Cedex 07, France
(E-mail: `rafik.abdesselam@univ-lyon2.fr`)

Abstract. The choice of a proximity measure between objects has a direct impact on the results of any operation of classification, comparison, evaluation or structuring a set of objects. In many application fields, for a given problem, the user is prompted to choose one among the many existing proximity measures. However, according to the notion of topological equivalence chosen, some are more or less equivalent.

In this paper, we propose a new comparison approach of proximity measures for the purpose of discrimination and in a new concept of topological equivalence. This approach exploits the concept of the local neighborhood. It defines discriminant equivalence between two proximity measures as having the same neighborhood structure on the objects of a set of explanatory continuous variables according to a target qualitative variable that we want to explain.

According to the notion of topological equivalence based on the concept of neighborhood graphs, we use adjacency binary matrices, associated with proximity measure, Between and Within groups to classify. Some of the proximity measures are more or less equivalent, which means that they produce, more or less, the same discrimination results. We then propose to define the topological equivalence between two proximity measures through the topological structure induced by each measure.

It believes that two proximity measures are topologically equivalent if they induce the same neighborhood structure on the objects in purpose of discrimination. The comparison adjacency matrix is a useful tool for measuring the degree of resemblance between two empirical proximity matrices in a discriminating context. To view these proximity measures, we propose an hierarchy of proximity measures which are grouped according to their degree of resemblance in a topological context of discrimination.

We illustrate the principle of this approach on a simple real example of continuous explanatory data for about a dozen proximity measures of the literature.

Keywords: proximity measure, discrimination and classification, dissimilarity and adjacency matrices, neighborhood graph, topological equivalence.

1   Introduction

Compare objects, situations or ideas are essential tasks to identify something, assess a situation, structuring a set of tangible and abstract elements etc.

In a word to understand and act, you must know compare. This comparison, that the brain accomplishes naturally, however be explained if one wants to perform a machine. For this, we used the proximity measures.

Proximity measures are characterized by specific mathematical properties. Are they all the same? Can they be used in the practice of undifferentiated way? In other words, is that, for example, the proximity measure between individuals plunged in a multidimensional space as R^p, influence or not the result of a supervised classification? Is that how the similarity or dissimilarity between objects is measured affects the result of this method? If yes, how to decide what measure of similarity or dissimilarity must be used.

This problem is important in practical applications. It is the same in many areas when we want to group individuals into classes. How to measure the distance directly impacts the composition groups obtained. In Table 1, we give some conventional proximity measures, defined on R^p.

MEASURE	SHORT	FORMULA
EUCLIDEAN	EUC	$u_E(x,y) = \sqrt{\sum_{j=1}^{p}(x_j - y_j)^2}$
MAHALANOBIS	MAH	$u_{Mah}(x,y) = \sqrt{(x-y)^t \sum^{-1}(x-y)}$
MANHATTAN	MAN	$u_{Man}(x,y) = \sum_{j=1}^{p}|x_j - y_j|$
MINKOWSKI	MIN	$u_{Min_\gamma}(x,y) = (\sum_{j=1}^{p}|x_j - y_j|^\gamma)^{\frac{1}{\gamma}}$
TCHEBYTCHEV	TCH	$u_{Tch}(x,y) = \max_{1 \leq j \leq p}|x_j - y_j|$
COSINE DISSIMILARITY	COS	$u_{Cos}(x,y) = 1 - \frac{<x,y>}{\|x\|\|y\|}$
CANBERRA	CAN	$u_{Can}(x,y) = \sum_{j=1}^{p}\frac{|x_j - y_j|}{|x_j| + |y_j|}$
SQUARED CHORD	SC	$u_{SC}(x,y) = \sum_{j=1}^{p}(\sqrt{x_j} - \sqrt{y_j})^2$
WEIGHTED EUCLIDEAN	WE	$u_{WE}(x,y) = \sqrt{\sum_{j=1}^{p}\alpha_i(x_j - y_j)^2}$
CHI-SQUARE	χ^2	$u_{\chi^2}(x,y) = \sum_{j=1}^{p}\frac{(x_j - m_j)^2}{m_j}$
HISTOGRAMM INTERSECTION	HI	$u_{HI}(x,y) = 1 - \frac{\sum_{i=1}^{p}(\min(x_i,y_i))}{\sum_{j=1}^{p}y_j}$
NORMALIZED EUCLIDEAN	NE	$u_{NE}(x,y) = \sqrt{\sum_{j=1}^{p}(\frac{x_j - y_j}{\sigma_j})^2}$

Table 1. Some proximity measures.

Where p is the dimension of space, $x = (x_j)_{j=1,...,p}$ and $y = (y_j)_{j=1,...,p}$ two points in R^p, $(\alpha_j)_{j=1,...,p} \geq 0$, $\sum^{-1}$ the inverse of the variance and covariance matrix, σ_j^2 the variance, $\gamma > 0$ and $m_j = \frac{x_j + y_j}{2}$.

2 Topological equivalence

This approach is based on the concept of a topological graph which uses a neighborhood graph in a discriminant context. The basic idea is quite simple: we can associate a neighborhood graph to each proximity measure from which we can say that two proximity measures are equivalent if the topological

graphs induced are the same. To evaluate the similarity between proximity measures, we compare neighborhood graphs and quantify to what extent they are equivalent.

2.1 Topological graphs

For a proximity measure u, we can build a neighborhood graph on a set of individuals-objects where the vertices are the individuals and the edges are defined by a neighborhood relationship property. We thus simplify have to define the neighborhood binary relationship between all couples of individuals. We have plenty of possibilities for defining this relationship. For instance, we can use the definition of the Relative Neighborhood Graph (RNG), [16], where two individuals are related if they satisfy the following property:

$$\begin{cases} \text{V}_u(x,y) = 1 \ if \quad \text{u(x,y)} \leq \max(u(x,z), u(y,z)) \ ; \ \forall z \in R^p, \ z \neq x, y \\ \text{V}_u(x,y) = 0 \ otherwise \end{cases} \tag{1}$$

Geometrically, this property means that the hyper-lunula (the intersection of the two hyper-spheres centered on two points) is empty. The set of couples that satisfy this property result in a related graph such as that shown in Figure 1. For the example shown, the proximity measure used is the Euclidean distance. The topological graph is fully defined by the adjacency matrix as in Figure 1.
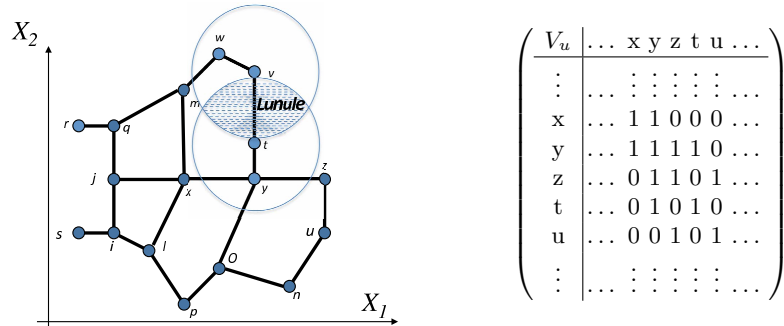
Fig. 1. Topological graph built on RNG property.

In order to use the topological approach, the property of the relationship must lead to a related graph. Of the various possibilities for defining the binary relationship, we can use the properties in a Gabriel Graph (GG), [15], or any other algorithm that leads to a related graph such as the Minimal Spanning Tree (MST), [7]. For a given neighborhood property (MST, GG, RNG), each measure u generates a topological structure on the objects which are totally described by the adjacency matrix V_u.

For this work, we use only the Relative Neighborhood Graph, [23].

2.2 Comparison of proximity measures

We denote $\{x^j; j = 1, p\}$ the set of p explanatory quantitative variables and y the qualitative variable to explain, partition of $n = \sum_{k=1}^{q} n_k$ individuals-objects in q groups $\{G_k; k = 1, q\}$.

From the previous material, using topological graphs represented by an adjacency matrix, we can evaluate the similarity between two proximity measures via the similarity between the topological graphs each one produces. To do so, we just need the adjacency matrix associated with each graph.

For any proximity measure u, we built according to the property (1), the overall adjacency matrix V_u that presents itself as a juxtaposition of adjacency matrices (binary and symmetric) Within $V_u^{G_k}$ and Between $V_u^{G_k l}$ groups:

$$\begin{cases} \mathrm{V}_u^{G_k}(x,y) = 1 \;\; if \;\; \mathrm{u(x,y)} \leq \max(u(x,z), u(y,z)) \,;\, \forall x, y, z \in G_k, \, z \neq x, y \\ \mathrm{V}_u^{G_k}(x,y) = 0 \;\; otherwise \end{cases}$$

$$\begin{cases} \mathrm{V}_u^{G_k l}(x,y) = 1 \;\; if \;\; \mathrm{u(x,y)} \leq \max(u(x,z), u(y,z)) \,;\, \forall x \in G_k, y \in G_l, \, z \neq x, y \\ \mathrm{V}_u^{G_k l}(x,y) = 0 \;\; otherwise \end{cases}$$

• The first objective is to group and view the different proximity measures, according to their topological similarity in the context of discrimination.

Note that V_{u_i} and V_{u_j} are two adjacency matrices associated with both proximity measures u_i and u_j. To measure the degree of similarity between the two proximity measures, we just count the number of discordances between the two adjacency matrices.

So, to measure the topological equivalence of discrimination between the proximity measures u_i and u_j, we propose to test whether the associated adjacency matrices V_{u_i} and V_{u_j} are statistically different or not, using a non-parametric test on paired binary data. The degree of topological equivalence between two proximity measures is measured by the quantity:

$$S(V_{u_i}, V_{u_j}) = \frac{\sum_{k=1}^{n} \sum_{l=1}^{n} \delta_{kl}}{n^2} \quad \text{where} \quad \delta_{kl} = \begin{cases} 1 \text{ if } V_{u_i}(k,l) = V_{u_j}(k,l) \\ 0 \text{ otherwise.} \end{cases}$$

$S(V_{u_i}, V_{u_j})$ is the measure of similarity which varies in the range $[0, 1]$. A value of 1 means that the two adjacency matrices are identical and therefore the topological structure induced by the two proximity measures is the same, meaning that the proximity measures considered are equivalent. A value of 0 means that there is a full discordance between the two matrices.

The similarity $S(V_{u_i}, V_{u_j})$ is thus the extent of agreement between the adjacency matrices.

• The second objective is to establish a criterion for selection aid of the "best" proximity measure that well discriminates the q groups, among the considered proximity measures.

We note, $V_{u*} = diag(1_{G_1}, \ldots, 1_{G_k}, \ldots, 1_{G_q})$ the adjacency block diagonal reference matrix, "perfect discrimination of the q groups" according to an unknown proximity measure denoted $u*$. Where 1_{n_k} is the vector of order n_k which all components are equal to 1 and $1_{G_k} = 1_{n_k}{}^t 1_{n_k}$, is the symmetric matrix of order n_k which all the elements are equal to 1.

$$V_{u_i} = \begin{pmatrix} V_u^{G_1} & & & & \\ & \cdots & & & \\ V_u^{G_{k1}} & \cdots & V_u^{G_k} & & \\ & & & \cdots & \\ V_u^{G_{q1}} & \cdots & V_u^{G_{1k}} & \cdots & V_u^{G_q} \end{pmatrix} \; ; \; V_{u*} = \begin{pmatrix} 1_{G_1} & & & & \\ 0 & \cdots & & & \\ 0 & 0 & 1_{G_k} & & \\ 0 & 0 & 0 & \cdots & \\ 0 & 0 & 0 & 0 & 1_{G_q} \end{pmatrix}$$

Thus, we can also establish the degree of topological equivalence of discrimination $S(V_{u_i}, V_{u^*})$ between each considered proximity measures u_i and the reference measure u^*.

3   Application example

In this section, we describe the results obtained by applying proximity measures on real continuous data to illustrate this topological discriminant approach.

We consider a sample of small cars [8] with seven observed explanatory variables (price, urban consumption, engine capacity, maximum speed, maximum volume of trunk, weight/power ratio, length). The target qualitative variable to discriminate is the brand of the carmaker with two modalities-groups, French and Foreign cars.

We want to visualize the similarities between the proximity measures in order to see which measures are close to one another in a discriminant context. As we already have a similarity matrix between proximity measures, we can use any classic visualization techniques to achieve this. For example, we can build a dendrogram of hierarchical clustering of the proximity measures. We can also use Multidimensional scaling or any other technique to map the 12 considered proximity measures.

S	u_E	u_{Mah}	u_{Man}	u_{Min_γ}	u_{Tch}	u_{Cos}	u_{Can}	u_{SC}	u_{WE}	u_{χ^2}	u_{HI}	u_{NE}
u_E	1											
u_{Mah}	.746	1										
u_{Man}	.946	.746	1									
u_{Min_γ}	.977	.741	.923	1								
u_{Tch}	.905	.724	.859	.918	1							
u_{Cos}	.832	.741	.841	.837	.819	1						
u_{Can}	.796	.805	.814	.782	.746	.800	1					
u_{SC}	.936	.773	.927	.923	.887	.832	.814	1				
u_{WE}	1	.746	.946	.977	.905	.832	.796	.936	1			
u_{χ^2}	.941	.769	.946	.977	.891	.828	.809	.995	.941	1		
u_{HI}	.660	.660	.678	.655	.655	.673	.682	.642	.660	.646	1	
u_{NE}	.751	.850	.741	.737	.728	.755	.864	.769	.751	.764	.655	1
u^*	.497	.524	.506	.492	.483	.510	.510	.506	.497	.501	.456	.501

Table 2. Topological equivalence - Similarities $S(V_{u_i}, V_{u_j})$ and $S(V_{u_i}, V_{u^*})$.

Table 2 summarizes the similarities between the 12 conventional proximity measures of Table 1. The application of an algorithm to build an hierarchy of the partition, Ascendant Hierarchical Clustering according to ward [24] criterion, allows to obtain the dendrogram of Figure 2.

The vector of similarities $S(V_{u^*}, V_{u_i})$, between the reference measure and the proximity measures considered, is positioned as illustrative element in the analysis.
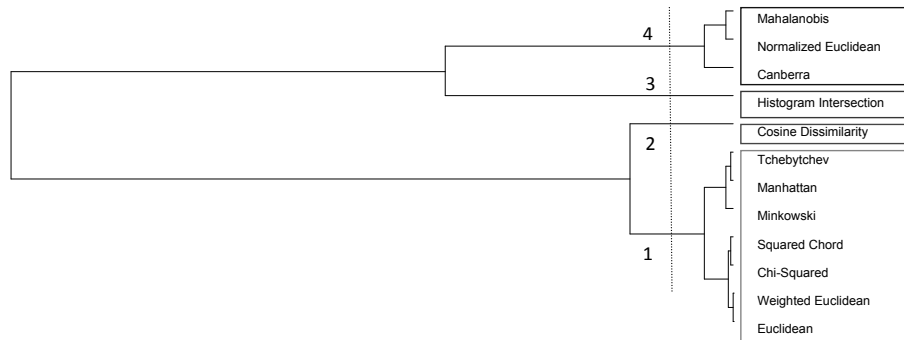
Fig. 2. Hierarchical Tree - Topological structure with Relative Neighbors Graph.

	Classe 1	Classe 2	Classe 3	Classe 4
Frequency	7	1	1	3
Active measures	$u_E, u_{Man}, u_{Min_\gamma}, u_{Tch}, u_{SC}, u_{WE}, u_{\chi^2}$	u_{Cos}	u_{HI}	u_{Mah}, u_{NE}, u_{Can}
Illustrative measure			u^*	

Table 3. Assignment of the reference measure.

Given the results presented in Table 3, for the selection of the "best" proximity measure among the 12 measures considered, the unknown reference measure u^*, projected as illustrative element, would be closer to measures of class 3, that is to say, the histogramm intersection measure u_{HI}.

4   Conclusion and perspectives

The choice of a proximity measure is highly subjective, it is often based on habits or on criteria such as *a posteriori* interpretation of the results. This work proposes a new approach of equivalence between proximity measures in a discrimination context. This topological approach is based on the concept of neighborhood graph induced by the proximity measure. From a practical point of view, in this paper, the compared measures are all built on explanatory quantitative data, but this work may well extend to qualitative data by choosing the correct topological structure and the adapted proximity measures. We are considering to extend this work to other topological structures and use a comparison criterion, other than classification techniques to validate the degree of equivalence between two proximity measures. For example, a criterion based on a nonparametric test (e.g., the concordance coefficient of Kappa) on the binary data of the adjacency matrix associated to proximity measures. This will allow to give a statistical significance between the two similarity matrices and to validate or not the topological equivalence of discrimination, that is to say, if they really induce or not the same structure of the neighborhood groups objects to be separated.

References

1. R. Abdesselam, A.D. Zighed, *Statistical comparisons for topological equivalence of proximity measures*. SMTDA 2012, 2nd Stochastic Modeling Techniques and Data Analysis, International Conference, 2012, Chania Crete Greece.

2. V. Batagelj, M. Bren, *Comparing resemblance measures*. In Proc. International Meeting on Distance Analysis (DISTANCIA'92),(1992)

3. V. Batagelj, M. Bren, *Comparing resemblance measures*. In Journal of classification **12** (1995) 73–90

4. M. Bouchon-Meunier, B. Rifqi and S. Bothorel, *Towards general measures of comparison of objects*. In Fuzzy sets and systems **2, 84** (1996) 143–153

5. K.R. Clarke, P.J. Somerfield andM.G. Chapman, *On resemblance measures for ecological studies, including taxonomic dissimilarities and a zero-adjusted Bray-Curtis coefficient for denuded assemblages*. In Journal of Experimental Marine Biology & Ecology **330, 1** (2006) 55–80

6. R. Fagin, R. Kumar and D. Sivakumar, *Comparing top k lists*. In Proceedings of the fourteenth annual ACM-SIAM symposium on Discrete algorithms, Society for Industrial and Applied Mathematics (2003)

7. J.H. Kim and S. Lee, *Tail bound for the minimal spanning tree of a complete graph*. In Statistics Probability Letters **4, 64** (2003) 425–430

8. J. Lambin, *La recherche marketing, Analyser - Mesurer - Prvoir*. Edt McGraw-Hill (1990).

9. M.J. Lesot, M. Rifqi and H. Benhadda,*Similarity measures for binary and numerical data: a survey*. In IJKESDP **1, 1** (2009) 63-84

10. H. Liu, D. Song, S. Ruger, R. Hu and V. Uren, *Comparing dissimilarity measures for content-based image retrieval*. In Information Retrieval Technology Springer 44–50

11. D. Malerba, F. Esposito, F., Gioviale and V. Tamma, *Comparing dissimilarity measures for symbolic data analysis*. In Proceedings of Exchange of Technology and Know-how and New Techniques and Technologies for Statistics **1** (2001) 473–481

12. D. Malerba, F. Esposito and M. Monopoli, *Comparing dissimilarity measures for probabilistic symbolic objects*. In Data Mining III, Series Management Information Systems **6** (2002) 31–40

13. N. Mantel, *A technique of disease clustering and a generalized regression approach*. In Cancer Research, **27** (1967) 209–220.

14. T. Noreault, M. McGill and M.B. Koll, *A performance evaluation of similarity measures, document term weighting schemes and representations in a Boolean environment*. In Proceedings of the 3rd ACM conference on Research and development in information retrieval (1980)

15. J.C. Park, H. Shin and B.K. Choi, *Elliptic Gabriel graph for finding neighbors in a point set and its application to normal vector estimation*. In Computer-Aided Design Elsevier **38, 6** (2006) 619–626

16. F.P. Preparata and M.I. Shamos, *Computational geometry: an introduction*. In Springer (1985)

17. Richter, M. M., *Classification and learning of similarity measures*. In Proceedings der Jahrestagung der Gesellschaft fur Klassifikation, Studies in Classification, Data Analysis and Knowledge Organisation. Springer Verlag (1992)

18. M. Rifqi, M. Detyniecki and B. Bouchon-Meunier, *Discrimination power of measures of resemblance*. IFSA'03 Citeseer (2003)

19. J.W. Schneider and P. Borlund, *Matrix comparison, Part 1: Motivation and important issues for measuring the resemblance between proximity measures or ordination results.* In Journal of the American Society for Information Science and Technology **58 11** (2007) 1586–1595

20. J.W. Schneider and P. Borlund, *Matrix comparison, Part 2: Measuring the resemblance between proximity measures or ordination results by use of the Mantel and Procrustes statistics.* In Journal of the American Society for Information Science and Technology **11 58** (2007) 1596–1609.

21. E. Spertus, M. Sahami and O. Buyukkokten, *Evaluating similarity measures: a large-scale study in the orkut social network.* In Proceedings of the eleventh ACM SIGKDD international conference on Knowledge discovery in data mining ACM (2005)

22. A. Strehl, J. Ghosh and R. Mooney, *Impact of similarity measures on web-page clustering.* In Workshop on Artificial Intelligence for Web Search AAAI (2000) 58–64

23. G.T. Toussaint, *The relative neighbourhood graph of a finite planar set.* In Pattern recognition **12 4** (1980) 261–268

24. J.R. Ward, *Hierarchical grouping to optimize an objective function.* In Journal of the American statistical association JSTOR **58 301** (1963) 236–244

25. Zwick, R., Carlstein, E. and Budescu, D. V., *Measures of similarity among fuzzy concepts: A comparative analysis.* In Int. J. Approx. Reason **2, 1** (1987) 221–242

26. A.D. Zighed, R. Abdesselam, A. Hadgu, *Topological comparisons of proximity measures.* PAKDD 2012. The 16th Pacific-Asia Conference on Knowledge Discovery and Data Mining. In P.-N. Tan et al. (Eds.), Part I, LNAI 7301, Springer-Verlag Berlin Heidelberg (2012) 379391.

Control Charts for Zero-Inflated Processes with Estimated Parameters

Athanasios C. Rakitzis and Philippe Castagliola

LUNAM Université, Université de Nantes & IRCCyN UMR CNRS 6597
Nantes, France
e-mail: `athanasios.rakitzis@univ-nantes.fr`,
e-mail: `philippe.castagliola@univ-nantes.fr`

Abstract. Zero-inflated probability models are used to model count data that has an excessive number of zero counts. These models are mostly useful in modeling high-yield processes that produce a low fraction of non-conforming units or health-related processes where it is of interest the monitoring of a rare disease. Shewhart-type control charts have been proposed for the monitoring of zero-inflated processes. Usually their performance is evaluated under the assumption of known process parameters. However, in practice their values are rarely known and have to be estimated from an in-control historical Phase I data set. In this work, we investigate the performance of Shewhart-type control charts for zero-inflated Poisson (ZIP) and zero-inflated binomial (ZIB) processes when the process parameters are estimated from a Phase I data set of size m. Practical guidelines regarding the necessary size m of the Phase I data set, in order to obtain the desired in-control performance of the examined charts, are also given.

Keywords: Average run length, Moment estimator, Probability generating function, Standard deviation run length, Shewhart control charts, Zero-Inflated binomial distribution, Zero-Inflated Poisson distribution.

1   Introduction

Control charts are considered as the most widely used technique for monitoring a process and identifying changes in it. When the monitoring of a high-yield process is of interest, the considered quality characteristic cannot always be conveniently represented numerically. In such cases, the common practice is to classify each inspected item (or unit) as either conforming or non-conforming according to the specifications of the quality characteristic. Usually, for the monitoring of such processes, attributes control charts like the $np-$ or the $c-$ charts are used (Montgomery [10]). Due to technological progress and automation of manufacturing technology, many processes are now characterized by low defective rates. Consequently, these processes demonstrate an excessive number in zeros. This excess in zeros results in an over-dispersed distribution (Woodall [14]) and, therefore, in the under-estimation of the mean and the

variance of the process. Thus, the standard attribute $np-$ and $c-$ control charts cannot be efficiently used due to an increased rate of false alarms. Therefore, the development of control charts under more appropriate probability models is necessary. Zero-inflated models (see Johnson et al. [9, p.351-356]) have been recommended as alternative models that take into account the excessive number of zeros. Control charts based on the zero-inflated Poisson (ZIP) and the zero-inflated Binomial (ZIB) distributions have already been studied in the literature. See, for example, Xie and Goh [15], Xie et al. [16], Sim and Lin [13] (for Shewhart-type control charts) and Noorossana et al. [11], Fatahi et al. [6], He et al. [8] (for CUSUM- and EWMA-type charts).

The development of all the previously mentioned control schemes is based on the assumption that the process parameters are known. However, this rarely happens in practice and they are usually estimated from an in-control historical (or preliminary) data set (Phase I sample). It is known that when the parameters are estimated, the performance of the control charts differs from the known parameters case due to the variability of the estimators during the Phase I analysis. The $np-$ and $c-$ control charts with estimated parameters have been studied by Braun [1], Chakraborti and Human [3,4], Castagliola and Wu [2] and Chen and Song [5]. It seems that only He et al. [7] have studied the effect of parameter estimation on the Shewhart chart for monitoring ZIP processes while, to the best of our knowledge, the case of ZIB processes has not been examined so far.

In this work, we examine the performance of upper-sided Shewhart-type control charts for ZIP and ZIB processes for the estimated parameters case. Guidelines about the required number m of Phase I samples, in order to have similar in-control performance in both the estimated and known parameter cases, are provided.

The remainder of this paper is organized as follows: In Section 2, we present the run length properties of the upper-sided ZIP- and ZIB-Shewhart control charts with known parameters while the estimated parameter case is discussed in Section 3. In Section 4, numerical comparisons between the known and the estimated parameter case are provided along with practical guidelines for the statistical design of the upper-sided ZIP- and ZIB-Shewhart control charts in the estimated parameters case. Finally, Section 5 contains concluding remarks.

2 The upper-sided ZIP and ZIB charts with known parameters

2.1 The upper-sided ZIP chart with known λ_0

The zero-inflated Poisson (ZIP) distribution is a generalization of the standard Poisson distribution that can be used to model count processes containing an excessive number of zeros. By definition, if X is a ZIP random variable, it is defined on $\{0, 1, \dots\}$ (as for the standard Poisson distribution) and its probability mass function (p.m.f.) is given by

$$f_{ZIP}\left(x\left|\phi, \lambda\right.\right) = \begin{cases} \phi + (1-\phi) f_P\left(0\left|\lambda\right.\right), \ x = 0 \\ (1-\phi) f_P\left(x\left|\lambda\right.\right), \ x = 1, 2, \dots \end{cases},$$

where

$$f_P\left(x\,|\lambda\right) = e^{-\lambda}\frac{\lambda^x}{x!},$$

is the p.m.f. of the standard Poisson distribution with parameter $\lambda > 0$ and $\phi \in [0,1]$. If $\phi = 0$, the ZIP distribution coincides with the standard Poisson distribution while, if $\phi = 1$, it reduces to the Dirac distribution on $x = 0$. Moreover, the cumulative distribution function (c.d.f.) of X is given by

$$F_{ZIP}\left(x\,|\phi,\lambda\right) = \phi + (1 - \phi)F_P\left(x\,|\lambda\right),$$

where

$$F_P\left(x\,|\lambda\right) = \sum_{z=0}^{x} e^{-\lambda}\frac{\lambda^z}{z!},$$

is the c.d.f. of the standard Poisson distribution with parameter λ. The mean and the variance of the ZIP distribution with parameters (ϕ, λ) are, respectively, given by the following two expressions

$$E(X) = \lambda\left(1 - \phi\right),\ \ V(X) = \lambda\left(1 + \lambda\phi\right)\left(1 - \phi\right).$$

Let us now assume that we want to establish an upper-sided Shewhart control chart for monitoring a ZIP process for increases in λ. We assume that the *zero-inflated* parameter ϕ is known and that it remains unchanged in both cases. Therefore, the upper control limit of the upper-sided ZIP-Shewhart control chart with known parameters is given by

$$UCL_{ZIP} = \left\lfloor \lambda_0(1 - \phi) + K\sqrt{\lambda_0(1 + \lambda_0\phi)(1 - \phi)} \right\rfloor,$$

where $\lfloor\ldots\rfloor$ denotes the rounded down integer, λ_0 is the in-control parameter value for λ and $K > 0$ is a constant that plays the role of chart's design parameter. Let $Y_1, Y_2, \ldots$ be independent random variables such that $Y_i \sim ZIP(\phi, \lambda_1)$, i.e., a ZIP distribution with parameters (ϕ, λ_1), where λ_1 is an out-of-control parameter value for λ with $\lambda_1 > \lambda_0$. Then, the probability $\beta = P\left(Y_i > UCL_{ZIP}\right)$ that the number Y_i of non-conformities exceeds the upper-control limit UCL_{ZIP} is equal to

$$\beta = 1 - F_{ZIP}\left(UCL_{ZIP}|\phi,\lambda_1\right).$$

2.2 The upper-sided ZIB chart with known p_0

As for the ZIP distribution, the zero-inflated binomial (ZIB) distribution is a generalization of the standard binomial distribution that takes into account the excessive number of zeros. By definition, if X is a ZIB random variable, it is defined on $\{0, 1, \ldots, n\}$ (as for the standard binomial distribution) and its p.m.f. is given by

$$f_{ZIB}\left(x\,|\phi,n,p\right) = \begin{cases} \phi + (1 - \phi)\,f_B\left(0\,|n,p\right), & x = 0 \\ (1 - \phi)\,f_B\left(x\,|n,p\right), & x = 1, 2, ..., n \end{cases},$$

where

$$f_B\left(x \mid n, p\right) = \binom{n}{x} p^x (1-p)^{n-x},$$

is the p.m.f. of the standard binomial distribution, $p \in [0, 1]$ is the probability of a predefined event (e.g., a non-conforming unit) and ϕ is as for the ZIP distribution. If $\phi = 0$, the ZIB distribution coincides with the standard binomial distribution with parameters n and p while, for $\phi = 1$, the ZIB distribution reduces to the Dirac distribution on $x = 0$. The c.d.f. of X is given by

$$F_{ZIB}\left(x \mid \phi, n, p\right) = \phi + (1-\phi)F_B\left(x \mid n, p\right),$$

where

$$F_B\left(x \mid n, p\right) = \sum_{z=0}^{x} \binom{n}{z} p^z (1-p)^{n-z},$$

is the c.d.f. of the standard binomial distribution with parameters n and p. The mean and the variance of the ZIB distribution with parameters (ϕ, n, p) are, respectively, given by the following two expressions

$$E(X) = np\left(1-\phi\right), \quad V(X) = np\left(1 - p + np\phi\right)\left(1-\phi\right).$$

In a similar manner, the upper control limit of the upper-sided ZIB-Shewhart control chart with known parameters is given by

$$UCL_{ZIB} = \left\lfloor np_0(1-\phi) + K\sqrt{np_0(1-p_0+np_0\phi)(1-\phi)} \right\rfloor,$$

where p_0 is the in-control parameter value for p and $K > 0$ is a constant that plays the role of the chart's design parameter. Clearly, this chart is suitable for monitoring a ZIB process for increases in p. As for the case of ZIP-Shewhart chart, parameter ϕ is known and remains unchanged. Let $Y_1, Y_2, \ldots$ be independent random variables with $Y_i \sim ZIB(\phi, n, p_1)$, i.e., the number of non-conforming units in a sample of size n is a ZIB random variable with parameters (ϕ, n, p_1) and $p_1 > p_0$. Then, the probability $\beta = P\left(Y_i > UCL_{ZIB}\right)$ that Y_i is above UCL_{ZIB} is equal to

$$\beta = 1 - F_{ZIB}\left(UCL_{ZIB} \mid \phi, n, p_1\right).$$

2.3 Run length properties

The run length of the ZIP- and ZIB-Shewhart control charts with known parameters is a geometric random variable L with parameter β. Thus, the Average Run Length (ARL) and the Standard Deviation Run Length ($SDRL$) of the ZIP- and ZIB-Shewhart control charts with known parameters, are equal to

$$ARL = \frac{1}{\beta}, \quad SDRL = \frac{\sqrt{1-\beta}}{\beta},$$

where β is the probability defined for the ZIP- and ZIB-Shewhart control charts in the previous sub-sections.

3 The upper-sided ZIP- and ZIB-Shewhart control charts with estimated parameters

3.1 The upper-sided ZIP-Shewhart control chart with estimated λ_0

Let us now assume that we have a Phase I data set composed by m independent random variables $\{X_1, X_2, \ldots, X_m\}$ with $X_i \sim ZIP(\phi, \lambda_0)$. We also assume that the value of ϕ is known from previous knowledge or that it has been accurately estimated (see also He et al. [7]). Thus, the moment estimator $\widetilde{\lambda}_0$ of λ_0 is given by

$$\widetilde{\lambda}_0 = \frac{1}{m(1-\phi)} \sum_{i=1}^{m} X_i = \frac{W}{m(1-\phi)},$$

where $W = \sum_{i=1}^{m} X_i$ is a discrete random variable defined on $\{0, 1, \ldots\}$. Since the probability generating function (p.g.f.) $G_X(s)$ of the ZIP distribution with parameters ϕ and λ_0 is $G_X(s) = \phi + (1-\phi)e^{-\lambda_0(1-s)}$ (see Johnson et al. [9, p.353]), the p.g.f. of W is given by

$$G_W(s) = \left(\phi + (1-\phi)e^{-\lambda_0(1-s)} \right)^m,$$

and, thus, W is not a ZIP random variable. Therefore, the p.m.f. of W can be numerically evaluated for different values of ϕ, λ_0 and m via the formula

$$f_W(w \,|\, m, \phi, \lambda_0) = P(W = w) = \frac{1}{w!} \frac{d^w}{ds^w} G_W(s) \bigg|_{s=0}.$$

When λ_0 is estimated by $\widetilde{\lambda}_0$, the UCL of the upper-sided ZIP-Shewhart control chart becomes

$$\widetilde{UCL}_{ZIP} = \left\lfloor \widetilde{\lambda}_0(1-\phi) + K\sqrt{\widetilde{\lambda}_0(1+\widetilde{\lambda}_0\phi)(1-\phi)} \right\rfloor.$$

Let $\widetilde{\beta}$ be the probability that the number Y_i of non-conformities exceeds $\widetilde{UCL}_{ZIP}$, conditionally to $W = w$, i.e.,

$$\widetilde{\beta} = P\left(Y_i > \widetilde{UCL}_{ZIP} \,\Big|\, W = w \right).$$

By replacing $\widetilde{UCL}_{ZIP}$ with its respective value, $\widetilde{\lambda}_0$ with $W/(m(1-\phi))$ and using the condition $W = w$, we get

$$\widetilde{\beta} = 1 - F_{ZIP}\left(\left\lfloor \frac{w}{m} + K\sqrt{\frac{w}{m}\left(1 + \frac{w\phi}{m(1-\phi)}\right)} \right\rfloor \,\bigg|\, \phi, \lambda_1 \right),$$

since $Y_i \sim ZIP(\phi, \lambda_1)$.

Let L be the run length of the upper-sided ZIP-Shewhart control chart with estimated parameter λ_0. Since the distribution of W is defined for $w \in \{0, 1, \ldots\}$, the (unconditional) ARL and $SDRL$ are, respectively, given by

$$ARL = \sum_{w=0}^{\infty} f_W(w \,|\, m, \phi, \lambda_0) \left(\frac{1}{\widetilde{\beta}} \right),$$

$$SDRL = \sqrt{E(L^2) - ARL^2},$$

where

$$E(L^2) = \sum_{w=0}^{\infty} f_W(w\,|\,m, \phi, \lambda_0) \left(\frac{2 - \widetilde{\beta}}{\widetilde{\beta}^2} \right).$$

3.2 The upper-sided ZIB-Shewhart control chart with estimated p_0

We assume that we have a Phase I data set composed of m independent random variables $\{X_1, X_2, \ldots, X_m\}$ with $X_i \sim ZIB(\phi, n, p_0)$. As for the upper-sided ZIP-Shewhart control chart, we assume that the value of ϕ is known from previous knowledge or that it has been accurately estimated. The moment estimator $\widetilde{p}_0$ of p_0 is given by

$$\widetilde{p}_0 = \frac{1}{mn(1 - \phi)} \sum_{i=1}^{m} X_i = \frac{V}{mn(1 - \phi)},$$

where $V = \sum_{i=1}^{m} X_i$ is a discrete random variable defined on $\{0, 1, \ldots, mn - 1, mn\}$. Since the p.g.f. $G_X(s)$ of the ZIB distribution with parameters ϕ, n and p_0 is $G_X(s) = \phi + (1 - \phi)(1 - p_0 + p_0 s)^n$, (see Johnson et al. [9, p.354]), the p.g.f. of V is equal to

$$G_V(s) = (\phi + (1 - \phi)(1 - p_0 + p_0 s)^n)^m,$$

and, thus, V is not a ZIB random variable. As for W, the p.m.f. of V can be evaluated numerically for various choices of m, n, ϕ and p_0 by using the formula

$$f_V(v\,|\,m, \phi, n, p_0) = P(V = v) = \frac{1}{v!} \frac{d^v}{ds^v} G_V(s) \bigg|_{s=0}.$$

When p_0 is estimated by $\widetilde{p}_0$, the upper control limit of the upper-sided ZIB-Shewhart control chart becomes

$$\widehat{UCL}_{ZIB} = \left\lfloor n\widetilde{p}_0(1 - \phi) + K\sqrt{n\widetilde{p}_0\left(1 - \widetilde{p}_0 + n\widetilde{p}_0\phi\right)(1 - \phi)} \right\rfloor.$$

Let $\widetilde{\beta}$ be the probability that the number Y_i of non-conforming units in a sample of size n is greater than $\widehat{UCL}_{ZIB}$, conditionally to $V = v$, i.e.,

$$\widetilde{\beta} = P\left(Y_i > \widehat{UCL}_{ZIB}\,\bigg|\,V = v\right).$$

By replacing $\widehat{UCL}_{ZIB}$ with its respective value, $\widetilde{p}_0$ by $V/(mn(1-\phi))$ and using the condition $V = v$, we get

$$\widetilde{\beta} = 1 - F_{ZIB}\left(\left\lfloor \frac{v}{m} + K\sqrt{\frac{v}{m}\left(1 - \frac{v(1 - n\phi)}{nm(1 - \phi)}\right)} \right\rfloor \bigg|\,\phi, n, p_1\right),$$

since $Y_i \sim ZIB(\phi, n, p_1)$.

Let L be the run length of the upper-sided ZIB-Shewhart chart with estimated parameter $\widetilde{p}_0$. Since the distribution of V is defined on $\{0, 1, \ldots, mn - 1, mn\}$, the (unconditional) ARL and $SDRL$ are, respectively, given by

$$ARL = \sum_{v=0}^{mn} f_V(v \,|\, m, \phi, n, p_0) \left(\frac{1}{\widetilde{\beta}} \right),$$

$$SDRL = \sqrt{E(L^2) - ARL^2},$$

where

$$E(L^2) = \sum_{v=0}^{mn} f_V(v \,|\, m, \phi, n, p_0) \left(\frac{2 - \widetilde{\beta}}{\widetilde{\beta}^2} \right).$$

4 Numerical Study

In the current section, we present the results on an extensive numerical study concerning the performance and design aspects of the upper-sided ZIP- and ZIB-Shewhart control charts with estimated parameters. In Tables 1 and 2, we provide the in-control ARL and $SDRL$ values of the upper-sided ZIP- and ZIB-Shewhart control charts, respectively, for different sets of parameters (ϕ, λ_0) (for the ZIP distribution) and (ϕ, n, p_0) (for the ZIB distribution). Also the size m of the preliminary sample is $m \in \{200, 500\}$ while the case $m = \infty$ denotes the known parameter case. Due to the discrete nature of the ZIP and the ZIB distribution, it is not always possible to have the desired in-control ARL value. Thus, we provide the value of K that gives an in-control ARL value (in the known parameter case) *as close as possible* to the desired value $ARL_0 = 370.4$.

ϕ	λ_0	K	$m = 200$		$m = 500$		$m = \infty$	
			ARL	$SDRL$	ARL	$SDRL$	ARL	$SDRL$
0.9	1	6.66	551.34	3760.98	360.69	630.97	526.64	526.14
	2	6.41	1323.70	194012.80	525.54	1234.63	189.92	189.42
	5	5.72	$> 10^6$	$> 10^6$	1215.88	8527.50	314.19	313.69
0.8	1	6.33	1293.82	5212.46	837.76	1472.54	263.32	262.82
	2	5.49	1460.34	8920.58	831.59	1595.72	301.87	301.37
	5	4.47	2847.98	142615.80	993.08	2544.38	365.09	364.59
0.7	1	5.18	642.64	1503.30	532.30	775.35	175.55	175.05
	2	4.50	661.39	1718.82	489.48	744.56	201.24	200.74
	5	3.65	874.05	3851.17	524.24	911.09	243.39	242.89

Table 1. In-control ARL and $SDRL$ values of the upper-sided ZIP-Shewhart chart

Tables 1 and 2 reveal that it is not possible to have a common in-control ARL value when $m = \infty$ for all the considered pairs of (ϕ, λ_0) or (ϕ, n, p_0). In some cases, the in-control ARL values are smaller while, in other cases, they are larger than 370.4. This fact is attributed to the discrete nature of the ZIP and

				$m=200$		$m=500$		$m=\infty$	
ϕ	n	p_0	K	ARL	$SDRL$	ARL	$SDRL$	ARL	$SDRL$
0.9	100	0.005	7.25	559.42	2532.77	389.17	669.73	111.33	110.83
		0.010	6.68	579.06	4409.98	372.34	662.26	544.25	543.75
		0.020	6.43	1536.77	448794.70	568.04	1408.54	196.73	196.23
0.8	200	0.005	6.34	1346.46	5597.84	863.42	1532.02	267.65	267.15
		0.010	5.50	1577.62	10527.94	878.91	1719.67	312.05	311.55
		0.020	4.48	1348.85	20837.46	622.72	1326.20	247.83	247.33
0.7	500	0.005	4.35	816.56	2405.26	567.61	898.78	239.05	238.55
		0.010	3.66	951.43	4446.60	557.35	984.23	251.70	251.19
		0.020	3.06	1372.93	22576.55	560.21	1253.97	248.92	248.42

Table 2. In-control ARL and $SDRL$ values of the upper-sided ZIB-Shewhart chart

the ZIB distribution. Also, we mention that for (relatively) large preliminary samples (i.e., for $m = 200$ or 500), very large values (larger than 10^6) can be occurred for the in-control ARL and (especially) $SDRL$.

Since the in-control ARL values are very different in the known and in the estimated parameter case, it is of great practical interest to know how large the size m of the Phase I sample must be in order to have approximately the same in-control ARL values in both the known and the estimated parameter case, for the same value of K. In Table 3 we provide the minimal values of m for $\phi \in \{0.9, 0.8, 0.7\}$, $\lambda_0 \in \{1, 2, \ldots, 8\}$ (ZIP case), satisfying $\Delta = \frac{|ARL_{0,m} - ARL_{0,\infty}|}{ARL_{0,\infty}} < 0.05$, i.e., the relative difference within the in-control $ARL_{0,m}$ (estimated parameter case) and the in-control $ARL_{0,\infty}$ (known parameter case) is not larger than 5%.

λ_0	$\phi = 0.9$	$\phi = 0.8$	$\phi = 0.7$
1	194	$> 10^5$	$> 10^5$
2	$> 10^5$	$> 10^5$	$> 10^5$
3	$> 10^5$	274	$> 10^5$
4	644	$> 10^5$	239
5	$> 10^5$	$> 10^5$	$> 10^5$
6	991	$> 10^5$	343
7	$> 10^5$	605	$> 10^5$
8	$> 10^5$	$> 10^5$	462

Table 3. Minimal values of m for $\lambda_0 \in \{1, 2, 3, 4, 5, 6, 7, 8\}$ and $\phi \in \{0.9, 0.8, 0.7\}$ satisfying $\Delta = \frac{|ARL_{0,m} - ARL_{0,\infty}|}{ARL_{0,\infty}} < 0.05$.

The respective results for the ZIB case are given in Table 4, for $\phi \in \{0.9, 0.8, 0.7\}$, $n \in \{100, 200, 500\}$, $p_0 \in \{0.001, 0.002, 0.005, 0.010, 0.020, 0.030\}$.

As it can be noticed in Tables 3 and 4, depending on the values of (ϕ, λ_0) (ZIP case) or (ϕ, n, p_0) (ZIB case), the minimal value of m satisfying $\Delta < 0.05$ can be very large and, in some cases, larger than 100000. Also, neither in the

ϕ	n	p_0	m	ϕ	n	p_0	m	ϕ	n	p_0	m
0.9	100	0.001	$> 10^5$	0.8	100	0.001	$> 10^5$	0.7	100	0.001	$> 10^5$
		0.002	$> 10^5$			0.002	$> 10^5$			0.002	$> 10^5$
		0.005	$> 10^5$			0.005	$> 10^5$			0.005	$> 10^5$
		0.01	201			0.01	$> 10^5$			0.01	$> 10^5$
		0.02	$> 10^5$			0.02	$> 10^5$			0.02	$> 10^5$
		0.03	$> 10^5$			0.03	289			0.03	$> 10^5$
	200	0.001	100		200	0.001	$> 10^5$		200	0.001	$> 10^5$
		0.002	$> 10^5$			0.002	100			0.002	$> 10^5$
		0.005	201			0.005	$> 10^5$			0.005	$> 10^5$
		0.01	$> 10^5$			0.01	$> 10^5$			0.01	$> 10^5$
		0.02	664			0.02	$> 10^5$			0.02	249
		0.03	$> 10^5$			0.03	$> 10^5$			0.03	361
	500	0.001	$> 10^5$		500	0.001	$> 10^5$		500	0.001	$> 10^5$
		0.002	201			0.002	$> 10^5$			0.002	$> 10^5$
		0.005	$> 10^5$			0.005	$> 10^5$			0.005	$> 10^5$
		0.01	$> 10^5$			0.01	424			0.01	$> 10^5$
		0.02	1596			0.02	854			0.02	$> 10^5$
		0.03	$> 10^5$			0.03	$> 10^5$			0.03	$> 10^5$

Table 4. Minimal values of m for $p_0 \in \{0.001, 0.002, 0.005, 0.01, 0.02, 0.03\}$, $n \in \{100, 200, 500, 1000\}$ and $\phi \in \{0.9, 0.8, 0.7\}$ satisfying $\Delta = \frac{|ARL_{0,m} - ARL_{0,\infty}|}{ARL_{0,\infty}} < 0.05$.

case of the upper-sided ZIP-Shewhart nor in the case of the upper-sided ZIB-Shewhart control chart we can identify a trend on m, concerning the parameters (ϕ, λ_0) or (ϕ, n, p_0). Our numerical analysis revealed also that as m approaches the case $m = \infty$, the in-control ARL values converge to a specific value, but this value is not necessarily the in-control ARL value in the known parameter case. We refer to Rakitzis and Castagliola [12] for more details.

Clearly, in practice is not always possible to wait for a long time until the required Phase I samples are accumulated. In order to assist practitionerts, we provide Tables 3 and 4 which contain the in-control ARL and $SDRL$ values along with "corrected" values K' of the chart's design parameter K that takes the size m of the Phase I sample into account. Thus, given the size m of the Phase I sample and using $K = K'$, the in-control ARL value corresponding to the estimated parameter case will be *as close as possible* to the in-control ARL value in the known parameters case, for the specific combination of (ϕ, λ_0) (for the ZIP distribution) or (ϕ, n, p_0) (for the ZIB distribution).

For example, in the case of the upper-sided ZIP-Shewhart chart, for $\phi = 0.8$ and $\lambda_0 = 2$, the in-control ARL $(SDRL)$ is equal to $ARL = 301.87$ (301.37) with $K = 5.49$. When the size of the Phase I sample is $m = 200$, then, the "corrected" value for the chart parameter is $K' = 4.55$ which gives in-control ARL $(SDRL)$ equal to $ARL = 300.99$ (825.09), very close to the in-control ARL value in the known parameter case. It is also worth to mention that using the "corrected" value for K, a reduction in the in-control $SDRL$ value is also attained (i.e., from $SDRL = 8920.58$ to $SDRL = 825.09$). Similar conclusions can be deduced for the ZIB control schemes.

λ_0	m	K'	$\phi = 0.9$ ARL	$SDRL$	K'	$\phi = 0.8$ ARL	$SDRL$	K'	$\phi = 0.7$ ARL	$SDRL$
1	100	5.73	524.39	$> 10^6$	4.68	262.19	1364.69	4.00	174.63	436.38
	200	6.65	525.42	3663.80	4.98	264.25	564.90	4.18	173.12	289.19
	500	7.20	533.43	1080.53	5.24	263.06	388.41	4.33	175.25	213.80
2	100	4.35	190.41	115107.80	4.18	300.49	3869.89	3.62	201.46	669.05
	200	4.97	191.89	764.69	4.55	300.99	825.09	3.82	199.03	375.55
	500	5.38	189.08	317.12	4.78	301.13	476.88	3.95	200.38	273.62
5	100	3.64	319.44	$> 10^6$	3.39	363.80	143914.40	3.00	245.19	2402.66
	200	4.43	319.63	66296.99	3.78	367.75	2279.71	3.21	242.27	649.32
	500	4.98	313.01	899.86	4.04	365.36	726.50	3.35	243.22	375.08

Table 5. "Corrected" values K' of the upper-sided ZIP-Shewhart chart and in-control $(ARL, SDRL)$ values

ϕ	n	p_0	K'	$m = 100$ ARL	$SDRL$	K'	$m = 200$ ARL	$SDRL$	K'	$m = 500$ ARL	$SDRL$
0.9	100	0.005	4.37	108.21	329.16	4.74	109.17	177.42	5.00	111.26	125.66
		0.010	5.70	555.13	908087.60	6.58	546.33	3613.64	7.22	555.21	1148.48
		0.020	4.36	200.30	209643.70	4.98	197.60	907.93	5.39	196.52	333.04
0.8	200	0.005	4.68	268.24	1458.30	4.99	269.55	583.24	5.25	267.77	398.07
		0.010	4.19	315.95	4917.25	4.55	313.71	887.69	4.79	312.42	500.90
		0.020	3.45	251.02	23967.60	3.79	247.40	970.52	4.02	248.00	428.56
0.7	500	0.005	3.54	243.07	1043.81	3.75	239.48	499.74	3.88	239.01	340.09
		0.010	3.00	255.06	2762.43	3.21	250.15	688.87	3.35	249.81	390.23
		0.020	2.46	242.75	30135.24	2.69	243.91	1222.66	2.85	250.85	472.84

Table 6. "Corrected" values K' of the upper-sided ZIB-Shewhart chart and in-control $(ARL, SDRL)$ values

5   Conclusions

In this work we studied the performance of upper-sided Shewhart-type control charts for zero-inflated processes with estimated parameters. Assuming that the zero-inflated parameter ϕ is known, we used the distribution of the moment estimator $\widetilde{\lambda}_0$ of λ_0 (for a ZIP process) and the distribution of the moment estimator $\widetilde{p}_0$ of p_0 (for a ZIB process) in order to evaluate the performance of the respective schemes for several Phase I sample sizes, in terms of ARL and $SDRL$. Our analysis revealed that for processes with an excessive number of zeros, even for large preliminary samples, the performance of the upper-sided ZIP- and ZIB-Shewhart control charts in the estimated parameter is substantially different to the performance in the known parameter case. In order to assist practitioners, practical guidelines for the statistical design of the proposed schemes, when the size m of the preliminary sample is predetermined, were also provided.

References

1. W. J. Braun. Run length distributions for estimated attributes charts. *Metrika*, 50:121–129, 1999.
2. P. Castagliola and S. Wu. Design of the c and np charts when the parameters are estimated. *International Journal of Reliability, Quality and Safety Engineering*, 19(2):1250010, 2012.
3. S. Chakraborti and S. W. Human. Parameter estimation and performance of the $p-$ chart for attributes data. *IEEE Transactions on Reliability*, 55:559–566, 2006.
4. S. Chakraborti and S. W. Human. Properties and performance of the $c-$ chart for attributes data. *Journal of Applied Statistics*, 35:89–100, 2008.
5. Y.-C. Chen and W. T. Song. The effects of sample sizes in Phase I and II on p control chart performance. *Communications in Statistics-Theory and Methods*, 41:4047–4068, 2012.
6. A. A. Fatahi, R. Noorossana, P. Dokouhaki, and B. F. Moghaddam. Zero-inflated Poisson EWMA control chart for monitoring rare-health-related events. *Journal of Mechanics in Medicine and Biology*, 12(4):1250065, 2012.
7. B. He, M. Xie, T. N. Goh, and P. Ranjan. On the estimation error in zero-inflated Poisson model for process control. *International Journal of Reliability, Quality and Safety Engineering*, 10(2):159–169, 2003.
8. S. He, W. Huang, and W. H. Woodall. CUSUM chart for monitoring a zero-inflated Poisson process. *Quality and Reliability Engineering International*, 28:181–192, 2012.
9. N. L. Johnson, A. W. Kemp, and S. Kotz. *Univariate Discrete Distributions*. John Wiley & Sons, 3rd edition, 2005.
10. D. C. Montgomery. *Introduction to Statistical Quality Control*. John Wiley & Sons, Inc., New York, USA, 6th edition, 2009.
11. R. Noorossana, A. A. Fatahi, P. Dokouhaki, and M. Babakhani. ZIB–EWMA control chart for monitoring rare health events. *Journal of Mechanics in Medicine and Biology*, 11(4):881–895, 2011.
12. A. C. Rakitzis and P. Castagliola. The effect of parameter estimation on the performance of one-sided Shewhart control charts for zero-inflated processes. *Communications in Statistics-Theory and Methods*, 2014. (accepted).
13. C. H. Sim and M. H. Lim. Attribute charts for zero-inflated processes. *Communications in Statistics – Simulation and Computation*, 37:1440–1452, 2008.
14. W. H. Woodall. The use of control charts in health-care and public-health surveillance. *Journal of Quality Technology*, 38:88–103, 2006.
15. M. Xie and T. N. Goh. SPC of a near zero-defect process subject to random shocks. *Quality and Reliability Engineering International*, 9:376–386, 1993.
16. M. Xie, B. He, and T.N. Goh. Zero-inflated Poisson model in statistical process control. *Computational Statistics and Data Analysis*, 38:191–201, 2001.

Stochastic Evolution of Stock Market Volume-Price Distributions

Paulo Rocha[1], Frank Raischel[2], João P. da Cruz[3,4], and Pedro G. Lind[4,5]

[1] Mathematical Department, FCUL University of Lisbon, 1749-016 Lisbon, Portugal
(e-mail: `paulorocha99@hotmail.com`)
[2] Instituto Dom Luiz, CGUL, University of Lisbon, 1749-016 Lisbon, Portugal
(e-mail: `raischel@cii.fc.ul.pt`)
[3] Closer Consulting LTD, 4-6 University Way, London E16-2RD, United Kingdom
(e-mail: `joao.cruz@closer.pt`)
[4] Centro Física Teórica e Computacional, Avenida Prof. Gama Pinto 2, 1649-003
Lisboa, Portugal
(e-mail: `joao.cruz@closer.pt`)
[5] ForWind and Institute of Physics, University of Oldenburg, DE-26111 Oldenburg,
Germany
(e-mail: `pedro.g.lind@forwind.de`)

Abstract. Using available data from the New York stock market (NYSM) we test
four different biparametric models to fit the correspondent volume-price distributions
at each 10-minute lag: the Gamma distribution, the inverse Gamma distribution,
the Weibull distribution and the log-normal distribution. The volume-price data,
which measures market capitalization, appears to follow a specific statistical pattern,
other than the evolution of prices measured in similar studies. We find that the inverse
Gamma model gives a superior fit to the volume-price evolution than the other models.
We then focus on the inverse Gamma distribution as a model for the NYSM data and
analyse the evolution of its distribution parameters as a stochastic process. Assuming
that the evolution of these parameters is governed by coupled Langevin equations, we
derive the corresponding drift and diffusion coefficients, which then provide insight
for understanding the mechanisms underlying the evolution of the stock market.
Keywords: Stochastic Distributions,Volatility,Stock Market.

1 Scope and Motivation

In 1973 a breakthrough in financial modelling was proposed by Black and Scholes, who reinterpreted the Langevin equation for Brownian motion to predict value European options, assuming the underlying asset follows a stochastic process in the form[1,2]

$$\frac{dS_t}{S_t} = \mu dt + \sigma dW_t, \tag{1}$$

for $S_0 > 0$, where S_t is the asset price, μ is the mean rate of the asset return and W_t describes a Wiener process, with distribution $W_t \sim N(0, t)$. The value of σ,

so-called volatility, measures the risk associated to the fluctuation of the asset return. Thus, by making a good estimate of its value one is able to establish a criterion for selling and buying in order to optimize the profit.

The BS, and similar stochastic approaches based on Gaussian uncorrelated noise sources, have since then received both strong criticism and improvements, such as stochastic volatility models[3]. It has been acknowledged that in more realistic models the statistics of extreme events, leading to heavy tails in the distributions, as well as correlations between noise sources and other components need to be taken into account.

In this paper we put this important extension in a more general context. From a purely mathematical perspective, for each stochastic variable obeying a given Langevin equation there is a probability density function (PDF) associated to it that fulfils a Fokker-Planck equation[4]. Probability density functions are defined by a few parameters that characterize the corresponding statistical moments. The generalization of the Black-Scholes model to incorporate stochastic volatility is a particular case of having one probability density function whose parameters are themselves stochastic variables governed by stochastic differential equations. By modelling such "stochastic" probability density functions one is able to properly describe how they evolve and, thus, evaluate how uncertain is a given prediction of the corresponding variable. We focus here on the evolution of the volume-price, i.e. on changes in capitalization, which should have more the character of a conserved quantity than the price per se. While the price and volume distribution are useful for portfolio purposes, to have access to the overall distribution of volume-prices provides information about the entire capital traded in the market.

In this paper, we show that heavy tails are present in the statistics of the capitalization, and we specifically present a stochastic evolution equation for the tail parameter. In the context of finance models, such approach can eventually enable one to improve measures of risk and to provide additional insight in risk management.

We start in Sec. 2 by describing the data collected from the New York stock market and in Sec. 3 we apply four typical models in finance to fit the empirical data. We will argue that inverse Gamma is a good model for the cumulative distributions of volume-prices and therefore, in Sec. 4, we concentrate in its fit parameters to mathematically describe the stochastic evolution of volume-price distributions. Conclusions close the paper in Sec. 5.

2   Data

We construct a database of several listed shares extracted from the New York stock market (NYSM) every ten minutes starting in March 16th, 2011 to January 1st, 2014. From the data, we compute volumes distributions for each ten minutes, in order to obtain a full description of the temporal evolution of the transactions. All the data were collected from the website `http://finance.-yahoo.com/` every 10 minutes during almost three years (907 days), yielding a total of $N_p \sim 10^5$ data points.
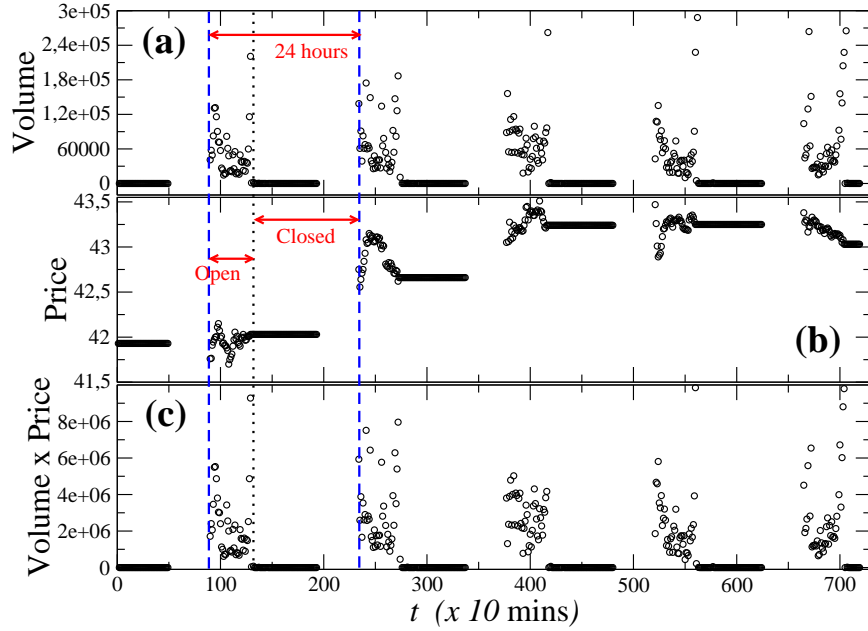
Fig. 1. Illustration of the volume and price evolution for one company during four days: **(a)** volume V, **(b)** price p and **(c)** volume-price pV time-series.

Each register refers to one specific listed company and is composed by the following fields: last trade price, volume, day's high price, day's low price, last trade date, 200 days-moving average, average daily volume and company name. In total, we were able to have a total of $N_e \sim 2000$ listed companies for each time-span of 10 minutes. Since we do not have access to the instantaneous trading price of each transaction for each company, we consider the last trade price as the estimate of the price change on each set of ten minutes trading volume.

Figure 1a and 1b show the evolution of the trading volume V and the last trade price p respectively for one single company during approximately 5 working days. We define the volume-price $s = pV$ as the product of both these properties (see Fig. 1c) and will concentrate henceforth in analysing its joint evolution. This image gives us an idea of how our volume-price s and the separated components, volume V and price p, change along one day in one particular company and, consequently, it reflects the change in capitalization of a given company.

In Fig. 1 we also indicate that the period of six and half hours during which the price change, corresponds exactly to the period at which the NYSM is open, generally from 9:30 am to 4:00 pm (east time). After the market closes, there is still a 4-hour window during which trading occurs, so-called after-hours trading, typically from 4:00 to 8:00 pm. We maintain these largely inactive periods for future studies on the statistics of the after-hours trade. In the context of this study, the changes in capitalization during these periods can be neglected.
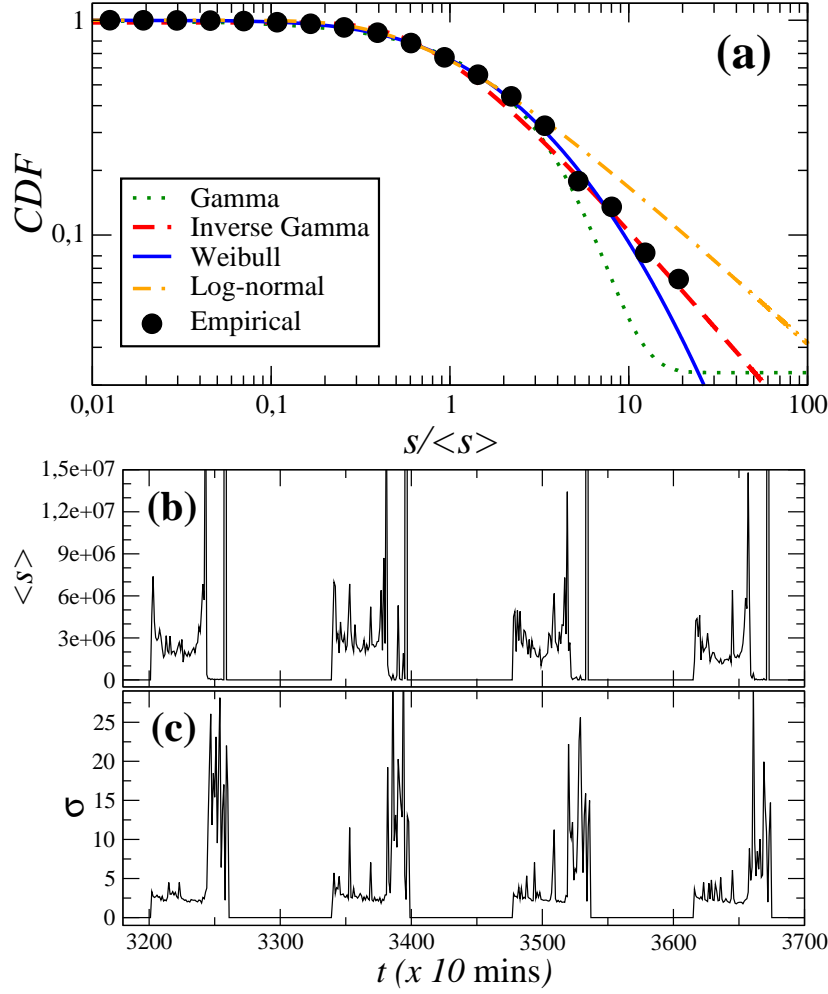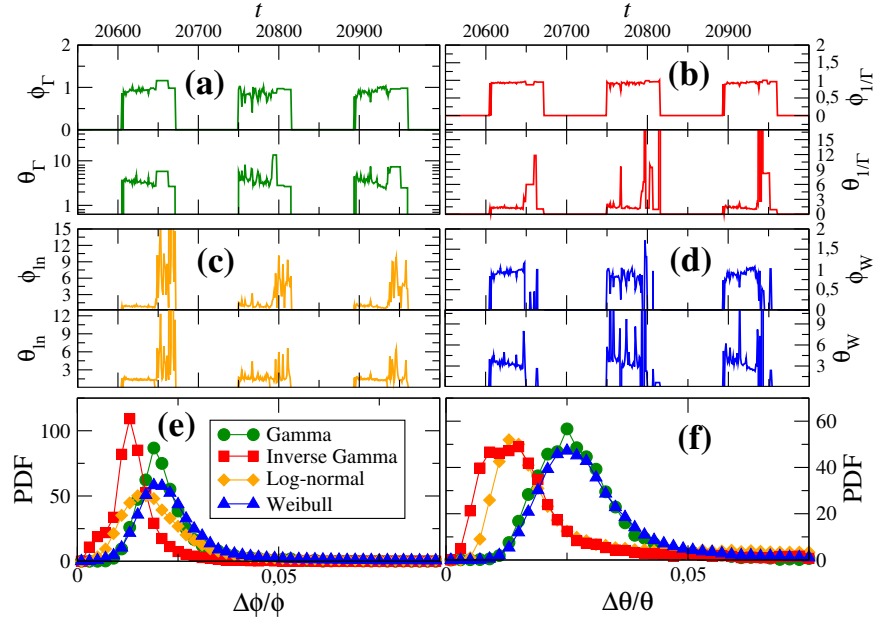
Fig. 2. (a) Numerical cumulative density function fitted by the four different distributions: log-normal distribution $\Gamma-$distribution, inverse $\Gamma-$distribution, Weibull-distribution. To characterize the evolution of the density functions one first considers the time series of the **(a)** empirical volume-price average $\langle s \rangle$ and of the **(b)** corresponding standard deviation σ.

For each 10-minute interval we compute the cumulative density distribution (CDF) of all N_e volume-prices and record its respective average $\langle s \rangle$ over the listed companies, and standard deviation σ. For convenience, we take the volume-price normalized to its average $\langle s \rangle$ when computing the CDF. In Fig. 2a we show the CDF for a particular 10-minute span and in Fig. 2b and 2c one plots the typical evolution of the average and standard deviation respectively.

The choice of the normalized volume-price is the best for assessing the underlying "geometry" of the market as a complex network[5], and therefore we consider henceforth the normalized volume-price $s/\langle s \rangle$. Volume-price repre-

Fig. 3. Time series of the two parameters characterizing the evolution of the cumulative density function (CDF) of the volume-price s: **(a)** Γ-distribution **(b)** inverse Γ-distribution, **(c)** log-normal distribution and **(d)** Weibull distribution. Each point in these time series correspond to 10-minute intervals. Periods with no activity correspond to the period where market is closed, and therefore will not be considered in our approach. **(e-f)** Probability density function of the resulting relative error correspondent to the fitting parameters ϕ and θ for each distribution. In all plots, different colors correspond to different distribution models.

sents the amount of capital of a particular listed company that is exchanged in the market. The normalized distribution of volume-price represents the distribution of links between investors and companies.

	Param. err. $\Delta\phi/\phi$		Param. err. $\Delta\theta/\theta$	
	Average	Std Dev.	Average	Std Dev.
$\Gamma-$distribution	2.21e-2	8.54e-3	2.82e-2	1.16e-2
Inverse $\Gamma-$distribution	**1.43e-2**	**6.46e-3**	**3.43e-2**	**5.49e-2**
Weibull	3.13e-2	5.29e-2	4.89e-2	9.77e-2
Log-normal	3.78e-2	7.53e-2	5.60e-2	9.28e-2

Table 1. The average and standard deviations of the value distributions for each parameter error, $\Delta\phi/\phi$ and $\Delta\theta/\theta$, in Fig. 3e-f. The best fit is indeed obtained for the inverse Gamma distribution.

3 Four models for volume-price distributions

In order to find a good fit to the empirical CDF we will consider four well-known bi-parametric distributions, namely the Gamma distribution, inverse Gamma distribution, log-normal distribution and the Weibull distribution. We fit the empirical CDF data (bullets in Fig. 2a) with these four different models, which are often used for finance data analysis[6].

The Gamma probability density function (PDF) is given by

$$F_\Gamma(s) = \frac{s^{\phi_\Gamma - 1}}{\theta_\Gamma^{\phi_\Gamma} \, \Gamma[\phi_\Gamma]} exp\left[-\frac{s}{\theta_\Gamma}\right],$$ (2)

the inverse Gamma PDF by

$$F_{1/\Gamma}(s) = \frac{\theta_{1/\Gamma}^{\phi_{1/\Gamma}}}{\Gamma[\phi_{1/\Gamma}]} s^{-\phi_{1/\Gamma}-1} exp\left[-\frac{\theta_{1/\Gamma}}{s}\right],$$ (3)

the log-normal PDF by

$$F_{\ln}(s) = \frac{1}{s\theta_{\ln}\sqrt{2\pi}} exp\left[-\frac{(\log s - \phi_{\ln})^2}{2\theta_{\ln}^2}\right]$$ (4)

and the Weibull PDF by

$$F_W(s) = \frac{\phi_W}{\theta_W^{\phi_W}} s^{\phi_W - 1} exp\left[-\left(\frac{s}{\theta_W}\right)^{\phi_W}\right].$$ (5)

In Fig. 2a we plot the corresponding fit of each of these models for the empirical CDF. In Fig. 3(a-d) we show a short time-interval of the series of each pair of parameter.

For each model above, we take into account the relative error of each parameter value, $\Delta\phi/\phi$ and $\Delta\theta/\theta$, computed using a least square scheme when making the fit. Figure 3e and 3f show the distributions of the observed relative errors of ϕ and θ respectively. From these two plots it seems that each distribution fits quite well the empirical CDF data, since relative errors are mostly under five percent. From the inspection of Fig. 3e and 3f as well as Tab. 1, one sees that the best fit seems to be for the inverse Gamma distribution and therefore we will consider henceforth only this distribution.

4 The stochastic evolution of inverse Gamma tails

To explore the inverse Gamma distribution model, we first consider the meaning of its two parameters. A closer look at Eq. (3) leads to the conclusion that while θ characterizes the shape of the distribution for the lowest range of volume-prices, the parameter ϕ characterizes the power law tail $\sim s^{-\phi-1}$. Since it is this tail that incorporates the large fluctuations of volume-prices, in this section
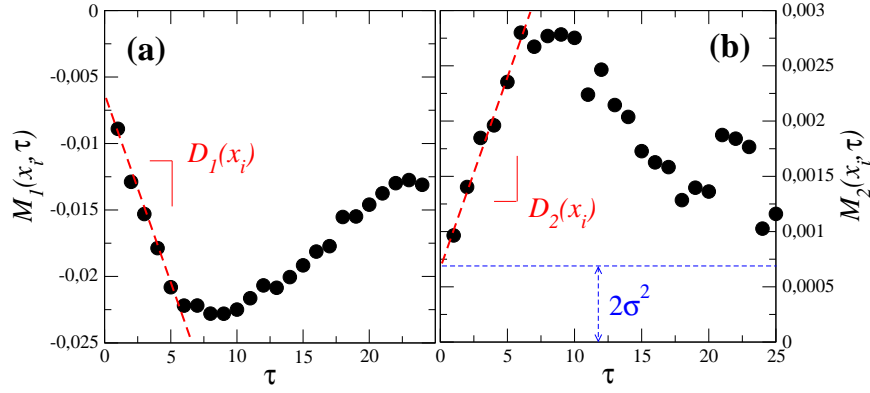
Fig. 4. Illustration of the conditional moments computed directly from the time series of the ϕ time-series for the inverse-Γ: **(a)** first conditional moment $M^{(1)}$ and **(b)** first conditional moment $M^{(2)}$, from which one can conclude about the possible existence of measurement noise sources (see text). Here x_i is the bin including the average value $\langle \phi \rangle$.

we focus on the evolution of the parameter ϕ solely. Label $1/\Gamma$ is dropped for simplicity.

Taking the time series of the parameter ϕ we derive the stochastic evolution equation as thoroughly described in Ref. [7]. This approach retrieves two functions, called the drift and diffusion coefficients[4], $D_1(\phi)$ and $D_2(\phi)$, governing the stochastic evolution of ϕ:

$$d\phi = D_1(\phi)dt + \sqrt{D_2(\phi)}dW_t. \tag{6}$$

Where W_t represents the typical Wiener process, with $\langle W_t \rangle = 0$ and $\langle W_t W_t' \rangle = 2\delta(t - t')$. Typically the drift term governs the deterministic contributions for the overall evolution of ϕ, while the diffusion term governs the corresponding (stochastic) fluctuations.

Functions $D_1(\phi)$ and $D_2(\phi)$ can be computed directly from the data[7] computing the first and second conditional moments respectively ($n = 1, 2$):

$$D_n(\phi_i) = \lim_{\tau \to 0} \frac{1}{n!\tau} M_n(\phi_i, \tau), \tag{7}$$

where ϕ_i represents one specific bin-point in the range of observable values and the conditional moment is given by

$$M_n(\phi_i, \tau) = \langle (\phi(t + \tau) - \phi(t))^n \rangle|_{\phi(t)=\phi_i}. \tag{8}$$

Figure 4a and 4b show the first and second conditional moments respectively, as a function of τ, for a given bin value ϕ_i. For the lowest range of τ values one sees a linear dependence of the conditional moments, which enables to directly extract the corresponding value of the drift and diffusion in Eq. (7). Further, there is a clear offset in both moments, which indicates the presence of an additional stochastic process superimposed on the intrinsic stochastic
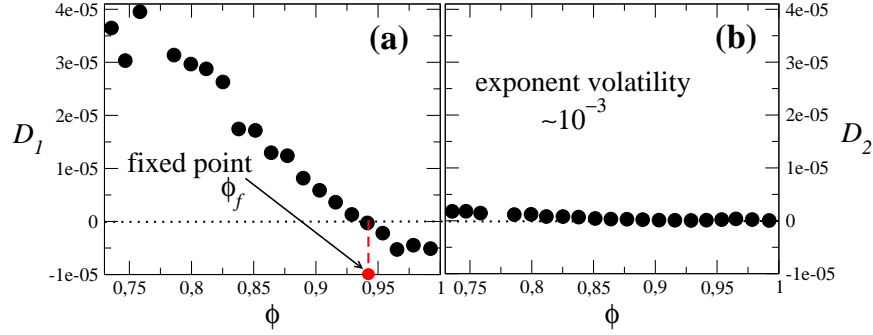
Fig. 5. (a) The drift and (b) diffusion coefficients characterizing the stochastic evolution of the parameter ϕ that describes the tail of the inverse-Γ distribution (see text).

dynamics, called measurement noise[8], whose amplitude can be estimated as $\sigma = \sqrt{M_2(\langle\phi\rangle, 0)/2}$[9]. See Fig. 4b.

By computing the slopes of M_1 and M_2 for each bin in variable ϕ yields a complete definition of both drift D_1 and diffusion D_2 coefficients for the full range of observed ϕ values. Figures 5a and 5b show the drift and diffusion respectively. While the diffusion term has an almost constant amplitude, $\sqrt{D_2} \sim 10^{-3}$, the drift is linear on ϕ with a negative sloped and a fixed point close to one, $\phi_f \sim 0.93$.

This last observation is interesting from the point of view of the inverse Gamma PDF: the volume-price tails fluctuate around an inverse square law $\sim s^{-2}$ driven by a restoring force which can be modelled through Hooke's law. Furthermore, the fluctuations around the inverse square law are quantified by the diffusion amplitude $\sqrt{D_2}$ of the tail parameter, which can be interpreted as a sort of "parameter volatility".

5   Discussion and Conclusions

In this paper we analyse New York stock market volume-price distributions during the last two years sampled every ten minutes. We tested four models commonly applied to finance data and presented evidence that the inverse Gamma distribution is the model yielding the least error.

Further, we considered the parameter controlling the tail of the inverse Gamma distribution and extracted a Langevin equation governing its stochastic evolution directly from the parameter's time series. While the deterministic contribution (drift) depends linearly on the parameter, with a restoring force around unity approximately, the stochastic contribution (diffusion) is almost constant. Considering both contributions together, our findings show that the tail of the volume-price distributions tend to evolve stochastically around an inverse square law with a constant parameter volatility.

This parameter volatility can be proposed as a risk measure for the expected tail of New York assets. The analysis propose here can be extended to other

markets or even in other contexts where non-stationary processes are observed. If the inverse Gamma distribution is commonly the best model for volume-price distributions is up to our knowledge an open question. The confidence of each model can be further tested using other methods such as the Kolmogorov-Smirnov test[10].

It must be noticed that the above approach is only valid for Markovian processes, which seems to be the case of the parameter here considered, which was tested comparing two-point and three-point conditional probabilities. Moreover, the Langevin analysis here proposed can also be extended to both parameters characterizing the inverse Gamma model. Further research will be necessary to access the reliability of the stochastic reconstruction of the volume-price evolution, and a comparison to theoretical agent models. These and other issues will be addressed elsewhere.

Acknowledgments

References

1. F. Black and M. Scholes Journal of Political Economy **81**(3), 637654 (1973).
2. R.C. Merton, Bell Journal of Economics and Management Science **4**(1), 141183 (1973).
3. S.L. Heston, Rev. Financ. Std **6**(2), 327343 (1993).
4. H. Risken, *The Fokker-Planck Equation* (Springer, Heidelberg,1984).
5. J.P. da Cruz, P.G. Lind, Physics Letters A **377** (2013).
6. S. Camargo, S.M.D. Queirós and Celia Anteneodo, Eur. Phys. J. B **86** 159 (2013).
7. R. Friedrich, J. Peinke, M. Sahimi and M.R.R. Tabar, Phys. Rep. **506** 87 (2011).
8. F. Boettcher, J. Peinke, D. Kleinhans, R. Friedrich, P.G. Lind, M. Haase, Phys. Rev. Lett. **97** 090603 (2006).
9. P.G. Lind, M. Haase, F. Boettcher, J. Peinke, D. Kleinhans and R. Friedrich, Physical Review E 81 041125 (2010).
10. D. Kleinhans, Phys. Rev. E **85** 026705 (2012).

Including Path Continuity Properties in Process Estimation

Lino Sant

Department of Statistics and Operations Research,
Faculty of Science, University of Malta, Msida, Malta
(e-mail: `lino.sant@um.edu.mt`)

Abstract. Estimation of parameters for processes with independent increments is many times effected exclusively through fitting an infinitely divisible distribution on increments obtained from finitely many readings. Ignoring path properties, which have been involved in data generation in the first place, must have negative effects. Much work has been done to improve the quality of simulated data from that generated through cumulative sums of independent random variates. Exact simulation tries to put in more realism about path properties. In this paper we study this situation within the simple context of Brownian motion, proposing two estimators which incorporate properties related to path continuity. Results obtained from simulations with data generated by various types of algorithms are compared and contrasted with ones obtained from the less sophisticated variance estimator.

Keywords: estimation from stationary and independent increments, simulated paths , continuity of paths.

1 Introduction

Parameter estimation, intended so as to help determine the type of stochastic process one should use for specific data generating mechanisms, is common in many applications of probability and statistical theory. Once the pioneers of random processes paved a highway towards deep structural results within the realm of the mathematically possible, effective use of stochastic models required a number of tasks. One important statistical task centres around devising reliable algorithms to estimate parameters and functionals of particular processes from a finite number of observations.

One widely used technique involved specifying a probability density function which captures the true distribution of the observations in a form which facilitates the estimation problem. The stationary, independent increments assumption, for example, simplifies many estimation tasks enormously by allowing standard methods like maximum likelihood to take over. However this type of assumption encapsulates much less than what would identify a particular process completely. Independent, stationary increments on their own are not sufficient to force a process to be Lévy. We need right continuity of paths

besides stochastic continuity. There are many processes which could provide observations whose differences are effectively identically distributed, as well as independent, but nowhere close to being the process we want. For example, the class of all cumulative sums of centred normals with variance δt cannot be identified with Wiener processes or with the class of all finite evaluations of a continuous path chosen in compliance with Wiener measure and sampled at discrete times. Similar considerations apply to Lévy processes.

2   Context

Rather than go for Lévy processes, we plan to take a step or two backwards and limit ourselves to Brownian motion, which in its simplicity offers a neater context to come to grips with the basics. We consider Brownian motion B_t, $t \in \mathbb{R}_+$, observed as a finite sequence of readings over equally spaced intervals of time at $0 = t_0 < t_1 < ... < t_n = t$. Random variables B_{t_i} have increments $B_{t_{i+1}} - B_{t_i}$ which are independent, centred, normally distributed with variance $\sigma^2(t_{i+1} - t_i)$. The purely distributional properties of the increments might be what interests a statistician especially if he uses Brownian approximations to complex estimators via Donsker's theorem, or the Hungarian construction, to mention but just two much used approximations.

From the stochastic processes point of view the estimation of a process exclusively through increments loses a lot of information by ignoring the path properties of the parent process. Processes which jump at fixed times t_i in normal increments are processes in their own right. Brownian motion is much more than that; including, as it does, the possibility of fleshing itself out on paths which are continuous with probability 1. We propose to study the differences between two scale estimators, which somehow recognize this property, with the classical one which ignores it.

The sequence of partial sums of centred iid normal random variables $S_n = \sum_{i=1}^{n} X_i$ is a discrete-parameter stochastic process, which interests statisticians for they come across it in many situations involving estimations of all sorts. Donsker's theorem tells us that this process can be **approximated** by Brownian motion. We zoom on the differences between these two processes. Elementary theory tells us that $\max_{0 \le s \le t} B_s$ is distributed as $|B_t|$. And this result utilizes continuity of the paths. The distribution of the maximum of S_n above, suitably scaled, is different from that of $|B_t|$. Exact distributions of sum of independent, identically distributed random variables are hard to come by and very messy to establish. A number of published asymptotic results using Brownian approximations are available. The level of dissatisfaction with random walk approximations of this type as articulated in [1], has been brought to notice more than once. We displace this argument slightly by asking "What are we missing when we estimate Brownian motion solely through the independent increments assumption?"

We develop this idea further by exploiting differences between the exact distributions for the maximum of finite sums and the Brownian running maximum translated into statistics which depend on path continuity in the Brownian case. We quote some results and supply an accompanying graph:

$$\mathbb{E}[\max_{1 \leq i \leq n} S_i] = \frac{\sigma}{\sqrt{2\pi}} \sum_{i=1}^{n-1} \frac{1}{\sqrt{i}} \tag{1}$$

$$\mathbb{E}[\max_{1 \leq s \leq t} B_s] = \sqrt{\frac{2t}{\pi}} \tag{2}$$
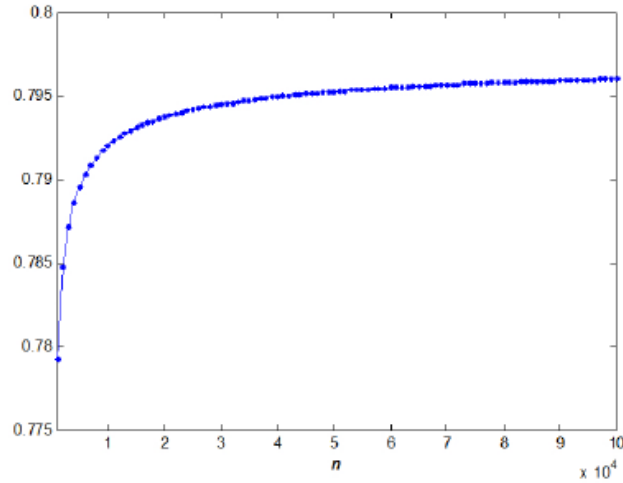
Fig. 1. Increase in Expected Maximum of Sums with no of terms n

The first equation is proved in [7]. We note that the expectation for the Brownian expression is always greater than for finite sums suitably scaled; $\sigma = \frac{1}{\sqrt{n}}$. We note how slow is the convergence of the finite sums to $\frac{1}{\sqrt{2\pi}} \approx 0.797884560802865$. At $n = 100000$ the sum equals 0.796040232112369. The emphasis on continuous paths for getting from one time instant to the next, enforced probabilistically by Wiener measure, lifts the expectation of the maximum value slightly higher than if we performed independent jumps at each time instant.

In a precise sense these problems have to be analysed in reverse within the context of simulation. Generating sample values, which are supposed to come from a Brownian process through independent normal increments, is very approximative. In some applications this just will not do.

3 Accurate Simulation of Brownian Paths

Simulated Brownian paths have many uses. Not only are they used in replicating physical and virtual phenomena which resemble Brownian motion, but they are used extensively in complex computations of various statistical functionals for which explicit analytical formulas are not known or not easily computable. High frequency financial data, for instance, needs to be collected and analyzed in a particular manner with a close watch on running maxima and local minima. This will enable modelling and pricing of barrier options products which constitute but one example as mentioned in [1]. In such cases the evaluation of functionals of Brownian paths needs to be carried out with high precision, not only in financial and actuarial applications but in others within the natural sciences.

The ability to replicate running maxima and minima credibly is therefore one feature which would be requested from simulations of Brownian motion. As we have noted the behaviour of these two extremes depend a lot on the continuity of paths. Reproducing faithfully maxima and minima has motivated a lot of work aimed at producing algorithms which are marketed as giving "exact" simulations. Much ingenuity has been displayed recently resulting in new developments this area. Actually most research has targeted more generally diffusion processes, with crucial input of techniques from importance and rejection sampling [3].

Our interest in simulation stems more from the fact that we would like to test our estimators using good simulated data. One cannot test accurately the quality of an estimator if the data on which the testing is effected is not exactly what it is supposed to be : random selections from a Brownian motion in our case. One of the arguments being pushed in this paper is that poorly representative simulated data may favour weaker algorithms, because certain important features, like properties inherited from continuity of paths, would be missing in the readings which will be used for calibration and evaluation purposes. So we settled for four methods, two which ignore continuity of paths, and two which have continuity inbuilt in their construction.

Furthermore we shall use data generated by four different algorithms:

- using cumulative sums of normal iid rv's [IID]
- using Brownian bridge interpolations [BB]
- using a Fourier series expansion of the sample paths [FS]
- using first passage times to construct an "exact algorithm" [EX]

The first algorithm needs no comment. The second consists of a random $N(0,1)$ end-point at $t = 1$, with mid-points being generated as points of a Brownian bridge in the manner of Lévy's construction. The third is implemented through the series expansion:

$$B_t = tZ_0 + \frac{\sqrt{2}}{\pi} \sum_{n=1}^{\infty} \frac{Z_n}{n} \sin n\pi t, \ 0 \leq t \leq 1$$

Continuity of paths is inbuilt through the series of functions, though continuity of the limit path would be assured only in the presence of uniform

convergence. The fourth algorithm would be classified as an "exact" simulation. It uses a rejection algorithm as developed in [5] for the generation of a sequence of hitting times of Brownian motion as it crosses fixed boundaries starting from zero. The position of the path at intermediate time points t_i are worked out using the distribution of Brownian bridge which is boxed in value between the values of the boundaries within which the path lives. The relevant distributional result is given further down in this paper.

4 The Wiener Measure

Sampling paths of a Wiener process randomly means that the probability of a given measurable set of paths being picked up is precisely the Wiener measure of that set. Individual paths have Wiener measure 0; let alone paths which pass through finitely many points at given corresponding instants of time. Being unable to go directly for Wiener measure, we have to hook on to it through particular properties of Brownian motion. Gaussianity of the finite-dimensional distributions of a process is a very important central property, but not sufficient to declare the process to be Wiener. So, as we have indicated, we shall somehow insist on continuity of the paths. Continuity of paths, when the readings are at finitely many points, obviously cannot be imposed directly. So we look for properties which continuity imposes on the behaviour over time on the process, and which are recoverable from, and reflected in, the running maxima and minima processes. Denoting these processes by $M_t = \max\limits_{0 \leq s \leq t} B_s$ and $m_t = \min\limits_{0 \leq s \leq t} B_s$, respectively, the technique for using, as well as enforcing, continuity properties on the paths is to box individual paths between these two processes and relate the three processes probabilistically. We shall need some important results relating to the above, which we now state. First we give two forms of the joint distributions of (m_t, B_t, M_t) for $a \leq x \leq b$, and $a \leq 0$, $b \geq 0$:

$$\mathbb{P}[m_t \leq a, B_t \in dx, M_t \geq b] = \frac{dx}{\sigma\sqrt{2\pi t}} e^{\frac{-(x-2(M-m))^2}{2\sigma^2 t}} \qquad (3)$$

$$\mathbb{P}[m_t > a, B_t \in dx, M_t < b] = \frac{dx}{\sigma\sqrt{2\pi t}} \sum_{k=-\infty}^{\infty} e^{\frac{-(x+2k(b-a)^2)}{(2\sigma^2 t)}} - e^{\frac{-(x-2a+2k(b-a))^2}{(2\sigma^2 t)}} \qquad (4)$$

By marginalizing through B_t we obtain the conditional distribution function for the running maximum and minimum:

$$\mathbb{P}[M_t \geq b, m_t \leq a | B_t = x] = exp\left(\frac{2(b-a)(x-2(b-a))}{\sigma^2 t}\right) \qquad (5)$$

We obtain a formula for Wiener measure on $\mathcal{C}([0,1])$ suitably augmented by a set of probability 0, which we denote by $\mathbb{P}_{\mathbb{W}}$, by integrating out x from a to b to obtain:

$$\mathbb{P}_{\mathbb{W}}[\{f \in \mathcal{C}([0,1] : a < f(s) < b, \forall s \text{ s.t. } 0 \le s \le t\}] =$$

$$\sum_{k=-\infty}^{\infty} \Phi\left(\frac{b + 2k(b-a))}{\sigma\sqrt{2\pi t}}\right) - \Phi\left(\frac{a + 2k(b-a))}{\sigma\sqrt{2\pi t}}\right)$$

$$+ \sum_{k=-\infty}^{\infty} \Phi\left(\frac{b - 2a + 2k(b-a))}{\sigma\sqrt{2\pi t}}\right) - \Phi\left(\frac{a - 2a + 2k(b-a))}{\sigma\sqrt{2\pi t}}\right) \qquad (6)$$

These formulas will be found in various forms and variants in [2]. The last one is of particular interest to us. It has been known since the classical book by Feller on probability theory, not to mention Lévy's book on stochastic processes published in the 1940's. We shall denote the probability above in this formula by $\Psi_{\mathbb{W}}(a, b, t, \sigma)$. Though it involves a series, the formula it is derived from, namely (4), converges uniformly in $x \in [a, b]$ and does so very fast [6].

5 The Estimators

We propose now to take on an estimation problem for which the classical method, using exclusively distributional properties of independent increments, should be unbeatable. Not only does it exhibit unbiasedness but it achieves the Cramér-Rao minimum. We consider estimation of the variance σ^2 for which we devise two estimators which take continuity of paths into consideration. Such estimators should be more useful in estimation problems for linear and nonlinear diffusions. Generalizing this work to diffusions should be straightforward. It will not be attempted here, but left for future work because generalization will only make the notation and formulas so much more complicated as to hide the real issues. Since most results are asymptotic, sample size and discretization errors exert a strong influence. Largely we stay within the scope of maximum likelihood estimators. Such estimators are not unique in general. In some cases, more than one likelihood function can be used fruitfully. In our case we shall involve the running maximum and minimum in one estimator and the Wiener measure in the other, so as to factor in constraints which continuous paths satisfy.

Denoting increments by $X_i = B_{t_i} - B_{t_{i-1}}$ and letting $M_i = \max_{0 \le i \le n} B_{t_i}$, $m_i = \min_{0 \le i \le n} B_{t_i}$ we write the joint density function using the usual iid assumption and multiply in the conditional distribution function from (5) :

$$\frac{1}{(\sqrt{2\pi}\sigma t)^n} \exp\left(\frac{-1}{2\sigma^2 \delta t} \sum_{i=1}^{n} X_i^2\right) \exp\frac{2(M_n - m_n)(B_n - 2(M_n - m_n))}{t\sigma^2}$$

We generate our first estimator as the maximizer of the log likelihood:

$$\widehat{\sigma^2}_1 = \arg\min_{s^2} \left[n\log(s) + \frac{1}{2\delta t s^2}\left(\sum_{i=1}^{n} X_i^2 - \frac{4}{n}(M_n - m_n)(B_n - 2(M_n - m_n))\right)\right] \tag{7}$$

For the second estimator we involve the Wiener measure by maximizing the probability that the path is included within the latest values of the maximum and minimum:

$$\widehat{\sigma^2}_2 = \arg\min_{s^2} \left[n\log(s) + \frac{1}{2\delta t s^2} \left(\sum_{i=1}^{n} X_i^2 \right) - \log(\Psi(m_n, M_n, t, s)) \right] \qquad (8)$$

These two estimators introduce continuity of paths by stealth, as it were. They penalize parameter estimates which distributionally make current sample values of the running maximum and minimum less likely in two different senses. In this sense they can be considered as being of the maximum likelihood type. In fact the usual properties can be proved to be asymtotically true but we shall not indulge in this here.

6 Estimator Performance

We proceed to discuss how we shall test the performance of the estimators. It is customary to evaluate the qualities of estimators in terms of the usual, simple statistical properties like unbiasedness and efficiency. We shall indeed compute means and variances over large samples. Furthermore as benchmark performer we shall take the likelihood-based, common unsophisticated variance estimator :

$$\widehat{\sigma^2}_0 = \frac{1}{n\delta t} \sum_{i=1}^{n} X_i^2 \qquad (9)$$

Theoretically this is an unbiased, minimum variance estimator- but only relative to the information which we use in constructing it. This information excludes any reference to continuity of paths. Unexpected departures from its proven properties will make us uncomfortable about the quality of the data on which we are testing. So the usual statistical properties are worth checking. However, from a more pragmatic point of view, in many contexts there are other criteria in evaluating estimation procedures which would be more crucial.

Especially within financial modelling exercises, the more frequently closer to the true value, in absolute terms, the individual estimates are, the much better the estimators are to be considered. This observation leads us to formulate a criterion that estimators which have a higher probability of giving estimates closer to the true values than others are somehow to be preferred. Roughly speaking, we judge estimators which have higher rates of convergence in achieving consistency to be preferable. More precisely, given estimators $\hat{\boldsymbol{\theta}}_1, \hat{\boldsymbol{\theta}}_2$, if $\mathbb{P}[|\hat{\boldsymbol{\theta}}_1 - \boldsymbol{\theta}| > |\hat{\boldsymbol{\theta}}_2 - \boldsymbol{\theta}|] > 0.5$ then we declare $\hat{\boldsymbol{\theta}}_2$ to be preferable; more than 50 % of all samples should give $\hat{\boldsymbol{\theta}}_2$ estimates which are closer to the true value. We shall investigate how this probability changes as the number of observations over a time interval of the same length increases.

In our setting, again for the sake of transparency, we take $\sigma^2 = 1$ and the time interval is $[0, 1]$ with n equally spaced instants at which we have the observations B_i. Four sets of data were generated by the corresponding four algorithms mentioned earlier. Each set consists of four collections of outputs from 1000 simulated "paths". The difference between the collections is the frequency at which the paths were measured. These frequencies correspond to the four values $n = 100, 200, 500$ and 1000 (128, 256, 512 and 1024 for DS2) giving equally spaced time instants $0, \frac{1}{n}, ..., \frac{n}{n}$ over the unit time interval. DS1 was generated using algorithm IID, DS2 using BB , DB3 using FS and DB4 using EX. Each sequence of n readings, corresponding to one path was used to give estimates for σ^2 by each of the three methods described above.

7   Estimation Results from Simulations

Table 1 gives us the usual statistical measures for estimates from the benchmark estimator. As far as DS1 and DS2 are concerned, everything is as expected. Only the distributional properties of Brownian motion are taken into consideration by the simulating algorithms and $\widehat{\sigma^2}_0$ picks them up well enough. From DS3 and DS4, however, we see actually a deterioration of the estimate means as the sample size increases! The situation with the variance is also worse than for the other 2 algorithms. This evidence indicates that the closer the data generating mechanism follows the behaviour of selections from Brownian motion, the less faithfully are usual distributional properties observed because of discretization.

No of obs	Estimator $\widehat{\sigma^2}_0$							
	DS1		DS2(*)		DS3		DS4	
	Mean	Variance	Mean	Variance	Mean	Variance	Mean	Variance
1000	0.99989	0.000498	0.99978	0.000504	0.97924	0.000921	0.98390	0.007510
500	0.99803	0.000985	0.99838	0.000993	0.98900	0.001048	0.99140	0.000981
200	1.00099	0.002279	0.99648	0.001991	0.99452	0.002518	0.99530	0.002300
100	0.99662	0.005442	0.99950	0.003980	0.99407	0.005551	0.99602	0.004811

Table 1. Means and Variances of $\widehat{\sigma^2}_0$ on All Datasets.

(*) sample sizes for DS2 were in fact 1024, 512 , 256 , 128

Tables 2 and 3 reveal that the behaviour of $\widehat{\sigma^2}_1$ is statistically very similar to that of $\widehat{\sigma^2}_2$. The second estimator is consistently more accurate and has less variability within its results for the datasets which represent Brownian motion worst. We also see that increasing sample size improved the quality of the estimates throughout. Compared to results for $\widehat{\sigma^2}_0$ we see that on DS3 and DS4 the two proposed estimators are indeed superior even though not by much. Considering that we are comparing performances on territory on which $\widehat{\sigma^2}_0$ should reign supreme, the two estimators have done well.

	Estimator $\widehat{\sigma^2}_1$							
No of obs	DS1		DS2(*)		DS3		DS4	
	Mean	Variance	Mean	Variance	Mean	Variance	Mean	Variance
1000	1.00477	0.000550	1.00493	0.000558	0.98477	0.000770	0.98930	0.006344
500	1.00822	0.001190	1.00872	0.001201	0.99910	0.001054	1.00150	0.001113
200	1.02424	0.003561	1.01710	0.002761	1.01835	0.003410	1.01940	0.003400
100	1.04560	0.010754	1.03711	0.007026	1.03762	0.009348	1.04358	0.009627

Table 2. Means and Variances of $\widehat{\sigma^2}_1$ on All Datasets.

(*) sample sizes for DS2 were in fact 1024, 512 , 256 , 128

	Estimator $\widehat{\sigma^2}_2$							
No of obs	DS1		DS2(*)		DS3		DS4	
	Mean	Variance	Mean	Variance	Mean	Variance	Mean	Variance
1000	1.00277	0.000507	1.00252	0.000507	0.98204	0.000824	0.98690	0.006660
500	1.00333	0.001001	1.00374	0.001056	0.99440	0.000961	0.99700	0.000986
200	1.01595	0.002589	1.00725	0.002130	1.00861	0.002625	1.00910	0.002400
100	1.02938	0.007224	1.02345	0.005010	1.02854	0.007669	1.03122	0.007269

Table 3. Means and Variances of $\widehat{\sigma^2}_2$ on All Datasets.

(*) sample sizes for DS2 were in fact 1024, 512 , 256 , 128

Finally we consider direct confrontation between our estimators and the benchmark. Table 4 gives very clear indications. For relatively low frequency data, the increase in information which is incorporated in $\widehat{\sigma^1}_2$ fails to beat the robust performance of the benchmark especially on the latter's home territory with data generated by IID and BB. For high frequency however the tables are turned with a remarkable increase in precision of $\widehat{\sigma^2}_1$. Over 70% of the estimates from $\widehat{\sigma^2}_1$ come closer to the true value than the benchmark.

Dataset DS1 using IID				
No of obs	1000	500	200	100
Probability	0.452	0.461	0.408	0.406

Dataset DS2 using BB				
No of obs	1024	512	256	128
Probability	0.461	0.467	0.451	0.391

Dataset DS3 using FS				
No of obs	1000	500	200	100
Probability	0.787	0.574	0.464	0.409

Dataset DS4 using EX				
No of obs	1000	500	200	100
Probability	0.719	0.569	0.434	0.401

Table 4. Estimated probs of Estimator $\widehat{\sigma^2}_1$ Giving Closer Estimates than $\widehat{\sigma^2}_0$

Dataset DS1 using IID				
No of obs	1000	500	200	100
Probability	0.486	0.512	0.451	0.481
Dataset DS2 using BB				
No of obs	1024	512	256	128
Probability	0.491	0.507	0.497	0.451
Dataset DS3 using FS				
No of obs	1000	500	200	100
Probability	0.799	0.631	0.516	0.475
Dataset DS4 using EX				
No of obs	1000	500	200	100
Probability	0.743	0.607	0.509	0.466

Table 5. Estimated probs of Estimator $\widehat{\sigma^2}_2$ Giving Closer Estimates than $\widehat{\sigma^2}_0$

Table 5 gives the same message as the previous one. It actually displays the excellent performance throughout of $\widehat{\sigma^2}_2$ which does better than $\widehat{\sigma^2}_1$. This in a sense was to be expected. Sampling from Brownian paths should reflect Wiener measure. And $\widehat{\sigma^2}_2$ tries to favoor parameter estimates which do exactly that directly.

8 Conclusion

The aim of this paper was to study ways in which incorporating path properties of a process, whose parameter is being estimated, improves estimator performance. This was implemented on a simple setting involving Brownian motion. Given the discrete structure of data available in many applications, knowledge of what happens between actual readings is missing. But that does not mean we do know what should happen probabilistically. The two estimators we proposed incorporates features which respond to path continuity features. And the results indicate that for high frequency data, the estimators are superior. When the time gap between readings is longer the effect of what should happen in between seems to relax. For empirical of analysis financial data this should have repercussions.

References

1. Becker M., "Exact simulation of final, minimal and maximal values of Brownian motion and jump-diffusions with applications to option pricing", *Computational Management Science* 7, 1, 1-17 , (2010).
2. Borodin A.N. and Salminen P., "Handbook of Brownian Motion - Facts and Formulae", 2. Aufl. Probability and its Applications, Birkhäuser, Basel, 2002.
3. Beskos, A., Papaspiliopoulos O., Roberts, G. and Fearnhead P., "Exact and computationally efficient likelihood-based estimation for discretely observed diffusion processes", J. R. Stat. Soc. Ser. B Stat. Methodol. 68 333382 (2006).

4. Beskos, A., Peluchetti S. and Roberts G., "ϵ-Strong simulation of the Brownian path", *Bernouilli* 18, 4, 1223-1248, (2012).

5. Burq Z.A. and Jones O.D., "Simulation of Brownian motion at first-passage times", *Mathematics and Computers in Simulation* 77, 64-71 , (2008).

6. Choi B.S. and Roh J.H., "On the trivariate joint distribution of Brownian motion and its maximum and minimum", *Statistical and Probability Letters*, 83, 1046-1053, (2013).

7. Tang Strait P., "On the Maximum and Minimum of Partial Sums of Random Variables" *Pacific Journal of Mathematics*, 53, 2 , 585-593 (1974).

Estimation of Lévy Processes through Stochastic Programming

Lino Sant[1] and Mark Anthony Caruana[2]

[1] Department of Statistics and Operations Research,
Faculty of Science, University of Malta, Msida, Malta
(e-mail: `lino.sant@um.edu.mt`)
[2] Department of Statistics and Operations Research
Faculty of Science, University of Malta, Msida, Malta
(e-mail: `mark.caruana@um.edu.mt`)

Abstract. Estimation of Lévy processes with the use of the characteristic function has lately shifted much of its attention to nonparametric settings. However the parametric context still offers scope for study. The nature of neighbourhoods of the minima sought for by the integrated square error estimator (ISEE), and its variants, could be meaningfully related to a number of useful properties possessed by the estimator. Furthermore the numerical problems associated with the actual computation of parameter estimates have not been given exhaustive attention. In this paper through a slight reformulation of the ISEE formula, local geometric features of the optimal solution used in ISEE are studied. This formulation is subsequently proposed within a stochastic programming framework. The latter provides a powerful, productive methodology and an alternative theoretical framework which are entertained within this study. Results are presented and discussed.
Keywords: Lévy Processes, Characteristic Function, Stochastic Programming.

1 Introduction

In recent decades, there has been a sharp rise of interest in the study of Lévy processes. Evidence of this is given by the extensive amount of literature which has been focused not only on the application of Lévy processes in various fields − most prominently in finance − but also on parameter estimation problems. Some of the methods of estimation found in literature minimize some form of distance function that involves the characteristic function of a Lévy process and its empirical counterpart. As discussed in Sant and Caruana [9], the use of the empirical characteristic function in the parameter estimation problem causes a number of computational issues triggered by oscillatory integrands. Weight functions are usually used to control these oscillations thus reducing computational problems. However, there is no link between the choice of the weight function and the characteristic function. In response to this problem, the stochastic programming framework will allow the use of some properties

of the characteristic function of continuous probability distributions to address the above mentioned computational issues. Throughout this paper we shall be using only continuous probability distributions.

2 Context

Given Lévy process $(Z_s)_{s \in \mathbb{R}_+}$, with independent and identically distributed increments which we denote by X_j, $j = 1 \ldots, n$, we define the corresponding characteristic function $\rho(t, \boldsymbol{\theta}(s)) = \mathbb{E}[exp(itZ_s)]$, where for each s, $\boldsymbol{\theta}(s) \in \mathbb{R}^d$ is the vector of parameters which the process inherits from the infinitely divisible distribution corresponding to random variable Z_s. Usually, little time is spent to consider the shape that this vector of parameters can take. We note that $\rho(t, \boldsymbol{\theta}(ns/m)) = \mathbb{E}\left[exp(itZ_{ns/m})\right] = \rho(t, \boldsymbol{\theta}(s))^{n/m}$ from the infinite divisibility property forces $\rho(t, \boldsymbol{\theta}(s)) = \rho(t, \boldsymbol{\theta}(1))^s$.

This functional equation is of the Pixeder type and does not allow any type of parametrization. In fact, the Lévy-Khintcine and Lévy-Itô formulas propose their own parametrizations related to specific measure-theoretic and functional relationships. We address ourselves more to the parametrizations which are in common use and which in many cases have to obey certain structures before the corresponding family of distributions can be declared infinitely divisible (eg. the gamma distribution has to have its second parameter constant to achieve infinite divisibility). Using the polar representation we can write:

$$\rho(t, \boldsymbol{\theta}(s)) = R(t, \boldsymbol{\theta}(1))^s \exp[is\vartheta(t, \boldsymbol{\theta}(1))] = \rho_{\mathcal{R}}(t, \boldsymbol{\theta}(s)) + i\rho_{\mathcal{I}}(t, \boldsymbol{\theta}(s))$$

and we see that $R(t, \boldsymbol{\theta}(s)) = R(t, \boldsymbol{\theta}(1))^s$ and $s\vartheta(t, \boldsymbol{\theta}(s)) = s\vartheta(t, \boldsymbol{\theta}(1))$.

In fact inspecting the usual parametrizations for the common distributions, stable distributions, extreme value distributions and mixtures the relationships for the components of $\boldsymbol{\theta}$ are of the form: $\boldsymbol{\theta}_j(s) = as$ or $\boldsymbol{\theta}_j(s) = a$.

In what follows we shall work with $\rho(t, \boldsymbol{\theta}(\Delta s))$ where Δs is a fixed time increment separating increments X_j obtained from readings of a Lévy process with corresponding characteristic function which we shall denote from now onwards as $\rho(t, \boldsymbol{\theta})$. Furthermore it makes sense that as a minimal assumption we take continuity of ρ with respect to $\boldsymbol{\theta}$ on some compact subset $\mathbf{K} \subseteq \mathbb{R}^d$ whereon $\boldsymbol{\theta}$ is allowed to vary. In effect estimations over unbounded subsets are in practice, not only hypothetical, but also impractical.

Next, we look at the problem of parameter estimation through the use of the characteristic function but with an unusual choice of objective function for minimization. In fact the corresponding problem can be reframed as a stochastic programming one.

3 Applying the Stochastic Programming Framework

A stochastic program can be written in the form

$$\arg\min_{\boldsymbol{\theta}}\{f(\boldsymbol{\theta}) = \mathbb{E}[F(\boldsymbol{\theta}, X)]\}, \tag{1}$$

and we shall formulate the location of the true parameter $\boldsymbol{\theta}_0$ from X_j in this way.

For $t \in \mathbb{R}$, $\boldsymbol{\theta} \in \mathbf{K}$ dropping the suffix for a general X_j we have the random functions:

$$
\begin{aligned}
F(t, \boldsymbol{\theta}, \omega) &= |e^{itX(\omega)} - \rho(t, \boldsymbol{\theta})|^2 - 1 \\
&= \rho_{\mathcal{R}}^2(t, \boldsymbol{\theta}) + \rho_{\mathcal{I}}^2(t, \boldsymbol{\theta}) - 2\cos(tX(\omega))\rho_{\mathcal{R}}(t, \boldsymbol{\theta}) - 2\sin(X(\omega))\rho_{\mathcal{I}}(t, \boldsymbol{\theta})
\end{aligned}
$$

with corresponding bounded functional f for bounded distribution functions W over $\mathbb{R}_+$ defined as follows:

$$
\begin{aligned}
f(\boldsymbol{\theta}) &= \int_0^\infty \mathbb{E}[F(t, \theta)] dW(t) = \mathbb{E}\left[\int_0^\infty F(t, \boldsymbol{\theta}) dW(t)\right] \\
&= \int_0^\infty \{\rho_{\mathcal{R}}^2(t, \boldsymbol{\theta}) + \rho_{\mathcal{I}}^2(t, \boldsymbol{\theta}) - 2\rho_{\mathcal{R}}(t, \boldsymbol{\theta}_0)\rho_{\mathcal{R}}(t, \boldsymbol{\theta}) - 2\rho_{\mathcal{I}}(t, \boldsymbol{\theta}_0)\rho_{\mathcal{I}}(t, \boldsymbol{\theta})\} dW(t)
\end{aligned}
$$

The above expectation can be approximated by making use of the set of previously defined increments X_j, which give rise to the following sequence of random elements with values in $\mathcal{C}(\mathbf{K})$:

$$
F_n(\boldsymbol{\theta}, \omega) = \frac{1}{n} \sum_{j=1}^n \int_0^\infty \left(\left|e^{itX_j(\omega)} - \rho(t, (\theta))\right|^2 - 1\right) dW(t) \tag{2}
$$

$$
= \frac{1}{n} \sum_{j=1}^n G_j(\omega, \boldsymbol{\theta}) \tag{3}
$$

We assume that $\rho(t, \boldsymbol{\theta})$, and hence all functions F, f, F_n, are continuous with respect to $\boldsymbol{\theta}$ as it varies on a compact, metrizable set $\mathbf{K} \subseteq \mathbb{R}^d$. Hence, all functions can be considered as elements of $\mathcal{C}(\mathbf{K})$, the space of continuous functions on $\mathbf{K}$, which we recover as a separable Banach space under the supremum norm, which we denote by $\| \bullet \|$, where $\|F\| = \sup_{\boldsymbol{\theta} \in \mathbf{K}} |F(\boldsymbol{\theta})|$.

Next, we determine the asymptotic behavior of F_n in the following theorem. Later we shall see that F_n can be used to approximate the stochastic programming problem defined in (1).

Theorem 1. *The sequence of random elements $F_n(\boldsymbol{\theta}, \omega)$ converges $\mathbb{P}$ a.s. and in $\mathbb{L}^p$ to $f(\boldsymbol{\theta})$. Furthermore under the condition that there exist constants C_1, C_2 such that for all $\boldsymbol{\theta}_1$ $\boldsymbol{\theta}_2 \in \mathbf{K}$:*

$$
\begin{aligned}
|\rho_{\mathcal{R}}(t, \boldsymbol{\theta}_2) - \rho_{\mathcal{R}}(t, \boldsymbol{\theta}_1)| &\leq C_1 \|\boldsymbol{\theta}_2 - \boldsymbol{\theta}_1)\| \\
|\rho_{\mathcal{I}}(t, \boldsymbol{\theta}_2) - \rho_{\mathcal{I}}(t, \boldsymbol{\theta}_1)| &\leq C_2 \|\boldsymbol{\theta}_2 - \boldsymbol{\theta}_1)\|
\end{aligned}
$$

the sequence $F_n(\boldsymbol{\theta}, \omega)$ obeys the CLT: $\sqrt{n}[F_n(\boldsymbol{\theta}, \omega) - f(\boldsymbol{\theta})]$ converges in distribution to a Gaussian random element.

Proof.
The inequality $\|G_j(\omega, \bullet)\| = \sup_{\boldsymbol{\theta}} \int_0^\infty \{|\exp(itX_j(\omega) - \rho(t, \boldsymbol{\theta}))|^2 - 1\} dW(t) \leq \sup_{\boldsymbol{\theta}} \int_0^\infty 3 dW(t) = 3$. This ensures that $\forall j$, $\mathbb{E}[\|G_j\|^p] < \infty$, $\forall p \geq 0$. By the

Strong Law of Large numbers for iid random variables with values in Banach spaces, the $\mathbb{P}$ a.s. limit of $F_n(\boldsymbol{\theta}, \omega)$ is the expectation of each G_j which is $f(\boldsymbol{\theta})$. Using the Dominated Convergence theorem we can deduce that convergence occurs also in $\mathbb{L}^p$ for $p \geq 1$ where we use results first obtained by Fortet and Mourier [1] and proved in detail in Ledoux and Talagrand [6], Corollary 7.10. We need distributional results and something about rates of convergence. These are usually supplied by the CLT. However, the CLT does not hold for Banach space-valued random elements with only the iid and finite variance assumptions. For $\mathcal{C}(\mathbf{K})$-valued random variables the CLT is assured under special conditions. Broadly speaking the condition that guarantees convergence of the CLT type is that the corresponding measures can be supported on a Hilbert subspace. We adapt them for our circumstances by using a Lipshcitz type condition which needs only concern the characteristic function under study.

The random function $\boldsymbol{\theta} \to \int_0^\infty F(t, \boldsymbol{\theta}, \omega) dW(t)$ is bounded in $\mathbb{L}^2(\mathbf{K})$ and it is Lipschitz continuous:

$|F(t, \boldsymbol{\theta}_2, \omega) - F(t, \boldsymbol{\theta}_1, \omega) \leq 2|\rho_\mathcal{R}(t, \boldsymbol{\theta}_2) - \rho_\mathcal{R}(t, \boldsymbol{\theta}_1)| + 2|\rho_\mathcal{I}(t, \boldsymbol{\theta}_2) - \rho_\mathcal{I}(t, \boldsymbol{\theta}_1)| + |\rho_\mathcal{R}^2(t, \boldsymbol{\theta}_2) - \rho_\mathcal{R}^2(t, \boldsymbol{\theta}_1)| + |\rho_\mathcal{I}^2(t, \boldsymbol{\theta}_2) - \rho_\mathcal{I}^2(t, \boldsymbol{\theta}_1)| \leq 4(C_1 + C_2)\|\boldsymbol{\theta}_2 - \boldsymbol{\theta}_1\|$.

The $G_j(\omega, \boldsymbol{\theta})$'s are independent copies of the random element above. Results for the CLT in Banach spaces as given in Jain and Marcus [3] allow us to conclude that suitably scaled and centered, the averaged random sequence of functions $\sqrt{n}\,[F_n(\boldsymbol{\theta}) - f(\boldsymbol{\theta})]$ converges in distribution to a random element of $\mathcal{C}(\mathbf{K})$. More precisely we have weak convergence to a Gaussian probability measure in the space of Borel probability measures on $\mathcal{C}(\mathbf{K})$. Furthermore the corresponding variance is

$$\mathbb{V}\mathrm{ar}\left[\int_0^\infty \left\{|\exp(itX) - \rho(t, \boldsymbol{\theta})|^2 - 1\right\} dW(t)\right].$$

$\square$

Since $F_n(\boldsymbol{\theta}, \omega)$ converges $\mathbb{P}$ almost surely to $f(\boldsymbol{\theta})$ then it makes sense to solve the following program:

$$\arg\min_{\boldsymbol{\theta}}\left(F_n(\boldsymbol{\theta}, \omega) = \frac{1}{n}\sum_{j=1}^n \int_0^\infty \{|\exp(itx_j) - \rho(t, \boldsymbol{\theta})|^2 - 1\} dW(t)\right) \quad (4)$$

as an approximation to (1) and use corresponding methods to approach the required solution. The link is provided by the functional $\psi(g) = \inf_{\boldsymbol{\theta} \in \mathbf{K}} g(\boldsymbol{\theta})$. ψ shares some geometrical properties with the norm, but clearly it is not linear. It is in fact the minimum of linear functionals, all of whom are elements of $\mathcal{M}(\mathbf{K})$, the dual of $\mathcal{C}(\mathbf{K})$, which is the space of all Radon measures on $\mathbf{K}$. Furthermore, ψ is concave and hence is Hadamard differentiable at any $g \in \mathcal{C}(\mathbf{K})$.

Although we know that $F_n(\boldsymbol{\theta}, \omega)$ converges $\mathbb{P}$ a.s. to $f(\boldsymbol{\theta})$, we still need to show that as the number of increments increases then $\hat{\boldsymbol{\theta}} = \arg\min_{\boldsymbol{\theta}}(F_n(\boldsymbol{\theta}, \omega))$ will approach the true value $\boldsymbol{\theta}_0 = \arg\min_{\boldsymbol{\theta}}(f(\boldsymbol{\theta}))$. This result is proven in theorem 2.

Theorem 2. *The sequence of random variables $\psi(F_n(\boldsymbol{\theta}, \omega)) = \inf_{\boldsymbol{\theta} \in \mathbf{K}} F_n(\boldsymbol{\theta}, \omega)$ converges in probability to the constant $f(\boldsymbol{\theta}_0) = \int_0^\infty |\rho(t, \boldsymbol{\theta}_0)|^2 dW(t)$.*

Furthermore $\psi(F_n(\boldsymbol{\theta}, \omega)) - f(\boldsymbol{\theta}_0) = o_{\mathbb{P}}(1)$ *and* $\lim_{n \to \infty} \arg \min_{\boldsymbol{\theta}} F_n((\theta), \omega) = \boldsymbol{\theta}_0$.

Proof.

For a fixed ω, the function $F(t, \boldsymbol{\theta}, \omega)$, being quadratic in $\rho_{\mathcal{R}}$ and $\rho_{\mathcal{I}}$, achieves its minimum value when $\rho_{\mathcal{R}} = cos(tX(\omega))$ and $\rho_{\mathcal{I}} = sin(tX(\omega))$ which in general may have no solution or more than one. On the other hand, $\mathbb{E}[F(t, \theta)]$ being quadratic in $\rho_{\mathcal{R}}$ and $\rho_{\mathcal{I}}$, achieves its minimum value when $\boldsymbol{\theta} = \boldsymbol{\theta}_0$. Unicity of characteristic functions assures uniqueness of this minimum $F(t, \boldsymbol{\theta}_0)$. It follows that for $f(\boldsymbol{\theta})$ we have:

$$\inf_{\boldsymbol{\theta} \in \mathbf{K}(F)} \int_0^\infty \mathbb{E}[F(t, \boldsymbol{\theta})] dW(t) = f(\boldsymbol{\theta}_0).$$

We are interested in the subdifferential $\partial \psi$ at our special function f. In effect for $g \in \mathcal{C}(\mathbf{K})$, $\partial \psi(g)$ is a set of elements of $\mathcal{M}(\mathbf{K})$, which following proposition 4.5.18 in Gasinski and Papageorgiou [2] we proceed to describe. It is the set of all positive Radon measures of total mass 1 concentrated on the points where g attains its minima:

$\partial \psi(g) = \{\mu \in \mathcal{M}(\mathbf{K}) : \mu \geq 0 \ \& \ \langle \mu, 1 \rangle = 1 \ \& \ \mathrm{supp}(\mu) \subseteq \{\boldsymbol{\theta} \in \mathbf{K} : \psi(g) = g(\boldsymbol{\theta})\}\}$

Evaluated at our special function f, this subdifferential becomes: $\langle \partial \psi(f), h \rangle = \inf_{\boldsymbol{\theta} \in \mathbf{K}(f)} h(\boldsymbol{\theta})$.

Thus $\partial \psi(f)$, operating on h, returns the minimum of h restricted to the points where f achieves its minimum. In our case this happens at the single point $\boldsymbol{\theta}_0$. Using the Delta Method theorem for normed spaces, discussed in van der Vaart [10], with the Hadamard differentiable map ψ operating on the convergent series of random elements $F_n(\boldsymbol{\theta}, \omega)$ we get the convergence in probability results. The last limit follows from unicity of all minima involved.

$\square$

This theorem assures us that, as the sample size increases, locating the value of $\boldsymbol{\theta}$ which minimizes the sample value $F_n(\boldsymbol{\theta}, \omega)$ will get us closer to $\boldsymbol{\theta}_0 = \arg \min_{\boldsymbol{\theta} \in \mathbf{K}} f(\boldsymbol{\theta})$. This brings us securely to stochastic programming territory. In fact, the problem $\min_{\boldsymbol{\theta}} F_n(\boldsymbol{\theta}, \omega)$ can be considered as a two-stage stochastic program.

In the following section we discuss a method by which this stochastic program can be solved.

4 Solving the Stochastic Program

A number of different methods can be used to solve two-stage or multi-stage stochastic programs. Shapiro [8] solves multi-sage stochastic programs with a linear objective function and linear constraints by making use of the Stochastic Dual Dynamic Programming Algorithm (SDDP) which in turn was introduced by Pinto and Pereira [7]. Shapiro argues that the backward step of the SDDP is the standard cutting plane algorithm and applied it to the problem he was studying. However Kelly's [5] cutting plane algorithm was designed on the

assumption that the objective function is convex over the feasible region. The objective function $F_n(\boldsymbol{\theta}, \omega)$ is not convex in general and hence Kelly's cutting plane algorithm cannot be used. The way forward is to replace the cutting plane algorithm with another method which can handle non-convex objective functions. The algorithm proposed by Karmitsa et. al. [4] still makes use of cutting planes and furthermore can be used for non-convex and non-smooth objective functions. The original minimization problem is first converted into a program with a linear objective function while the non-linearity and non-convexity of the original problem are moved to the constraint as shown below:

$$\arg\min_{\boldsymbol{\theta},z}\{z | F_n(\boldsymbol{\theta}, \omega) - z \leq 0\} \tag{5}$$

Next, a sequence of auxiliary linear problems is built where the constraint in (5) is approximated by a number of cutting planes. During each iteration a search direction for the auxiliary problem is computed using the Feasible Direction Interior Point Method (FDIPM).

In the following section the performance of the method of estimation discussed in this paper is compared with that of other methods of estimation found in literature.

5 Simulation Results

Increments of three distinct Lévy processes were simulated using three different probability distributions. Using these increments, the parameters of the characteristic function of each distribution were estimated using not only the stochastic programming framework discussed above (which from now on we denote by SPM) but also other commonly used methods such as the method of maximum likelihood (MLE) and the Integrated squared error estimator (ISEE). When the integrand in (4), i.e. $\left\{\frac{1}{n}\sum_{j=1}^{n}|\exp(itx_j) - \rho(t, \boldsymbol{\theta})|^2 - 1\right\}$ is compared with the integrand in the ISEE, i.e. $\left|\frac{1}{n}\sum_{j=1}^{n}[\exp(itx_j)] - \rho(t, \boldsymbol{\theta})\right|^2$, one can easily show that for continuous distributions, the former goes to zero as $t \to \pm\infty$, while the latter does not and keeps on oscillating within a band as $t \to \pm\infty$. This indicates why our estimator behaves more smoothly.

The probability distributions chosen for these simulations are: the Stable distribution with parameters ($\alpha = 0.4, \beta = 0.5, \sigma = 1, \mu = 3$), the gamma distribution with parameters ($\alpha = 2, \beta = 3$) and an extreme value distribution: the Gumbel distribution with parameters ($\mu = 7, \beta = 0.05$). The results obtained for the stable distribution using SPM were compared with the ISEE. Table 1 contains the simulation results of the parameter estimates for the stable distribution. The weight function which is necessary in ISEE was chosen to be $\exp(-t^2)$. The limits of integration in the SPM and ISEE are taken from 0 to some constant T. In particular, two different values of T were chosen, namely, 10 and 20.

It is evident from table 1, that for both values of T, the estimates obtained from SPM have less bias and less variance than the estimates obtained from ISEE.

T	$\hat{\alpha}$	$\hat{\beta}$	$\hat{\sigma}$	$\hat{\mu}$	$\hat{\alpha}$	$\hat{\beta}$	$\hat{\sigma}$	$\hat{\mu}$
	Estimates using SPM				Estimated Variance			
10	0.41296	0.50995	0.96899	3.05113	6.589E-05	0.01278	0.00044	0.00100
20	0.40541	0.50131	1.00343	3.03293	2.640E-05	0.01284	0.00013	0.00023
	Estimates using ISEE				Estimated Variance			
10	0.29874	0.49235	0.92826	3.14041	0.01793	0.00900	0.022675	0.02989
20	0.29923	0.49821	0.93229	3.13334	0.01630	0.01525	0.021106	0.02888

Table 1. Estimates for the Lévy Stable process.

Next we compare the results obtained for the Gumbel and Gamma distributions. In this case the estimates are compared with the simulations results obtained by using the method of maximum likelihood.

	Gamma (2, 3)				Gumbel (7, 0.5)			
SPM	Estimates		Variance		Estimates		Variance	
10	2.00259	2.99445	0.00044	0.001443	6.99779	0.04955	2.284E-07	9.05E-08
20	2.00052	2.99996	0.00035	0.001221	6.99924	0.04977	1.670E-07	8.63E-08
	Estimates		Variance		Estimates		Variance	
MLE	2.00103	2.99498	0.00039	0.00142	6.99993	0.049926	1.455E-06	6.96E-07

Table 2. Estimates for the Gamma and Gumbel distribution.

It appears from table 2 that the results obtained from the method of maximum likelihood are comparable with the results obtained from the SPM method. In some cases, in particular when $T = 20$, the estimates obtained by the SPM for the Gamma distribution appear to be slightly better than the results obtained by the MLE. Furthermore the SPM estimates for the Gumbel distribution appear to have less variance.

6   Conclusion

The aim of this paper was to propose a method of parameter estimation that makes use of the stochastic programming framework as well as the properties of the real and imaginary parts of the characteristic function. These features reduce the computation problems triggered by the oscillatory nature of the empirical characteristic function. This enabled us to work with integrands whose behaviour was controlled nicely for numerical procedures to converge conformably. It was shown that as $n \to \infty$ the optimal solution of the proposed stochastic program approaches $\mathbb{P}$ a.s. the true vector of parameters. Furthermore, when compared with other methods of estimation, such as ISEE and MLE, the SPM was found to give better results when compared to former and gave comparable results to the latter. However, contrary to the MLE, the SPM is particularly useful when dealing with probability distributions, like most infinitely divisible distributions or most stable distributions, whose density function is not known in closed form.

References

1. Fortet R. and Mourier E., "Lois des grandes nombres pour des elements aleatoires prenant leurs valeurs dans un espace de Banach", *Comptes rendus hebdomadaires de l'Academeie des Sciences*, Paris, 237, 18-20, (1953).
2. Gasinski, L. and Papageorgiou N. S., *Nonlinear Analysis* , Chapman & Hall/CRC, Taylor & Francis Group, (2005).
3. Jain N. C, and Marcus M. B., "Central limit theorems for C(S)-valued random variables", *Journal of Functional Analysis* 19, 3, 216-231, (1975).
4. Karmitsa N., Tanaka M., Herskovits J., "Nonconvex Nonsmooth Minimisation via Cutting Planes and Feasible Direction Interior Point Method", *Turku Centre for Computer Science*, (2009).
5. Kelly J. E. Jr., "The Cutting-Plane Method for Solving Convex Programs", *Journal of the Society for Industrial and Applied Mathematics*, 8, 4, 703-712, (1960).
6. Ledoux M. and Talagrand M., *Probability in Banach Spaces*, Springer-Verlag Berlin Heidelberg, (1991, 2011).
7. Pereira M.V.F. and Pinto L.M.V.G., "Multi-stage stochastic optimization applied to energy planning", *Mathematical Programming*, 52, 359-375, (1991).
8. Shapiro A., "Analysis of stochastic dual dynamic programming method", *European Journal of Operational Research*, 209, 63-72, (2011).
9. Sant L. and Caruana M. A., "Products of Characteristic functions in Lévy Process Parameter Estimation" *Proceedings, 2nd Stochastic Modelling Techniques and Data Analysis International Conference*, 661 669, (2012).
10. van der Vaart A. W., *Asymptotic Statistics*, Cambridge University Press, pg 297, (2000).

Nonlinear filtering and heterogeneous swarms of autonomous agents - An exactly solvable model

Guillaume Sartoretti[1], Max-Olivier Hongler[1], and Roger Filliger[2]

[1] Swiss Federal Institute of Technology in Lausanne
EPFL Campus, CH-1015 Lausanne, Switzerland
(e-mail: {`guillaume.sartoretti,max.hongler`}`@epfl.ch`)
[2] Bern University of Applied Sciences
Quellgasse 21, 2501 Biel/Bienne, Switzerland
(e-mail: `roger.filliger@bfh.ch`)

Abstract. We consider slightly heterogeneous swarm of agents controlled by one leader. We study the global dynamics by using a newly established connection binding multi-agents dynamics and nonlinear optimal state estimation (nonlinear filtering). For a whole nonlinear class of mutual interactions, we are able to exactly characterize the resulting swarm dynamics. Our leader-follower dynamics are interpretable as a feedback particle filtering problem which itself is similar to a finite-dimensional, nonlinear filter problem originally proposed by V. E. Beneš. The state estimation problem can be explicitly solved as it merely uses a change of probability measure on an Ornstein-Uhlenbeck process. The agents interactions, driven by common observations of the randomly corrupted leaders position, correspond to the innovation kernel that underlies any Bayesian filter. Numerical results fully corroborate our theoretical findings and intuition.

Keywords: Heterogeneous swarm, Multi-agent dynamics, Leader-based model, Nonlinear filtering, Feedback Particle Filter, Exact Results, Numerical Simulations.

1 Introduction

Among the vast and steadily increasing amount of literature devoted to the dynamics of a large number of mutually interacting autonomous agents, analytically solvable models stylizing some aspects of reality are welcome (Hongler *et al.*[1], Eftimie[2], Bellomo and Dogbe[3], Bertin *et al.*[4]). Despite specific features inherent in analytical approaches, these contributions enhance our understanding of the emergence of collective phenomena like synchronization, aggregation, pattern formation, behavioral phase transitions, fashion trend formation, and others. Most analytical studies focus on the dynamics of homogeneous swarms (i.e., those involving identical agents). Either the agents local rules are given and the ultimate goal is to analytically derive the emerging collective patterns or inversely, given a collective behavior, the goal is to unveil

the agents local rules and their interactions. Purely homogeneous swarms are however rather scarcely encountered in reality.

In this paper, we focus our attention on slightly heterogeneous populations in which one special agent (we call it the *leader*) is able to drive the whole swarm towards a desired objective (Wang and Han[5]). Several types of leaders can be distinguished depending on the ways they affect their fellows. Either the leader is external and hence is explicitly recognized by ordinary agents of the swarm (Couzin *et al.*[6], Aureli and Porfiri[7]), or it acts as a *shill* who appears ordinary to its fellows while in fact obeying a hidden master (Dyer *et al.*[8], Gribovskiy *et al.*[9], Wang and Guo[10]). Besides very particular models (Sartoretti and Hongler[11,12]), there is generally little hope for an analytical investigation of the collective behavior of a shill- or leader-infiltrated (and hence heterogeneous) swarm. The objective of this paper is to unveil a class of dynamical models for which this investigation can be achieved.

Our source of inspiration is taken from the realm of estimation problems. In noise filtering, one considers the evolution of a stochastically driven system $\mathcal{S}$, monitored by an observer $\mathcal{O}$, which is itself delivering noisy information. The filtering goal at time t is to construct the best possible estimation of the state $\mathcal{S}$ by processing information delivered only from $\mathcal{O}$ up to time t. The filtering process is achieved via *sequential Bayesian* steps. Specifically, one starts with a *prediction step* to estimate the relevant conditional probability density function (pdf) based on the $\mathcal{S}$-dynamics, and then one updates this pdf based on the $\mathcal{O}$-dynamics. For linear $\mathcal{S}$-evolutions driven by White Gaussian Noise (WGN) and $\mathcal{O}$-measurements also corrupted by WGN, the filtering problem is completely solvable, and its explicit solution is known as the *Kalman-Bucy filter*. Indeed, due to linearity and Gaussian driving noise, both the prediction and the updating steps preserve their Gaussian character. Therefore the underlying filtering problem remains finite-dimensional as all operations are expressible via means and covariances only. For nonlinear evolution, the Gaussian character is lost, generally leading to infinite-dimensional problems. Analytical treatments are then precluded and only numerical approaches are feasible. One numerical method is given by particle filters, specifically *feedback particles algorithms* (FPA) (Yang *et al.*[13]). These algorithms are directly based on dynamics of randomly interacting particles and can therefore be identified with specific agents dynamics. The FPA prediction step is achieved by attributing the $\mathcal{S}$-dynamics to a homogeneous swarm of agents. The updating process, realized by mutual agents interactions will globally minimize, in real time, the Kullback-Leibler distance between the $\mathcal{S}$ pdf and the swarm empirical distribution. In this paper, we view the $\mathcal{S}$-dynamics as playing the role of a leader evolving among a homogeneous swarm of N ordinary agents. When $N \to \infty$, this dynamic is reducible to a *mean-field game* (Pequitoy *et al.*[14], Guéant *et al.*[15]) with here an infinitesimally short time horizon, (as only real time updating – excluding smoothing – is realized). The FPA offers, therefore, a natural framework to construct leader driven swarms of agents. As a natural consequence, solvable filtering problems, like the Kalman-Bucy case, provide directly solvable heterogeneous swarms dynamics. Here, our intention is to construct a class of multi-agents models which simultaneously keep the

associated FPA finitely dimensional and yet escape from the pure Gaussian world. The idea on which we base our construction, is to consider a class of "Girsanov-changes" of probability measures applied to Ornstein-Uhlenbeck dynamics (i.e., linear dynamics with Gaussian noise sources). Here one considers the class of Girsanov changes of measures studied in Taylor[16], Hongler[17], Dai Pra[18], Benes[19] and Daum[20].

We organize the paper as follows: in section 2, the explicit connection between the filtering problem and the driving of a swarm of agents infiltrated by a leader is exposed. In section 3, we introduce our specific example of non-Gaussian interacting agents, controlled by a leader and for which the associated FPA is analytically solvable. Finally, in Section 4, we report numerical experiments to illustrate our analytical findings.

2 Multi-Agent Dynamics and Feedback Particle Filtering

Consider a swarm of N Brownian agents $\mathcal{A}_i$, $i = 1, 2, \cdots, N$, and one additional leader agent $\mathcal{A}$ with dynamics:

$$
\begin{cases}
dX_i(t) = f\left(X_i(t)\right) dt + \mathcal{K}\left(X_i(t), \boldsymbol{X}(t), dZ(t)\right) + \sigma\, dW_i(t), \\[2mm]
\text{leaders dynamics} \quad
\begin{cases}
dY(t) = f\left(Y(t)\right) dt + \sigma\, dW(t), \\[2mm]
dZ(t) = h\, Y(t) dt + \sigma_o dW_y(t),
\end{cases}
\end{cases}
\tag{1}
$$

where $h > 0$ is a constant, $f : \mathbb{R} \to \mathbb{R}$, $dW_i(t)$, $dW(t)$ and $dW_y(t)$ are mutually independent WGN processes and the vector $\boldsymbol{X}(t) = (X_1(t), X_2(t), \cdots, X_N(t))$ describes the dynamic state of the N homogeneous agents. The *leader* agent $Y(t)$ affects the dynamics of the $X_i(t)$ via the interaction kernel $\mathcal{K}(X_i, \boldsymbol{X}, dZ)$. We emphasize that the leader's dynamics $Y(t)$ itself is independent from the swarms state $\boldsymbol{X}(t)$. Agents are only able to observe the corrupted leaders position $Z(t)$, (the leader effectively hides its real position $Y(t)$ from the other fellows).

In Eq.(1), we focus our attention on the class of interaction kernels:

$$
\mathcal{K}\left[X_i(t), \boldsymbol{X}(t), dZ(t)\right] = \nu\left(X_i(t), t\right) \otimes \left\{ dZ(t) - \underbrace{\frac{h}{2}\left[X_i(t) + \frac{1}{N}\sum_{k=1}^{N} X_k(t)\right] dt}_{\mathcal{G}[X_i(t), \boldsymbol{X}(t)]} \right\},
\tag{2}
$$

where the coupling strength $\nu = \nu(X_i(t), t)$ is a positive convex function in $X_i(t)$ and where, due to the presence of multiplicative WGN processes, we define $\otimes$ to denote the Stratonovich interpretation of the underlying stochastic integrals (Jazwinski[21]). In Eq.(2), $\mathcal{G}\left[X_i(t), \boldsymbol{X}(t)\right]$ is a consensual position given by the average between agent $\mathcal{A}_i$'s position and the whole swarm barycenter. The interaction kernel relates the position increment $\mathcal{G}dt$ with the

leader's unveiled position increment $dZ(t)$ and weights this stimulus with the coupling strength ν. The assumptions on ν imply that $\mathcal{K}\left[X_i(t), \boldsymbol{X}(t), dZ(t)\right]$ tends, in real time, to steadily reduce the distance between $\mathcal{G}\left[X_i(t), \boldsymbol{X}(t)\right] dt$ and $dZ(t)$. Although the multiplicative factor $\nu(X_i(t), t)$ in Eq.(2) remains yet undetermined, its complete specification can be fixed by introducing a cost structure. In general, one requires that for some running cost functional $\mathcal{J}\left[\mathcal{K}, X_i(t), \boldsymbol{X}(t), \mathcal{Z}(t), t\right]$ and final cost $\Psi\left(X_i(T), \boldsymbol{X}(T), dZ(T)\right)$ at time horizon T, the interaction $\mathcal{K}$ minimizes the associated optimization problem. Formally, the interaction kernel (and hence ν) would be the unique minimizer over a set $\mathbb{K}$ of admissible controls, namely:

$$\mathcal{K}\left[X_i(t), \boldsymbol{X}(t), dZ(t)\right]$$

$$= \min_{K \in \mathbb{K}}\left\{\left(\int_t^T \mathcal{J}\left[K, X_i(s), \boldsymbol{X}(s), dZ(s), s\right] ds\right) + \Psi\left(X_i(T), \boldsymbol{X}(T), dZ(T)\right)\right\}.$$
$$(3)$$

The coupled set of Eqs.(1), (2) and (3) can be interpreted as a multi-player differential game (Bensoussan[22]). For large populations, one can use the empirical density $P^{(N)}(x, t)$ to construct the mean field posterior density $P(x, t \mid \mathcal{Z}(t), x_0)$:

$$P^{(N)}(x, t)dx = \frac{1}{N}\sum_{n=1}^N \mathbf{1}\left\{X_n(t) \in [x, x+dx]\right\} \approx P(x, t \mid \mathcal{Z}(t), x_0)dx, \quad (4)$$

where the condition $\mathcal{Z}(t)$ stands for the information history of the process Z until time t and x_0 for the common initial location of the whole swarm. In the $N \to \infty$ limit, we have:

$$\lim_{N \to \infty}\frac{1}{N}\sum_{k=1}^N X_k(t) = \int_{\mathbb{R}} x' P(x', t \mid \mathcal{Z}(t), x_0)dx' = \mathbb{E}\left\{X(t) \mid \mathcal{Z}(t)\right\}. \quad (5)$$

The Fokker-Planck equation which governs this mean field posterior density reads (with a self explaining abuse of notation for $\mathcal{K}$):

$$\frac{\partial}{\partial t}P(x, t \mid \mathcal{Z}(t), x_0) = -\frac{\partial}{\partial x}\left\{[f(x) + \mathcal{K}\left(x, \mathbb{E}\left\{X(t) \mid \mathcal{Z}(t)\right\}\right)] P(x, t \mid \mathcal{Z}(t), x_0)\right\}$$

$$+ \frac{\sigma^2}{2}\frac{\partial^2}{\partial x^2}P(x, t \mid \mathcal{Z}(t), x_0).$$
$$(6)$$

Note that Eqs.(6) and (3) define in a forward/backward coupling, a so called differential *mean-field game problem*.

Feedback particles filters. For vanishing forward time horizon (i.e., $T = t$) in Eq.(3), a simpler situation arises (the backward in time coupling becomes trivial) and the minimization is reduced to solving an Euler-Lagrange variational

problem (ELP) for $\Psi\left(x, \mathbb{E}\left\{X(t) \mid \mathcal{Z}(t)\right\}\right)$. Choosing the objective criterion Ψ as the Kullback-Leibler distance d_K:

$$
\begin{cases}
\Psi\left(x, \mathbb{E}\left\{X(t)\right\}, dZ(t)\right) := d_K\left\{P(x', t \mid \mathcal{Z}(t), x_0); Q(x, t \mid x_0)\right\}, \\[2ex]
d_K\left\{P(x', t \mid \mathcal{Z}(t), x_0); Q(x, t \mid x_0)\right\} := \int_{\mathbb{R}} P(x', t \mid \mathcal{Z}(t), x_0)\left\{\ln\left[\frac{P(x', t \mid \mathcal{Z}(t), x_0)}{Q(x', t \mid x_0)}\right]\right\} dx',
\end{cases}
\tag{7}
$$

with $Q(x, t \mid x_0)$ being the transition probability density of the diffusion process $Y(t)$ defined in Eq.(1) we find the ELP:

$$
\begin{cases}
-\frac{\partial}{\partial x}\left\{\frac{1}{P(x, t \mid \mathcal{Z}(t), x_0)}\frac{\partial}{\partial x}\left[P(x, t \mid \mathcal{Z}(t), x_0)\nu(x, t)\right]\right\} = \frac{h}{\sigma^2}, \\[2ex]
\lim_{|x| \to \infty} P(x, t \mid \mathcal{Z}(t), x_0)\nu(x, t) = 0,
\end{cases}
\tag{8}
$$

which leads to:

$$
\begin{cases}
\nu(x, t) = \frac{h}{\sigma^2 P(x, t \mid \mathcal{Z}(t), x_0)}\left\{\int_{-\infty}^{x}\left[\mathbb{E}\left\{X(t) \mid \mathcal{Z}(t)\right\} - x'\right] P(x', t \mid \mathcal{Z}(t), x_0) dx'\right\}, \\[2ex]
\mathbb{E}\left\{X(t) \mid \mathcal{Z}(t)\right\} = \int_{-\infty}^{+\infty} x' P(x', t \mid \mathcal{Z}(t), x_0) dx'.
\end{cases}
\tag{9}
$$

Eqs.(1) and (2), together with $\nu(x, t)$ given in Eq.(9) produce a nonlinear continuous time feedback particle filter. This allows for a direct reinterpretation of the leader-based dynamics in terms of a stochastic filtering problem. A class of examples is detailed in the next section.

It is worthwhile noting that the leader influences the swarm through the variance σ (and the parameter h), and not only through its position. As σ grows, the agents uncertainties of the actual leader's position increase. Consequently the coupling strength $\nu(x, t)$ decreases, the agents variances increase and the swarm tends to form a widespread group of agents around the leader. Alternatively, small values for σ allow for very compact swarm formation.

3 Finite Dimensional Filtering with Weber Parabolic Functions

Let us now introduce a specific filtering problem, which will be related to the control of the multi-agents dynamics. The nonlinear filtering problem is to estimate the value of the one-dimensional state $Y(t)$, at time t, given a set of measurements prior to t: $\mathcal{Z}(t) = \{Z(s) \mid 0 \le s \le t\}$. We will treat hereafter time-continuous measurements and assume that the leader state $Y(t)$ – starting at position y_0 – evolves according to the stochastic differential equation:

$$
\begin{aligned}
dY(t) &= \overbrace{\left\{\frac{d}{dy}\left[\log \mathcal{Y}_B(y)\right]\Big|_{y=Y(t)}\right\}}^{:= f_B[Y(t)]} dt + dW(t), \\
Y(0) &= y_0
\end{aligned}
\tag{10}
$$

in which $W(t)$ is the standard Brownian motion and where $\mathcal{Y}_B(y)$ is the Weber parabolic function, which solves the ordinary differential equation:

$$\frac{d^2}{dy^2}\mathcal{Y}_B(y) = \left[\frac{y^2}{4} + \left(B - \frac{1}{2}\right)\right]\mathcal{Y}_B(y) \tag{11}$$

with B a control parameter. From the definition of $f_B[Y(t)]$, we easily see that

$$\frac{d}{dy}f_B(y) + f_B^2(y) = \frac{\frac{d^2}{dy^2}\mathcal{Y}_B(y)}{\mathcal{Y}_B(y)} = \frac{y^2}{4} + \left(B - \frac{1}{2}\right). \tag{12}$$

This leads to a Beneš type of finite-dimensional filtering problem (a fully analytical treatment of filtering problems in the Beneš class can be found in Daum[20]). In the sequel, we impose the parameter range $B \in \mathbb{R}^+$ which ensures the positivity of $\mathcal{Y}_B(y)$ ($\forall y \in \mathbb{R}$). For $B \in [0, 1/2]$, we further observe that the generalized potential $-\log[\mathcal{Y}_B(y)]$ is locally attractive near the origin and asymptotically repulsive for $|y| \to \infty$. In the parameter range $B > 1/2$, the potential is systematically repulsive $\forall y \in \mathbb{R}$ (Hongler[17]). Figure 1 shows the shape of $\mathcal{Y}_B(y)$ and $f_B(y)$ for different values of the control parameter B.
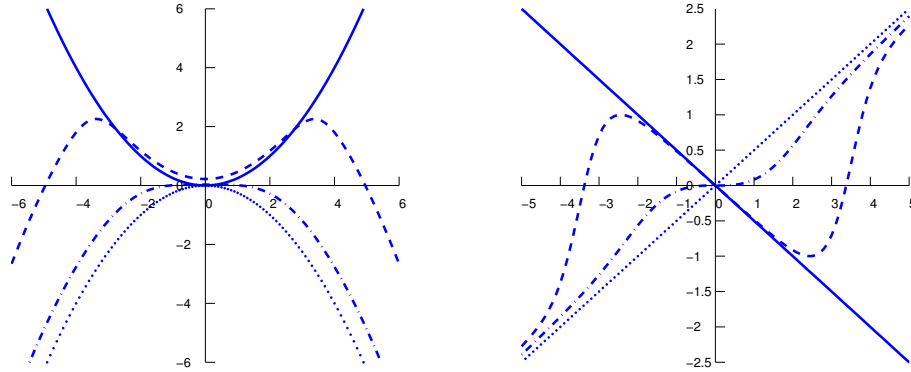
Fig. 1. Shape of $\mathcal{Y}_B(y)$ (left) and $f_B(y)$ (right) for $B = 0$ (plain line), $B = 0.01$ (stripped line), $B = 0.5$ (stripped-dotted line) and $B = 1$ (dotted line). For $B = 0$, the filtering problem is linear and the dynamics are stable. For $B = 1$, the filtering problem is again linear but with unstable dynamics. In between, we have a nonlinear filtering problem and the conditional probability density changes – with increasing B – from unimodal to bimodal and back to unimodal.

For $B = 0$ and $B = 1$ respectively, we obtain linear dynamics:

$$\begin{cases} \mathcal{Y}_0(y) = e^{-\frac{1}{4}y^2} & \Rightarrow \quad f_0(y) = -\frac{1}{2}y \\ \mathcal{Y}_1(y) = e^{+\frac{1}{4}y^2} & \Rightarrow \quad f_1(y) = +\frac{1}{2}y. \end{cases} \tag{13}$$

Using the framework introduced in Daum[20], the continuous time filter is given by the normalized probability density $P(y, t|\mathcal{Z}_t)$ of observing $Y(t) := y$

conditioned on the set of measurements up to time t, $\mathcal{Z}(t)$, and can be written as:

$$P(y,t) := P(y,t \mid \mathcal{Z}(t)) = \frac{\mathcal{Y}_B(y) \cdot e^{-\frac{(y-m)^2}{2s}}}{\mathcal{J}_0(m,s,B)} \tag{14}$$

(computational details are given in the Appendix) with $\mathcal{J}_0(m,s,B)$ the normalization function:

$$\mathcal{J}_0(m,s,B) = 2\sqrt{\frac{\pi s}{2+s}} \left[\sqrt{\frac{2+s}{2-s}}\right]^B e^{\frac{m^2 s}{2(4-s^2)}} \cdot \mathcal{Y}_B\left(\frac{2m}{\sqrt{4-s^2}}\right). \tag{15}$$

(see Appendix). The measurement *dependent* quantities $m := m(Z(t);t)$ are given by

$$m = m(Z(t);t) = \frac{\tanh(pt)}{p}\left[h\int_0^t \frac{\sinh(ps)}{\sinh(pt)}dZ(s) + \frac{py_0}{\sinh(pt)}\right] \tag{16}$$

and similarly, the measurement *independent* quantities $s := s(t)$ reads:

$$s = s(t) = \frac{1}{p}\tanh(pt) \tag{17}$$

with the definition $p = \sqrt{h^2 + \frac{1}{4}}$. With this expression for $P(y,t)$, we have the conditional mean:

$$\langle Y_t \rangle := \mathbb{E}(Y_t|\mathcal{Z}(t)) = \frac{4m}{4-s^2} + \frac{2s}{\sqrt{4-s^2}}f_B\left[\frac{2m}{\sqrt{4-s^2}}\right] \tag{18}$$

and after tedious elementary manipulations, we have the conditional variance:

$$var(Y_t) := \mathbb{E}((Y_t - \langle Y_t \rangle)^2|\mathcal{Z}(t)) = \frac{2s}{2+s} + \frac{4s^2}{4-s^2}\left\{\frac{m^2}{4-s^2} + B - f_B^2\left(\frac{2m}{\sqrt{4-s^2}}\right)\right\}. \tag{19}$$

Remark: For the linear cases $B = 0$ and $B = 1$ from Eq.(13), we consistently find the following classical results:

$$P(y,t) = \frac{\exp\left\{-\frac{((2+s)y-2m)^2}{4s(2+s)}\right\}}{\sqrt{2\pi\frac{2s}{2+s}}}, \qquad \langle Y_t \rangle = \frac{2}{2+s}m, \qquad var(Y_t) = \frac{2}{2+s}s \tag{20}$$

for $B = 0$ and

$$P(y,t) = \frac{\exp\left\{-\frac{((2-s)y-2m)^2}{4s(2-s)}\right\}}{\sqrt{2\pi\frac{2s}{2-s}}}, \qquad \langle Y_t \rangle = \frac{2}{2-s}m, \qquad var(Y_t) = \frac{2}{2-s}s \tag{21}$$

for $B = 1$. As predicted by the linear version of the feedback filter, when $B = 0$ and $B = 1$ the coupling strength $\nu(x, t)$ reduces to the standard **state independent** Kalman gain:

$$\nu(x, t) = \nu(t) = \frac{h}{\sigma^2} var(Y_t). \tag{22}$$

4   Numerical Results

Numerical results are obtained by simulating (1) for a finite swarm of agents and one leader. Thanks to the consistency of the estimator (see Yang *et al.*[13]), one can still use the results from the mean field analysis for a large enough N. In this case $P(y, t)$ must be fitted to the empirical histogram of the agents' position at time t to find the values for m and s. The control $\nu(x, t)$ can then be computed from its integral expression in Eq.(9), while $\langle Y \rangle_t$ can be computed from Eq.(18). The derivative $\frac{d}{dx}\nu(x, t)$ is computed by using the relation $\frac{\frac{d}{dx}P(x,t)}{P(x,t)} = f_B(x) + \frac{x-m}{s}$, which can be written as:

$$\frac{d}{dx}\nu(x, t) = \frac{h}{\sigma^2} \left(\langle Y \rangle_t - x \right) - \nu(x, t) \cdot \left(f_B(x) - \frac{x - m}{s} \right). \tag{23}$$

Note that this natural fitting strategy used to estimate $P(y, t)$ is – computationally – very costly. Extensive numerical computations have shown that $\nu(x, t)$ can safely be computed from Eq.(9) when directly using the empirical histogram of the agents' position instead of the fitted function in Eq.(14). The derivative $\frac{d}{dx}\nu(x, t) \simeq \frac{\nu(x+h,t)-\nu(x,t)}{h}$ is computed by selecting a sufficiently small value h.

Numerical results in linear cases. Figures 2 and 3 show in red the time evolution of the noisy leader's unveiled position. The mean value from the swarm of agents (likewise, the output of the feedback particle filter) produces the smooth blue curve. As the agents' control is updated based on the unveiled position of the leader, a small delay can be observed between the leader's movements and the swarm's reactions. The filter performs well: as expected, the swarms barycentric position is nearly always closer to the actual position of the leader than to the unveiled position. This means that the control on the agents leads to a better approximation of the actual leaders position.

Numerical results in nonlinear cases. We now consider the parameter range $0 < B < 0.5$ where the dynamics of the leader is nonlinear and exhibits an attractive potential in the central region (i.e., around the origin) and a repulsive potential for $|x| \gg 0$. Between these two regions, the potential changes from attractive to repulsive and the agents experience strong nonlinear dynamics. Note that the dynamics in the attractive region is meta-stable, and a leader starting within this region ultimately escapes to infinity.
During the sojourn time of the leader in the attractive region, the close-by agents undergo quasi linear dynamics. They stay in this attractive region and
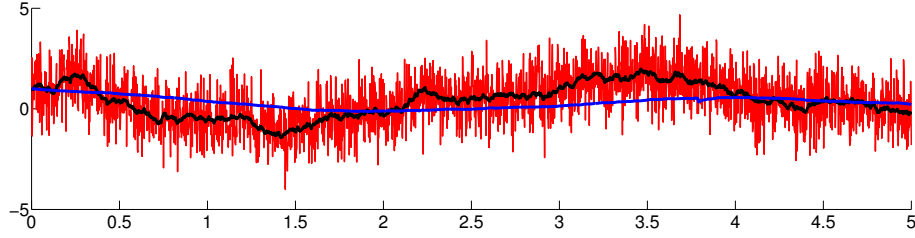
Fig. 2. Leader's position $Y(t)$ from Eq.(10) (black), along with its unveiled position $\mathcal{Z}(t)$ (red), for $B = 0$, $\sigma = h = 1$ and $t \in [0; 5]$. In blue the mean value $\langle Y \rangle_t$ measured from a swarm of $N = 1000$ agents. The particles start with $Y_i(0) = x_0 = 1 \; \forall i$, while $Z(0) = Y(0) = x_0$.
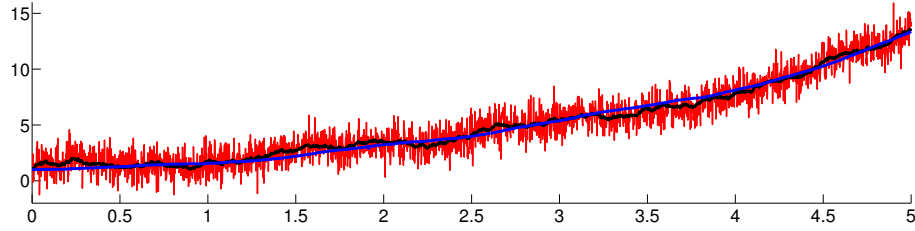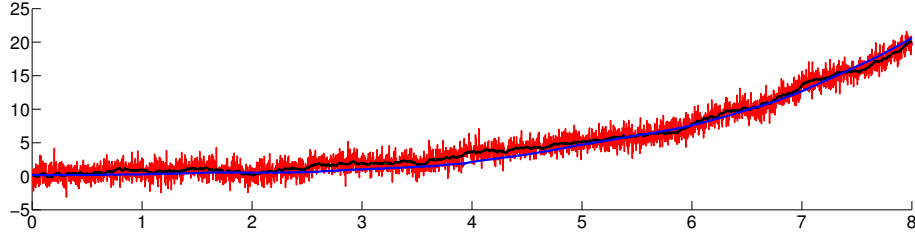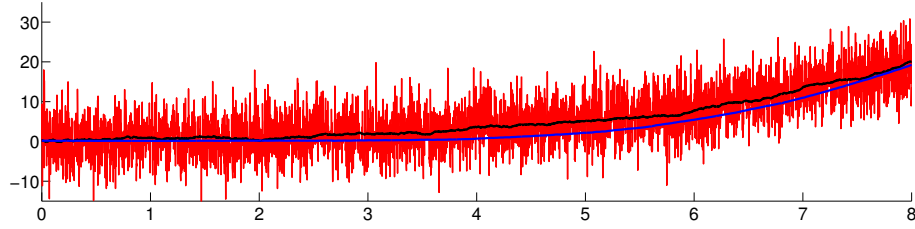

Fig. 3. Leader's position $Y(t)$ from Eq.(10) (black), along with its unveiled position $\mathcal{Z}(t)$ (red), for $B = 1$, $\sigma = h = 1$ and $t \in [0; 5]$. In blue the value $\langle Y \rangle_t$ measured from a swarm of $N = 1000$ agents. The particles start with $Y_i(0) = x_0 = 0.1 \; \forall i$, while $Z(0) = Y(0) = x_0$.

self-arrange in the vicinity of the leaders position to empirically build the a posteriori distribution $P(y, t)$. As soon as the leader escapes from the attractive region, the other agents start feeling their barycentric control and ultimately follow the leader outside the attractive region. The barycenter of an infinite swarm follows the leaders position with nearly no delay; but in our case, as $N < \infty$ agents, a delay can possibly be observed between the exit times of the leader and the agents. Figures 4 and 5 show the results of a representative numerical simulation for $N = 1000$ agents, with a very narrow and shallow attractive region ($B = 0.49$). Observe the explicit delay between the exit times of the leader and the swarm for $\sigma = 5$ in Figure 5.

5   Summary and Conclusion

Heterogeneous multi-agent systems are notoriously difficult to describe analytically, especially if the underlying dynamics is intrinsically nonlinear. In this note, we present a class of dynamics from which explicit and fully analytical results can be derived. The core of our construction relies on recent approaches that have been obtained in the realm of nonlinear estimation problems. The so-called particle filter method – commonly used to tackle nonlinear estimation problems - can be reinterpreted as a general leader-follower problem in which

Fig. 4. Leader's position $Y(t)$ from Eq.(10) (black), along with its unveiled position $\mathcal{Z}(t)$ (red), for $B = 0.49$, $\sigma = h = 1$ and $t \in [0; 8]$. In blue the value $\langle Y \rangle_t$ measured from a swarm of $N = 1000$ agents. The particles start with $Y_i(0) = x_0 = 0.2 \; \forall i$, while $Z(0) = Y(0) = x_0$.

Fig. 5. Leader's position $Y(t)$ from Eq.(10) (black), along with its unveiled position $\mathcal{Z}(t)$ (red), for $B = 0.49$, $\sigma = 5$, $h = 1$ and $t \in [0; 8]$. In blue the value $\langle Y \rangle_t$ measured from a swarm of $N = 1000$ agents. The particles start with $Y_i(0) = x_0 = 0.2 \; \forall i$, while $Z(0) = Y(0) = x_0$.

a swarm of interacting agents try to follow a leader whose unveiled position is corrupted by noise. In stochastic filtering, only finite-dimensional problems can possibly be solved analytically. When linear dynamics is driven by Gaussian noise, all relevant probability distributions remain Gaussian, and hence calculations can be limited to the first two moments (Kalman-Bucy filter). The intimate connection existing between multi-agent systems and estimation problems show that, for nonlinear dynamics, analytical results are in general hopeless. However, for one class of non-Gaussian finite-dimensional filtering problems – pioneered by Beneš – explicit analytical models are available. It is therefore natural to study how the Beneš' class enables us to construct nonlinear solvable multi-agents systems, as is done here. The core analytical tools leading to solvable finite-dimensional filtering problems rely on an underlying Riccati equation that we explicitly solved (in the scalar situation) via Weber parabolic cylinder functions. Using these special functions, we are able to answer two open questions originally formulated in Daum[20] (our Eq.(18) answers Daum's open question 2, and our class of nonlinear dynamics answer Daum's open question 6). Our multi-agent class of dynamics enables us to explicitly observe how a leader can control the spreading factor of the agents around its position by tuning the strength of the observation noise.

References

1. M.-O. Hongler, R. Filliger, and O. Gallay. Local versus nonlocal barycentric interactions in 1d agent dynamics. *Mathematical Biosciences and Engineering*, 11(2):303–315, 2014.
2. R. Eftimie. Hyperbolic and kinetic models for self-organized biological aggregations and movement: A brief review. *Journal of mathematical biology*, 65(1):35–75, 2012.
3. N. Bellomo and C. Dogbe. On the modeling of traffic and crowds: A survey of models, speculations, and perspectives. *SIAM Review*, 53(3):409–463, 2011.
4. E. Bertin, M. Droz, and G. Grégoire. Boltzmann and hydrodynamic description for self-propelled particles. *Physical Review E - Statistical, Nonlinear, and Soft Matter Physics*, 74(2), 2006.
5. J. Han Wang X. and H. Han. Special agents can promote cooperation in the population. *PLoS ONE 12, vol. 6*, 2011.
6. I. D. Couzin, J. Krause, N. R. Franks, and S. A. Levin. Effective leadership and decision-making in animal groups on the move. *Nature*, 433(7025):513–516, 2005.
7. M. Aureli and M. Porfiri. Coordination of self-propelled particles through external leadership. *EPL*, 92(4), 2010.
8. Dyer J. R. G. Faria J. J. and J. Krause. A novel method for investigating the collective behaviour of fish: Introducing 'robofish'. *Behavioral Ecology and Sociobiology 8, vol. 64, 1211-1218*, 2010.
9. Gribovskiy A., Halloy J., Deneubourg J.-L., H. Bleuler, and F. Mondada. Towards mixed societies of chickens and robots. *IEEE/RSJ 2010 International Conference on Intelligent Robots and Systems, Conference Proceedings pp. 4722-4728*, 2010.
10. L. Wang and L. Guo. Robust consensus and soft control of multi-agent systems with noises. *Journal of Systems Science and Complexity 3, vol. 21, 406-415*, 2008.
11. G. Sartoretti and Hongler M.-O. Soft control of swarms - analytical approach. In *Proceedings - International Conference on Agents and Artificial Intelligence 2013*, 2013.
12. G. Sartoretti and M.-O. Hongler. *Soft control of self-organized locally interacting brownian planar agents*, volume 8111 LNCS, PART 1 of *Lecture Notes in Computer Science (including subseries Lecture Notes in Artificial Intelligence and Lecture Notes in Bioinformatics)*. Springer, 2013.
13. T. Yang, P. G. Mehta, and S. P. Meyn. Feedback particle filter. *IEEE Transactions on Automatic Control*, 58(10):2465–2480, 2013.
14. S. Pequitoy, A.P. Aguiary, B. Sinopoli, and D.A. Gomes. Nonlinear estimation using mean field games. *NETGCOOP: International conference on NETwork Games, COntrol and OPtimization*, pages 1–10, 2011.
15. O. Guéant, J.-M.. Lasry, and P.-L. Lions. *Mean field games and applications*, volume 2003 of *Lecture Notes in Mathematics*. 2011.
16. J. C. Taylor. The minimal eigenfunctions characterize the Ornstein-Uhlenbeck process. *The Annals of Probability*, 17(3):1055–1062, 1989.
17. M.-O. Hongler. Study of a class of nonlinear stochastic process - boomerang behavior of the mean. *Physica D*, 2:353–369, 1981.
18. P. Dai Pra. Stochastic control approach to reciprocal diffusion processes. *Applied Mathematics and Optimization*, 23(3):313–329, 1991.
19. V. E. Beneš. Exact finite dimensional filters for certain diffusion with nonlinear drifts. *Stochastics*, 5:65–92, 1981.
20. F. E. Daum. Exact finite-dimensional nonlinear filters. *Proceedings of the 24th IEEE Conference on Decision Control*, pages 1938–1945, 1985.

21. A. H. Jazwinski. *Stochastic Processes and Filtering Theory*. Academic Press, 1970.
22. A. Bensoussan, J. Frehse, and P. Yam. *Mean Field Games and Mean Field Type Control Theory*. Springer, 2013.
23. I. S. Gradshteyn and I. M. Ryzhik. *Table of integrals series and products*. Academic Press, 1980.

Appendix - Details of Calculations

For the readers ease we introduce notations and collect formulas useful for the computation of the conditional probability density.

5.1 Collection of useful formulas

$$\sinh(x+y) = \sinh(x)\cosh(y) + \cosh(x)\sinh(y),$$

$$\cosh(x+y) = \cosh(x)\cosh(y) + \sinh(x)\sinh(y).$$

$$\int_{\mathbb{R}} e^{-ax^2 - 2bx - c} dx = \sqrt{\frac{\pi}{a}} e^{\frac{b^2 - ac}{a}}, \qquad a > 0$$

$$\int_{\mathbb{R}} \cosh[x\alpha] e^{-\frac{(x-\mu)^2}{\gamma}} dx = \sqrt{\pi\gamma} \cosh[\mu\alpha] e^{\frac{1}{4}\gamma\alpha^2} \tag{24}$$

$$\int_{\mathbb{R}} x \cosh[x\alpha] e^{-\frac{(x-\mu)^2}{\gamma}} dx = \sqrt{\pi\gamma} \left[\frac{\alpha\gamma}{2} \sinh(\mu\alpha) + \mu\cosh(\mu\alpha) \right] e^{\frac{1}{4}\gamma\alpha^2} \tag{25}$$

$$\int_{\mathbb{R}} x \sinh[x\alpha] e^{-\frac{(x-\mu)^2}{\gamma}} dx = \sqrt{\pi\gamma} \left[\frac{\alpha\gamma}{2} \cosh(\mu\alpha) + \mu\sinh(\mu\alpha) \right] e^{\frac{1}{4}\gamma\alpha^2} \tag{26}$$

From sections 9.24 and 9.25 of Gradshteyrn and Ryzhik[23], we extract:

$$\mathcal{D}_{-B}(x) = \frac{e^{-\frac{x^2}{4}}}{\Gamma(B)} \int_{\mathbb{R}^+} e^{-x\zeta - \frac{\zeta^2}{2}} \zeta^{B-1} d\zeta, \quad (\mathcal{R}(B) > 0) \quad \text{(see Gradshteyrn and Ryzhik[23], 9.241/2)} \tag{27}$$

$$\begin{cases} \mathcal{Y}_B(x) := \frac{1}{2}\left[\mathcal{D}_{-B}(x) + \mathcal{D}_{-B}(-x)\right] = \sqrt{\frac{2}{\pi}} \frac{e^{-\frac{x^2}{4}}}{\Gamma(B)} \int_{\mathbb{R}^+} \cosh(x\zeta) e^{-\frac{\zeta^2}{2}} \zeta^{B-1} d\zeta, \\[2mm] \frac{d^2}{dx^2}\{\mathcal{Y}_B(x)\} = \left[\frac{x^2}{4} + \left(B - \frac{1}{2}\right)\right]\mathcal{Y}_B(x), \quad (B \geq 0), \quad \text{(see Gradshteyrn and Ryzhik[23], 9.255/1)} \end{cases} \tag{28}$$

5.2 Quadratures

Let us define the couple of quadratures:

$$\mathcal{J}_i(m, s, B) = \int_{\mathbb{R}} x^i \mathcal{Y}_B(x) e^{-\frac{(x-m)^2}{2s}} dx, \quad i = 0, 1. \tag{29}$$

684

0$^{\text{th}}$-order moment - $\mathcal{J}_0(m, B)$ Using the integral representation given in Eq.(28), we can write:

$$\mathcal{J}_0(m, s, B) = \int_{\mathbb{R}} \left\{ \mathcal{Y}_B(x) e^{-\frac{(x-m)^2}{2s}} \right\} dx$$

$$= \sqrt{\frac{2}{\pi}} \frac{1}{\Gamma(B)} \int_{\mathbb{R}^+} \zeta^{[B-1]} e^{-\frac{\zeta^2}{2}} \left\{ \int_{\mathbb{R}} \cosh(\zeta x) e^{-\frac{(x-m)^2}{2s} - \frac{x^2}{4}} dx \right\} d\zeta$$

$$\mathcal{J}_0(m, s, B) = \sqrt{\frac{2}{\pi}} \frac{e^{-\frac{m^2}{2(2+s)}}}{\Gamma(B)} \int_{\mathbb{R}^+} \zeta^{[B-1]} e^{-\frac{\zeta^2}{2}} \left\{ \int_{\mathbb{R}} \cosh(\zeta x) e^{-\frac{(2+s)}{4s}\left(x - \frac{2m}{2+s}\right)^2} dx \right\} d\zeta$$

Now we use Eq.(24) with $\gamma = 4s/(2+s)$ and $\mu = 2m/(2+s)$ to get

$$\mathcal{J}_0(m, s, B) = 2\sqrt{\frac{2}{\pi}} \sqrt{\frac{\pi s}{(2+s)}} \frac{e^{-\frac{m^2}{2(2+s)}}}{\Gamma(B)} \int_{\mathbb{R}^+} \zeta^{[B-1]} e^{-\frac{\zeta^2}{2}\left[\frac{2-s}{2+s}\right]} \cosh\left[\frac{2m\zeta}{2+s}\right] d\zeta$$

Let us introduce the renormalization $\eta := \zeta\sqrt{\frac{2-s}{2+s}}$, which implies

$$\mathcal{J}_0(m, s, B) = \sqrt{\frac{2}{\pi}} 2\sqrt{\frac{\pi s}{2+s}} \frac{e^{-\frac{m^2}{2(2+s)}}}{\Gamma(B)} \left[\sqrt{\frac{2+s}{2-s}}\right]^B \underbrace{e^{+\frac{m^2}{(4-s^2)}} e^{-\frac{m^2}{(4-s^2)}}}_{=1} \int_{\mathbb{R}^+} \eta^{[B-1]} \cosh\left[\frac{2m\,\eta}{\sqrt{4-s^2}}\right] e^{-\frac{\eta^2}{2}} d\eta.$$

$$(30)$$

Finally, using the definition Eq.(28), we end up with:

$$\mathcal{J}_0(m, s, B) = 2\sqrt{\frac{\pi s}{2+s}} \left[\sqrt{\frac{2+s}{2-s}}\right]^B e^{\frac{m^2 s}{2(4-s^2)}} \mathcal{Y}_B\left(\frac{2m}{\sqrt{4-s^2}}\right). \qquad (31)$$

First order moment - $\mathcal{J}_1(m, s, B)$ From the definitions Eqs.(27) and (29), one can write:

$$\mathcal{J}_1(m, s, B) := \int_{\mathbb{R}} \left\{ x\,\mathcal{Y}_B(x) e^{-\frac{(x-m)^2}{2s}} \right\} dx$$

From the previous equation and the definition of $\mathcal{J}_0(m, s, B)$ given in Eq.(29), we can write:

$$\frac{d}{dm} \mathcal{J}_0(m, s, B) = \int_{\mathbb{R}} \left\{ \left[\frac{(x-m)}{s}\right] \mathcal{Y}_B(x) e^{-\frac{(x-m)^2}{2s}} \right\} dx = \frac{1}{s}\mathcal{J}_1(m, s, B) - \frac{m}{s}\mathcal{J}_0(m, s, B).$$

This is equivalent to the relation:

$$\mathcal{J}_1(m, s, B) = m\mathcal{J}_0(m, s, B) + s\left[\frac{d}{dm}\mathcal{J}_0(m, s, B)\right]. \qquad (32)$$

Using Eqs.(31) and (32), the conditioned expectation reads:

$$\mathbb{E}(x|\mathcal{Z}_t) = \frac{\mathcal{J}_1(m.b, B)}{\mathcal{J}_0(m, s, B)}\Big|_t = m + s\left[\frac{d}{dm}\left(\log\{\mathcal{J}_0(m, s, B)\}\right)\right]\Big|_t = \frac{4}{4-s^2}m(z) + \frac{2s}{\sqrt{4-s^2}}f_B\left(\frac{2\,m(z)}{\sqrt{4-s^2}}\right)$$

$$(33)$$

Modeling and analysis of cyclic inhomogeneous Markov processes: a wind turbine case study

Teresa Scholz[1,2], Vitor V. Lopes[3,4], Pedro G. Lind[5], and Frank Raischel[6,7]

[1] Center for Theoretical and Computational Physics, University of Lisbon, Portugal
[2] Energy Analysis and Networks Unit, National Laboratory of Energy and Geology, Lisbon, Portugal
  (e-mail: `teresa.scholz@lneg.pt`)
[3] DEIO-CIO, Science faculty, University of Lisbon, Portugal
[4] Universidad de las Fuerzas Armadas-ESPE, Latacunga, Ecuador
[5] ForWind-Center for Wind Energy Research, Institute of Physics, Carl-von-Ossietzky University of Oldenburg, Oldenburg, Germany
[6] Department of Theoretical Physics, University of Debrecen, Debrecen, Hungary
[7] Center for Geophysics, IDL, University of Lisbon, Portugal

Abstract. A method is proposed to reconstruct a cyclic time-inhomogeneous Markov process from measured data. First, a time-inhomogeneous Markov model is fit to the data, taken here from measurements on a wind turbine. From the time-dependent transition matrices, the time-dependent Kramers-Moyal coefficients of the corresponding stochastic process are computed. Further applications of this method are discussed.
Keywords: time-inhomogeneous Markov process; cyclic Markov process; Kramers-Moyal coefficients.

1 Introduction

Many complex systems can be described, within a certain level of modelization, as stochastic processes. A general stochastic process can be characterized in the linear noise approximation through a Fokker-Planck equation, in continuous variables. For dealing with discrete variables in discrete time steps, often Markov Chains are the models of choice. Although in many cases both approaches converge in the limit of small time steps and increments of the stochastic variables, this correspondence is in general non-trivial[11]. In the Fokker-Planck picture, the so-called Kramers-Moyal (KM) coefficients provide a complete description of a given stochastic process[2].

In the past decades, numerical procedures have been established to estimate the KM coefficients from measured stochastic data, which are applicable for any stationary, i.e. time-homogeneous, Markov process. These methods require large sequences of data, but they are robust[1], have well-known errors and limitations[3], require little intervention and are typically parameter-free[1,5].

However, for non-stationary Markov processes, much fewer methods and results are available to our knowledge. In this case, estimations of the time-dependent KM coefficients can be obtained by two approaches: either the data from the inhomogeneous

process is split into shorter, homogeneous sequences, on which then an estimate of the KM coefficients can be performed through the aforementioned methods[13]. Or, if the inhomogeneous process is also cyclic, a parametrized time-dependent *ansatz* for the KM coefficients can be fit to the data[14]. Compared to the stationary processes, both approaches for the inhomogeneous case require a much higher level of pre-analysis, guesswork and iterative improvement.

In this paper, we present a method that allows to estimate the transition matrices of a time-inhomogeneous Markov model from data. As reported in a previous publication[6], this method provides results with a considerable level of accuracy. Under well-known limitations, the discrete Markov model corresponds to a continuous stochastic process in the form of a Fokker-Planck equation, which is completely characterized, in this case, through its time-dependent KM coefficients. From the transition matrices, we can immediately calculate these KM coefficients, and therefore characterize the dynamical features underlying the time-dependent stochastic process.

We apply this methodology to data from a turbine in a wind park, where measurements of the wind velocity and direction, and the electric power output of the turbine are taken in 10 minute intervals. The results presented from this analysis show the general applicability of our method and are in agreement with previous findings.

This paper is organized as follows. We start in Sec. 2 by introducing both the cyclic time-dependent Markov model and the procedure for extracting stochastic evolution equations directly from data series. In Sec. 3 we describe the data and in Sec. 4 we present the time-dependent functions that define the stochastic evolution of the state of the wind turbine. Section 5 concludes the paper.

2   Methodology

This section describes the methodology used for the data analysis. In Sec. 2.1 the cyclic inhomogeneous Markov model to represent the daily patterns in the data is described and in Sec. 2.2 we explain how stochastic evolution equations are derived directly from the Markov process transition matrices.

2.1   Modelling cyclic time-dependent Markov processes

The goal of this time-inhomogeneous Markov process is to get a model that accurately reproduces the long-term behavior while considering the daily patterns observed in the data. Thus, the proposed objective function combines two maximum likelihood estimators: the first term maximizes the likelihood of the cycle-average probability; and, the second term maximizes the likelihood of the time-dependent probability. The final optimization problem is transformed into a convex one using the negative logarithm of the objective function. This section gives a brief overview over the final optimization problem. A detailed description of the objective function, the parametrization of the time-variant probability functions, and the constraints that must be added to the optimization problem to ensure its Markov properties is provided in [6].

A discrete finite Markov process $\{X_t \in S, t \geq 0\}$ is a stochastic process on a discrete finite state space $S = \{s_1, ..., s_n\}$, $n \in \mathbb{N}$, whose future evolution depends only on its current state [8].

It can be fully described by the conditional probability $Pr\{X_{t+1} = s_j \mid X_t = s_i\}$ of the Markov process moving to state s_j at time step $t + 1$ given that it is in state s_i at time t. It is called the t-th step transition probability, denoted as $p_{i,j}(t)$.

Being time-dependent, the Markov process has associated transition probability matrices P_t that change with time. Considering n possible states, the matrices P_t have dimension $n \times n$ with entries $[P_t]_{i,j} = p_{i,j}(t)$ for all $i, j = 1, \ldots, n$, satisfying $p_{i,j}(t) \geq 0$ and $\sum_j p_{i,j}(t) = 1$.

Markov process is called cyclic with period $T \in \mathbb{R}$, if T is the smallest number, such that $p_{i,j}(mT + r) = p_{i,j}(r)$ for all $m \in \mathbb{N}$ and $0 \leq r < T$. See Ref. [9]. Since this paper deals with discrete data, T and r can considered to be multiples of the time step Δt between successive data points and therefore integers. One can describe the cyclic Markov process by T transition matrices P_r, $r = 0, ..., T - 1$. The remainder of time step t modulo T will be denoted as r_t and consequently $r_t = r_{t+mT}$. We fix $T = 1$ day and use $\Delta t = 1$.

In this paper, the transition probabilities $p_{i,j}(z)$ are modeled by Bernstein polynomials, namely

$$p_{i,j}(z) = \sum_{\mu=0}^{k} \beta_\mu^{i,j} b_{\mu,k}(z), \tag{1}$$

where $z = r/T$ indicates the time of the day ($T = 1$ day), $b_{\mu,k}(z)$ is the μ-th Bernstein basis polynomial of order k, and $\beta_\mu^{i,j} \in \mathbb{R}$. The choice of these polynomials has several advantages properly described in [6].

To maximize the likelihood of the time-dependent transition probabilities given the data, the objective function must consider the time of the day z when the transition happens. The corresponding term of the objective function is thus given by $\sum_{(i,j)_z \in \mathcal{S}_z} \log(p_{i,j}(z))$, where $\mathcal{S}_z$ is the set of observed transitions together with the time z when they happen. This estimator allows to compute the intra-cycle transition probability functions, and thus to represent the daily patterns present in the data.

A second term is added to this function, namely $\sum_{(i,j) \in \mathcal{S}} \log(p_{i,j}^{avg})$, where $\mathcal{S}$ is the set of transitions observed in the data and $p_{i,j}^{avg}$ is the cycle-average (daily) probability of transition from state s_i to s_j. It is given by $p_{i,j}^{avg} = \frac{1}{k+1} \sum_{\mu=0}^{k} \beta_k^{i,j}$. This second term is the maximum likelihood estimator for the daily average probability and its addition to the objective function increases the consistency of the long-term behavior of the Markov process with the data.

Using the resulting overall objective function the optimization problem to be solved for the transition probability coefficients $\beta_\mu^{i,j}$ is translated into the minimization of

$$\mathcal{L} = - \sum_{(i,j) \in \mathcal{S}} \log(\frac{1}{k+1} \sum_{\mu=0}^{k} \beta_\mu^{i,j}) - \sum_{(i,j)_z \in \mathcal{S}_z} \log(\sum_{\mu=0}^{k} \beta_\mu^{i,j} b_{\mu,k}(z)) \tag{2}$$

subject to

$$\sum_j \beta_\mu^{i,j} = 1 \tag{3a}$$

$$\beta_0^{i,j} = \beta_k^{i,j} \tag{3b}$$

$$\beta_0^{i,j} = \tfrac{1}{2}(\beta_1^{i,j} + \beta_{k-1}^{i,j}) \tag{3c}$$

$$\beta^{i,j}(w) \le 1 \tag{3d}$$

$$0 \le \beta^{i,j}(w) \tag{3e}$$

with $i, j = 1, \ldots, n$ and $\mu = 0, \ldots, k$, k being the order of the Bernstein polynomials and w the number of subdivisions. Constraint (3a) assures the row-stochasticity of the transition matrices, while constraints (3b) and (3c) impose $\mathcal{C}^0$- and $\mathcal{C}^1$-continuity at $z = 0$. Constraints (3d) and (3e) bound the transition probabilities between 0 and 1. These constraints are derived using a property of the Bernstein polynomials to always lie in the convex hull defined by their control points $(\frac{k}{\mu}, \beta_\mu)$, $\mu = 0, ..., k$. This convex hull bound can be tightened by subdivision using the de Casteljau algorithm. In the resulting constraints (3d) and (3e), w is the number of subdivisions.

2.2 Extracting the stochastic evolution equation

In this section we characterize general stochastic processes through a Fokker-Planck equation. We consider a N-dimensional stochastic process $\mathbf{X} = (X_1(t), \ldots, X_N(t))$ whose probability density function (PDF) $f(\mathbf{X}, t)$ evolves according to the Fokker-Planck equation (FPE) [2]

$$\frac{\partial f(\mathbf{X}, t)}{\partial t} = -\sum_{i=1}^{N} \frac{\partial}{\partial x_i} \left[D_i^{(1)}(\mathbf{X}) f(\mathbf{X}, \mathbf{t}) \right]$$
$$+ \sum_{i=1}^{N} \sum_{j=1}^{N} \frac{\partial^2}{\partial x_i \partial x_j} \left[D_{ij}^{(2)}(\mathbf{X}) f(\mathbf{X}, t) \right] \quad . \tag{4}$$

The functions $D_i^{(1)}$ and $D_{ij}^{(2)}$ are the first and second Kramers-Moyal coefficients respectively, more commonly called the drift and diffusion coefficients.

These coefficients provide a complete description of a given stochastic process and are defined as

$$\mathbf{D}^{(k)}(\mathbf{X}) = \lim_{\Delta t \to 0} \frac{1}{\Delta t} \frac{\mathbf{M}^{(k)}(\mathbf{X}, \Delta t)}{k!} \quad , \tag{5}$$

where $\mathbf{M}^{(k)}$ are the first ($k = 1$) and second ($k = 2$) conditional moments. $\mathbf{D}^{(1)}$ is the drift vector and $\mathbf{D}^{(2)}$ the diffusion matrix.

If the underlying process is stationary and therefore both drift and diffusion coefficients do not explicitly depend on time t, the conditional moments can be directly derived from the measured data as [1,5]:

$$M_i^{(1)}(\mathbf{X}, \Delta t) = \langle Y_i(t + \Delta t) - Y_i(t) | \mathbf{Y}(t) = \mathbf{X} \rangle$$
$$M_{ij}^{(2)}(\mathbf{X}, \Delta t) =$$
$$\langle (Y_i(t + \Delta t) - Y_i(t))(Y_j(t + \Delta t) - Y_j(t)) | \mathbf{Y}(t) = \mathbf{X} \rangle, \tag{6}$$

where $\mathbf{Y}(t) = (Y_1(t), \ldots, Y_N(t))$ exhibits the N-dimensional vector of measured variables at time t and $\langle \cdot | \mathbf{Y}(t) = \mathbf{X} \rangle$ symbolizes a conditional averaging over the entire measurement period, where only measurements with $\mathbf{Y}(t) = \mathbf{X}$ are taken into account. In practice binning or kernel based approaches with a certain threshold are applied in order to evaluate the condition $\mathbf{Y}(t) = \mathbf{X}$. See e.g. Ref. [1] for details.

If the process is non-stationary and time-inhomogeneous, we must consider an explicit time-dependence of the KM coefficients, which translates into time-dependent conditional moments that can be calculated using a short-time propagator[1]. In our case, this short-time propagator corresponds to the transition probabilities $p_{i,j}(t)$, yielding for the conditional moments

$$M^{(l)}(P_k, v_k, \theta_k, t + \Delta t) = \begin{pmatrix} \sum_j p_{k,j}(t) \, (v_j - v_k)^l \\ \sum_j p_{k,j}(t) \, (P_j - P_k)^l \\ \sum_j p_{k,j}(t) \, (\theta_j - \theta_k)^l \end{pmatrix} . \tag{7}$$

3   Data: wind and power at one wind turbine

The data for this study was obtained from a wind power turbine in a wind park located in a mountainous region in Portugal. The time series consists of a three-year period (2009-2011) of historical data gotten from the turbine data logger. The sampling time of 10 minutes leads to 144 samples each day. The data-set comprises three variables, wind power, speed and direction (nacelle orientation). The wind speed information was collected from the anemometer placed in the wind turbine hub. Due to confidentiality, wind power and speed data values are reported as a fraction of the rated power and the cut-out speed, respectively.

For this Markov model, each state is defined by the values of all three variables, namely the wind speed, wind direction and power output. Figure 1 shows the data observations and the state partitions projected into the wind direction and speed plane (right) and the wind power and speed plane (left). As expected, the observations projected into the wind power and speed plane define the characteristic power curve of the wind turbine.
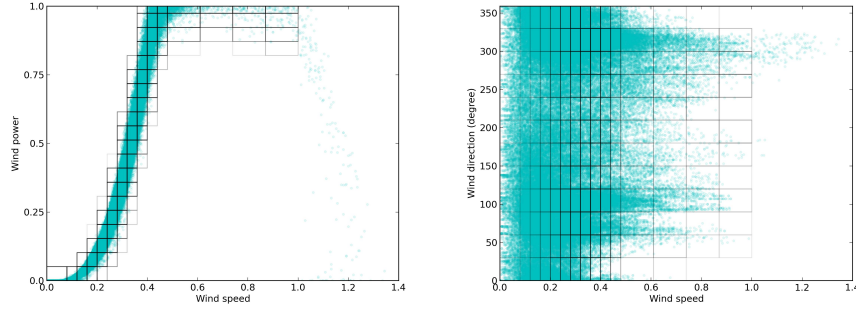
Fig. 1. Representation of all data points projected into the: a) wind direction and speed plane (left); and, b) wind power and speed plane (right). Each rectangle is the projection of a state polyhedron into the two planes. Overall, they define the final state partition for the three-dimensional variable space.

The data space is discretized unevenly to get a good resolution of the high-slope region of the power curve. In a previous work [7], this partition was used in a time-homogeneous Markov chain and proved to lead to an accurate representation of the original data. The wind direction and power are divided by an equally spaced grid leading to 12 and 20 classes, respectively. The wind speed is divided as follows: values below the cut-in speed define one class; between the cut-in and rated wind speed the discretization is narrowed by selecting 10 classes ; and between the rated and cut-out wind speed discretization is widened and 4 classes are defined. Data points with wind speed above the cut-out wind speed are discarded. The complete state set is constructed by listing all possible combinations of the classes of each variable. Due to physical constraints between the variables, most of the states are empty and can are therefore discarded. This reduces the number of states from 3840 to 778, for this turbine.

To compare the model with the original data, wind power, speed and direction time series were simulated adapting the method described by Sahin and Sen [10] to the cyclic time-inhomogeneous Markov model as follows. First, we compute the cumulative probability transition matrices P_r^{cum} with entries $[P_r^{\mathsf{cum}}]_{i,j} = \sum_{j'=0}^{j} p_{i,j'}(r)$. Then an initial state s_i, i.e. $X_0 = s_i$, is randomly selected. A new datapoint X_{t+1} is generated by uniformly selecting a random number ϵ between zero and one and choosing for X_{t+1} the corresponding state $s_{i'}$ such that the probability of reaching it from the current state s_i fullfils $[P_{r_t}^{\mathsf{cum}}]_{i,i'} \geq \epsilon$. Based on this discrete state sequence, a real value for the wind power/speed/direction variables is generated by sampling each state partition uniformly.

Figures 2 and 3 compare the original data with the synthesized data and demonstrate, that the model can capture the data's long-term statistics (fig. 2) as well as the daily patterns (fig. 3).
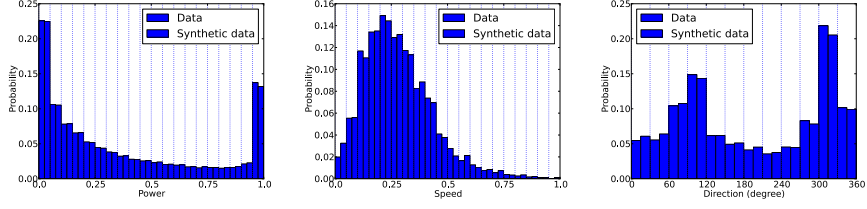
Fig. 2. Comparison of the probability distribution of wind power (left), wind speed (middle) and wind direction (right) of the original with the synthesized data.
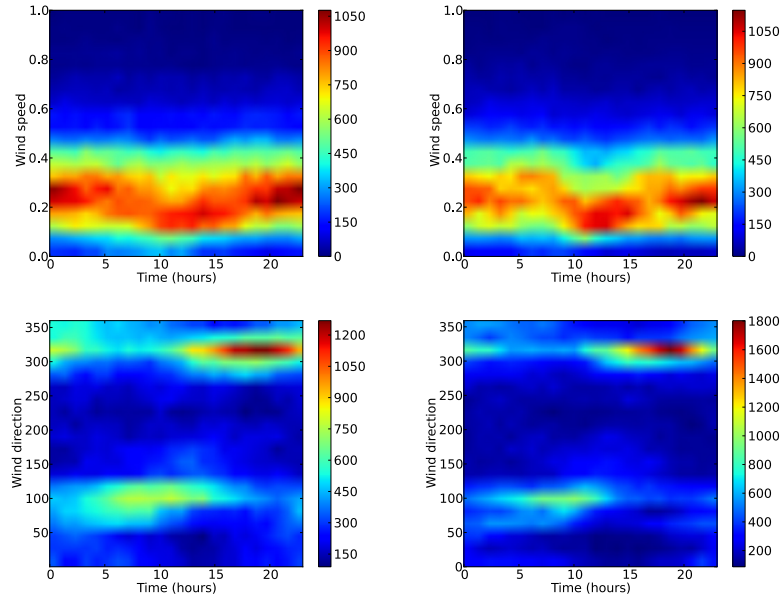
Fig. 3. Two dimensional histograms of the synthetic time-series data, generated with the time-variant Markov model (left) and the original data (right): speed-time (top) and direction-time (bottom).

4 The evolution of drift and diffusion in wind power output

With the procedure outlined in Sec. 2 and having the 144 transition matrices generated as described in Sec. 3 and 2.1, we can now reconstruct the time-dependent stochastic process by calculating the KM coefficients $\mathbf{D}^{(i)}(\hat{\mathbf{X}}, t)$ at each time step $t = 1, \ldots, 144$. Although we obtain the KM coefficients as a function of all three stochastic variables, $[P, v, \theta]$, we here consider only their dependency on the velocity and power production, $\hat{\mathbf{X}} = [\mathbf{P}, \mathbf{v}]$, averaging over the contributions from θ.

The results of this process are presented in Fig.4, where the reconstructed KM coefficients are plotted for three time steps, namely at 6, 12 and 18 hours. The support of the coefficients is limited to the available data which follows the power curves in the v-P plane. From the inspection of Figs. 4, changes in time seem not significative. This means, that even though both the Markov and the stochastic evolution model

contain additional degrees of freedom due to their time-dependent formulation, they are capable of capturing the v-P-dependency, which is invariant. This is expected since the wind turbine operation characteristics should not change through the daily cycle. However, it can be seen in fig. 5 that the procedure is capable of detecting even subtle temporal changes in the transition matrix, which lead to strong daily changes in the KM coefficients.

For all plotted times, the drift coefficients $D^{(1)}$ indicate a restoring force towards the power curve, in accordance with previous results[12]. The diffusion coefficients— only the diagonal components are shown here—show an order of magnitude weaker diffusion in the velocity than in the power, where the latter shows a strong component for diffusion in the $P-$ direction for the high slope region of the power curve. These results again are consistent with our previous analysis of a time-homogeneous model [12]. Remarkably, the out-of the $v, P-$ plane diffusion of the direction component $D^{(2)}_{\theta\theta}$ is strongest for both very high and very low velocities, and for intermediate velocities off the power curve.

Next, we present a closer inspection of the time-dependence of both drift and diffusion, by considering their temporal evolution at a specific point, namely at $(v, P) = (0.34, 0.53)$, which is close to the center of the power curve. Apparently, our method creates smooth curves for the temporal evolution. This is expected since, as a consequence of the parametrization of the Markov model, it can be shown that the conditional moments used to derive the Drift and Diffusion coefficients also can be expressed by Bernstein polynomials in time. Most strikingly, it can be seen that the temporal evolution of both the drift and diffusion coefficient is decoupled between the components. Furthermore, for the same component the evolution of the diffusion coefficient seems to be delayed with respect to the drift. The dominant component is always the power production P, whose drift changes from a positive maximum at 6 h to a negative minimum at 17 h, i.e. the restoring force oscillates from a tendency to higher P values in the morning to a tendency to lower P values in the evening.

It should be noted that the chosen point (v, P) is not necessarily characteristic of the wind field or of the turbine's power production. Other points along the power curve, specifically for low velocities and near the rated wind speed are either more frequent or more characteristic, and their analysis should give increased insight into the temporal evolution of wind speed and power production.
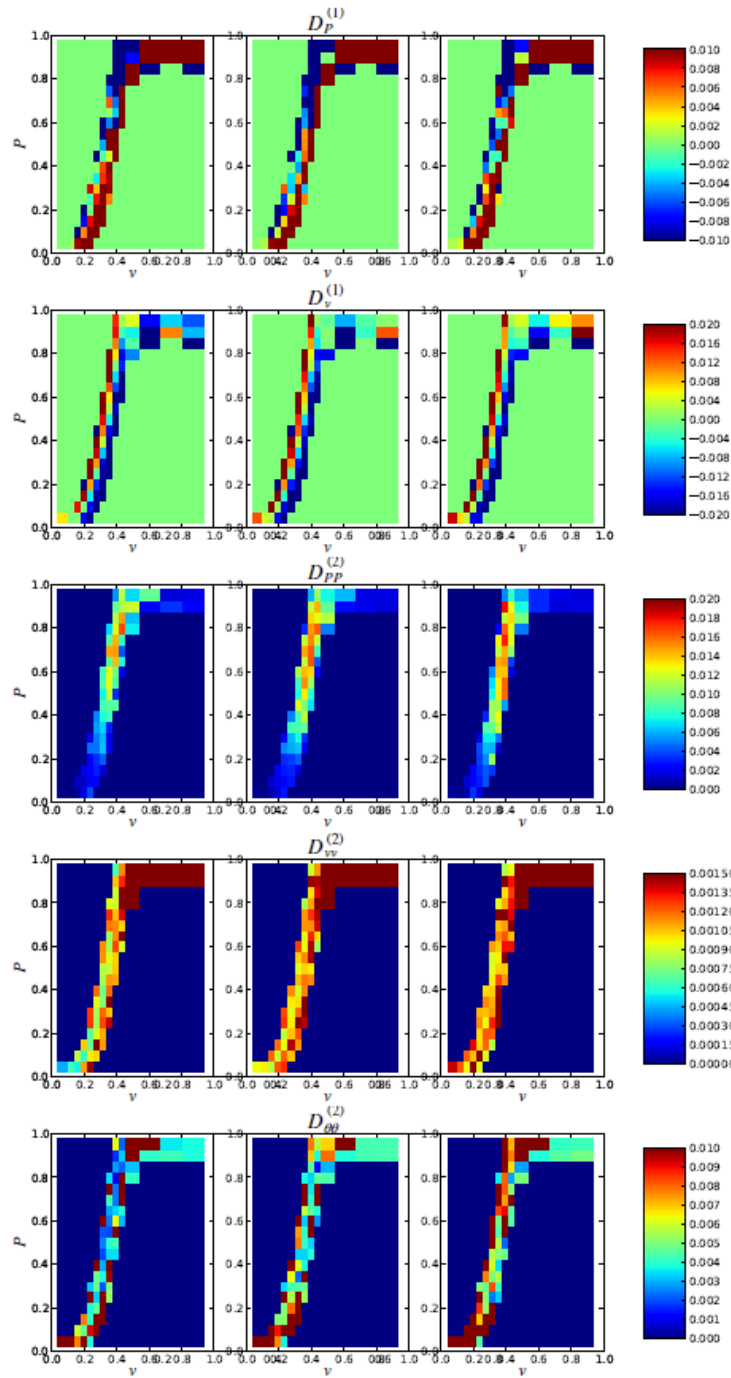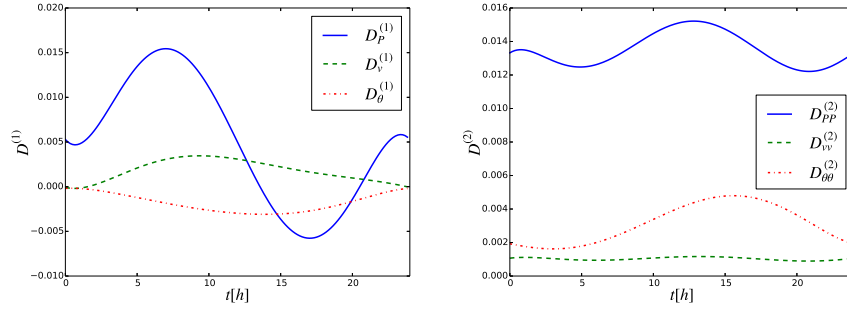
Fig. 4. The first (top two rows) and second (bottom three rows) Kramers-Moyal coefficients for various times (left: 6hours, middle: 12hours, right: 18hours).

Fig. 5. The first (left) and second (right) Kramers-Moyal coefficient, by components, near the center of the power curve, $(v, P) = (0.34, 0.53)$,as a function of time.

5 Conclusions

We have shown in this paper how a time-dependent multi-dimensional stochastic process can be reconstructed from experimental data. Our method provides results in terms of the time-dependent transition matrix of a Markov model, from which the time-dependent Kramers-Moyal coefficients for a corresponding continuous process can be calculated. Application of this method to data from a turbine in a wind park gives results consistent with a previous time-independent method, and adds surprising new insight into the temporal dynamics of the wind field and the machine power production. Preliminary results have shown that the dependence with time observed in Fig. 5 changes depending which region of the power curve we choose. A more systematic study for the full power-velocity range will be carried out in an extended study. Future research will also address the question of applicability of our method to more general cases, dealing also with the reliability and relative errors of this approach.

The aforementioned equivalence of the transition Matrix and the KM coefficients is valid if two requirements are fulfilled. First, the transition amplitudes need to have Gaussian shape, which corresponds to the existence of Gaussian noise in the stochastic process. The validity of this assumption has been checked previously for a similar system and can be reasonably assumed in this case. Secondly, the binning of the stochastic variables for determining the Markov process transition matrix must be small enough[11]. We will investigate the validity of this assumption and the corresponding errors in a forthcoming publication.

Acknowledgements

References

1. R. Friedrich, J. Peinke, M. Sahimi and M.R.R. Tabar, Phys. Rep. **506** 87 (2011).
2. H. Risken, *The Fokker-Planck Equation* (Springer, Heidelberg,1984).
3. D. Kleinhans, Phys. Rev. E **85** 026705 (2012).
4. F. Boettcher, J. Peinke, D. Kleinhans, R. Friedrich, P.G. Lind, M. Haase, Phys. Rev. Lett. **97** 090603 (2006).
5. P.G. Lind, M. Haase, F. Boettcher, J. Peinke, D. Kleinhans and R. Friedrich, Physical Review E 81 041125 (2010).
6. T. Scholz, V.V. Lopes, A. Estanqueiro, "A cyclic time-dependent markov process to model daily patterns in wind turbine power production", Energy **67**(0), 557-568, 2014.
7. V.V. Lopes, T. Scholz, A. Estanqueiro, and A.Q. Novais, "On the use of Markov chain models for the analysis of wind power time series", Environment and Electrical Engineering (EEEIC), 2012 11th International Conference on, 770-775, 2012.
8. J.G. Kemeny and J.L. Snell, "Finite Markov Chains", New York : Springer-Verlag, 1976.
9. A. Platis and N. Limnios and M. Le Du, "Dependability analysis of systems modeled by non-homogeneous Markov chains", Reliability Engineering and System Safety, **61**(3), 235-249, 1998.
10. A.D. Sahin and Z. Sen, "First-order Markov chain approach to wind speed modelling", Journal of Wind Engineering and Industrial Aerodynamics, **89**(3-4), 263-269, 2001.
11. N.G. van Kampen, *Stochastic Processes in Physics and Chemistry* (North Holland, 2007).
12. F.Raischel, T.Scholz, V.V.Lopes and P.G.Lind, "Uncovering wind turbine properties through two-dimensional stochastic modeling of wind dynamics", Phys. Rev. E **88** 042146 (2013).
13. A. M.van Mourik, A.Daffertshofer, P.J.Beek, "Estimating Kramers Moyal coefficients in short and non-stationary data sets", Physics Letters A **351**, Issue 1-2, 13-17, 2006.
14. C.Micheletti, G.Bussi, A.Laio, "Optimal Langevin Modeling of out-of-Equilibrium Molecular Dynamics Simulations", The Journal of Chemical Physics **129**, 7, 2008.

Estimating Multi-Factor Discretely Observed Vasicek Term Structure Models with non-Gaussian Innovations

Takayuki Shiohama[1]

Department of Management Science, Faculty of Engineering, Tokyo University of Science, Tokyo, Japan
(E-mail: `shiohama@ms.kagu.tus.ac.jp`)

Abstract. In this paper, we propose a multi-factor model in which the discretely observed short-term interest rates follow a non-Gaussian and dependent process. The state space formulation has the advantages of taking into account both the cross-sectional and time-series restrictions on the data and measurement errors in the observed yield curve. Clarifying the non-Gaussianity and dependency of the dynamics of short-term interest rates, we show that these features are important to capture the dynamics of the observed yield curve.
Keywords: Asymptotic expansion, state space model, term structure model, Vasicek model.

1 Introduction

Term structure of interest rates describes the relationship between the yield on a zero-coupon bond and its maturity. Learning about the nature of bond yield dynamics plays a critical role in monetary policy, derivative pricing and forecasting, and risk-management analysis. It is necessary to capture accurately the term structure of interest rates in order to evaluate the price of interest rate derivatives. A number of theoretical term structure models have been proposed in the literature. The early models which are still widely used include these by Vasicek[10] and Cox et al.[4].

Although single-factor Vasicek model has been widely used in the theoretical literature, empirical research reports that it fails to appropriately capture the behavior of short rates. The aim of this paper is to develop a closed-form valuation for pricing zero-coupon bonds for the multi-factor Vasicek term structure models where the innovations of underlying short rate processes have non-Gaussian and dependent processes. Honda *et al.*[7] and Shiohama and Tamaki[9] consider the higher-order asymptotic valuation for zero-coupon bonds and the European call options on zero-coupon bonds using single-factor discretely observed Vasicek models with non-Gaussian and dependent error structure. Miura *et al.*[8] develop a closed-form valuation for pricing defaultable bonds incorporating a stochastic risk-free interest rate and defaultable intensity processes have non-Gaussian and dependent processes.

This paper is organized as follows: Section 2 explains the multi-factor term structure model which is based on the discretely sampled Vasicek model with non-Gaussian innovation. The analytic expression for the approximate zero-coupon bond prices is obtained. Section 3 discusses the state-space formulation of the model and the estimation procedures. Section 4 presents the data used and the empirical results for the proposed models are illustrated. Finally, some conclusions are offered in Section 5.

2 The Multi-Factor Models

The model for the analysis is the discretely sampled short rates with interval Δ. The spot interest rate is assumed to be the sum of K state variables $X_{j,t}$

$$r_t = \sum_{j=1}^{K} X_{j,t},$$

and the state variable are driven by the non-Gaussain and dependent innovations. These models are considered in Honda *et al.*[7], Shiohama and Tamaki [9], and Miura *et al.*[8]. Each factor $X_{j,t}$ is of the form

$$X_{j,t} - X_{j,t-1} = \kappa_j(\mu_j - X_{j,t-1})\Delta + \Delta^{1/2}Z_{j,t}, \quad j = 1, \ldots, K, \tag{1}$$

where $Z_{j,t}$ are independent such that $E[Z_{i,t}Z_{j,t}] = 0$ for $i \neq j$, μ_j are the long-term mean of $X_{j,t}$, κ_j are their mean reversion parameters. The innovations $\{Z_{j,t}\}$ are forth order stationary in the following sense.

Assumption 1 *For $j \in \{1, 2, \ldots, K\}$, the process $\{\boldsymbol{Z} = (Z_{1,t}, \ldots, Z_{K,t})'\}$ is fourth-order stationary in the sense that*

1. $E[Z_{j,t}] = 0$,
2. $cum(Z_{j,t}, Z_{j,t+u}) = c_{Z_j}(u)$,
3. $cum(Z_{j,t}, Z_{j,t+u_1}, Z_{j,t+u_2}) = c_{Z_j}(u_1, u_2)$,
4. $cum(Z_{j,t}, Z_{j,t+u_1}, Z_{j,t+u_2}, Z_{j,t+u_3}) = c_{Z_j}(u_1, u_2, u_3)$.

Assumption 2 *The k-th order cumulants $c_{Z_j}(u_1, \ldots, u_{k-1})$ of $Z_{j,t}$, $j = 1, \ldots, K$, for $k = 2, 3, 4$ satisfy*

$$\sum_{u_1, \cdots, u_{k-1}=-\infty}^{\infty} |c_{Z_j}(u_1, \ldots, u_{k-1})| < \infty.$$

Assumptions 1 and 2 are satisfied by a wide class of time series models containing the univariate ARMA and GARCH processes.

Hereafter we assume that the current time is set at $t = 0$, and that the initial factors $X_{j,0}$ are observable and fixed. Then r_t is discretely sampled at times $0, \Delta, 2\Delta, \ldots, n\Delta(\equiv T)$ over $[0, T]$. For the notational convenience, we use following notation. Let

$$A_{j,u} = \mu_j(u\Delta - B_{j,u}), \qquad B_{j,u} = \frac{1}{2\kappa_j}(1 + v_j)(1 - v_j^u),$$

$$a_{j,u} = \frac{2}{\kappa_j\Delta}\left\{1 - \frac{1}{2}v_j^{u-1}(1 + v_j)\right\},$$

where $v_j = 1 - \kappa_j \Delta$ for $j = 1, \ldots, K$ and $u = 1, \ldots, n$. Then it follows from Honda $et\ al.$[7] that

$$P(0,T) = E_0^Q \left[\exp \left(- \int_0^T r_t dt \right) \right] = E_0^Q \left[\exp \left(- \sum_{j=1}^K \int_0^T X_{j,t} dt \right) \right]$$

$$= \prod_{j=1}^K E_t^Q \left[\exp \left(\int_0^T X_{j,t} dt \right) \right] \approx \prod_{j=1}^K E_0^{\tilde{Q}} \left[\exp \left\{ -\Delta \left(\frac{1}{2} r_0 + \sum_{u=1}^{n-1} r_u + \frac{1}{2} r_n \right) \right\} \right]$$

$$= \prod_{j=1}^K \exp(-A_{j,n} - B_{j,n} r_0) AF_{j,n}$$

where $E_0^{\tilde{Q}}$ is the expectation under the asymptotic risk-neutral measure, which is discussed in Miura $et\ al.$[8], and

$$AF_{j,n} = E_0^{\tilde{Q}} \left[\exp \left(- \frac{\Delta^{3/2}}{2} \sum_{u=1}^n a_{j,u} Z_{j,n-u+1} \right) \right]. \tag{2}$$

Let

$$Y_{j,n} = \Delta^{1/2} \sum_{u=1}^n b_{j,u} Z_{j,n-u+1} \quad \text{and} \quad b_{j,u} = \frac{\Delta}{2} a_{i,j} = \frac{1}{\kappa_j} \left\{ 1 - \frac{1}{2} v_j^{u-1} (1 + v_j) \right\}. \tag{3}$$

Using the process $\{Y_{j,n}\}$, we express the product of the $AF_{j,n}$ terms as

$$\prod_{j=1}^K AF_{j,n} = E_0^{\tilde{Q}} \left[\exp \left(- \sum_{j=1}^K Y_{j,n} \right) \right].$$

We give an analytic approximation of the zero coupon bond prices for the multi-factor discretely observed Vasicek term structure models with non-Gaussian and dependent innovations by the Edgeworth expansion of the joint density function of $\boldsymbol{Y}_n = (Y_{1,n}, \ldots, Y_{K,n})'$. It is easy to observe that the processes $\{Y_{j,n}\}, j = 1, \ldots, K$ are fourth-order stationary with $\text{Var}(Y_{j,n}) = \sigma_{j,n}^2$, and the third and fourth order cumulant is denoted by

$$\text{cum}(Y_{j,n}, Y_{j,n}, Y_{j,n}) = n^{-1/2} C_{Y_j}^{(3)} \quad \text{and} \quad \text{cum}(Y_{j,n}, Y_{j,n}, Y_{j,n}, Y_{j,n}) = n^{-1} C_{Y_j}^{(4)}.$$

We need following assumption.

Assumption 3 *The J-th order $(J \geq 5)$ cumulants of $\{Y_{j,n}\}$, $j = 1, \ldots, K$ are of order $O(n^{-J/2+1})$.*

Since we calibrate this model to the market interest rates, we need to include the risk premium before we pricing the zero-coupon bonds. We assume that the jth factor's market price of risk λ_j is constant and define $\bar{\mu}_j = \mu_j - \lambda_i \sigma_{X_j} / \kappa_j$.

By using the asymptotic expansion for the defaultable bond price of Miura $et\ al.$[8], we can derive the following formula for the nominal price of a pure discount bond with face value 1 maturing at time T.

Theorem 1 *Under Assumptions 1–3, the current bond price of the K-factor discretely observed Vasicek term structure model is expressed as*

$$P(0,T) = \exp\left(A(T) - \sum_{j=1}^{K} B_{j,n} X_{j,0}\right) D(T) \tag{4}$$

where

$$A(T) = \sum_{j=1}^{K} A_{j,n} = \sum_{j=1}^{K}\left[-\bar{\mu}_j(n\Delta - B_{j,n}) + \frac{1}{2}\sigma_{j,n}^2\right],$$

$$D(T) = \prod_{j=1}^{K} \exp\left(-\frac{1}{6\sqrt{n}}C_{Y_j}^{(3)} + \frac{1}{24n}C_{Y_j}^{(4)}\right),$$

$$B_{j,n} = \frac{1}{2\kappa_j}(2 - \kappa_j\Delta)(1 - (1 - \kappa_j\Delta)^n).$$

The proof of Theorem 1 is omitted, since it is analogous to the results obtained from Honda *et al.*[7] and Miura *et al.*[8].

The analytic expressions for the bond price and yield given in Theorem 1 are based on the discrete time models with non-Gaussian and dependent innovations. According to this expression, the linkage between continuous and discrete scheme for short rate models are apparent. If $Z_{j,t}$s are standard normal distribution, then as $\Delta \to 0$, bond price tends to the standard multi-factor Vasicek term structures.

3   State Space Representation and Estimation

The application of Kalman filtering methods in the estimation of term structure models using cross-sectional and time series data has been investigated by Duan and Simonate[5], Chen and Schott[3], and Babbs and Nowman[1,2].

To estimate the model, we use the state-space representation of the term structure models with non-Gaussian innovations. Our proposed models is discrete scheme with non-Gaussian driven innovations, hence the corresponding state-space model is also non-Gaussian, however the Kalman filter can still be applied to obtain approximate moments of the model and the resulting filter is quasi-optimal.

Let $R_t(\tau)$ denote the continuously compounded yield on a zero-coupon bond of maturity τ with corresponding discrete sample size $\tau/\Delta = n$. The state-space formulation of the model consists of the measurement and transition equations. To construct measurement equation, we need N zero-coupon rates and use the following relationship between the zero-coupon yield and the price of zero-coupon bonds,

$$R_t(\tau) = -\frac{\ln P(0,\tau)}{\tau} = -\frac{1}{\tau}\left((A(\tau) + \ln D(\tau)) - \sum_{i=1}^{K} B_{j,n} X_{j,n}\right).$$

Then the measurement equation has the following form with $K = 3$

$$
\begin{bmatrix} R_t(\tau_1) \\ R_t(\tau_2) \\ \vdots \\ R_t(\tau_N) \end{bmatrix} = \begin{bmatrix} -\frac{A(\tau_1)-\ln D(\tau_1)}{\tau_1} \\ -\frac{A(\tau_2)-\ln D(\tau_2)}{\tau_2} \\ \vdots \\ -\frac{A(\tau_N)-\ln D(\tau_N)}{\tau_N} \end{bmatrix} + \begin{bmatrix} \frac{B_{1,n_1}}{\tau_1} & \frac{B_{2,n_1}}{\tau_1} & \frac{B_{3,n_1}}{\tau_1} \\ \frac{B_{1,n_2}}{\tau_2} & \frac{B_{2,n_2}}{\tau_2} & \frac{B_{3,n_2}}{\tau_2} \\ \vdots & \vdots & \vdots \\ \frac{B_{1,n_N}}{\tau_N} & \frac{B_{2,n_N}}{\tau_N} & \frac{B_{3,n_N}}{\tau_N} \end{bmatrix} \begin{bmatrix} X_{1,t} \\ X_{2,t} \\ X_{3,t} \end{bmatrix} + \begin{bmatrix} \varepsilon_{t,1} \\ \varepsilon_{t,2} \\ \vdots \\ \varepsilon_{t,N} \end{bmatrix},
$$

or

$$
\boldsymbol{R}_t = \boldsymbol{A}(\boldsymbol{\Psi}) + \boldsymbol{H}(\boldsymbol{\Psi})\boldsymbol{X}_t + \boldsymbol{\varepsilon}_t,
$$

where $\boldsymbol{\Psi}$ denotes the unknown parameter vectors to be estimated and $\boldsymbol{\varepsilon}_t \sim N(\boldsymbol{0}, \boldsymbol{V}_\varepsilon)$ with $\boldsymbol{V}_\varepsilon = \mathrm{diag}(h_1^2, \ldots, h_N^2)$.

To obtain the transition equation for the state-space model, we need conditional mean and variance of the state variable process. Using recursive substitution in (1) and remind that $v_j = 1 - \kappa_j \Delta$, $X_{j,n}$ can be represented as

$$
X_{j,n} = (1 - v_j^n)\bar{\mu}_j + v_j^n X_{j,0} + \Delta^{1/2} \sum_{u=1}^{n} v_j^{u-1} Z_{j,n-u+1}.
$$

For simplicity, we assume that sequence $\{Z_{j,n}\}$ is i.i.d. with zero mean and finite variance $\sigma_{Z_j}^2$. Then the variance of $X_{j,n}$ becomes

$$
\sigma_{X_j}^2 = \sigma_{Z_j}^2 \left[\frac{1 - v_j^{2(n-1)}}{2\kappa_j - \kappa_j^2 \Delta} \right]. \tag{5}
$$

The exact discrete-time models is a VAR(1), and the transition system as follows

$$
\begin{bmatrix} X_{1,t} \\ X_{2,t} \\ X_{3,t} \end{bmatrix} = \begin{bmatrix} \bar{\mu}_1 \kappa_1 \Delta \\ \bar{\mu}_2 \kappa_2 \Delta \\ \bar{\mu}_3 \kappa_3 \Delta \end{bmatrix} + \begin{bmatrix} 1 - \kappa_1 \Delta & 0 & 0 \\ 0 & 1 - \kappa_2 \Delta & 0 \\ 0 & 0 & 1 - \kappa_3 \Delta \end{bmatrix} \begin{bmatrix} X_{1,t-1} \\ X_{2,t-1} \\ X_{3,t-1} \end{bmatrix} + \begin{bmatrix} \eta_{t,1} \\ \eta_{t,2} \\ \eta_{t,3} \end{bmatrix},
$$

or

$$
\boldsymbol{X}_t = \boldsymbol{C}(\boldsymbol{\Psi}) + \boldsymbol{F}(\boldsymbol{\Psi})X_{t-1} + \boldsymbol{\eta}_t(\boldsymbol{\Psi})
$$

where $\eta_t \sim N(\boldsymbol{0}, \boldsymbol{V}_\eta)$ with $\boldsymbol{V}_\eta = \mathrm{diag}(\sigma_{X_1}^2, \sigma_{X_2}^2, \sigma_{X_3}^2)$.

Now that we have placed our models in state-space form, we can construct the Kalman filter for the three-factor model in which we want to minimize the mean squared error between $R_t(\tau_i)$ and $\widehat{R_t}(\tau_i)$.

Example Let $\{Z_{j,t}\}$ follows a GARCH(1,1) process

$$
Z_{j,t} = h_j^{1/2} \varepsilon_{j,t}, \quad h_{j,t} = \omega_j + \alpha_j Z_{j,t-1}^2 + \beta_j h_{j,t-1},
$$

where $\{\varepsilon_{t,j}\}$ is a sequence of i.i.d. standard Normal random variables. The parameter values must satisfy $\omega_j > 0$, $\alpha_j, \beta_j \geq 0$, $\alpha_j + \beta_j < 1$, and $1 - 2\alpha_j^2 - (\alpha_j + \beta_j)^2 > 0$. Accordingly, $\sigma_{X_j^2}$ in (5) should be

$$
\sigma_{X_j}^2 = \frac{\omega_j}{1 - \alpha_j - \beta_j} \left[\frac{1 - v_j^{2(n-1)}}{2\kappa_j - \kappa_j^2 \Delta} \right].
$$

$C_{Y_j}^{(3)}$ and $C_{Y_j}^{(4)}$ in the definition of $D(T)$ in Theorem 1 should become

$$C_{Y_j}^{(3)} = 0,$$

$$C_{Y_j}^{(4)} = \frac{3}{n} \int_{-\pi}^{\pi} |B_{j,2}(\lambda)^2| f_{Z_j^2}(\lambda) \mathrm{d}\lambda - 2 \frac{3\{(1-(\alpha_j+\beta_j)^2)\}}{1-(\alpha_j+\beta_j)^2 - 2\alpha_j^2} \frac{1}{n} \sum_{u=1}^{n} b_{j,u}^4,$$

where $B_2(\lambda) = \sum_{u=1}^{n} b_{j,u}^2 e^{ij\lambda}$ and

$$f_{Z_j^2,2}(\lambda) = \frac{\sigma_{\nu_j}^2}{2\pi} \frac{1 + \beta_j^2 - 2\beta_j \cos\lambda}{1 + (\alpha_j+\beta_j)^2 - 2(\alpha_j+\beta_j)\cos\lambda}$$

with

$$\sigma_{\nu_j}^2 = \frac{2\omega_j^2(1+\alpha_j+\beta_j)}{\{1-(\alpha_j+\beta_j)\}\{1-2\alpha_j^2 - (\alpha_j+\beta_j)^2\}}.$$

Using this parametrization in the state space representation, we can estimate the GARCH(1,1) driven multi-factor term structure models explicitly.

4   Data Analysis

The data used consist of Japanese Government Bond (JGB) yields which are zero-coupon adjusted obtained from Bloomberg. We use weekly sampled data and set $\Delta = 1/52$. Data cover the period October 1, 1999 to December 27, 2013, a total of $T = 744$ observations. The maturities included are 1/4, 1/2, 1,2,3,4,5,6,7,8,9,10,15,20, and 30 years, a total of $N = 15$ different maturities. Application of the Kalman filter to the one-, two- and three-factor models with discretely observed non-Gaussian models are discussed. For fair comparison, we also estimate corresponding multi-factor Vasicek term structure models.

Table 1 gives the sum of the squared errors for estimated models with various maturities. For the bond yield with τ_i maturity, the entry in the cell is given by

$$SSE(\tau_i) = \sum_{t=1}^{T} (R_t(\tau_i)^{(obs)} - \widehat{R}_t(\tau_i)^{(model)})^2,$$

and the total mean squared error is calculated as

$$Total\ SSE = \sum_{i=1}^{N} \sum_{t=1}^{T} (R_t(\tau_i)^{(obs)} - \widehat{R}_t(\tau_i)^{(model)})^2.$$

We see from Table 1 that the total sum of the squares errors are small for the non-Gaussian models compared with those corresponding one-, two- three-factors of Vasicek model. As the number of factors increase, the calibration errors get smaller. We also observe that the non-Gaussian models perform better for the maturities no longer than 10 years, whereas for the long maturities

	Vasicek model (a)			non-Gaussian model (b)			Difference(%) (b)/(a)-1		
	$K=1$	$K=2$	$K=3$	$K=1$	$K=2$	$K=3$	$K=1$	$K=2$	$K=3$
3 Month	31.84	2.94	1.88	28.83	4.11	1.67	-9.43	39.81	-11.03
6 Month	27.61	0.93	0.63	28.20	1.78	0.57	2.12	90.58	-9.76
1 Year	22.57	1.29	1.23	23.16	1.20	1.23	2.64	-6.45	-0.31
2 Year	15.35	5.25	3.48	13.67	3.37	3.10	-10.97	-35.77	-10.94
3 Year	12.13	7.48	3.59	9.34	4.71	3.40	-23.05	-37.10	-5.38
4 Year	10.49	7.87	3.33	8.35	5.72	3.21	-20.41	-27.34	-3.73
5 Year	11.03	7.64	3.15	9.74	6.25	3.10	-11.66	-18.28	-1.44
6 Year	13.34	7.87	3.77	12.73	6.12	3.65	-4.58	-22.21	-3.26
7 Year	15.17	7.56	4.79	15.22	6.06	4.66	0.29	-19.80	-2.82
8 Year	19.59	9.09	6.71	19.76	7.14	6.57	0.89	-21.39	-2.17
9 Year	19.47	7.56	5.94	19.37	6.39	5.89	-0.52	-15.39	-0.77
10 Year	18.29	6.78	5.36	17.84	6.34	5.39	-2.43	-6.43	0.52
15 Year	13.02	10.73	10.73	14.84	13.44	11.04	14.03	25.22	2.95
20 Year	20.34	12.61	6.03	20.88	14.54	6.12	2.70	15.33	1.57
30 Year	33.38	27.95	6.88	33.51	22.86	7.15	0.41	-18.22	4.05
Total	283.61	123.54	67.50	275.45	110.03	66.75	-2.88	-10.93	-1.11

Table 1. Sum of the squared errors with different maturities and models

Vasicek term structure models perform better. This is because, the distribution of $\{Y_{j,n}\}$ tends be normal as the sample size n increases by the Central Limit Theorem. Hence the non-Gaussian modelling is much better to fit the short maturities of bond yield, where the underlying short rates exhibit highly non-Gaussian behavior.

Table 2 shows the parameter estimation results. As for the sum of the long-run mean levels, the Vasicek models tends to have quite high levels with 6.1% for two-factor and 6.3% for three-factor models, whereas those with non-Gaussian models have -2% and 2.6% for two- and three- factor models, respectively. We see that the three-factor models with non-Gaussian models can appropriately capture the long-run interest rate level. Most of the estimates for the sum of the risk premiams are negative. This is because, in general, the risk in a bond associate with the spot rate is proportional to the sensitivity of the bond price, that is $\partial P(0,T)/\partial X_{j,0} < 0$.

For the skewness effects on the zero-coupon yield can be seen as the parameter values of $C_j^{(3)}$, and these values vary from -1.5 to 2.0 among one-, two-, and three-factors. According to these values, we see that the effect of the skewness of underlying innovation process is small. On the other hand, the kurtosis effect on the zero-coupon yields is apparent for some factors in two- and three-factor models.

The observed term structure of Japanese Government Bond (JGB) yield with fitted yield curve with various models estimated are displayed in Figure 1. We choose JGB yield of December 20, 2013 as an example. This figure shows a typical shape for the JGB yield under the Quantitative and Qualitative easing policy with low interest rate level for short maturities. According to these two

parameter	Vasicek model			non-Gaussian model		
	1-factor	2-factor	3-factor	1-factor	2-factor	3-factor
μ_1	-0.290	0.140	7.330	0.189	-0.873	-0.802
μ_2		6.030	-4.370		-1.210	2.200
μ_3			3.350			1.280
λ_1	2.380	-2.040	-0.039	2.430	-12.000	8.120
λ_2		0.909	3.010		3.720	-10.000
λ_3			1.800			-0.507
κ_1	0.009	0.560	0.251	0.003	0.325	0.212
κ_2		0.094	0.396		0.093	0.415
κ_3			0.009			0.023
σ_1	0.012	0.114	0.001	0.015	0.003	0.019
σ_2		0.085	0.003		0.183	0.019
σ_3			4.27E-04			0.002
$C_1^{(3)}$				0.709	2.020	-0.622
$C_1^{(4)}$				-0.636	7.320	-0.103
$C_2^{(3)}$					-1.480	-0.451
$C_2^{(4)}$					0.487	3.110
$C_3^{(3)}$						0.999
$C_3^{(4)}$						2.460

Table 2. Estimates of one-, two- , and three- factor Vasicek models and non-Gaussian models

figures, the fitting performances for the non-Gaussian modelling is superior to those with Vasicek term structure modelling.
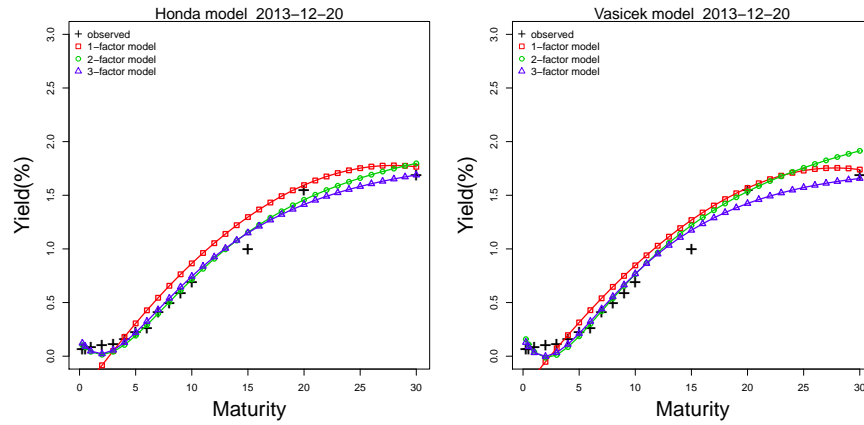
Fig. 1. Wiener stochastic paths (left) and stochastic Logistic paths (right)

5 Summary and Conclusions

In this paper we have introduced the multi-factor discretely observed Vasicek term structure models, and presented a method to estimate these models by the Kalman filter. The advantages of incorporating non-Gaussian effect for the short rate process are clear by investigating Japanese Government Bond yield calibration. The following is possible research topics. A particle filtering method should be used to compute estimates of the model parameters as well as the state variables. Evaluation for the various interest rate derivatives using proposed model should be investigated.

References

1. S. H. Babbs and K. B. Nowman. An application of generalized Vasicek term structure models to the UK gilt-edged market: a Kalman filtering analysis. *Applied Financial Economics*, **8**, 637–644, 1998.
2. S. H. Babbs and K. B. Nowman. Kalman filtering of generalized Vasicek term structure models. *Journal of Financial and Quantitative Analysis*, **34**, 115-130, 1999.
3. R. -R. Chen and L. Scott. Maximum likelihood estimation for a multifactor equilibrium model of the term structure of interest rates. *Journal of Fixed Income.* **3**, 14–31, 1993.
4. C. Cox, J. Ingersoll and S. A. Ross. A theory of the term structure of interest rates. *Econometrica*, **53**, 385–407, 1985.
5. J. C. Duan and J.-D. Simonate. Estimating and testing exponential-affine term structure models by Kalman filter. Discussion paper, Centre universitaire de recherche et analyze des organizations (CIRANO), 1995.
6. J. D. Duffie and R. Kan. A yield-factor model of interest rates. *Mathematical Finance*, **6**, 379–406, 1996.
7. T. Honda, K. Tamaki and T. Shiohama. Higher order asymptotic bond price valuation for interest rates with non-Gaussian dependent innovations. *Finance Research Letters*, **7**, 60–69, 2010.
8. M. Miura, K. Tamaki and T. Shiohama. Asymptotic expansion for term structures of defaultable bonds with non-Gaussian dependent innovations. *Asia-Pacific Financial Markets*, **20**, 311-344, 2013.
9. T. Shiohama and K. Tamaki. Asymptotic expansion for interest rates with non-Gaussian dependent innovations. In Nishiyama, Y. (Ed.), *Interest rates: Term structure models, monetary policy, and prediction.* New York: Nova Science Publishers, 19–61, 2012.
10. O. Vasicek. An equilibrium characterization of the term structure. *Journal of Financial Economics*, **5**, 177–188, 1977.

Probabilistic Approach for Comparing Partitions

Osvaldo Silva[1], H. Bacelar-Nicolau[2], Fernando C. Nicolau[3], and Áurea Sousa[4]

[1] Dep. of Math., CES-UA, University of Azores, Ponta Delgada, Azores, Portugal
  (Email: osilva@uac.pt)
[2] Faculty of Psychology, LEAD; ISAMB, CEA; University of Lisbon, Lisboa, Portugal
  (Email: hbacelar@fp.ul.pt)
[3] FCT, Department of Mathematics, New University of Lisbon, Monte da Caparica, Portugal
  (Email: fernandonicolau@netcabo.pt)
[4] Dep. of Math., CEEAplA, University of Azores, Ponta Delgada, Azores, Portugal
  (Email: aurea@uac.pt)

Abstract: The comparison of two partitions in Cluster Analysis can be performed using various classical coefficients (or indexes) in the context of three approaches (based, respectively, on the count of pairs, on the pairing of the classes and on the variation of information). However, different indexes usually highlight different peculiarities of the partitions to compare. Moreover, these coefficients may have different variation ranges or they do not vary in the predicted interval, but rather only in one of their subintervals. Furthermore, there is a great diversity of validation techniques capable of assisting in the choice of the best partitioning of the elements to be classified, but in general each one tends to favour a certain kind of algorithm. Thus, it is useful to find ways to compare the results obtained using different approaches. In order to assist this assessment, a probabilistic approach to comparing partitions is presented and exemplified. This approach, based on the *VL (Validity Linkage) Similarity*, has the advantage, among others, of standardizing the measurement scales in a unique probabilistic scale. In this work, the partitions obtained from the agglomerative hierarchical cluster analysis of a dataset in the field of teaching are evaluated using classical and probabilistic (of *VL* type) indexes, and the obtained results are compared.

Keywords: Hierarchical cluster analysis, comparing partitions, affinity coefficient, *VL* methodology

1 Introduction

The Cluster Analysis aims to identify groups (classes or clusters) of entities (individuals, objects, etc.), that are relatively homogeneous and well separated, based on similarities or dissimilarities between them.

There are multiple indexes for comparing partitions, which complicates the decision-making, given that different indexes generally evaluate different peculiarities of the partitions to compare. Moreover, there is a great diversity of validation techniques capable of assisting in the choice of the best partitioning of the elements to be classified, but in general each one of them tends to favour a certain kind of algorithm.

Thus, it is imperative to find ways to compare the results obtained using different approaches.

In Section 2 the indexes for the comparison of partitions are introduced using classical coefficients. Section 3 is dedicated to the comparison of partitions using probabilistic coefficients of the *VL* type. In Section 4, we compare the results obtained with the implementation of the two approaches, classical and probabilistic, to a real data set, under a wider validation work in Cluster Analysis, using resampling methods. Finally, Section 5 presents the main conclusions.

2 Coefficients for comparison of partitions pairs

The comparison of two partitions in Cluster Analysis can be performed using various indexes or classical coefficients in the context of three approaches (based respectively on the count of pairs, on the pairing of the classes and on the variation of information). However, each of these coefficients assumes a certain value, depending on its analytic expression, and some have different variation ranges or they do not vary in the predicted interval, but rather only in one of its subintervals. In order for these coefficients to be more easily comparable, one should keep in mind their intrinsic characteristics, categorizing them into groups with similar characteristics.

To compare two partitions, *P* and *P'*, of one same dataset of *n* cardinal based on the count of pairs, one can begin by constructing an associated 2 × 2 contingency table, as Table 1.

Table 1. Contingency table based on the count of pairs

Partition *P*	Partition *P'*	
	a	*b*
	c	*d*

Table 1 mentions the pairs of elements that exist in the two partitions, where "*a*" is the number of pairs of elements that are in the same classes in both partitions, "*b*" is the number of pairs of elements that belong to the same classes in a partition *P* but to different classes in the other partition (*P'*), "*c*" is the number of pairs belonging to different classes in the *P* partition and to the same classes in the *P'* partition and "*d*" is the number of pairs of elements belonging to different classes in both partitions. The total number of pairs of objects is $a + b + c + d = n \times (n-1) / 2$.

Silva (2012) contains a list of indexes for the comparison of binary data, which are functions of the four values of Table 1 and are also used for comparing partitions. In this list, the indexes are subdivided into similarity coefficients that consider the joint absence "*d*", similarity coefficients that do not take into account the joint absence "*d*" and other coefficients of association. For each of the coefficients the respective formula

is shown, as well as the symbol with which it is usually designated, its variation range and its author(s).

These indexes should be evaluated relatively to common properties, and can be sensitive to the number of classes in the partitions. Some of the indexes (for example, Hubbert and Rand) tend to have high values in the case of partitions with more classes, others in the case of partitions with a small number of classes (e.g. Jaccard). The adjusted Rand index has none of these undesirable characteristics (Milligan and Cooper, 1985; Jain and Dubes, 1988), which is why this is one of the indexes pertaining to the methodology used in this work. The standardized Ochiai index (a particular case of the affinity coefficient, e. g., Bacelar-Nicolau, 1985), has also been used with good results in the context of partitions comparison (Silva, 2004; Silva, 2012).

As noted above, the evaluation of the partitions comparison indexes based on the count of pairs must take into account the scale of variation and the relation that can be established between the various indexes from their mathematical expressions. Several studies of classification and comparison of these coefficients have been proposed by many authors since Sneath and Sokal (1963). Sibson (1972) made the grouping of coefficients into monotonic classes, establishing an equivalence relation in the set of comparison coefficients for binary data. Bacelar-Nicolau (1980, 1987) determined "*distributionally equivalent*" classes of coefficients, a concept that we will use in this work, as mentioned in the next section.

3 Comparison of pairs of partitions using probabilistic coefficients

Lerman (1970) proposed the use of a similarity coefficient of probabilistic nature between binary variables, which he then expanded to proximity coefficients between structures of the same type (Lerman, 1973, 1981). Bacelar-Nicolau (e.g., 1980, 1987) conducted a distributional study of the comparison coefficients for binary data, having verified and proved the distributional equivalence of a broad class of coefficients, under the assumption of fixed margins of the 2×2 contingency table associated with each pair of elements of the set to be classified. For other coefficients as well as in the hypothesis of free margins, although distributional exact equivalence does not occur, we can find classes of equivalent coefficients with respect to their asymptotic distribution, and take always, as information associated with a coefficient, its limit function of distribution (Bacelar-Nicolau, 1980, 1987; Lerman, 1981), which is a probabilistic similarity coefficient γ on the scope of *VL* methodology. Thus, we have

for a similarity coefficient, S :

$$\gamma = F_S(s) = Prob_{H_0}\left(S \leq s\right) \cong Prob_{H_0}\left(S* \leq s*\right) \cong \phi\left(s*\right)$$

where H_0 is an adequate reference hypothesis, F_S is the distribution function of S, $S^* = (S - E(S))/\sigma_S$, s^* is a realization of S^*, ϕ is the distribution function of the standard normal distribution and $E(S)$ and σ_S are respectively the mean value and the standard deviation, usually asymptotic. The probabilistic coefficient takes values in [0,1] (follows the Uniform distribution (0, 1)), and is generally calculated asymptotically because the exact distribution function may not be known. The *VL* coefficient was later extended to other types of data and to mixtures of different types of data (e.g. Bacelar-Nicolau, 1988, Nicolau, 1983; Nicolau and Bacelar-Nicolau, 1998; Bacelar-Nicolau *et al*, 2009, 2010).

The approach to comparing partitions, using probabilistic coefficients of the *VL* type, is based on studies of the comparison coefficients for binary data by Bacelar-Nicolau and proceeds as follows:

i) We start with a similarity index, S, for comparing two partitions, *P* and *P'*, based on the count of pairs of elements that exist in the two partitions.

ii) We calculate the value of $\gamma_{PP'}$ of the distribution function of the similarity index *S* used in point *s*, under the assumption of the considered reference:

$$\gamma_{PP'} = F_S(s) = Prob_{H_0}(S \leq s) \cong Prob_{H_0}(S^* \leq s^*) \cong \phi(s^*)$$

Two partitions, *P* and *P'*, will be considered the more consistent the larger is the value of $F_S(s)$, that is, the more unlikely is overcoming the *s* realization of *S* under the reference hypothesis.

As it has been pointed out by several authors (e.g., Lerman, 1973, 1981; Bacelar-Nicolau, 1980, 1987; Dubes and Jain, 1988), the different indexes do not show all values in [0, 1] and a proportion of the similarity between both partitions is assigned randomly. However, it is shown that the most used indexes are equivalent from the distributional point of view (Bacelar-Nicolau, 1980, 1987). The application of the *VL* methodology to these coefficients allows us to obtain comparison indexes of partitions that can be interpreted on a probabilistic scale. Thus, using a probabilistic coefficient we can choose only one classical coefficient in each (asymptotically) distributionally equivalent class of coefficients, in order to compare partitions.

4 Comparison of results obtained by classical and probabilistic approaches on a set of real data

The data (from a sample of 164 students) was obtained through a questionnaire containing twenty-two questions concerning attitudes/beliefs of students in the area of Social and Human Sciences regarding the subject of Statistics (Silva *et al*., 2007). Each

student selected one and only one of seven possible answers to each question (1 - *strongly disagree*, ..., 4 - *neither agree nor disagree*, ..., 7 - *strongly agree*).

An Agglomerative Hierarchical Cluster Analysis (*AHCA*), using the affinity coefficient (e.g., Bacelar-Nicolau, 1985) between variables and the probabilistic aggregation criteria *AVL*, *AV1* and *AVB* (e.g., Nicolau, 1983; Bacelar-Nicolau, 1985; Nicolau and Bacelar-Nicolau, 1998), was applied in order to obtain a typology of variables under study. The tables with the values of validation indexes to select the most significant partition, obtained from the initial data matrix, and the interpretation of the classes corresponding to this partition, in four classes, can be found in Silva et al. (2007). It has been noted that the most significant partition is the same for all three aggregation criteria.

The results were obtained for the case of evaluation and comparison of partitions using resampling methods. In the present study, we evaluate the most significant partition provided by the AHCA of the data, based on the affinity coefficient and on the aggregation criteria mentioned above. The procedure can briefly be described as follows: 1) from the original data 50 subsamples were generated, with a sampling rate defined *a priori* (80%), using simple random sampling; 2) the same model of AHCA was applied to data matrixes (subsamples) randomly generated by the Monte Carlo simulation method, to determine the partitions with the same number of classes presented by the most significant partition obtained from the original data; 3) this partition was compared to each of the partitions obtained in 2), based on the count of pairs, using each of the classical coefficients from the list in Silva (2012) or the associated *VL* probabilistic coefficient; statistics were also calculated regarding location and dispersion associated with each index, in order to analyze the respective behaviour.

Table 2 shows the values of summary statistics (measures of central tendency, dispersion and quantiles) for classical coefficients (Table 2-a) and probabilistic coefficients (Table 2-b) in the situation where joint absence "*d*" is not considered.

Silva (2012) also contains similar tables for the coefficients where the joint absence "*d*" is considered, as well as for other association coefficients.

It can be seen in Table 2-a) and in Silva (2012) that the most part of the classical comparison coefficients takes values in the interval [0,1]. However, the interval between the minimum and maximum values of the sampling distribution is very variable. The maximum value of the distribution reaches the upper limit 1 of the range in many of the coefficients, reaching a minimum often above 0.5 for the first two considered coefficients classes (similarity coefficients that consider the joint absence "d" and similarity coefficients that do not consider the joint absence "d"), but not for other association coefficients (Silva, 2012).

Table 2-a). Values of summary statistics related to classical coefficients that do not consider joint absence "*d*"

	S	J	O	CZ	K1	DW1	DW2	SS2	BB1	BB2	SO	JO	K2	FMG1
Min	.609	.432	.607	.603	.609	.547	.609	.276	.547	354	.299	1.219	.761	.544
Max	1.000	1.000	1.000	1.000	1.000	1.000	1.000	1.000	1.000	500	1.000	2.000	10.333	.938
Mean	.955	.908	.941	.941	.942	.934	.950	.870	.929	479	.891	1.884	2.491	.879
SD	.095	.177	.117	.119	.116	.138	.097	.238	.139	043	.222	.233	3.769	.118
Center	.804	.716	.803	.801	.804	.773	.804	.638	.773	427	.650	1.609	5.505	.741
.005	.609	.432	.607	.603	.609	.547	.609	.276	.547	354	.299	1.219	.761	.544
.01	.609	.432	.607	.603	.609	.547	.609	.276	.547	000	.299	1.219	.761	.544
.025	.673	.438	.609	.609	.610	.609	.673	.281	.609	379	.371	1.220	.761	.547
.05	.765	.513	.683	.678	.687	.609	.765	.345	.609	379	.371	1.374	.761	.620
.1	.765	.513	.683	.678	.687	.609	.765	.345	.609	379	.371	1.374	.770	.620
.25	.969	.912	.954	.954	.954	.969	.939	.838	.939	484	.938	1.908	1.054	.891
.5	1.000	1.000	1.000	1.000	1.000	1.000	1.000	1.000	1.000	500	1.000	2.000	2.491	.938
.75	1.000	1.000	1.000	1.000	1.000	1.000	1.000	1.000	1.000	500	1.000	2.000	5.798	.938
.9	1.000	1.000	1.000	1.000	1.000	1.000	1.000	1.000	1.000	500	1.000	2.000	10.333	.938
.95	1.000	1.000	1.000	1.000	1.000	1.000	1.000	1.000	1.000	500	1.000	2.000	10.333	.938
.975	1.000	1.000	1.000	1.000	1.000	1.000	1.000	1.000	1.000	500	1.000	2.000	10.333	.938
.990	1.000	1.000	1.000	1.000	1.000	1.000	1.000	1.000	1.000	500	1.000	2.000	10.333	.938
.995	1.000	1.000	1.000	1.000	1.000	1.000	1.000	1.000	1.000	500	1.000	2.000	10.333	.938

Similarly, measurements of location and dispersion of various classical coefficients show high variation. However, the sampling distributions of the associated probabilistic coefficients described in Table 2-b) feature ranges of similar magnitude with approximate minimum and maximum values.

Table 2-b). Values of summary statistics related to probabilistic coefficients that do not consider joint absence "d"

	S	J	O	CZ	K1	DW1	DW2	SS2	BB1	BB2	SO	JO	K2	FMG1
Min	.000	.004	.002	.002	.002	.003	.000	.006	.003	.002	.004	.374	.194	.002
Max	.682	.698	.691	.691	.691	.683	.697	.707	.696	.691	.688	1.000	.962	.691
Mean	.559	.557	.559	.559	.559	.561	.555	.554	.558	.560	.560	.438	.463	.559
SD	.233	.249	.242	.242	.242	.238	.249	.261	.247	.241	.242	.152	.305	.242
Center	.341	.351	.347	.347	.347	.343	.349	.357	.349	.346	.346	.687	.779	.347
.005	.000	.004	.002	.002	.002	.003	.000	.006	.003	.002	.004	.374	.194	.002
.01	.000	.004	.002	.002	.002	.003	.000	.006	.003	.000	.004	.374	.194	.002
.025	.002	.004	.002	.003	.002	.009	.002	.007	.011	.010	.009	.374	.194	.002
.05	.023	.013	.014	.013	.014	.009	.029	.014	.011	.010	.009	.374	.194	.014
.1	.023	.013	.014	.013	.014	.009	.029	.014	.011	.010	.009	.374	.195	.014
.25	.559	.509	.543	.544	.541	.600	.456	.447	.529	.550	.583	.374	.217	.540
.5	.682	.698	.691	.691	.691	.683	.697	.707	.696	.691	.688	.374	.360	.691
.75	.682	.698	.691	.691	.691	.683	.697	.707	.696	.691	.688	.479	.365	.691
.9	.682	.698	.691	.691	.691	.683	.697	.707	.696	.691	.688	.530	.702	.691
.95	.682	.698	.691	.691	.691	.683	.697	.707	.696	.691	.688	1.000	.962	.691
.975	.682	.698	.691	.691	.691	.683	.697	.707	.696	.691	.688	1.000	.962	.691
.990	.682	.698	.691	.691	.691	.683	.697	.707	.696	.691	.688	1.000	.962	.691
.995	.682	.698	.691	.691	.691	.683	.697	.707	.696	.691	.688	1.000	.962	.691

Figure 1 illustrates the variation of mean values of some coefficients, both classic (taking values in the range [0,1]) and probabilistic. As it can be seen, the mean values of the classical indexes, considering the values obtained in 50 resamplings, vary greatly from index to index.
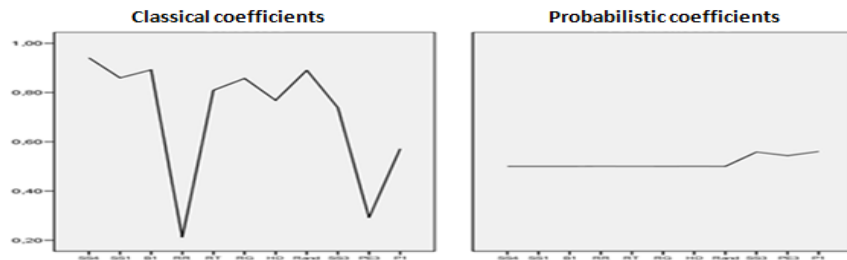

Fig. 1. Variation of means obtained for some classical and probabilistic coefficients

In the context of the *VL* approach it is found that, contrary to the respective basic indexes, the values obtained for means and other location measures of the sampling distribution of the probabilistic coefficient have been very close, as can be seen in Figures 1 and 2, as well as in Silva (2012).
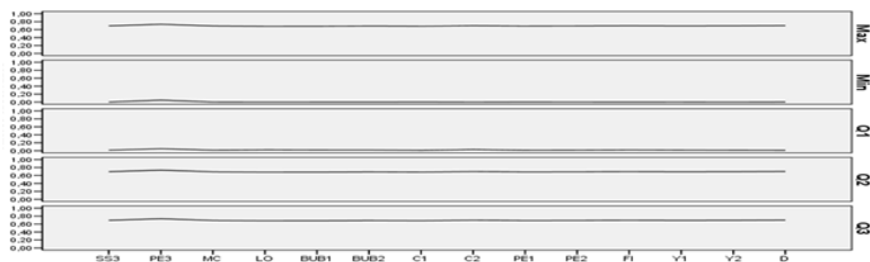
Fig. 2. Variation of the values of some summary statistics for the probabilistic *VL* coefficients associated with classical association coefficients.

These results are consistent with the theory that shows the property of (exact or asymptotic) distributional equivalence between comparison coefficients for binary data (Bacelar-Nicolau, 1980, 1987), mentioned in Section 3. The comparison of partitions using probabilistic coefficients of *VL* type is therefore a simpler and more robust approach than the comparison based on classical coefficients: instead of determining several of these indexes, we will choose a single index in each of the (exact or asymptotically) distributionally equivalent classes and use the *VL* probabilistic coefficient associated to it, which also has the advantage of standardizing the measurement scale on the same probabilistic scale. Finally, the variation ranges and

other statistics provided by the *VL* coefficient tables allow us evaluate the quality of the most significant partition provided by the three models of probabilistic classification. This conclusion is supported by an appropriate set of validation coefficients, which are not presented in this work.

5 Conclusions

In this work, we compare the performances of classical indexes with an associated probabilistic approach for the comparison of pairs of partitions. The described resampling methodology is part of a work on the evaluation of the stability of the obtained classifications in a AHCA.

Usual classical indexes show not to be a convenient choice since they may have distinct display ranges as well as quite different values for other statistics of location and dispersion or they do not take values in the entire variation interval but only in part of that interval. The probabilistic approach to the comparison of partitions using probabilistic coefficients of *VL* type has, among others, the advantage that all classical indexes used lead, exactly or asymptotically, to very close values of the probabilistic index (theoretically conduct to the same value, in the case of the reference hypothesis considered here) and in a probabilistic scale (0, 1). Thus, instead of determining various indexes the *VL* approach can be applied to any of the indexes belonging to a given class of distributionally equivalent indexes to carry out the comparison of partitions pairs with the same number of classes.

References

1. Bacelar-Nicolau, H., Contributions to the Study of Comparison Coefficients in Cluster Analysis, PhD Thesis (in Portuguese), Universidade de Lisboa (1980).

2. Bacelar-Nicolau, H., The Affinity Coefficient in Cluster Analysis, Methods of Operations Research, vol. 53, Martin J. Bekmann et al (ed.), Verlag Anton Hain, Munchen, pp. 507-512 (1985).

3. Bacelar-Nicolau, H., On the Distribution equivalence in Cluster Analysis, In Proceedings of the NATO ASI on Pattern Recognition Theory and Applications, Springer - Verlag, New York, pp. 73-79 (1987).

4. Bacelar-Nicolau, H., Two Probabilistic Models for Classification of Variables in Frequency Tables, In: Bock, H.-H. (Eds.), Classification and Related Methods of Data Analysis, North Holland, pp. 181-186 (1988).

5. Bacelar-Nicolau, H.; Nicolau, F.C.; Sousa, Á.; Bacelar-Nicolau, L., Measuring Similarity of Complex and Heterogeneous Data in Clustering of Large Data Sets, Biocybernetics and Biomedical Engineering, vol. 29, no. 2, pp. 9-18 (2009).

6. Bacelar-Nicolau, H.; Nicolau, F.C.; Sousa, Á.; Bacelar-Nicolau, L., Clustering Complex Heterogeneous Data Using a Probabilistic Approach, In *Proceedings of Stochastic Modeling Techniques and Data Analysis International Conference* (SMTDA2010), 85-93 (2010) (electronic publication) .

7. Jain, A. K.; Dubes, R. C., *Algorithms for Clustering Data.* Prentice Hall, Englewood Cliffs, NJ (1988).

8. Lerman, I. C., *Les Bases de la Classification Automatique.* Paris, Gauth.-Villars (1970).

9. Lerman, I. C., Étude Distributionnelle de Statistiques de Proximité entre Structures Algébriques Finies de Même Type – application à la Classification Automatique. In: *Cahiers du B.U.R.O.*, Nº. 19, Paris (1973).

10. Lerman, I. C., Classification et Analyse Ordinale des Données, Dunod, Paris (1981).

11. Milligan, G. W.; Cooper, M. C., An Examination of Procedures for Determining the Number of Clusters in a Data Set. Psychometrika, 50, 159-179, (1985).

12. Nicolau, F.C., Cluster Analysis and Distribution Function, Methods of Operations Research, vol. 45, 431-433 (1983).

13. Nicolau, F.C. and Bacelar-Nicolau, H., Some Trends in the Classification of Variables, In: Hayashi, C., Ohsumi, N., Yajima, K., Tanaka, Y., Bock, H.-H., Baba, Y. (Eds.), Data Science, Classification, and Related Methods. Springer-Verlag, pp. 89-98 (1998).

14. Sibson, R., Multidimensional Scalling in Theory and Pratice. In: *Les Méthodes Mathématiques de l`Archéologie*, Centre d`Analyse Documentaire pour l`Archéologie, Marseille, 43-73 (1972).

15. Silva, A., Saporta, G. e Bacelar-Nicolau, H., *Missing Data and Imputation Methods in Partition of Variables.* Classification, Clustering and Data Mining Applications, Springer, 631-637 (2004).

16. Silva O.; Bacelar-Nicolau, H. e Nicolau, F., Utilização da Análise Classificatória para Avaliar as Atitudes/Crenças em relação à Estatística de Alunos da Área de Ciências Sociais e Humanas. In: *Actas do XIV Congresso Anual da Sociedade Portuguesa de Estatística*, (Ferrão, M. et al. Eds.) Edições S.P.E, 751-759 (2007).

17. Silva, O., Contributions to the Evaluation and Comparison of Partitions in Cluster Analysis*, PhD Thesis (in Portuguese), Universidade dos Açores, Ponta Delgada (2012).

18. Sneath, P. H.; Sokal, R. R., *Principles of Numerical Taxonomy.* Freeman, San Francisco (1963).

Hierarchical Cluster Analysis of Groups of Individuals: Application to Business Data

Áurea Sousa [1], Helena Bacelar-Nicolau[2], and Osvaldo Silva[3]

[1] Dep. of Math., CEEAplA, University of Azores, Ponta Delgada, Azores, Portugal
(Email: aurea@uac.pt)
[2] Faculty of Psychology, LEAD; ISAMB, CEA; University of Lisbon, Lisboa, Portugal
 (Email: hbacelar@fp.ul.pt)
[3] Dep. of Math., CES-UA, University of Azores, Ponta Delgada, Azores, Portugal
(Email: osilva@uac.pt)

Abstract: We present one example, in which the data are issued from a questionnaire in order to find satisfaction typologies (with the services provided by an automobile company) of independent groups of individuals. The Agglomerative Hierarchical Cluster Analysis (*AHCA*) was based on two approaches: one based on a particular case of the generalized weighted affinity coefficient, which deals with classical data, and the other one on the weighted generalized affinity coefficient for the case of symbolic/complex data. Both measures of comparison between elements were combined with classical and probabilistic aggregation criteria. We used the global statistics of levels (*STAT)* to evaluate the quality of the obtained partitions.

Keywords: Hierarchical cluster analysis, Affinity coefficient, Independent groups of individuals*, VL* Methodology, Classical data, Symbolic data.

1 Introduction

Recent computational advances allow us to summarize very large datasets in terms of their underlying concepts, which can only be described by symbolic or complex data. Each entry of a symbolic data table can contain one or several values such as subsets of categories, intervals of the real dataset $\mathcal{R}$, or frequency distributions (e. g., Bacelar-Nicolau, 2000; Bock and Diday, 2000; Bacelar-Nicolau et al., 2009, 2010). A symbolic variable Y with domain (or range or observation space) $\mathcal{Y}$ is a mapping $E \longrightarrow B$ defined on a set E of statistical entities (individuals, classes, objects,…). Depending of the specification of B in terms of $\mathcal{Y}$, symbolic variables can be classified as: classical single-valued, set-valued, interval, multi-valued (categorical or quantitative), and modal (probabilistic) variables. A variable Y is modal with observation space $\mathcal{Y}$ if, for each $a \in E, Y(a) = \pi_a$ is a non-negative measure on $\mathcal{Y}$, such as a frequency distribution, a probability distribution or a weighting (Bock and Diday, 2000). Here, in the case of symbolic data we will focus on Ascendant Hierarchical Cluster Analysis (*AHCA*) of data units described by modal variables. The *VL* methodology (*V* for Validity, *L* for Linkage) is a probabilistic approach for clustering methods, based on the cumulative distribution function of basic similarity coefficients, and the probabilistic aggregation criteria

under this methodology resort essentially to probabilistic notions for the definition of the comparative functions (e.g. Lerman 1970, 1981; Nicolau, 1983; Bacelar-Nicolau, 1985, 1987, 1988; Nicolau and Bacelar-Nicolau, 1998). In this work, two classical aggregation criteria, Single Linkage (*SL*) and Complete Linkage (*CL*), as well as three probabilistic aggregation criteria - in the scope of the *VL* methodology- *AVL*, *AV1*, and *AVB*, are used to look for satisfaction typologies of independent groups of individuals in two contexts: classical data and symbolic/complex data. The measures of comparison between elements are based on the affinity coefficient.

Two different approaches of *AHCA* of independent groups of individuals are described in Section 2. In the first one the data units (independent groups of individuals) are described by classical single-valued variables defined on an ordinal scale and a particular case of the generalized weighted affinity coefficient was used. The second one is based on the weighted generalized affinity coefficient for the case of symbolic data. In Section 3 we refer some experimental results from Business area. Section 4 contains some concluding remarks about this work and its results.

2 AHCA of independent groups of subjects

From the affinity coefficient between two discrete probability distributions proposed by Matusita (1951) as the basic similarity measure for comparing two probability laws of the same type, Bacelar-Nicolau (1980, 1988) introduced the affinity coefficient, as a basic similarity coefficient between pairs of variables or of subjects in cluster analysis context (corresponding to pairs of columns or rows of a data matrix). Later on she extended that coefficient to different types of data, including complex or symbolic data and variables of mixed types (heterogeneous data), possibly with different weights (Bacelar-Nicolau, 2000, 2002; Bacelar-Nicolau et al., 2009, 2010). The extension of the affinity coefficient for the case of symbolic data is called weighted generalized affinity coefficient. In the present work, we use two different approaches of *AHCA* of independent groups of individuals based on two different generalized approaches for the affinity coefficient.

Approach 1: particular case of the weighted generalized affinity coefficient
In this approach, the data are initially represented in *G* tables (one table for each one of the independent groups of individuals), containing, respectively, $N_1, N_2,…, N_G$, individuals described by *p* identical variables defined on an ordinal scale. Later, *G* new tables, each one containing the same number $n= min\{N_1, N_2, …, N_G\}$ of individuals (selected from a stratified random sampling) have to be obtained from the initial corresponding tables. Each new table corresponds to a (*n*×p) data table, and x_{ihj} (*i=1,…, n, h=1,..., G, j=1,..., p)* is the value of the individual *i*, belonging to the table T$_h$ (abbreviated, *h*), in the *j-th* variable (see Table 1). Then, the total scores of each independent group of individuals in each variable are computed as follows, where $x_{•hj} = \sum_{i=1}^{n} x_{ihj}$ (*i=1,…, n, h=1,..., G, j=1,..., p)* is the total score of the group *h* in the variable *j* (sum in the column *j* of T$_h$)*:*

Table 1. *G* new tables (same number $n = min\{N_1, N_2, \ldots, N_G\}$ of subjects)

Ind. i	T_1 (Group 1) $V_1 \quad \cdots \quad V_p$		Ind. i	T_G (Group G) $V_1 \quad \cdots \quad V_P$
1	$x_{111} \cdots x_{11p}$	...	1	$x_{1G1} \cdots x_{1Gp}$
2	$x_{211} \cdots x_{21p}$	...	2	$x_{2G1} \cdots x_{2Gp}$
⋮	⋮	...	⋮	⋮
n	$x_{n11} \cdots x_{n1p}$	...	*n*	$x_{nG1} \cdots x_{nGp}$
Total	$x_{\bullet 11} \cdots x_{\bullet 1p}$		*Total*	$x_{\bullet G1} \cdots x_{\bullet Gp}$

The computation of the affinity coefficient between the groups *h* and *h'*, with *h, h'*=1, …, *G*, and *h≠h'*, is based on the following data matrix (Table 2), and in the formula (1):

Table 2. Classical data matrix (approach 1)

	$V_1 \quad \cdots \quad V_p$
Group 1	$x_{\bullet 11} \cdots x_{\bullet 1p}$
Group 2	$x_{\bullet 21} \cdots x_{\bullet 2p}$
⋮	⋮
Group G	$x_{\bullet G1} \cdots x_{\bullet Gp}$

$$a(h, h') = \frac{1}{p}\sum_{j=1}^{p} \sqrt{\frac{x_{\bullet hj}}{x_{\bullet h\bullet}} \cdot \frac{x_{\bullet h'j}}{x_{\bullet h'\bullet}}}, \tag{1}$$

where $x_{\bullet h\bullet} = \sum_{j=1}^{p} x_{\bullet hj}$ (respectively, $x_{\bullet h'\bullet} = \sum_{j=1}^{p} x_{\bullet h'j}$) is the total score of the group *h,* in the *p* variables [sum in the row *h* (respectively, *h'*) of Table 2]*:*

Approach 2: weighted generalized affinity coefficient (case of modal data)
Given a set of *N* data units (typically groups of individuals: symbolic data units) described by *p* modal variables, $Y_1,\ldots,Y_p$ (each variable may have a different number of "modalities"), the weighted generalized affinity coefficient between the data units *k* and *k'* is given by:

$$a(k, k') = \sum_{j=1}^{p} \pi_j \, aff(k, k'; j) = \sum_{j=1}^{p} \pi_j \sum_{\ell=1}^{m_j} \sqrt{\frac{x_{kj\ell}}{x_{kj\bullet}} \cdot \frac{x_{k'j\ell}}{x_{k'j\bullet}}} \tag{2}$$

where: $aff(k, k'; j)$ is the generalized local affinity between *k* and *k'* over the *j-th* variable, m_j is the number of modalities of the *j-th* variable; $x_{kj\ell}$ is the number of individuals (in the unit *k*) which share the category ℓ of Y_j; $x_{kj\bullet} = \sum_{\ell=1}^{m_j} x_{kj\ell}$,

$x_{k'j\bullet} = \sum_{\ell=1}^{m_j} x_{k'j\ell}$, and the weights, π_j, verify the condition : $\pi_j \geq 0$ and $\sum \pi_j = 1$ (see Table 3).

Either the local affinities or the whole weighted generalized affinity coefficient, take values in the interval [0,1] and satisfy a set of proprieties which characterize affinity measurement as a robust similarity coefficient (e.g., Bacelar-Nicolau, 2002; Bacelar-Nicolau et al., 2009). The coefficient associated to the first approach is a particular case of the coefficient associated to this second approach.

Table 3. Symbolic data matrix $\underline{X}$ with integer frequency distributions

	$\cdots$	Y_j	$\cdots$	$Y_{j'}$	$\cdots$
$\vdots$	$\cdots$	$\cdots$	$\cdots$	$\cdots$	$\cdots$
k	$\cdots$	$\left(x_{kj1}, \cdots, x_{kjm_j}\right)$	$\cdots$	$\left(x_{kj'1}, \cdots, x_{kj'm_{j'}}\right)$	$\cdots$
$\vdots$	$\cdots$	$\cdots$	$\cdots$	$\cdots$	$\cdots$
k'	$\cdots$	$\left(x_{k'j1}, \cdots, x_{k'jm_j}\right)$	$\cdots$	$\left(x_{k'j'1}, \cdots, x_{k'j'm_{j'}}\right)$	$\cdots$
$\vdots$	$\cdots$	$\cdots$	$\cdots$	$\cdots$	$\cdots$

This approach is appropriated when we deal with large datasets.

3 Experimental results based on business data

Data were collected using a questionnaire applied to 450 customers in order to evaluate the satisfaction (latent variable) with the services provided by an automobile company, based on 18 component variables, which are described in Sousa et al. (2014). The variables (items) are measured in a scale with ordered modalities (1- *very dissatisfied (VD)*, 2- *generally dissatisfied (GD)*, 3- *neither satisfied nor dissatisfied (NSND)*, 4- *generally satisfied (GS)* and 5- *very satisfied (VS)*). The respondents are distributed by 11 professional occupations (O1- *Doctors, architects and engineers*; O2- *Teachers*; O3-*Businessmen*; O4-*Salesmen*; O5-*Employees of banks and insurance companies*; O6-*Military and police*; O7-*Administrative and similar*; O8- *Employees of the civil construction*; O9- *Employees of the commerce and industry*; O10- *Employees of hotels and restaurants*; O11- *Employees of other services*. The numbers of individuals in each modality of the variable "*Professional occupation*", with 11 modalities, are respectively 45, 40, 79, 42, 38, 40, 35, 34, 51, 24, 22.

The clustering of the 11 professional occupations was based on two approaches (see Section 2). The measures of comparison between elements were combined with two classical aggregation criteria, *Single Linkage* (*SL*) and *Complete Linkage* (*CL*), and three probabilistic aggregation criteria, *AVL*, *AV1*, and *AVB*. In the present work, the validation of the results is based on the global statistics of levels (*STAT*), as proposed by Lerman (1970, 1981) and Bacelar-Nicolau (1980, 1985), in both paradigms (classical and symbolic data).

In the first approach the data were initially represented in *11* tables (one table for each professional occupation), containing, respectively, 45, 40, 79, 42, 38, 40, 35, 34, 51, 24 and 22 subjects, described by *18* identical variables. Then, *11* new tables, composed by $n=22$ $(n = min\{45, 40, 79, 42, 38, 40, 35, 34, 51, 24, 22\})$ rows (selected from a stratified random sampling) were obtained from the initial corresponding tables (see Table 1). The *AHCA* of the professional occupations was based on a classical data matrix, as Table 2, composed by 11 rows and 18 variables (V_1 to V_{18}). The entry corresponding to the intersection between the *h-th* row and the *j-th* column of this data matrix contains the total scores of the group *h* (h=1,…,11) in the variable *j* (j=1,…,18). In this approach, the value of the affinity coefficient between the professional occupations *h* (O_h) and *h'* ($O_{h'}$) is given by formula (1).

```
O1   --*              O1   --*
     |                     |-------------*
O3   --|--------*      O3   --*             |--------*
       |        |                  |        |
O11  --*        |      O11  --*-------------*        |
                |--*                                 |--*
O4   --*--*     | |    O4   --*-----------*    | |
     |    |     | |                 |-----*    | |
O5   --*--|     | |    O10  --*-----------*    |     | |
          |-----*  |                     |-----*  |
O9   --*--|        |   O5   --*-----*          |        |
          |        |                 |-----------*        |
O10  --*--*        |   O9   --*-----*                 |
                   |                                      |
O2   --*           |   O2   --*--------*                 |
     |             |                   |-----------*      |
O7   --|-----*     |   O6   --*--------*           |      |
       |     |     |                               |-----*
O8   --*     |-----*   O7   --*--*           |
             |                       |-----------------*
O6   --*-----*        O8   --*--*
```
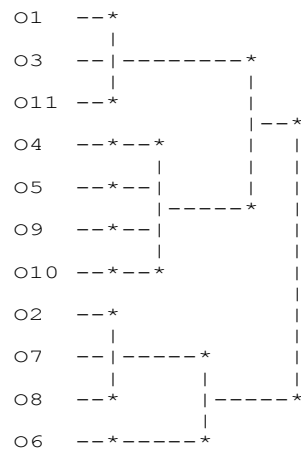
Fig. 1. Dendrogram obtained with *CL, AVL, AV1* and *AVB* (Approach 1)
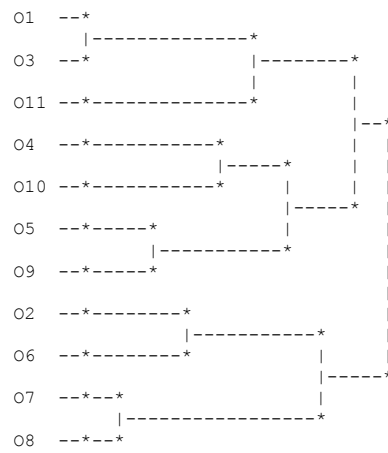
Fig. 2. Dendrogram obtained with *AVL* and *AV1* methods (Approach 2)

The selected partition is the partition into two clusters (*STAT*=5.5222), which was obtained at level 9 by all aggregation criteria (see Figure 1).

In the second approach (case of a symbolic data table for modal variables), from the initial data table (450 × 18), the subjects were distributed into 11 groups according to their professional occupation. The data units, O1 to O11, contain, respectively, 45, 40, 79, 42, 38, 40, 35, 34, 51, 24 and 22 individuals and each entry of the new data table contains a frequency distribution. In fact, the *11* professional occupations correspond to symbolic data units (rows of a symbolic data table as Table 3) described by *18* modal variables (V_1 to V_{18}) .

Figure 2 shows the dendrogram associated with the *AVL* and *AV1* methods. The best partition is the partition into three clusters (*STAT*=5.5372), which was obtained at level 8 by all aggregation criteria.

The clustering results provided by both approaches were compared. Note that at levels 7 and 8 both approaches provide the same partitions (respectively, into two and into three clusters).

Table 4. Responses given by the subjects belonging to each cluster (%)

			V1					*V2*					*V3*		
	1	*2*	*3*	*4*	*5*	*1*	*2*	*3*	*4*	*5*	*1*	*2*	*3*	*4*	*5*
C1	0%	0%	63%	25%	12%	0%	8%	14%	79%	0%	0%	0%	0%	4%	96%
C2	0%	0%	30%	65%	5%	0%	6%	55%	35%	3%	0%	0%	3%	45%	52%
C3	0%	0%	3%	96%	1%	0%	5%	81%	7%	8%	0%	0%	3%	82%	15%
			V4					*V5*					*V6*		
	1	*2*	*3*	*4*	*5*	*1*	*2*	*3*	*4*	*5*	*1*	*2*	*3*	*4*	*5*
C1	0%	0%	76%	20%	4%	8%	13%	55%	23%	2%	0%	8%	9%	79%	5%
C2	0%	0%	41%	57%	2%	4%	16%	69%	11%	0%	0%	6%	48%	41%	5%
C3	0%	0%	9%	91%	0%	1%	13%	80%	7%	0%	0%	5%	80%	7%	9%
			V7					*V8*					*V9*		
	1	*2*	*3*	*4*	*5*	*1*	*2*	*3*	*4*	*5*	*1*	*2*	*3*	*4*	*5*
C1	0%	5%	8%	86%	0%	0%	0%	4%	92%	4%	0%	0%	0%	4%	96%
C2	0%	4%	45%	48%	4%	0%	0%	37%	56%	7%	0%	0%	8%	40%	52%
C3	0%	3%	79%	11%	8%	0%	0%	66%	21%	13%	0%	0%	10%	75%	15%
			V10					*V11*					*V12*		
	1	*2*	*3*	*4*	*5*	*1*	*2*	*3*	*4*	*5*	*1*	*2*	*3*	*4*	*5*
C1	0%	0%	4%	51%	45%	0%	0%	3%	27%	69%	0%	0%	0%	17%	83%
C2	0%	3%	15%	59%	23%	0%	3%	14%	54%	29%	0%	0%	12%	41%	47%
C3	0%	3%	22%	70%	4%	0%	3%	18%	74%	5%	0%	0%	17%	68%	15%
			V13					*V14*					*V15*		
	1	*2*	*3*	*4*	*5*	*1*	*2*	*3*	*4*	*5*	*1*	*2*	*3*	*4*	*5*
C1	4%	16%	47%	27%	5%	0%	0%	14%	86%	0%	0%	0%	0%	15%	85%
C2	4%	16%	62%	15%	3%	0%	3%	45%	45%	6%	0%	0%	12%	43%	45%
C3	4%	9%	73%	11%	2%	0%	3%	79%	7%	11%	0%	0%	17%	73%	9%
			V16					*V17*					*V18*		
	1	*2*	*3*	*4*	*5*	*1*	*2*	*3*	*4*	*5*	*1*	*2*	*3*	*4*	*5*
C1	0%	0%	75%	16%	9%	0%	0%	75%	12%	13%	3%	17%	51%	23%	5%
C2	0%	0%	39%	59%	3%	0%	0%	39%	57%	5%	2%	18%	69%	9%	2%
C3	0%	0%	7%	93%	1%	0%	0%	7%	93%	1%	0%	13%	77%	10%	0%

The differences between the clustering results appear to be due, in part, to the sampling process associated to the first approach and to the fact that in this approach we work only with the total scores of each independent group of individuals in each variable. Thus, in the remainder text, we will only refer to the best partition provided by the second approach: ***Cluster 1:*** {O1, O3, O11}; ***Cluster 2:*** {O4, O5, O9, O10}; ***Cluster 3:*** {O2, O6, O7, O8}. From the observation of Table 4, it can be seen some of the main differences between the profiles associated to these three clusters.

In a 2D Zoom Star, axes are linked by a line that connects most frequent categorical values of each variable, so it allows us to identify the main characteristics of the objects. Figure 3 shows the 2D Zoom Stars associated to the clusters of the second approach. We observe that, for instance, most respondents included into cluster 3 are: generally satisfied with the aspects associated to variables V1, V3, V4, V9, V10, V11, V12, V15, V16 and V17; and neither satisfied nor dissatisfied with the aspects associated to variables V2, V5, V6, V7, V8, V13, V14 and V18 (see Figure 3 and Table 4).
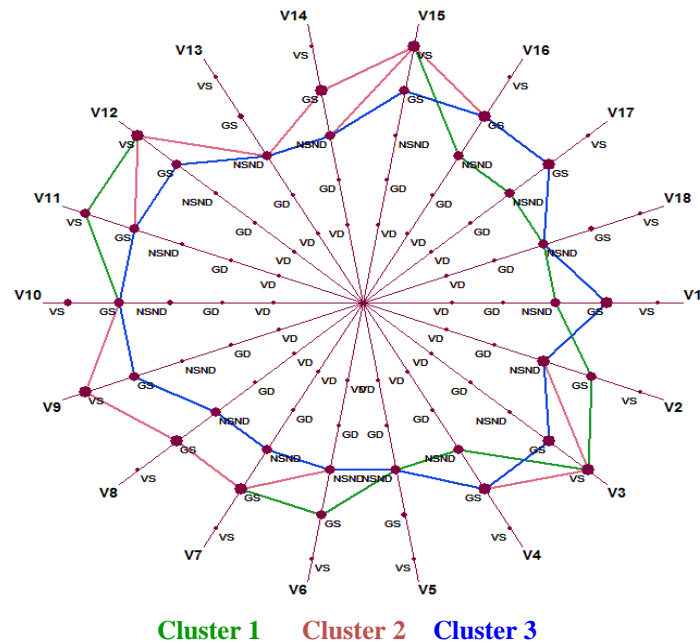
Fig. 3. 2D *Zoom Stars representation for the clusters- Approach 2*

4 Conclusions

The knowledge about the satisfaction profiles is useful, because customers respond better to the Market segmentation strategies which address their specific needs.

In the case of the first approach we loss information because we can´t work with the entire sample but only with a stratified random subsample, and this approach works only with the total scores of each independent group of individuals in each variable (that is, we also loss information about the scores of the groups in the modalities of the variables). Contrary, using the second approach (weighted generalized affinity coefficient, for complex or symbolic objects) it is possible to work with the entire dataset, and with the frequency distributions associated to the scores of each independent group of individuals in the modalities of each variable.

The differences between the clustering results (satisfaction typologies) provided by the two approaches of *AHCA* of independent groups of individuals were due, in part, to the smaller number of individuals of each group when we apply the first approach as a consequence of the sampling process. Nevertheless, we might have opted by inquiring a larger number of individuals in each group, during the planning of the investigation.

References

1. Bacelar-Nicolau, H., Contributions to the Study of Comparison Coefficients in Cluster Analysis, PhD Thesis (in Portuguese), Universidade de Lisboa (1980).
2. Bacelar-Nicolau, H., The affinity coefficient in cluster analysis, Methods of Operations Research, vol. 53, Martin J. Bekmann et al (ed.), Verlag Anton Hain, Munchen, pp. 507-512 (1985).
3. Bacelar-Nicolau, H., On the distribution equivalence in cluster analysis, In Proceedings of the NATO ASI on Pattern Recognition Theory and Applications, Springer - Verlag, New York, pp. 73-79 (1987).
4. Bacelar-Nicolau, H., Two Probabilistic Models for Classification of Variables in Frequency Tables, In: Bock, H.-H. (Eds.), Classification and Related Methods of Data Analysis, North Holland, pp. 181-186 (1988)
5. Bacelar-Nicolau, H., The Affinity Coefficient, In: Analysis of Symbolic Data: Exploratory Methods for Extracting Statistical Information from Complex Data, H.-H. Bock and E. Diday (Eds.), Series: Studies in Classification, Data Analysis, and Knowledge Organization, Springer-Verlag, Berlin, pp. 160-165 (2000).
6. Bacelar-Nicolau, H., On the Generalised Affinity Coefficient for Complex Data, *Biocybernetics and Biomedical Engineering*, vol. 22, no. 1, pp. 31-42, (2002).
7. Bacelar-Nicolau, H.; Nicolau, F.C.; Sousa, Á.; Bacelar-Nicolau, L., Measuring Similarity of Complex and Heterogeneous Data in Clustering of Large Data Sets, *Biocybernetics and Biomedical Engineering*, vol. 29, no. 2, pp. 9-18 (2009).
8. Bacelar-Nicolau, H.; Nicolau, F.C.; Sousa, Á.; Bacelar-Nicolau, L., Clustering Complex Heterogeneous Data Using a Probabilistic Approach, In *Proceedings of Stochastic Modeling Techniques and Data Analysis International Conference* (SMTDA2010), pp. 85-93 (2010) (electronic publication).
9. Bock, H.-H. and Diday, E., Analysis of Symbolic Data: Exploratory Methods for Extracting Statistical Information from Complex Data, Series: Studies in Classification, Data Analysis, and Knowledge Organization, Springer-Verlag, Berlin (2000).
10. Lerman, I. C., Sur l`Analyse des Données Préalable à une Classification Automatique (Proposition d'une Nouvelle Mesure de Similarité), Rev. Mathématiques et Sciences Humaines, vol. 32, no. 8, pp. 5-15 (1970).

11. Lerman, I. C., Classification et Analyse Ordinale des Données, Dunod, Paris (1981).

12. Matusita, K., On the Theory of Statistical Decision Functions, Ann. Instit. Stat. Math, vol. III, pp. 1-30 (1951).

13. Nicolau, F.C., Cluster Analysis and Distribution Function, Methods of Operations Research, vol. 45, pp. 431-433 (1983).

14. Nicolau, F.C. and Bacelar-Nicolau, H., Some Trends in the Classification of Variables, In: Hayashi, C., Ohsumi, N., Yajima, K., Tanaka, Y., Bock, H.-H., Baba, Y. (Eds.), Data Science, Classification, and Related Methods. Springer-Verlag, pp. 89-98 (1998).

15. Sousa, Á., Bacelar-Nicolau, H., Silva, O., Cluster Analysis of Business Data. *Asian Journal of Business and Management*, 2(1) 18-26 (2014).

Smoothing of probabilities of death for older people in life expectancy tables

Gustaf Strandell[1], Tomas Johansson[2]

[1]   Statistics Sweden, SCB, 701 89 Örebro, Sweden
    (E-mail: Gustaf.Strandell@scb.se)
[2]   Statistics Sweden, SCB, 701 89 Örebro, Sweden
    (E-mail: Tomas.Johansson@scb.se)

Abstract. This paper focuses on the smoothing procedure used at Statistics Sweden for handling of probabilities of death for persons in the highest ages, where the population is small and mortality is high. The paper also demonstrates how the smoothing affects the estimated average life expectancies at the national and regional levels.

Keywords: Life table, Probabilities of death, Smoothing, Life expectancy.

1 Introduction

Life expectancy tables in Sweden are based on data on population size and deaths during either a one-year or a five-year period. The tables are produced annually for the whole country, for its 21 counties and 290 municipalities (the table based on one year of data is only produced for the whole country). In addition to the remaining average life expectancies, the publication of the life expectancy table includes sex-specific probabilities of death for all ages.

In 2012, Statistics Sweden conducted a review of the calculations for the periodic life expectancy tables. The project had two main objectives, of which the second is addressed in this paper:

1. A quality assured production system, and
2. Review of the handling of probabilities of death for very old persons at the national and regional levels.

Usable estimates of probabilities of death q_x can be difficult to obtain for the highest ages in a population. Since there might be few survivors and hence few deaths in higher ages the observed probabilities of death can often be seen to fluctuate significantly between ages or between time periods.
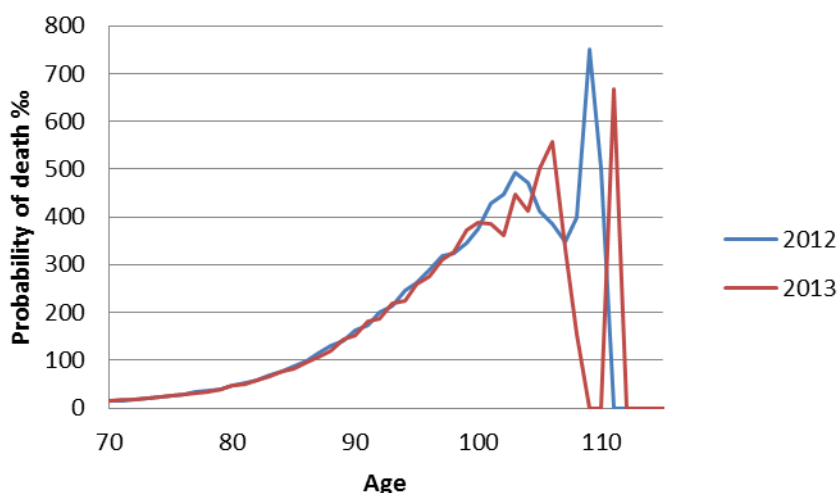
Fig.1. Non smoothed probabilities of death (‰) for the population of Sweden 2012 and 2013

To address this problem Statistics Sweden applies a smoothing procedure to the probabilities of death for the highest ages and over the years various methods to do this has been tried. Until 1986 Wittstein's method was used, which overestimated the probabilities of death for the oldest persons. Therefore in 1987, Sten Martinelle at Statistics Sweden constructed a new smoothing procedure which was used successfully for many years. However, this method, where by Martinelles modeled probabilities of death replaced the observed probabilities for ages 90 and above, relied heavily on mortality data for Sweden and some other countries up to 1987 and did not fully take into account the observed probabilities to be smoothed. Therefore, over time, the smoothing process deteriorated, resulting in a systematic underestimation of probabilities of death and an overestimation of the remaining life expectancy for newborns, e_0. Thus, in 2012, when the calculations for the life expectancy table were up for review it was decided that Martinelles method was to be evaluated, resulting in an updated method which provides smoothed probabilities of death with a better fit to the observed data.

This report focuses on the updated method used since 2012 by Statistics Sweden. It also demonstrates how the updated smoothing affects estimated average life expectancies at the national and regional levels.

2 The model for smoothing probabilities of death

The updated method used by Statistics Sweden for smoothing of the probabilities of death in high ages is based on the model chosen by Sten Martinelle for old-age mortality, Martinelle[3].

The basic assumption underlying the model states that age specific adult mortality for a single individual in a population, in terms of the force of mortality $\mu(x)$ where x denotes age, is well approximated by the Gompertz-Makeham formula

$$\mu(x) = A + Be^{kx} \qquad A \geq 0, B > 0, k > 0.$$

The constant B is called the 'frailty' of the individual and measures his or her inability to withstand destruction.

In the past many authors has pointed out that it is medically well established that frailty is different for different individuals in a population. It is hence customary to assume that frailty follows a probability distribution over a population rather than being the same number for all individuals. This line of thought has given rise to the study of so called frailty models within the theory of survival analysis, see for example Wienke[5]. It was proved by Beard[1] that if the frailty B is gamma distributed then the mean of the force of mortality taken over the population follows the Perks formula, as suggested by Perks already in 1932, Perks (1932):

$$\mu(x) = \frac{A + Be^{kx}}{1 + De^{kx}} \qquad A \geq 0, B > 0, D > 0, k > 0.$$

Martinelles main objection towards using Perks formula is that it implies that the force of mortality approaches a constant limit value B/D in high ages. He argues that there is no empirical evidence for a plateau in the mortality for centenarians. Therefore he modifies the assumption leading to Perks formula, and replaces the assumption of a gamma distributed frailty with an assumption of a frailty with a generalized gamma distribution which has been shifted to the right, thus assuming that it is impossible for the frailty to assume values very close to zero.

In the case where the constant A in the Gompertz-Makeham formula is assumed to be zero, which seems reasonable in Sweden in modern times, Martinelles model of the frangible man states the following:

If the force of mortality for individuals with frailty z follow the Gompertz-Makeham law $\mu(x \mid z) = ze^{kx}$ and the frailty variable z has a shifted gamma distribution with density

$$g(t) = \begin{cases} \dfrac{b^a (t-c)^{a-1}}{\Gamma(a)} e^{-b(t-c)} & \text{for } t > c \\ 0 & \text{for } t \leq c \end{cases}$$

($a, b, c > 0$), then the mean force of mortality over the population, $\mu(x)$, is given by

$$\mu(x) = \left(c + \frac{\eta}{1 + \eta \alpha^2 \int_{x_0}^{x} e^{kt} dt} \right) e^{kx}$$

Where η and α are the mean and the relative standard deviation of the variable $z - c$.

As usual the probabilities of death q_x is (with good approximation) associated with the force of mortality by

$$q_x = 1 - e^{-\mu(x)}.$$

Substituting the expression above for the modelled mean force of mortality into this expression for q_x, we end up with the formula we use for smoothing of the probabilities of death for high ages

$$q_x = 1 - e^{\left(c + \frac{\eta}{1 + \eta \alpha^2 \int_{x_0}^{x} e^{kt} dt} \right) e^{kx}}.$$

This far, the new updated procedure used by Statistics Sweden since 2012 follows Martinelles suggestions in Martinelle[3]. The fitting of the model to mortality data is however new and improved. Martinelle used a large set of historical mortality data for a number of countries to produce a more or less universal smoothing curve which was used for all regions and all time periods. Instead of using a large set of historical data the model is now, whenever possible, fitted using only probabilities of death observed for the region and the time period for which the life expectancy table is to be produced. Thus the smoothed probabilities now more explicitly take into account the observed difference in mortality between regions and between time periods.

The model for the age specific probabilities of death contains 4 parameters: α, k, c and η. The modeled probabilities dependence on α and k is indicated in the diagram below where $c = 1{,}363 \cdot 10^{-7}$ and $\eta = 5{,}535 \cdot 10^{-7}$.
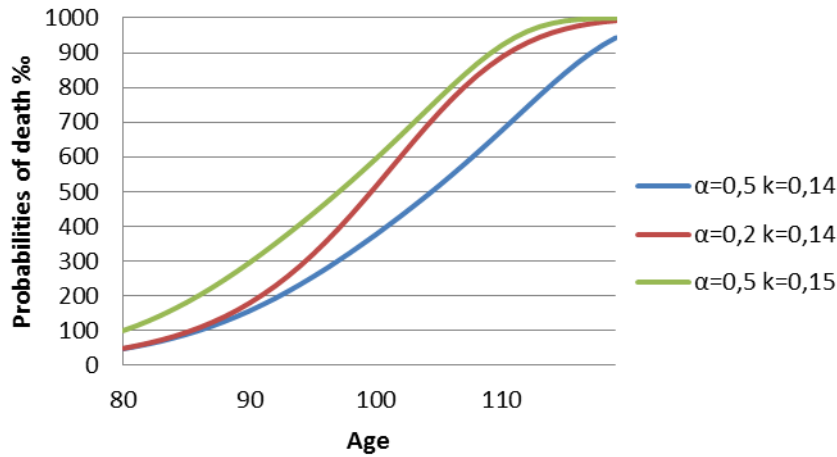
Fig.2. Modeled probabilities of death

For the very high ages a decrease in α leads to a steeper increase of the probabilities of death between ages, an increase in k leads to an almost constant increase of the probabilities for a broad interval of high ages.

It is technically cumbersome to fit this model to mortality data without first fixing two of the parameters. After testing numerous different parameter settings against data we decided to fix the parameters $\alpha \equiv 0,5$ and $k \equiv 0,14$. Our experimentation also showed that it is not recommended to use probabilities of death for all available ages to fit the model. We got much better results when we restricted the mortality data used as input to the fitting procedure to ages in a span between m and n, to be specified below, then when we used all ages or even all higher ages. Finally we decided it preferable to use age specific weights in the fitting of the model. The reason for this is that especially for smaller populations, the probabilities of death for certain ages can be zero (if no one dies) or one (if everybody dies) and these extreme values has a tendency to gain an unjustified influence on the modeled probabilities of death for the other ages. Therefore we decided to use the number of deaths per age as weights in the fitting of the model.

To fit the model to observed probabilities of death we use a weighted least square method: If the model $q_x = q_x(c, \eta)$, where α and k has been fixed as above, is to be fitted to the observed probabilities of death $\tilde{q}_m, ..., \tilde{q}_n$ over the age interval from age m to age n, we try to find c and η which minimizes the expression

$$\frac{1}{n-m+1} \sum_{x=m}^{n} v_x^{\ 2} (\tilde{q}_x - q_x(c, \eta))^2$$

where v_x are the nonnegative weights. To do this in practice we use the *model procedure* in SAS.

3 Results

At the national level, the model is fitted using probabilities of death observed in the age interval between $m = 90$ and $n = 100$ years. Since the number of individuals in the higher ages, and hence the number of deaths among them, has increased over the years the age at which the smoothing start to take place was also increased from 91 to 95 years.
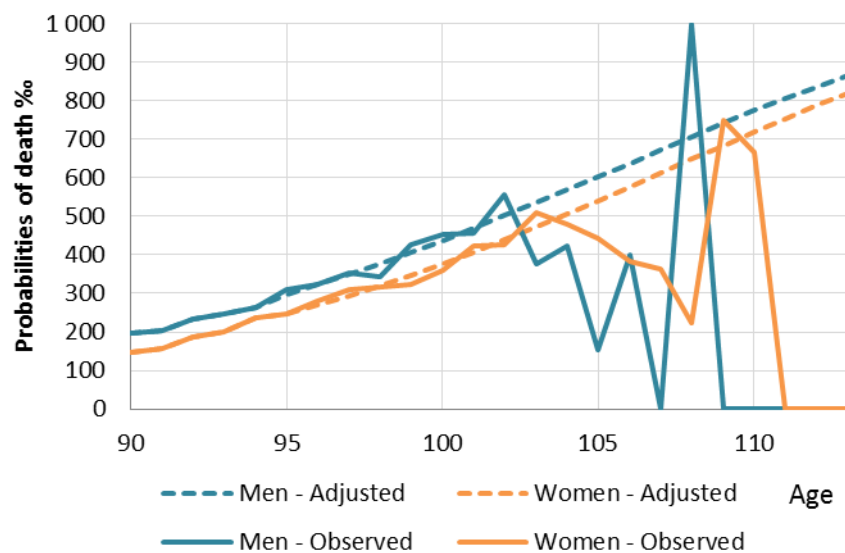
Fig.3. Observed and adjusted probabilities of death by sex and age (90 to 113) for Sweden 2012

The effect of the update of the smoothing method on the probabilities of death can be seen in the diagram below. For example the probability of death for women age 100 in 2011 was raised by over 10% with the updated method compared with the old method.
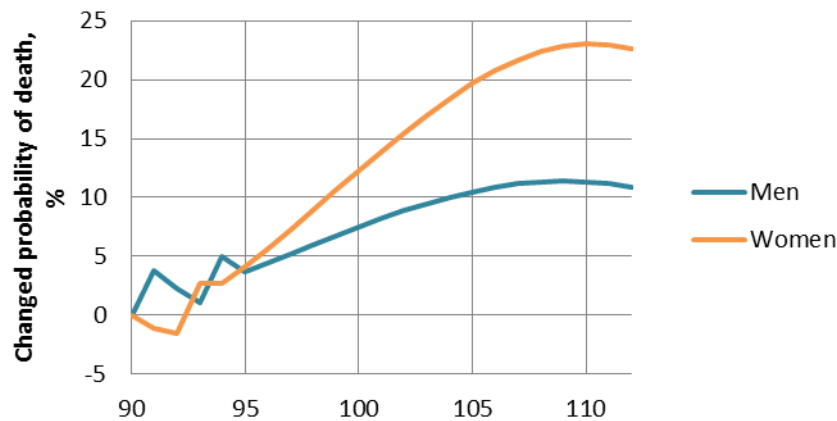
Fig.4. Difference in probability of death between new and old smoothing method 2011

Although the probabilities of death for ages 95 and over have clearly changed with the new method compared with the old one, the update of the smoothing method did not bring about particularly large changes in average life expectancies for the whole of Sweden. As suspected, the updated method gives life expectancies which are very close to those gained if the life expectancy table were to be produced without any smoothing. For the whole country the smoothing has thus more of a cosmetic effect on the mortality data (which is a good thing and can be very important for the presentation of the data).

Sex	Age	No smoothing	Old smoothing method	Updated smoothing method
Male	e0	79.8	79.81	79.79
	e85	5.51	5.54	5.5
Female	e0	83.67	83.7	83.67
	e85	6.61	6.66	6.61

Table.1. Average life expectancies for Sweden 2011

At the county level, in order to capture regional differences in mortality among the elderly, the model is also fitted using only the observed probabilities of death for the region at hand. However, the population in most counties is too small to appropriately apply the same method for the counties as for the national level. After extensive testing, it was decided that the fitting of the model would be based on observations in the age interval of 80 to 100. It was also decided that the smoothed probabilities of death would be used from the age of 90.
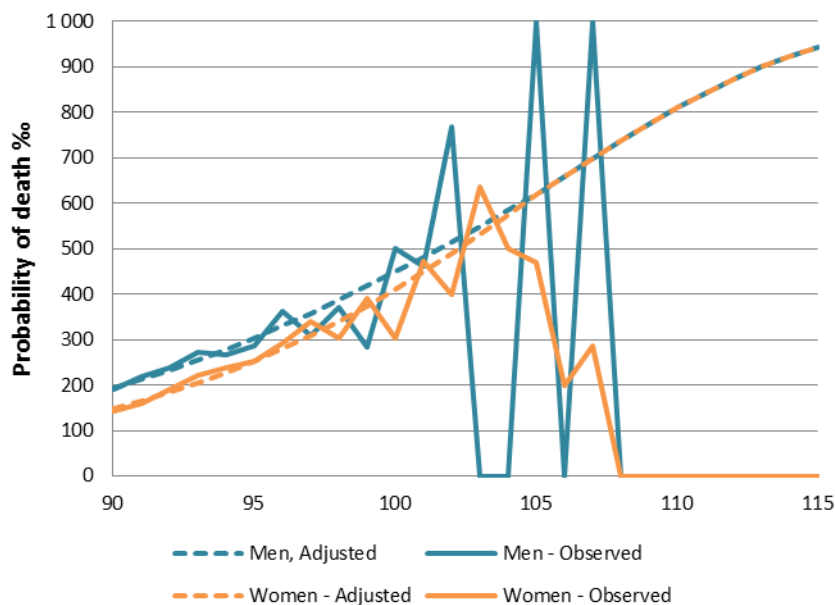
Fig.5. Observed and adjusted probabilities of death (‰) by sex and age (90 to 115) for Örebro county 2012

The updated smoothing method has a larger impact on the life expectancies for the counties than for the whole of Sweden, but the effects are not dramatic. Among the counties we noted the greatest change for the county of Norrbotten (2007-2011) where the updated method subtracts about a month from the mean total lifespan of women. Also for the counties, the updated method (compared with the old one) gives life expectancies which are closer to those gained if the life expectancy table were to be produced without any smoothing.

In the smoothing of the probabilities of death for municipalities, the population and hence the number of deaths are in many cases too small to use as basis for the fitting of the model. There are 290 municipalities In Sweden with populations ranging from just under 2 500 inhabitants to nearly 900 000 inhabitants. One-half of the municipalities have a population of around 15 000 inhabitants or less. Therefore, the smoothed probabilities of death at the corresponding county level are used for all the constituent municipalities from the age of 90. An exception is made for the three largest municipalities: Stockholm, Gothenburg and Malmö, where the adjustment of probabilities of death is based on the individual municipalities in the same way as for the counties.
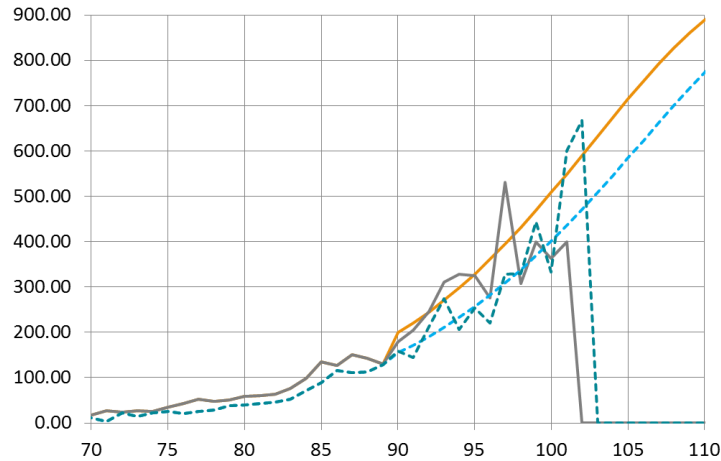
Fig.6. Observed and adjusted probabilities of death (‰) by sex and age for the municipality of Sandviken (population 40 000) 2013. The smoothing curves have been borrowed from the county of Gästrikland

The updated method has had a greater impact at the municipal level than at the national and county levels. Based on the period 2007-2011, the average life expectancy for newborn females is affected up to a shorter life expectancy of just over three months, compared with the old smoothing procedure. The largest increase in average life expectancy for newborns in a municipality was an increase of about two months.

At the national level and for some of the counties the effect of the smoothing on the average life expectancies is marginal for the most ages, compared to results gained without smoothing. However, for many municipalities the smoothing of the probabilities of death is absolutely necessary. Without it, for some municipalities, we would end up with very unstable average life expectancies. For example, for the small municipality of Jokkmokk in the north of Sweden, the smoothing subtracts 150 days from e_0 for women.
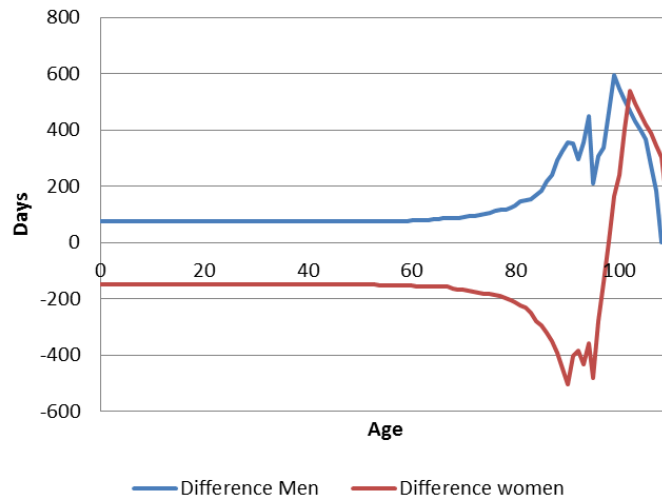
Fig.7. Difference in average life expectancy by age between smoothed and not smoothed results for Jokkmokk 2013

Conclusions

For the study of differences in mortality between time periods and between geographical regions it is important that the mortality data is analyzed using methods which preserve the differences. In this paper we have demonstrated a method for smoothing of mortality data for the elderly which does just that.

For the probabilities of death for the elderly the smoothing has a large effect for individual ages, and usable estimates of these probabilities are important in many applications. However, for large and stable regions like the whole of Sweden, the smoothing does not have a large effect on remaining life expectancies; actually our new updated method for smoothing gives results which are closer to 'non-smoothed' life expectancies than the old smoothing method. This is a good thing since we don't want to add model effects where they are not needed.

For smaller regions some form of model is necessary in the production of the life table and our smoothing procedure works well at the county level and for most of the municipalities. However for the smallest municipalities the methods needed to produce a reliable life table should be studied further.

References

1. R. E. Beard. Note on Some Mathematical Mortality Models, Colloquia on Ageing. CIBA Foundation, Vol 5. Churchill, London, 1959.
2. T. Johansson. G. Strandell. Slutrapport 2012 BVBE Livslängdstabeller. Statistics Sweden, 2012.
3. M. Martinelle. A Generalized Perks Formula for Old-Age Mortality, R&D Report, U/STM-38, Statistics Sweden, 1987.
4. W. Perks. On some Experiments in the Graduation of Mortality Statistics. Journal of the Institute of Actuaries. Vol LXIII, 1932.
5. A. Wienke. Frailty Models in Survival Analysis. Chapman &Hall/CRC Biostatistics Series, 2011.

Stochastic Modelings in Software Reliability

Nuria Torrado[1]

Centre for Mathematics
University of Coimbra, Coimbra, Portugal
(e-mail: nuria.torrado@gmail.com)

Abstract. The reliability of software systems has become a major concern for our modern society because the demand for complex software systems has increased within the first decade of the 21st century. A software reliability model (SRM) is a mathematical tool to evaluate the software quantitatively. A large number of models have been proposed in the literature to predict software failures (see, e.g. Singpurwalla and Wilson[18]), but a few incorporate some significant metrics data observed in software testing. In this work, we present a new procedure to predict numbers of software failures using metrics information, from a Bayesian perspective. This new Bayesian software reliability model has been developed in collaboration with R.E. Lillo and M.P. Wiper (see Torrado *et al.*[19]).
Keywords: nonhomogeneous Poisson process, software failures, Bayesian statistical methods.

1   Introduction

Software reliability is defined as the probability that the software will function without failure under given environmental conditions during a specified period of time. Most software reliability models (SRMs) are based on the assumption that the software is possibly imperfectly corrected after each failure or after various fixed time periods. Often, it will be the case that information in the form of software metrics such as code length or complexity will be generated each time the software is corrected. See Fenton and Pfleeger[4] for a review of the main ideas.

From a statistical point of view, the random variables that characterize software reliability are the epoch times in which a failure of software takes place or the times between failures. Most of the well known models for software reliability are centered around the interfailure times or the point processes that they generate. A software reliability model specifies the general form of the dependence of the failure process on the principal factors that affect it: fault introduction, fault removal, and the operational environment.

A number of analytical models have been proposed for software reliability assessment. Most of these models are based on the assumption that the software is possibly imperfectly corrected after each failure or after various fixed time

periods. Starting from Jelinski and Moranda[6] and Moranda[10] many models have been developed. For good recent reviews till 2007 see e.g. the book by Pham[12].

Most of the works in the literature are devoted to estimate model parameters. Some important early references are Jelinski and Moranda[6], Moranda[10], Goel and Okumoto[5], Littlewood and Verrall[7], Mazzuchi and Soyer[9], Musa and Okumoto[11], among others.

Some interesting software reliability modelling developed in the last two decades can be found in Boland and Singh[1], Rinsaka *et al.*[15], Shibata *et al.*[17], Wiper[20], Pievatolo *et al.*[13] and Torrado *et al.*[19].

In this paper, we shall develop an alternative approach to both Type I and Type II software reliability models based on exponential interfailure times or Poisson failure counts where the rates are modeled as Gaussian processes where software metrics data are used as inputs. This approach may be thought of as an extension of the work of Ray *et al.*[14] which generalizes this earlier, parametric regression based method to a nonparametric regression model.

Rather than use classical statistical inference techniques we shall here adopt a Bayesian approach, which has the advantages of being able to take into account any prior information available and also of taking parameter uncertainty into account when prediction of reliability is undertaken. Starting from Littlewood and Verrall[7], Bayesian approaches to many software reliability models have been considered.

In the article and in the presentation a short overview on the wide field of Bayesian inference in software reliability model is given, showing some results given by Torrado *et al.*[19] and also some of the current research the author is doing in moment.

2   Short review on software reliability modeling

The use of statistical methods in software engineering has been increasing in the last decades. In the context of this discipline, as we defined above, software reliability measures the probability that a piece of software runs without failing under certain operational conditions for a given time. In software testing, software is run under an operational profile, that is certain conditions simulating real usage and after a given test period, the software is modified in order to correct any observed faults. Testing then proceeds until the software is judged sufficiently reliable for release.

A software reliability model (SRM) is a mathematical tool to evaluate the software quantitatively. The SRM's have been extensively developed in the literature. Most SRM's are based on stochastic counting processes, such as binomial process, pure birth process and nonhomogeneous Poisson process (NHPP). One may refer to two excellent books by Singpurwalla and Wilson[18] and Pham[12] on this topic. These stochastic models attempt to model either the times between successive failures of a piece of software or the number of failures in fixed time periods. Our classification scheme (see Figure 1) follows that of Singpurwalla and Wilson[18], and divides models into two types: Type I and Type II.
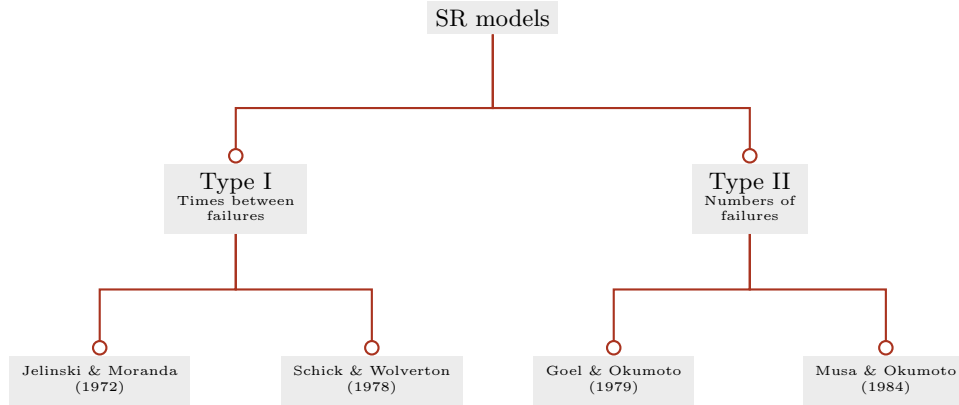
Fig. 1. Classification of software reliability (SR) models

Type I models are those that model the times between successive failures. Under these types of models, the random variables $T_1, T_2, \ldots$, are modeled directly. This is often done by specifying the failure rate function for each random variable, h_i, $i = 1, 2, \ldots$, an then invoking the exponentiation formula to obtain their survival function, $\bar{F}_i$. Typically, each h_i is a nondecreasing function on t, for $t \geq 0$ to reflect the fact that between failures the reliability of the software increases.

Type II models are those that model the number of failures up to a given time. These models are based on stochastic counting processes for $N(t)$, the number of times the software fails in an interval $[0, t]$. The earliest and best known Type II models are those which assume that $N(t)$ is described by a Poisson process whose mean value function is based on assumptions about how the software experiences failure.

It is remarkable that a model of either type defines a model of the other. Specifically, for a sequence of interfailure times $T_1, T_2, \ldots$, for which a Type I model has been proposed, there is an implicit Type II model (cf. Singpurwalla and Wilson[18]), because

$$N(t) = \max \left\{ n \mid \sum_{i=1}^{n} T_i \leq t \right\},$$

and conversely, for a Type II model there is a Type I model, because with $T_0 = 0$, and $i = 2, 3, \ldots$,

$$T_i = \inf \{t \mid N(t) = i\} - T_{i-1}.$$

It is noteworthy two differences between Type I and Type II models. First, the total number of potential failures of Type II models is assumed to be infinite, so that the number of observed failures is a random variable having a Poisson distribution, as opposed to a fixed number of faults N that is assumed by Type I models. Second, in the Type II models the interfailure times are

743

dependent whereas in the Type I models they were typically assumed independent.

2.1 Type I models

The Type I group of models is used to study the program hazard rate per fault at the failure intervals. The hazard rate function of the i'th interfailure time of some of these models are reported in Table 1.

Table 1. Some Type I software reliability models

Jelinski-Moranda	Moranda
$h_i(t) = \phi\,(N - i + 1)$	$h_i(t) = D\,k^{i-1}$

Goel-Okumoto	Schick-Wolverton
$h_i(t) = \phi\,(N - p(i - 1))$	$h_i(t) = \phi\,(N - i - 1)\,t$

The first model to be widely known and used is the model by Jelinski and Moranda[6] (hereafter JM). They assume that the software contains an unknown number, say N, of faults and that each time the software fails, a bug is detected and perfectly corrected. Furthermore, the failure rate of T_i is proportional to $N - i + 1$, the number of faults remaining in the code, that is, for some constant $\phi > 0$, the hazard rate at the i'th failure interval is given by

$$h_i(t) = \phi\,(N - i + 1)\,, \quad i = 1, \ldots, N.$$

The survival function is

$$\bar{F}_i(t) = e^{-\phi(N - i + 1)t}, \quad i = 1, \ldots, N.$$

The property of this model is that the failure rate is constant and the software during the testing stage is unchanged or frozen.

A modification to the JM model is the *Geometric Model* developed by Moranda[10]. He proposed a new model in which the program failure rate function is initially a constant D and decreases geometrically at failure times. In this case, the hazard rate function of the i'th interfailure times is

$$h_i(t) = D\,k^i,$$

and its survival function is

$$\bar{F}_i(t) = e^{-t\,D\,k^i},$$

where $D > 0$ is the initial program failure rate and k is the parameter of a geometric function $(0 < k < 1)$.

Goel and Okumoto[5] extend the JM model by assuming that a fault is removed with probability p whenever a failure occurs. This model is called the *JM model with imperfect debugging* and the hazard rate function of time between failures when the imperfect debugging is at the i'th failure interval becomes

$$h_i(t) = \phi \left(N - p(i-1) \right).$$

The survival function is

$$\bar{F}_i(t) = e^{-\phi(N-p(i-1))\,t}, \quad i = 1, \ldots, N.$$

The model by Jelinski and Moranda is a special case of the preceding when $p = 1$.

The model by Schick and Wolverton[16] (hereafter SW) is another modification of the JM model. They assumed that the hazard rate of T_i is proportional to both the number of remaining faults in the software and the elapsed time since last failure. Thus, the hazard rate function between the $(i-1)$'th and the i'th failure can be expressed as

$$h_i(t) = \phi \left(N - i - 1 \right) t,$$

where ϕ and N are the same as that defined in the JM model.

2.2 Type II models

In this subsection we shall describe briefly some Type II software reliability models. The models described here are only a small subset of those which appear in the literature.

The Type II models provide another analytical framework for describing the software failure phenomenon during testing. Recall that in this case, we look at $N(t)$ as the number of failures to time t. Then, $N(t)$ is modeled by a Poisson distribution with mean $\Lambda(t)$, that is, $\mathbb{E}\left[N(t)\right] = \Lambda(t)$. Under such models the reliability of the software for a mission of duration t is simply $\Pr(N(t) = 0)$.

The Goel-Okumoto model [5], referred to hereafter as GO, is a NHPP variant of the JM model. The GO model assumes that the cumulative number of failures detected by time t is a NHPP and its expectation could be described by the mean value function

$$\Lambda(t) = a(1 - e^{-bt}). \tag{1}$$

The intensity function is

$$\lambda(t) = \frac{d\Lambda(t)}{dt} = abe^{-bt}.$$

Observe that $\Delta(t) < \infty$ as $t \to \infty$. Therefore, this model cannot be applied to situations where new faults might be introduced in the process of debugging. Some NHPP models can incorporate the situation where new faults may be added during repairs, these models are the infinite failures models. It means that $\Delta(t) \to \infty$ as $t \to \infty$.

The Duane model [3], referred to hereafter as DU, originally devised for hardware reliability model, is an infinite failures model. This model is a NHPP with the expected number of failures

$$\Lambda(t) = at^b, \tag{2}$$

and the intensity function

$$\lambda(t) = abt^{b-1}.$$

This function is increasing for $b > 1$, decreasing for $b < 1$ and constant for $b = 1$. The DU model could be stochastically represented as a Weibull process, allowing for statistical procedures to be used in the application of this model in reliability growth. In particular, this model is the counting process of the record values from a Weibull distribution.

In these NHPP models, usually parameter a represents the mean number of software failures that will eventually be detected, and parameter b represents the probability that a failure is detected in a constant period.

Musa and Okumoto[11] proposed another model for infinite failures. This NHPP is also called the *logarithm Poisson model*, referred to hereafter as MO. The mean value function is

$$\Lambda(t) = a \ln(1 + bt), \quad t > 0,$$

and the intensity function is derived as

$$\lambda(t) = \frac{ab}{1 + bt}.$$

Let us mention an homogeneous pure birth process, referred to hereafter as HPBP, for software reliability which is another variation of the JM model. This model, proposed by Boland and Singh[1], is a birth process approach to the geometric SRM. In this case, the cumulative number of failures detected by time t is a HPBP with birth rates

$$\lambda_i = D \cdot k^i, \quad i = 0, 1, \dots.$$

Boland and Singh[1] showed that the mean value function is

$$\Lambda(t) = Dt + \sum_{i=1}^{\infty} (-1)^i \frac{(Dt)^{i+1}}{(i+1)!} \prod_{j=1}^{i} (1 - k^j),$$

and the intensity function

$$\lambda(t) = D \left(1 + \sum_{i=1}^{\infty} (-1)^i \frac{(Dt)^i}{i!} \prod_{j=1}^{i} (1 - k^j) \right).$$

Other types of mean value functions suggested by Yamada and Osaki[21], are the hyperexponential growth model and the Yamada-Osaki exponential growth model, respectively. Some of these models are reported in Table 2. For more details on software reliability models, see e.g. Pham [12] and Singpurwalla and Wilson[18].

Table 2. Some Type II software reliability models

Goel-Okumoto	Musa-Okumoto
$\Lambda(t) = a\big(1 - \exp(-bt)\big)$	$\Lambda(t) = a\,\ln(1 + bt)$

Duane	Boland and Singh
$\Lambda(t) = a\,t^b$	$\Lambda(t) = D\,t + \sum\limits_{i=1}^{\infty}(-1)^i\,\frac{(D\,t)^{i+1}}{(i+1)!}\prod\limits_{j=1}^{i}(1-k^j)$

Ohba	Yamada-Osaki
$\Lambda(t) = \sum\limits_{i=1}^{n} a_i\big(1 - \exp(-b_it)\big)$	$\Lambda(t) = a\sum\limits_{i=1}^{n} p_i\big(1 - \exp(-b_it)\big)$

3   A new software reliability model

In this subsection we present a new approach to both Type I and Type II software reliability models (see Section 2). Our model is a hierarchical non-parametric regression model based on exponential interfailure times or Poisson failure counts where the rates are modeled as Gaussian processes where software metrics data are used as inputs.

Gaussian process models have recently been used in Bayesian approaches to regression, classification and other areas. Formally, a Gaussian process is defined as following: A *Gaussian process* (hereafter GP) is a collection of random variables, any finite number of which have a joint Gaussian distribution.

It is well known that a GP is a generalization of the Gaussian probability distribution. Just as a Gaussian distribution is fully specified by its mean and covariance matrix, a GP is specified by a mean and a covariance function. We define the mean function $m(\boldsymbol{x})$ and the covariance function $C(f(\boldsymbol{x}), f(\boldsymbol{x}'))$ of a real process $f(\boldsymbol{x})$ as

$$m(\boldsymbol{x}) = \mathbb{E}\left[f(\boldsymbol{x})\right],$$
$$C(f(\boldsymbol{x}), f(\boldsymbol{x}')) = \mathbb{E}\left[(f(\boldsymbol{x}) - m(\boldsymbol{x}))\,(f(\boldsymbol{x}') - m(\boldsymbol{x}'))\right].$$

GPs are used in regression and classification problems. Here, we consider a regression problem where we have a data set $\mathcal{D}$ of M scalar observations with an arbitrary distribution with parameter λ_i and that the software being analyzed is possibly imperfectly corrected after each period. If we assume that we observe the times between successive M failures, say $T_1 = t_1, \ldots, T_M = t_M$, then, in this case, $\mathcal{D} = \{t_i : i = 1, \ldots, M\}$. We might also assume that interfailure times are exponentially distributed, that is,

$$T_i \mid \lambda_i \sim \mathcal{E}(\lambda_i).$$

When we assume that we observe the numbers of failures, say $N_1 = n_1, \ldots, N_M = n_M$ in M time periods of length $L_1, \ldots, L_M$ respectively, then $\mathcal{D} = \{n_i : i = 1, \ldots, M\}$.

We also assume that the numbers of failures follows a Poisson distribution, that is, for $i = 1, \ldots, M$, we have

$$N_i \mid \lambda_i \sim \mathcal{P}(L_i \lambda_i).$$

As part of the correction procedure, we shall suppose that after the $(i-1)$'th failure the software is possibly imperfectly corrected and software metrics, say $\boldsymbol{x}_i = (x_{i1}, \ldots, x_{ik})$ are generated for $i = 1, \ldots, M$. Such metrics may reflect both characteristics of the code such as number of lines or also measures of the amount of work undertaken on correction such as many hours or costs. Thus, it is reasonable to suppose that changes in the quality of the code will be reflected in changes in the values of the software metrics.

In both cases, the rate, λ_i can be modeled as a function of the software metrics, $\boldsymbol{x}_i$, available after the last correction as

$$\ln \lambda_i \mid f_i = f(\boldsymbol{x}_i) + \epsilon_i, \tag{3}$$

where $\epsilon_i \sim N(0, \sigma^2)$ and $f : \Re^k \to \Re$ can take different forms. The most important problem to consider is how to model the unknown function, f. One possibility is to assume that f is a linear function of the software metrics, say

$$f(\boldsymbol{x}_i) = \beta_0 + \sum_{j=1}^{k} \beta_j \, x_{ij} \,,$$

but there is quite a lot of evidence to illustrate that the relationship between software quality and software metrics is often highly non-linear and therefore, it seems preferable to use a more general, fully nonparametric model as for instance a GP model. Therefore, we have an approach to both Type I and Type II SR models which can be summarize, respectively, as following:

$$
\begin{aligned}
T_i \mid \lambda_i &\sim \mathcal{E}(\lambda_i), & N_i \mid \lambda_i &\sim \mathcal{P}(L_i \lambda_i), \\
\ln \lambda_i \mid f_i &= f(\boldsymbol{x}_i) + \epsilon_i, & \ln \lambda_i \mid f_i &= f(\boldsymbol{x}_i) + \epsilon_i, \\
\boldsymbol{f} \mid \boldsymbol{\theta} &\sim \mathcal{GP}(0, C(\boldsymbol{\theta})). & \boldsymbol{f} \mid \boldsymbol{\theta} &\sim \mathcal{GP}(0, C(\boldsymbol{\theta})).
\end{aligned}
$$

One possibility would be to use classical, nonparametric regression techniques, but here we prefer to use a Bayesian approach, as outlined in the next section.

4   A Bayesian approach to failure rate modeling

In this Section, we explain a Bayesian approach to software reliability modeling using Gaussian process prior distributions for the functional form, f. In our context, we propose using the Gaussian process as a prior distribution for the function f of (3). This, so called Gaussian process prior distribution is characterized by the form of the mean and covariance functions. Firstly, we

assume that the mean function is $\mathbb{E}[f(\boldsymbol{x})] = 0$ and as covariance function we shall assume the *squared exponential covariance function* defined as

$$\mathbb{C}(f(\boldsymbol{x}_i), f(\boldsymbol{x}_j) \mid \boldsymbol{\theta}) = \eta^2 \exp\left\{ -\frac{1}{2} \sum_{\ell=1}^{k} \rho_\ell^{-2} \left(x_{i\ell} - x_{j\ell}\right)^2 \right\}, \qquad (4)$$

where $\boldsymbol{\theta} = \left(\rho_1^2, \ldots, \rho_k^2, \eta^2\right)$ is the unknown parameter set, i.e., the *hyperparameter* set.

One advantage of the Gaussian process prior structure is that it leads to straightforward inference and prediction in the presence of normal noise. From (3), set $\zeta_i = \log \lambda_i$, when $\zeta_i = f(\boldsymbol{x}_i) + \epsilon_i$, for $i = 1, 2, \ldots$.

Assume now that for $i = 1, 2, \ldots$, the number of failures in a fixed time period of length T_i for the i'th release of the software follows a Poisson distribution and that the logged failure rate, ζ_i, is modeled as described above.

The basic Bayesian model is completed by defining prior distributions for the error variance, σ^2 and for the GP parameters, $\boldsymbol{\theta}$. Here, we assume inverse gamma priors, $\sigma^2 \sim \mathcal{IG}(\alpha_s, \beta_s)$, $\eta^2 \sim \mathcal{IG}(\alpha_e, \beta_e)$ and $\rho_j^2 \sim \mathcal{IG}(\alpha_{rj}, \beta_{rj})$, for $j = 1, \ldots, k$.

In Torrado *et al.*[19], we present an explicit and detailed Bayesian posterior inference for the failure rate model and applied this new model to three real data sets.

Our proposed model class includes many simpler models such as the JM model (see Section 2) which are independent of covariate information and also simpler regression functions. Furthermore, in many problems we may often have large numbers of metrics available and therefore, which model or which metrics to choose is an important problem. The standard approach to model selection in the classical context is to use selection criteria such as the Akaike or Bayesian information criterion. The most popular Bayesian selection criterion is the deviance information criterion (hereafter DIC). However, this criterion is highly dependent on the stability of the posterior (mean) parameter estimates and in the Gaussian process context, we have found that it is unstable. Therefore, we prefer to use a variant of the DIC, denoted DIC_3. This criterion is defined, for the Type II model with data $\boldsymbol{n} = (n_1, \ldots, n_M)$ and model $\mathcal{M}$ as

$$-4\,\mathbb{E}\left[\ln p(\boldsymbol{n}\boldsymbol{\theta}) \mid \boldsymbol{n}, \mathcal{M}\right] + 2\ln \widehat{p}(\boldsymbol{n} \mid \boldsymbol{n}, \mathcal{M}),$$

where

$$\widehat{p}(\boldsymbol{n} \mid \boldsymbol{n}, \mathcal{M}) = \prod_{i=1}^{M} \widehat{p}(n_i \mid \boldsymbol{n}, \mathcal{M}),$$

and

$$\widehat{p}(n_i \mid \boldsymbol{n}, \mathcal{M}) = \frac{1}{J} \sum_{j=1}^{J} p(n_i \mid \boldsymbol{n}, \lambda_{i,j}, \mathcal{M}) = \frac{1}{J} \sum_{j=1}^{J} \frac{\lambda_{i,j}^{n_i}\, e^{-\lambda_{i,j}}}{n_i!}.$$

This criterion is straightforward to calculate from the MCMC output and, in our experience, gives much more satisfactory results than the DIC. As with the AIC and BIC, lower values of this criterion imply better fitting models.

5　Applications to a real data set

Finally, we present the analysis of a real data set, see Torrado *et al.*[19] for the analysis of two other real data sets.

The data set, referred to hereafter as DS, was presented by Dalal and McIntosh[2]. This data set consists of number of failures in given time periods and therefore can be analyzed using Type II models. DS contains approximately 400000 new or changed non-commentary source lines (hereafter NCNCSL), the staff time spent testing and the number of faults found. In order to undertake Bayesian inference for the models described before, prior distributions for the GP parameter σ^2 and hyperparameters $\boldsymbol{\theta} = (\rho_1^2, \ldots, \rho_k^2, \eta^2)$ must be defined. As is typical in such problems, we shall assume independent, proper but relatively uninformative inverse gamma, $\mathcal{IG}(\alpha, \beta)$, priors, where $\alpha = \beta = 0.001$.

We shall consider three training sets for DS consisting of 99 (50%), 149 (75%) and 178 (90%) data, and three test sets consist of 99, 49 and 20 data, respectively. We then compute the estimated values of the deviance information criterion of our model using the new or changed noncommentary source lines (NCNCSL) as covariate. In order to study whether software metrics provide information to the model, we compare the GP model with two classical NHPP-SR models defined in Subsection 3. In particular, we shall consider a Bayesian approach to the GO model and the DU model as follows,

$$N_i \mid a, b \sim \mathcal{P}(\Lambda(t_i))$$
$$a \sim \mathcal{G}(\alpha_a, \beta_a)$$
$$b \sim \mathcal{G}(\alpha_b, \beta_b),$$

where $\Lambda(t)$ is defined in (1) for the GO model and in (2) for the DU model.

Table 3. DIC_3 criterion for DS

Model	50%	75%	90%
GP(NCNCSL)	299.80	517.90	625.73
GO-SRM	690.81	$1.0786e + 003$	$1.2929e + 003$
DU-SRM	694.12	$1.0744e + 003$	$1.3161e + 003$

From Table 3, it can be seen that our model can give the smallest DIC_3 value, i.e., in the estimation of software failure data is appropriate to use software metrics information.

Acknowledgements

References

1. P.J. Boland and H. Singh. A Birth-Process Approach to Moranda's Geometric Software Reliability Model, *IEEE Transactions on Reliability*, 52, 168–174, 2003.
2. S.R. Dalal and A.A. McIntosh. When to stop testing for large software systems with changing code, *IEEE Trans. Software Engineering*, 20, 318–323, 1994.
3. J.T. Duane. Learning curve approach to reliability monitoring, *IEEE Trans. Aerospace*, 2, 563–566, 1964.
4. N.E. Fenton and S.L. Pfleeger. *Software Metrics: A Rigorous & Practical Approach*, second ed. Boston: PWS Publishing, 1998.
5. A.L. Goel and K. Okumoto. Time-dependent error detection rate model for software reliability and other performance measures, *IEEE Trans. Rel.*, R-28, 206–211, 1979.
6. Z. Jelinski and P. Moranda. Software reliability research, in W. Freiberger (Ed.), *Statistical Computer Performance Evaluation*, New York: Academic Press, 465–484, 1972.
7. B. Littlewood and J.L. Verrall. A Bayesian reliability growth model for computer software, *Appl. Stat.*, 22, 332–346, 1973.
8. M.R. Lyu. *Handbook of Software Reliability Engineering*, IEEE Computer Society Press, McGraw-Hill, 1996.
9. T.A. Mazzuchi and R. Soyer. A Bayes empirical-Bayes model for software reliability, *IEEE Trans. Rel.*, R-37, 248–254, 1988.
10. P.B. Moranda. Prediction of software reliability and its applications, in *Proceedings of the Annual Reliability and Maintainability Symposium*, Washington DC, 327–332, 1975.
11. J.D Musa and K. Okumoto. A logarithmic Poisson execution time model for software reliability measurement, in Proc. of the seventh International Conference on Software Engineering, 230–237, 1984.
12. H. Pham. *System Software Reliability*, Springer, 2007.
13. A. Pievatolo, F. Ruggeri and R. Soyer. A bayesian hidden markov model for imperfect debugging, *Reliability Engineering and System Safety*, 103, 12–21, 2012.
14. B.K. Ray, Z. Liu and N. Ravishankar. Dynamic reliability models for software using time-dependent covariates, *Technometrics*, 48, 1–10, 2006.
15. K. Rinsaka, K. Shibata and T. Dohi. Proportional intensity-based software reliability modeling with time-dependent metrics, in Proceedings of the 30th Annual International Computer Software and Applications Conference, IEEE ,2006.
16. G.J. Schick and R.W. Wolverton. Assessment of software reliability, in Proc. in Operations Research, 395–422, 1978.
17. K. Shibata, K. Rinsaka and T. Dohi. PISRAT: Proportional intensity-based software reliability assessment tool, in Proceedings of the 13th International Symposium on Pacific Rim Dependable Computing, IEEE, 2007.
18. N.D. Singpurwalla and S. Wilson. *Statistical Methods in Software Engineering*, Springer: New York, 1999.
19. N. Torrado, M.P. Wiper and R.E. Lillo. Software reliability modeling with software metrics data via Gaussian processes, *IEEE Transactions on Software Engineering*, 39, 8, 1179–1186, 2013.
20. M.P. Wiper. Software reliability: Bayesian analysis, in F. Ruggeri, R. Kennet and W. Faltin (editors) Encyclopedia of Statistics in Quality and Reliability. Wiley, New York, 2007.
21. S. Yamada and S. Osaki, Software Reliability Growth Modeling: Models and Applications, *IEEE Trans. Software Engineering*, 11, 1431–1437, 1985.

Entropy Measures and the Generalized Fisher's Information

Thomas L. Toulias[1] and Christos P. Kitsos[1]

Department of Informatics, Technological Educational Institute of Athens
12243 Egaleo, Athens, Greece
(E-mail: {t.toulias, xkitsos}@teiath.gr)

Abstract. This paper investigates the generalized Fisher's entropy type information measure with respect to the multivariate γ–order Normal distribution and certain boundaries are obtained. Also the Rényi and Shannon entropies are evaluated and discussed.

Keywords: Fisher's entropy type information measure, γ–order Normal distribution, Rényi entropy.

1 Introduction

In principle, the information measures are divided to three main categories: parametric (typical example Fisher's information), non parametric (with Shannon information measure to be the most well known) and entropy type, see Cover and Thomas [1], which are adopted at this paper. The introduced new entropy type measure of information $J_\alpha(X)$ is a function of the density f_X of the p-variate random variable X, see Kitsos and Tavoularis [2], defined as

$$J_\alpha(X) := E\left(\|\nabla \log f(X)\|^\alpha\right) = \int_{\mathbb{R}^p} f(x)\,\|\nabla \log f_X(x)\|^a\,dx. \tag{1}$$

Notice that, $J_2 = J$, with J being the known Fisher's entropy type information measure.

Moreover, the known entropy power $N(X)$, defined through Shannon entropy $H(X)$, has been extended to

$$N_\alpha(X) = \nu_\alpha \exp\{\tfrac{\alpha}{p}H(X)\}, \tag{2}$$

with

$$\nu_\alpha = (\tfrac{\alpha-1}{e})\pi^{-\alpha/2}\left[\frac{\Gamma(\tfrac{p}{2}+1)}{\Gamma(p\tfrac{\alpha-1}{\alpha}+1)}\right]^{\tfrac{\alpha}{p}},\ \alpha > 1,$$

see Kitsos and Tavoularis [2] for details. Notice that, $\nu_2 = (2\pi e)^{-1}$ and $\mathbf{N}_2 = \mathbf{N}$, where N the known Shannon entropy power for the normal distribution.

Moreover, it can be proved that

$$J_\alpha(X)N_\alpha(X) \geq p, \tag{3}$$

which extends the well known result with $\alpha = 2$, see Kitsos and Tavoularis [2].

The so called Information Inequality, is generalized due to the introduced information measures, Kitsos and Tavoularis [2]. The Generalized Information Inequality (GII) is given by

$$\left[\frac{2\pi e}{p}\mathrm{Var}(X)\right]^{1/2} \left[\frac{1}{p}\nu_\alpha J_\alpha(X)\right]^{1/\alpha} \geq 1.$$

When $\alpha = 2$ we have $\mathrm{Var}(X)J_2(X) \geq p$, and therefore, the Cramer–Rao inequality (Cover and Thomas [1], Th. 11.10.1) holds. The lower boundary B_α^p for the introduced generalized information $J_\alpha(X)$ is

$$J_\alpha(X) \geq B_\alpha^p := \frac{p}{\nu_\alpha}\left[\frac{2\pi e}{p}\mathrm{Var}(X)\right]^{-\alpha/2}. \tag{4}$$

In Fig. 1 the lower boundaries B_α^p across α are depicted, assuming $\mathrm{Var}(X) = 1$ and for all dimensions p. Moreover, Fig. 2 depicts the boundaries B_α^1 across $\mathrm{Var}(X)$ and for parameter values $\alpha = 1, 2, \ldots, 100$.
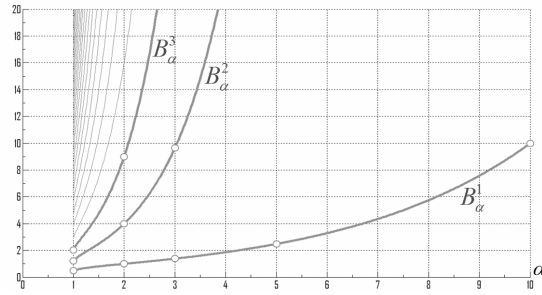
Fig. 1. Graphs of the boundaries B_α^p across α, with fixed $\mathrm{Var}\,X = 1$ for every dimension $p \geq 1$.

Let H denote the Shannon (differential) entropy of a r.v. X with p.d.f. f_X, i.e.

$$H(X) := \int_{\mathbb{R}^p} f_X(x) \log f(x)dx. \tag{5}$$

For any multivariate random variable X with zero mean and covariance matrix Σ, it holds

$$H(X) \leq \tfrac{1}{2}\log\{(2\pi e)^p\,|\det \Sigma|\}, \tag{6}$$

while the equality in (6) holds if and only if X is a normally distributed variable, i.e $X \sim N^p(\mu, \Sigma)$, see Cover and Thomas [1]. Moreover, the Normal distribution, according to Information Measures Theory, is adopted for the noise, acting additively to the input variable when an input–output time discrete channel is formed.
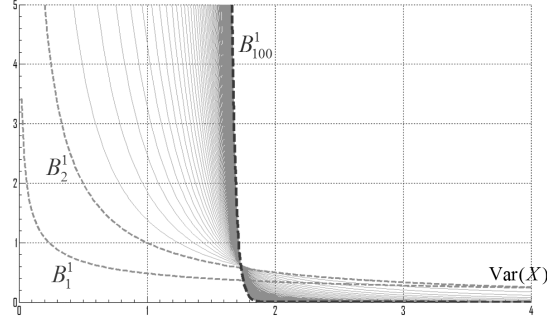
Fig. 2. Graphs of the boundaries B_α^p across $\mathrm{Var}\,X$ for parameters $\alpha = 1, 2, \dots, 100$.

Kitsos and Tavoularis in ([2] and [3]) introduced and studied the multivariate (and elliptically contoured) γ–ordered Normal distribution, i.e. $\mathcal{N}_\gamma^p(\mu, \Sigma)$, see also Kitsos and Toulias [4] and Kitsos *et al.* [5] for further reading. Recall the definition of $\mathcal{N}_\gamma$:

Definition 1. The p–dimensional random variable X follows the γ–order Normal, $\mathcal{N}_\gamma^p(\mu, \Sigma)$ with mean vector $\mu \in \mathbb{R}^p$ and positive definite scale matrix $\Sigma \in \mathbb{R}^{p \times p}$, when the density function, f_X, is of the form

$$f_X(x;\ \mu, \Sigma) = C_\gamma^p |\det \Sigma|^{-1/2} \, \exp\left\{ -\tfrac{\gamma-1}{\gamma} Q(x)^{\frac{\gamma}{2(\gamma-1)}} \right\}, \quad x \in \mathbb{R}^p, \qquad (7)$$

with Q the quadratic form $Q(x) = (x-\mu)\Sigma^{-1}(x-\mu)^{\mathrm{T}}$, $x \in \mathbb{R}^p$. We shall write $X \sim \mathcal{N}_\gamma^p(\mu, \Sigma)$. The normality factor C_γ^p is defined as

$$C_\gamma^p = \pi^{-p/2} \frac{\Gamma\left(\frac{p}{2}+1\right)}{\Gamma(p\frac{\gamma-1}{\gamma}+1)} \left(\tfrac{\gamma-1}{\gamma}\right)^{p\frac{\gamma-1}{\gamma}}. \qquad (8)$$

Notice that, for $\gamma = 2$, $\mathcal{N}_2^p(\mu, \Sigma)$ is the well known multivariate normal distribution. Moreover, the function $\phi(\alpha) = f_\alpha(\mu, \Sigma)^{1/\alpha}$ with $\Sigma = (\sigma^2/\alpha)^{2(\alpha-1)/\alpha}\mathbb{I}_p$, corresponds to extremal function for an inequality extending LSI due to Del Pino *et al.* [6]. The essential result is that the defined γ-ordered Normal distribution works as an extremal function to a generalized form of the Logarithmic Sobolev Inequality.

The family of $\mathcal{N}_\gamma^p(\mu, \Sigma)$, i.e. the family of the elliptically contoured γ–ordered Normals, provides a smooth bridging between the multivariate (and elliptically countered) Uniform, Normal and Laplace r.v. U, N and L, i.e. between $U \sim \mathcal{U}^p(\mu, \Sigma)$, $Z \sim \mathcal{N}^p(\mu, \Sigma)$, and $L \sim \mathcal{L}^p(\mu, \Sigma)$ respectively, with density functions

$$f_U(x;\ \mu, \Sigma) = \begin{cases} \frac{\Gamma(\frac{p}{2}+1)}{\pi^{p/2}\sqrt{|\det \Sigma|}}, & x \in \mathbb{R}^p, \text{ with } Q(x) \leq 1, \\ 0, & x \in \mathbb{R}^p, \text{ with } Q(x) > 1, \end{cases} \qquad (9)$$

$$f_Z(x;\ \mu, \Sigma) = \frac{1}{(2\pi)^{p/2}\sqrt{|\det \Sigma|}} \exp\left\{ -\tfrac{1}{2}Q(x) \right\}, \quad x \in \mathbb{R}^p, \qquad (10)$$

$$f_L(x;\ \mu, \Sigma) = \frac{\Gamma(\frac{p}{2}+1)}{p!\pi^{p/2}\sqrt{|\det \Sigma|}} \exp\left\{-\sqrt{Q(x)}\right\}, \quad x \in \mathbb{R}^p, \qquad (11)$$

respectively. That is, the $\mathcal{N}_\gamma^p$ family of distributions, not only generalizes the Normal one but also two other very significant distributions, as the Uniform and Laplace distributions, are induced. Indeed:

Theorem 1. *The multivariate γ-ordered Normal distribution, $\mathcal{N}_\gamma^p(\mu, \Sigma)$, for order values of $\gamma = 0, 1, 2, \pm\infty$ coincides with*

$$\mathcal{N}_\gamma^p(\mu, \Sigma) = \begin{cases} \mathcal{D}^p(\mu), & \gamma = 0 \ \ and \ \ p = 1, 2, \\ 0, & \gamma = 0 \ \ and \ \ p \geq 3, \\ \mathcal{U}^p(\mu, \Sigma), & \gamma = 1, \\ \mathcal{N}^p(\mu, \Sigma), & \gamma = 2, \\ \mathcal{L}^p(\mu, \Sigma), & \gamma = \pm\infty. \end{cases} \qquad (12)$$

2 Entropy and Information Measures

Besides the generalized entropy power N_α, another significant entropy measure that generalizes the Shannon entropy is the Rényi entropy. For a p–variate continues random variable with p.d.f. f_X, the Rényi entropy $R_\alpha(X)$ is defined, through the α–norm of $f_X \in \mathscr{L}^\alpha(\mathbb{R}^p)$, by

$$R_\alpha(X) := -\frac{\alpha}{\alpha-1} \log \|f_X\|_\alpha = \frac{1}{1-\alpha} \log \int_{\mathbb{R}^p} |f_X(x)|^\alpha dx, \quad \alpha > 0, \ \alpha \neq 1. \quad (13)$$

For the limiting case of $\alpha \to 1$ the Rényi entropy converges to the usual Shannon entropy $H(X)$ as in (5). Notice that we use the minus sign for R_α to be in accordance with the definition of (5).

Considering now a r.v. from the γ–GND family, the following holds.

Theorem 2. *For the p–variate, spherically contoured γ–order normally distributed $X_\gamma \sim \mathcal{N}_\gamma^p(\mu, \sigma^2 \mathbb{I}_p)$, the Rényi entropy of X_γ is given by*

$$R_\alpha(X_\gamma) = p\frac{\gamma-1}{\gamma(\alpha-1)} \log \alpha - \log(C_\gamma^p \sigma^{-p}). \qquad (14)$$

Proof. Consider the p.d.f. f_{X_γ} as in (7). From the definition (13) it is

$$R_\alpha(X_\gamma) = \frac{\alpha}{1-\alpha} \log(C_\gamma^p \sigma^{-p}) + \frac{1}{1-\alpha} \log \int_{\mathbb{R}^p} \exp\left\{-\frac{\alpha(\gamma-1)}{\gamma} \|\frac{x-\mu}{\sigma}\|^{\frac{\gamma}{\gamma-1}}\right\} dx,$$

and applying the linear transformation $z = (x - \mu)\sigma^{-1}$ with $dz = d\{(x - \mu)/\sigma\} = \sigma^{-p}dx$, the R_α above is reduced to

$$R_\alpha(X_\gamma) = \frac{\alpha}{1-\alpha} \log\left(C_\gamma^p \sigma^{-p}\right) + \frac{1}{1-\alpha} \log \left(\sigma^p \int_{\mathbb{R}^p} \exp\left\{-\frac{\alpha(\gamma-1)}{\gamma} \|z\|^{\frac{\gamma}{\gamma-1}}\right\} dz\right)$$

$$= \frac{\alpha}{1-\alpha} \log(C_\gamma^p \sigma^{p\frac{1-\alpha}{\alpha}}) + \frac{1}{1-\alpha} \log \int_{\mathbb{R}^p} \exp\left\{-\frac{\alpha(\gamma-1)}{\gamma} \|z\|^{\frac{\gamma}{\gamma-1}}\right\} dz.$$

Switching to hyperspherical coordinates, we get

$$R_\alpha(X_\gamma) = \tfrac{\alpha}{1-\alpha} \log K(\sigma) + \tfrac{1}{1-\alpha} \log \int_{\mathbb{R}_+} \exp\left\{ -\tfrac{\alpha(\gamma-1)}{\gamma} \rho^{\frac{\gamma}{\gamma-1}} \right\} \rho^{p-1} d\rho,$$

where $K(\sigma) = C_\gamma^p \sigma^{p(1-\alpha)/\alpha} \omega_{p-1}^{1/\alpha}$ with $\omega_{p-1} = 2\pi^{p/2}/\Gamma(p/2)$ denoting the volume of the $(p-1)$–sphere. Transforming $du := d(\tfrac{\gamma-1}{\gamma}\rho^{\gamma/(\gamma-1)}) = \rho^{1/(\gamma-1)} d\rho$ we obtain successively

$$
\begin{aligned}
R_\alpha(X_\gamma) &= \tfrac{\alpha}{1-\alpha} \log K(\sigma) + \tfrac{1}{1-\alpha} \log \int_{\mathbb{R}_+} e^{-\alpha u} \rho^{\frac{(p-1)(\gamma-1)-1}{\gamma-1}} du \\
&= \tfrac{\alpha}{\alpha-1} \log K(\sigma) + \tfrac{1}{1-\alpha} \log \int_{\mathbb{R}_+} e^{-\alpha u} \left(\rho^{\frac{\gamma}{\gamma-1}}\right)^{\frac{(p-1)(\gamma-1)-1}{\gamma}} du \\
&= \tfrac{\alpha}{1-\alpha} \log K(\sigma) + \tfrac{1}{1-\alpha} \log(\tfrac{\gamma}{\gamma-1})^{p\frac{\gamma-1}{\gamma}-1} + \tfrac{1}{1-\alpha} \log \int_{\mathbb{R}_+} e^{-\alpha u} u^{p\frac{\gamma-1}{\gamma}-1} du \\
&= \tfrac{\alpha}{1-\alpha} \log K(\sigma) + \tfrac{1}{1-\alpha} \log(\tfrac{\gamma}{\gamma-1})^{p\frac{\gamma-1}{\gamma}-1} - p\tfrac{\gamma-1}{\gamma} \cdot \tfrac{\log \alpha}{1-\alpha} + \tfrac{1}{1-\alpha} \log \Gamma(p\tfrac{\gamma-1}{\gamma}).
\end{aligned}
$$

Finally, by substitution of the expressions for $K(\sigma)$, ω_{p-1} and the normalizing factor C_γ^p, we obtain

$$R_\alpha(X_\gamma) = p \log \sigma - \tfrac{\alpha}{1-\alpha} \log C_\gamma^p + \tfrac{1}{1-\alpha} \log C_\gamma^p + p\tfrac{\gamma-1}{\gamma} \cdot \tfrac{\log \alpha}{\alpha-1},$$

and hence (14) holds true.

Corollary 1. *For the special cases of $\alpha = 0, 1, 2, +\infty$ Rényi entropy of $X_\gamma \sim \mathcal{N}_\gamma(\mu, \Sigma)$ reduces to*

$$R_\alpha(X_\gamma) = \begin{cases} +\infty, & \alpha = 0, & (\textit{Hartley entropy}) \\ p\frac{\gamma-1}{\gamma} - \log(C_\gamma^p/\sigma^p), & \alpha = 1, & (\textit{Shannon entropy}) \\ p\frac{\gamma-1}{\gamma} \log 2 - \log(C_\gamma^p/\sigma^p), & \alpha = 2, & (\textit{collision entropy}) \\ -\log(C_\gamma^p/\sigma^p), & \alpha = +\infty. & (\textit{min–entropy}) \end{cases}$$

Rényi entropy $R_\alpha(X_\gamma)$, as in (14), is an decreasing function of parameter α, and hence

$$R_{+\infty}(X_\gamma) < R_2(X_\gamma) < R_1(X_\gamma) < R_0(X_\gamma).$$

Example 1. For the multivariate and spherically contoured Uniform random variable $U \sim \mathcal{U}(\mu, \sigma^2 \mathbb{I}_p)$, the Hartley, Shannon, collision and the min– entropies coincide as,

$$R_\alpha(U) = \log \frac{\pi^{p/2}\sigma^p}{\Gamma(\frac{p}{2}+1)}, \quad \alpha \in \mathbb{R}_+,$$

while for the univariate case of $U \sim \mathcal{U}(\mu - \sigma, \mu - \sigma)$ we are reduced to

$$R_\alpha(U) = \log(2\sigma), \quad \alpha \in \mathbb{R}_+.$$

Notice that for a uniformly distributed r.v. the Rényi entropy R_α is α–invariant, depending only on the dimension $p \in \mathbb{N}$ and the scale parameter σ.

Example 2. For the multivariate and elliptically contoured Laplace random variable $L \sim \mathcal{L}(\mu, \sigma^2 \mathbb{I}_p)$, the Hartley, Shannon, collision and the min– entropies are given by,

$$R_\alpha(L) = \begin{cases} +\infty, & \alpha = 0, \quad \text{(Hartley entropy)} \\ p + \log\{p! \pi^{p/2} \sigma^p \, \Gamma(\tfrac{p}{2}+1)^{-1}\}, & \alpha = 1, \quad \text{(Shannon entropy)} \\ \log\{2^p p! \pi^{p/2} \sigma^p \, \Gamma(\tfrac{p}{2}+1)^{-1}\}, & \alpha = 2, \quad \text{(collision entropy)} \\ \log\{p! \pi^{p/2} \sigma^p \, \Gamma(\tfrac{p}{2}+1)^{-1}\}, & \alpha = +\infty. \quad \text{(min–entropy)} \end{cases}$$

Example 3. According to the classification Theorem 1 and Corollary 1, we can evaluate the usual Shannon entropy for the multivariate (and spherically contoured) Uniform, Normal and Laplace distributions with $\Sigma = \sigma^2 \mathbb{I}_p$, i.e.

$$H(X) = \begin{cases} \log \frac{\pi^{p/2}}{\Gamma(\frac{p}{2}+1)} \sqrt{|\det \Sigma|}, & \text{for } X \sim \mathcal{N}_1^p(\mu, \Sigma) = \mathcal{U}^p(\mu, \Sigma), \\ \frac{1}{2} \log\{(2\pi e)^p \, |\det \Sigma|\}, & \text{for } X \sim \mathcal{N}_2^p(\mu, \Sigma) = \mathcal{N}^p(\mu, \Sigma), \\ p + \log \frac{p! \pi^{p/2}}{\Gamma(\frac{p}{2}+1)} \sqrt{|\det \Sigma|}, & \text{for } X \sim \mathcal{N}_{\pm\infty}^p(\mu, \Sigma) = \mathcal{L}^p(\mu, \Sigma), \end{cases}$$

see also (6) for the Normal case, while for the univariate case $p = 1$, we are reduced to

$$H(X) = \begin{cases} \log 2\sigma, & \text{for } X \sim \mathcal{N}_1^1(\mu, \sigma^2) = \mathcal{U}^1(\mu, \sigma^2) = \mathcal{U}(\mu - \sigma, \mu - \sigma), \\ \log \sqrt{2\pi e}\sigma, & \text{for } X \sim \mathcal{N}_2^1(\mu, \sigma^2) = \mathcal{N}(\mu, \sigma^2), \\ 1 + \log 2\sigma, & \text{for } X \sim \mathcal{N}_{\pm\infty}^1(\mu, \sigma^2) = \mathcal{L}^1(\mu, \sigma^2) = \mathcal{L}(\mu, \sigma). \end{cases}$$

where $\mathcal{U}(\mu - \sigma, \mu - \sigma)$, $\mathcal{N}(\mu, \sigma^2)$ and $\mathcal{L}(\mu, \sigma)$ are the usual notations for the univariate Uniform, Normal and Laplace distributions respectively.

Now, we shall evaluate the generalized Fisher's entropy type information of a random variable following the multivariate γ-order Normal, $\mathcal{N}_\gamma^p$.

Theorem 3. *The generalized Fisher's information J_α of a r.v. $X_\gamma \sim \mathcal{N}_\gamma^p(\mu, \lambda\Sigma^*)$ where $\lambda \in \mathbb{R}_+ \setminus 0$ and Σ^* is a real matrix with unit orthogonal vectors, i.e. $\Sigma^* \in \mathbb{R}_\perp^{p\times p}$, is given by*

$$J_\alpha(X_\gamma) = \left(\tfrac{\gamma}{\gamma-1}\right)^{\frac{\alpha}{\gamma}} \frac{\Gamma\left(\frac{\alpha + p(\gamma-1)}{\gamma}\right)}{\lambda^{\alpha/2} \, \Gamma\left(p\frac{\gamma-1}{\gamma}\right)}. \tag{15}$$

Proof. From (1) we have

$$J_\alpha(X_\gamma) = \alpha^\alpha \int_{\mathbb{R}^p} \left\| \nabla f_{X_\gamma}^{1/\alpha}(x) \right\|^\alpha dx,$$

758

while from the definition of the density function f_{X_γ}, in (7), we have

$$\mathrm{J}_\alpha(X_\gamma) = \alpha^\alpha C_\gamma^p \int_{\mathbb{R}^p} \left\| \nabla \exp\left\{-\tfrac{\gamma-1}{\alpha\gamma} Q(x)^{\frac{\gamma}{2(\gamma-1)}}\right\} \right\|^\alpha dx$$

$$= \alpha^\alpha (\tfrac{\gamma-1}{\alpha\gamma})^\alpha C_\gamma^p \int_{\mathbb{R}^p} \exp\left\{-\tfrac{\gamma-1}{\gamma} Q^{\frac{\gamma}{2(\gamma-1)}}(x)\right\} \left\| \nabla Q^{\frac{\gamma}{2(\gamma-1)}}(x) \right\|^\alpha dx. \tag{16}$$

For the gradient of the quadratic form $Q(x)$ we have $\nabla Q(x) = \lambda^{-1}\nabla\{(x - \mu)\Sigma^{*-1}(x - \mu)^{\mathrm{T}}\} = 2\lambda^{-1}\Sigma^{*-1}(x - \mu)^{\mathrm{T}}$, while from the fact that Σ^* is an orthogonal matrix we have $\|\Sigma^{*-1}(x - \mu)^{\mathrm{T}}\| = \|x - \mu\|$. Therefore, (16) can be written as

$$\mathrm{J}_\alpha(X_\gamma) = \lambda^{-\alpha} C_\gamma^p \int_{\mathbb{R}^p} \exp\left\{-\tfrac{\gamma-1}{\gamma} Q^{\frac{\gamma}{2(\gamma-1)}}(x)\right\} Q^{\frac{\alpha\gamma}{2(\gamma-1)}-\alpha}(x) \|x - \mu\|^\alpha dx.$$

Applying the linear transformation $z = (x - \mu)(\lambda\Sigma^*)^{-1/2}$ in the above integral, it is $dx = d(x - \mu) = \sqrt{\lambda^p |\det \Sigma^*|} dz = \lambda^{p/2} dz$, the quadratic form Q is reduced to

$$Q(x) = (x-\mu)(\lambda\Sigma)^{*-1}(x-\mu)^{\mathrm{T}} = (x-\mu)(\lambda\Sigma^*)^{-1/2}[(x-\mu)(\lambda\Sigma^*)^{-1/2}]^{\mathrm{T}} = \|z\|^2,$$

and thus,

$$\mathrm{J}_\alpha(X_\gamma) = \lambda^{(p-\alpha)/2} C_\gamma^p \int_{\mathbb{R}^p} \|z\|^{\frac{\alpha}{\gamma-1}} \exp\left\{-\tfrac{\gamma-1}{\gamma}\|z\|^{\frac{\gamma}{\gamma-1}}\right\} dz.$$

Switching to hyperspherical coordinates, we get

$$\mathrm{J}_\alpha(X_\gamma) = \lambda^{(p-\alpha)/2} C_\gamma^p \omega_{p-1} \int_0^{+\infty} \rho^{\frac{\alpha}{\gamma-1}} \exp\left\{-\tfrac{\gamma-1}{\gamma}\rho^{\frac{\gamma}{\gamma-1}}\right\} \rho^{p-1} d\rho,$$

where $\omega_{p-1} = \frac{2\pi^{p/2}}{\Gamma(p/2)}$ is the volume of the $(p-1)$–sphere, $\mathbb{S}_{p-1}$, and hence

$$\mathrm{J}_\alpha(X_\gamma) = 2\frac{\pi^{p/2}}{\Gamma(\frac{\pi}{2})} \lambda^{(p-\alpha)/2} C_\gamma^p \int_0^{+\infty} \rho^{\frac{\alpha+(p-1)(\gamma-1)}{\gamma-1}} \exp\left\{-\tfrac{\gamma-1}{\gamma}\rho^{\frac{\gamma}{\gamma-1}}\right\} d\rho.$$

From the fact that $d(\frac{\gamma-1}{\gamma}\rho^{\frac{\gamma}{\gamma-1}}) = \rho^{\frac{1}{\gamma-1}}d\rho$ and the definition of the gamma function, we obtain successively

$$
\begin{aligned}
\mathrm{J}_\alpha(X_\gamma) &= 2\frac{\pi^{p/2}}{\Gamma(\frac{\pi}{2})}\lambda^{(p-\alpha)/2}C_\gamma^p \int_0^{+\infty} \rho^{\frac{\alpha+(p-1)(\gamma-1)}{\gamma-1}-\frac{1}{\gamma-1}} \exp\left\{-\frac{\gamma-1}{\gamma}\rho^{\frac{\gamma}{\gamma-1}}\right\} d(\frac{\gamma-1}{\gamma}\rho^{\frac{\gamma}{\gamma-1}}) \\
&= 2\frac{\pi^{p/2}}{\Gamma(\frac{\pi}{2})}\lambda^{(p-\alpha)/2}C_\gamma^p \int_0^{+\infty} \rho^{\frac{\alpha+p\gamma-\gamma-p}{\gamma-1}} \exp\left\{-\frac{\gamma-1}{\gamma}\rho^{\frac{\gamma}{\gamma-1}}\right\} d(\frac{\gamma-1}{\gamma}\rho^{\frac{\gamma}{\gamma-1}}) \\
&= 2\frac{\pi^{p/2}}{\Gamma(\frac{\pi}{2})}\lambda^{(p-\alpha)/2}(\frac{\gamma}{\gamma-1})^{\frac{\alpha-\gamma+p(\gamma-1)}{\gamma}} C_\gamma^p \times \\
&\quad \int_0^{+\infty} (\frac{\gamma-1}{\gamma}\rho^{\frac{\gamma}{\gamma-1}})^{\frac{\alpha-\gamma+p(\gamma-1)}{\gamma}} \exp\left\{-\frac{\gamma-1}{\gamma}\rho^{\frac{\gamma}{\gamma-1}}\right\} d(\frac{\gamma-1}{\gamma}\rho^{\frac{\gamma}{\gamma-1}}) \\
&= 2\frac{\pi^{p/2}}{\Gamma(\frac{\pi}{2})}\lambda^{(p-\alpha)/2}(\frac{\gamma}{\gamma-1})^{\frac{\alpha-\gamma+p(\gamma-1)}{\gamma}} C_\gamma^p \Gamma(\frac{\alpha+p(\gamma-1)}{\gamma}),
\end{aligned}
$$

and, finally, applying the normalizing factor C_γ^p as in (8), we derive (15) and the Theorem has been proved.

For the defined generalized Fisher's information measure and the γ–ordered Normal, it is clear that the values of $\mathrm{J}_\alpha(X_\gamma)$ depends on the two parameters α and γ. Therefore, we shall investigate under what values of α and γ there are bounds for $\mathrm{J}_\alpha(X_\gamma)$.

In the following Proposition we provide some inequalities for the generalized Fisher's entropy type information measure J_α for the family of the γ–order Normal distributions with positive order γ, i.e. for $\mathrm{J}_\alpha(X_\gamma)$ where $X_\gamma \sim \mathcal{N}_\gamma^p(\mu, \sigma^2\mathbb{I}_p)$, considering parameters $\alpha > 1$ and $\gamma > 2$.

Proposition 1. *The generalized Fisher's information measure J_α of a random variable X_γ following the multivariate and spherically contoured γ–order Normal distribution, i.e. $X_\gamma \sim \mathcal{N}_\gamma^p(\mu, \sigma^2\mathbb{I}_p)$, $\alpha, \gamma \geq 2$, satisfy the inequalities*

$$
\mathrm{J}_\alpha(X_\gamma) \begin{cases} > p\sigma^{-\alpha}, \text{ for } \alpha > \gamma, \\ = p\sigma^{-\alpha}, \text{ for } \alpha = \gamma, \\ < p\sigma^{-\alpha}, \text{ for } \alpha < \gamma. \end{cases} \tag{17}
$$

Proof. For the spherically contoured r.v. $X_\gamma \sim \mathcal{N}_\gamma^p(\mu, \sigma^2\mathbb{I}_p)$ we are reduced to (15) where $\lambda = \sigma^2$. Thus, for the proof the first branch of (17) we assume $\alpha > \gamma$, i.e. $\frac{\alpha}{\gamma} > 1$. Then, we have $\frac{\alpha+p(\gamma-1)}{\gamma} > 1 + p\frac{\gamma-1}{\gamma}$. This implies,

$$
\Gamma(\frac{\alpha+p(\gamma-1)}{\gamma}) > \Gamma(1 + p\frac{\gamma-1}{\gamma}) = p\frac{\gamma-1}{\gamma}\Gamma(p\frac{\gamma-1}{\gamma}), \tag{18}
$$

if $1 + p\frac{\gamma-1}{\gamma} \geq \Gamma_0$, where $\Gamma_0 \approx 1.4628$ denotes the point of minimum for the positive gamma function, $\Gamma(x)$, $x > 0$. That is, if the inequality $x = 1 + p\frac{\gamma-1}{\gamma} \geq \Gamma_0$ holds, then $\Gamma(x) \geq \Gamma(\Gamma_0)$, as the gamma function is an increasing function

for $x \geq \Gamma_0$. Inequality, $1 + p\frac{\gamma-1}{\gamma} \geq \Gamma_0$, is equivalent to, $\gamma \geq \frac{p}{p+1-\Gamma_0} \approx \frac{p}{p-0.4628} > 1$, which is true as $\gamma \geq 2$ in our assumption for the values of parameter γ. Thus, (18) holds indeed, for orders $\gamma \geq \frac{p}{p+1-\Gamma_0}$, and so,

$$\frac{\Gamma(\frac{\alpha+p(\gamma-1)}{\gamma})}{\Gamma(p\frac{\gamma-1}{\gamma})} > p\frac{\gamma-1}{\gamma}. \tag{19}$$

Our assumption, $\frac{\alpha}{\gamma} > 1$, together with the fact that, $\frac{\gamma}{\gamma-1} > 1$ for all defined orders $\gamma \in \mathbb{R}\backslash[0, 1]$, leads us to $(\frac{\gamma}{\gamma-1})^{\alpha/\gamma} > \frac{\gamma}{\gamma-1}$. Then, inequality (19) provides

$$\left(\frac{\gamma}{\gamma-1}\right)^{\frac{\alpha}{\gamma}} \frac{\Gamma(\frac{\alpha+p(\gamma-1)}{\gamma})}{\Gamma(p\frac{\gamma-1}{\gamma})} > \frac{\gamma}{\gamma-1}p\frac{\gamma-1}{\gamma} = p,$$

and, using (15), we derive that, $J_\alpha(X_\gamma) > p\sqrt{|\det \Sigma|}$ for $\alpha > \gamma$, i.e. the first branch of (17) holds. Similarly the other two branches also hold.

Corollary 2. *The generalized Fisher's information J_α of a spherically contoured r.v. $X_\gamma \sim \mathcal{N}_\gamma^p(\mu, \sigma^2\mathbb{I}_p)$, with $\alpha/\gamma \in \mathbb{N}^*$, is reduced to*

$$J_\alpha(X_\gamma) = \sigma^{-\alpha}(\gamma - 1)^{-\alpha\gamma} \prod_{k=1}^{\alpha/\gamma} \{\alpha - p + (p - k)\gamma\}.$$

The following Fig. 3 depicts the generalized Fisher's information J_α of the bi–variate (and spherically contoured) γ–order normally distributed random variables $X_\gamma \sim \mathcal{N}_\gamma^2(\mu, \mathbb{I}_2)$ across the parameter $\alpha > 1$, and for various shape parameters $\gamma = 1, 1.1, \ldots, 1.9, 2, 3, \ldots, 10$. The usual Normal distribution case of $\gamma = 2$ is also highlighted.
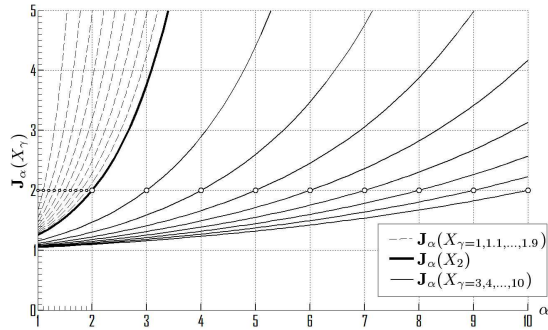
Fig. 3. Graphs of $J_\alpha(X_\gamma)$ across parameter $\alpha > 1$, with $X_\gamma \sim \mathcal{N}_\gamma^2(\mu, \mathbb{I}_2)$, and for various γ values.

3   Discussion

In this paper we considered the generalized form of the multivariate normal distribution, namely the γ–order Normal distribution, $\mathcal{N}_\gamma^p$. This generalization is obtained as an extremal of the LSI corresponding a power–generalization of the entropy type Fisher's information J_α. This generalized entropy type information measure, which extends the known entropy type Fisher's information, is discussed and evaluated for the γ–order normally distributed random variable, say X_γ.

Moreover, the corresponding Rényi and Shannon entropy were evaluated for X_γ, including the specific cases of the multivariate (and elliptically contoured) Uniform, Normal and Laplace distributions, resulting from $\mathcal{N}_\gamma^p$. Finally, certain boundaries of the J_α were obtained for the spherically contoured $\mathcal{N}_\gamma^p$ family of distributions.

References

1. T.M. Cover and J.A. Thomas. *Elements of Information Theory*, 2nd Ed., Wiley, 2006.
2. C.P. Kitsos and N.K. Tavoularis. Logarithmic Sobolev inequalities for information measures, *IEEE Trans. Inform. Theory*, 55, 6, 2554–2561, 2009.
3. C.P. Kitsos and N.K. Tavoularis. New entropy type information measures, in *Information Technology Interfaces*, V. Luzar–Stiffer, Z. Jarec and Z. Bekic (Eds), 255–259, 2009.
4. C.P. Kitsos and T.L. Toulias. New information measures for the generalized normal distribution, *Information*, 1, 13–27, 2010.
5. C.P. Kitsos, T.L. Toulias and P.C. Trandafir On the multivariate γ–ordered normal distribution, *Far East J. of Theoretical Statistics*, 38, 1, 49–73, 2012.
6. M. Del Pino, J. Dolbeault and I. Gentil. Nonlinear diffusions, hypercontractivity and the optimal L^p–Euclidean logarithmic Sobolev inequality, *J. Math. Anal. Appl.*, 293, 2, 375–388, 2004.

Branching Processes: Forecasting Human Population

Plamen I. Trayanov[1] and Maroussia Slavtchova-Bojkova[2]

[1] Faculty of Mathematics and Informatics, Sofia University
Sofia, Bulgaria
(e-mail: plamentrayanov@gmail.com)
[2] Faculty of Mathematics and Informatics, Sofia University,
Institute of Mathematics and Informatics, Bulgarian Academy of Sciences
Sofia, Bulgaria
(e-mail: bojkova@fmi.uni-sofia.bg)

Abstract. In this work we present a new technique using the Crump-Mode-Jagers branching process theory to model human population. We are addressing questions like: How the population grows according to given scenarios and how these results could be used in decision making to choose an appropriate demographic policy. Nowadays, such issues are especially important in view of the tasks before the knowledge-based society. Our aim is to estimate the growth of young population and the pensioners count and to forecast the development of the population structure in time.

Keywords: General Branching Process, Malthusian parameter, demography, population projections.

1   Introduction

Studying the population and forecasting its development and age structure is important for governments. It allows them to make an efficient policy so the negative developments are slowed down. It is important not only to make a policy to target the maximization of the total population count but to target the specific age groups that are important for the economy and the country as a whole. For example the study shows the working force in Bulgaria is diminishing, the number of young people finishing school and possibly going to universities is decreasing, which affects not only universities but businesses too. Less qualified specialists means some companies may struggle finding enough specialists in future and the less qualified work is less paid so the GDP of the country is affected. As a consequence the ability of the government to issue debt is more limited and more costly. This is an example that demographic problems are something that affects many aspects of life in the country. Most demographic problems however take much time to be solved so the social policy and demographic strategy must be lingering and long term.

The empirical results are derived using General Branching Process Theory. We choose the General Branching Process (GBP) as a model because of its generality and flexibility (see Jagers [7]). Modelling human population however requires some additional tools presented in Trayanov [16] and Trayanov and Slavtchova-Bojkova [17]. These models however are developed for a population

of women only so in this article we show how we can adjust them to include the population of men. In Section 1 we present a brief description of the proposed mathematical model of human population. In Section 2 we discuss the data we need and the available data. Then in Section 3 we present the empirical results and their implication for the population of Bulgaria.

2   Mathematical model

A branching process is a model describing particles or individuals who live and die according to some probabilistic laws and give birth to one or more individuals in different moments of time according to probabilistic laws (see Slavtchova-Bojkova and Yanev [14] and Jagers [7]). The General Branching Process (GBP) gives the most flexible and close to reality stochastic model for a population and is general enough to incorporate the complex stochastic processes of birth and death. Women in this model can give birth to different number of children and in different moments of time. In addition the life length of women and men are modelled by random variables. This generality of the model is the reason the theory of Branching processes is a natural candidate for modelling human population.

In this section we present a brief description of the theory behind our model. First we define a GBP starting from a woman aged 0 at time 0. If x is an individual, we denote λ_x to be his/her life length and ξ_x to be her point process describing her the births in time. A point process is a random measure that represents the number of children born to a woman in a particular interval. The number of children born in interval $[a, b]$ is denoted by $\xi([a, b])$. An accurate mathematical definition of point process can be found in Jagers [7] and Feller [4]. We denote $\xi_x(t) = \xi([0, t])$ and $\mu_x(t) = \mathbb{E}\xi_x(t)$ which is the expected number of children that woman x gives birth to till age t.

Let $f(s) = \mathbb{E}(s^{\xi(\infty)})$, $|s| \leq 1$, $L(t) = \mathbb{P}(\lambda_x \leq t)$ and $\hat{\mu}$ is the Laplace-Stieltjes transformation of μ and $S(t) = 1 - L(t)$. We denote z_t^a to be the number of people at time t on age less then a. The stochastic process z_t^a is called General Branching Process. A key mathematical result is that we can actually compute the expected number of individuals at time t on age less than a with the following theorem.

Theorem 1. *(see Jagers [7]) If $f(s) < \infty, |s| \leq 1$, then $m_t = \mathbb{E}(z_t) < \infty, \forall t$ and $m_t^a = \mathbb{E}(z_t^a)$ satisfies*

$$m_t^a = 1_{[0,a)}(t)\{1 - L(t)\} + \int\limits_0^t m_{t-u}^a \mu(du), \qquad (1)$$

where $1_{[0,a)}(t)$ is the indicator function on the interval $[0, a)$. If $m = \mu(\infty) < 1$, then $\lim\limits_{t \to \infty} m_t = 0$. If $m = 1$ and μ is non-lattice, then

$$m_t^a \to \frac{\int\limits_0^a \{1 - L(u)\} du}{\int\limits_0^\infty u\mu(du)}.$$

If further $\int\limits_0^\infty tL(dt) < \infty$, then

$$m_t^a \to \frac{\int\limits_0^\infty uL(du)}{\int\limits_0^\infty u\mu(du)}.$$

If $m > 1$, μ is non-lattice and $\alpha > 0$ is the Malthusian parameter defined by $\hat{\mu}(\alpha) = 1$, then for $0 \le a \le \infty$

$$m_t^a \sim e^{\alpha t}\frac{\int\limits_0^a e^{-\alpha u}\{1 - L(u)\}du}{\int\limits_0^\infty ue^{-\alpha u}\mu(du)}.$$

In the lattice cases corresponding assertions hold.

This theorem however gives us the expected population starting from a woman aged 0 at time 0. To calculate the expected population that starts from a woman aged b at time 0 we use the following theorem.

Theorem 2. *(see Trayanov [16]) If we denote $_bm_t$ to be the expected number of individuals started from a woman aged b and $_b\mu(t)$ to be her point process expectation then the following holds:*

$$_bm_t = {_bS(t)} + \int\limits_0^t m_{t-u}\,{_b\mu(b+du)}, \tag{2}$$

where $_bS(t)$ denotes the probability a woman of age b to survive to $b + t$, i.e.

$$_bS(t) = \frac{S(b+t)}{S(b)}. \tag{3}$$

To model real population however we need additional assumptions. We assume the fertility interval for each woman is $[12, 50]$ and women do not give birth outside it. In terms of GBP this means $\mathbb{P}(\xi[a, b) = 0)) = 1$, when $[a, b) \cap [12, 50] = \varnothing$ and $\mathbb{P}(\xi[\lambda, \infty) = 0) = 1$. This assumption is made because we do not have data for births on ages less than 12 and greater than 50 and because births outside this age interval are very few and can be disregarded. The second assumption is that a woman could have 0 or 1 child during a year and each birth is a live birth. This means the number of live births is equal to the number of women who gave birth. The assumption is made because of missing data for the number of women that give birth and available data for the number of children born each year. In addition we do not have data for the sex of the child born, so we assume the probability for a girl is $100/205$.

The model above gives us information of how a stationary population will change over time, but it is not sufficient to describe a dynamic population

with changing birth and death laws. This problem could be easily avoided however (see Trayanov and Bojkova[17]). We achieve this by making population projection for only one year forward using the model and then change the birth and death laws according to what we forecast them to be and repeat the same for the next year. This gives us projections year after year incorporating the point process forecast and the life length forecast. For every year we know the number of men by age and we can model their contribution by the same equation (2) noting that their function $\mu(t)$ is actually zero for every t. The contribution of a single man aged b at time t is actually his survivability function $_bS(t)$. This small enhancement in the model allows us to include the men in predicting the age structure. We must note that their survivability function is different from women's one and is modelled separately. Once we have a model for the survivability function and the birth probabilities by age we can substitute them in equation (1) and (2). We must note that equation (1) is actually a renewal equation and the renewal theory (see [9]) explains how it can be solved.

3 Incorporating the available data into the model

In order to calculate $_bm_t$ in Theorem 2 from real data we need the following mathematical result which reduces it to solving equation (1) in Theorem 1.

Theorem 3. *(see Trayanov [16]) If m_t has a continuous second derivative then a third order approximation of equation (2) is given by*

$$_bm_t \approx {_bS(t)} + \sum_{k=1}^{n} m_{b+k-0.5} \cdot {_b\mu(b+k-1, b+k)},$$

where the expected number of births in $[b+k-1, b+k)$ of a woman aged b is

$$_b\mu[b+k-1, b+k] = {_bS(b+k-1)} \cdot \mathbb{P}(\xi[b+k-1, b+k) = 1 | \lambda \geq b+k-1).$$

The probability $\mathbb{P}(\xi[b, b+1) = 1 | \lambda \geq b)$ can be calculated from the Age Specific Fertility Rate and the expected number of years lived by a woman in [b, b+1) (see Trayanov [16]).

   The data we use can be found in Eurostat database [3]. We use the number of births and deaths by age and sex, the population count by age and sex. We use data both by age reached during the year and by age of last birthday. There are some missing data about the death count for ages 80+ for some years so we need to fill them first. We use the Kannisto model (see Thatcher et al. [15]) for this purpose. Then we calculate the fertility and mortality rates using the methodology described in Wilmoth et al. [18] and Shkolnikov [13] and then calculate the age specific fertility and mortality probabilities (see Chiang [2], Keyfitz [8] and Mode [10]) for every year since 1960. These probabilities however contain noise which we want to filter first and we achieve this with smoothing splines. The smoothing splines theory is explained more accurately in Ramsay [12] and de Boor [1]. The software used for calculations is R project [11] with additional packages for fitting smoothing splines (see gam [5]) and demography (see demography [6]).

4 Forecasting scenarios. Empirical results

In this section we will focus on forecasting the age structure and the population count. We discuss two scenarios for forecasting. The first scenario is called "No Change" because it assumes the current birth and death probabilities don't change in time. It projects the current state into the future. Although this projection gives us information about the future it gives us information about the present state too, answering the question if the the current state persists through time what development it expresses.

The second scenario is called "Dynamic Scenario" because it tries to capture trends in birth and death probabilities. This scenario requires several procedures to calculate:

- Principal Components Analysis (PCA) is used for decomposition of log-death probabilities and the point process density function for each year from 1980 to 2012. This gives us the main directions in which these function historically changed and reduces the forecasting of enormous amounts of points for each curve to forecasting only several parameters (see Hyndman [6]).
- ARIMA model is used to fit and forecast the principal components of birth and death probabilities. We find the best model according to Akaike information criterion (AIC) and use it to forecast the curves (see Hyndman [6]).
- We feed the forecasts into the General Branching Process model and compute the expected future population by age.
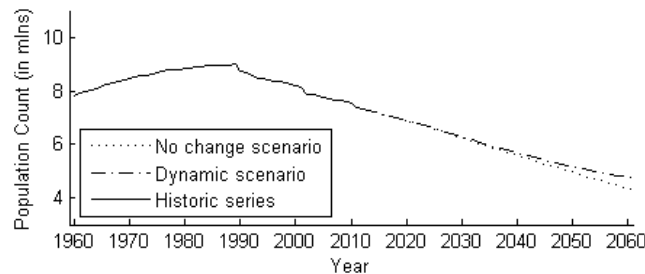
Fig. 1. Total population count.

The expected future total population count can be seen on Figure 1. We can see that according to both scenarios the population is decreasing rapidly in the next 50 years. There are 3.57 mil men and 3.76 mil women by the beginning of year 2012. The "No Change" scenario is expecting this count to be reduced to 2.03 mil men and 2.21 mil women by the end of 2061. The "Dynamic" scenario gives us slightly less pessimistic expectations for 2.21 mil men and 2.48 mil women by the end of 2061. This is a reduction of 38% and 32% respectively.

The two scenarios give similar forecasts for the total population count but forecast different structure of the population. This can be seen in Figures 3
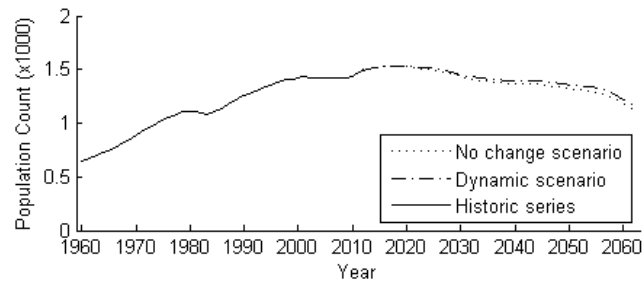
Fig. 2. Number of retired people.

and 6. In Figure 3 we can see the number of retired women is far greater than the number of retired men as of 2012 and the model is expecting this ratio to continue to grow. This is partly due to the smaller retirement age of women in Bulgaria (age 63) than men (which retire on age 65) but it is also result of different mortality rates for men and women. Women traditionally live longer than men. In Bulgaria the expected life length of women is 77 as of 2012 and is greater than the expected life length of men (70). The "Dynamic" scenario expects the life length for men to stay the same and for women to live 3 years longer in year 2060.
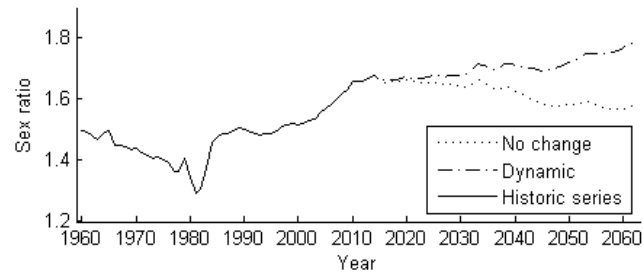
Fig. 3. Ratio of retired women against retired men.

An interesting feature in Figure 2 is that even though the percentage of pensioners is increasing in the past years it is expected to slow down in the near future and begin to decrease. It is interesting to see if this decrease of people on pension will help the economy recover. On Figure 4 is displayed the percentage of working people and how it will change over time. It shows that even though people on pension will decrease, those on working age will decrease even more so the economy will be under even greater demographic stress than it is now.

The "Dynamic" scenario shows that the population on working age is expected to decrease by 46%, whereas the people on pension are expected to decrease by 22%. This puts Bulgaria in a very difficult position because the working force will have to earn more to sustain the people on pension or the
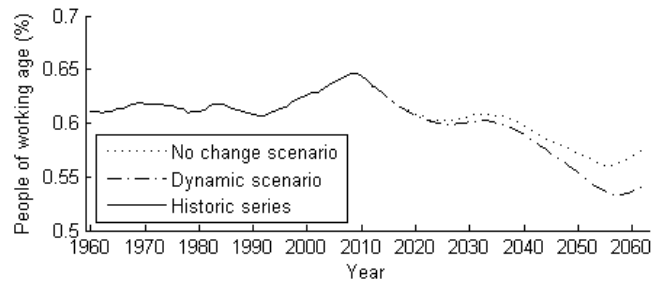
**Fig. 4.** Percentage of people on working age.

government will have to increase the retirement age. Calculations show that if we want to keep the current ratio of people on working age to people on pension in 2062, we need to gradually increase the retirement age of men by 4 years and to increase the retirement age of women even more - 6 years.
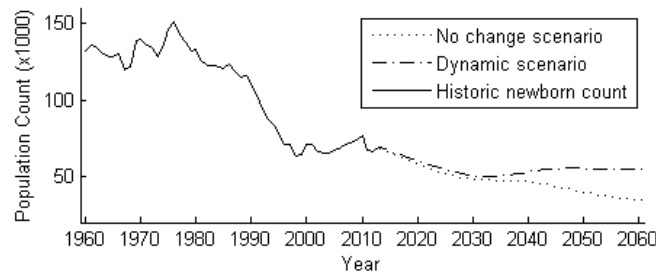

Fig. 5. Newborns count.

Another application of the model could be forecasting the number of newborns which can be used as a predictor of how many children will begin kindergarten or the number of people on age 6 or 7 years which is a predictor of how many children will begin school in the future. Figure 6 shows the number of children beginning school is expected to decrease till 2035 but then it will start growing again. This change of trend is caused by the current age structure of the population that will change over time. The number of newborns is shown on Figure 5. It is expected to decrease till year 2030 due to the bad age structure but eventually it will start growing again.

The number of people on age 18 and 19 is going to decrease till year 2017 by 25% and then start to increase for short while. This is important because the number of people on this age is the main source of students for universities. A decrease with 25% for 5 years puts the universities in difficult position. Calculations show that the number of young people of age between 18 and 30 is going to decrease too by 14% in year 2017 and continue decreasing till year 2026 by 34%. This results in fewer candidates for students and less young people in the economy.
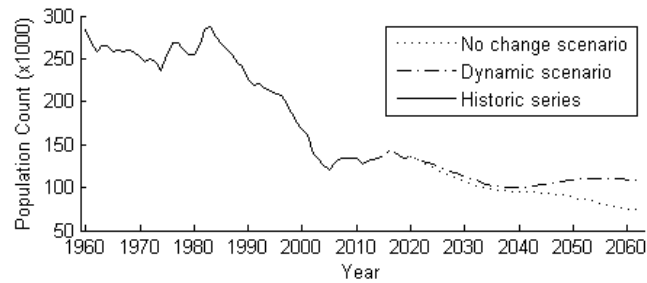
Fig. 6. People of age 6 or 7.
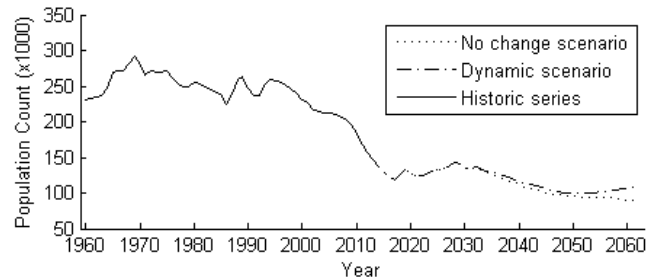
Fig. 7. People of age 18 and 19.

5 Final remarks

Modelling and forecasting the population is important for the country. It tells us about the current state and what is wrong with it so the government can make an efficient demographic policy. It tells us what to expect in the future so we can prepare. It gives us a tool to make social plans like how many new kindergartens we need to build in the future or can we expect a low number of students in the schools or universities. It answers economic questions - how many people will be on working age and how many on pension so the government could adjust their policy appropriately and efficiently. The forecast results for Bulgaria should teach us that we need to pay attention to demography and make a social policy that counteracts these trends. The demographic problems are difficult to solve, affect many aspects of life in the country and require a long term strategy to be solved.

References

1. Boor, C., *A Practical Guide to Splines.* Springer, 2001.
2. Chiang, C., *Life Table and Its Applications.* Krieger Pub Co, 1983.
3. Eurostat Database, `http://epp.eurostat.ec.europa.eu/portal/page/portal/statistics/search_database`.
4. Feller, W. *An introduction to probability theory an its applications, vol. 2.* Wiley, 1971.
5. Hastie, T., gam: Generalized Additive Models. R package version 1.09-1, `http://CRAN.R-project.org/package=gam`, 2011.
6. Hyndman, R., Booth, H., Tickle, L. and Maindonald, J., demography: Forecasting mortality, fertility, migration and population data. R package version 1.09-1, `http://CRAN.R-project.org/package=demography`, 2011.
7. Jagers, P., *Branching Processes with Biological Applications.* John Wiley & Sons Ltd, 1975.
8. Keyfitz N. and Caswell, H., *Applied Mathematical Demography.* Springer, 2005.
9. Mitov, K. and Omey, E., *Renewal Processes.* Springer, 2013.
10. Mode, C., *Stohastic Processes In Demography and Their Computer Implementation.* Springer, 1985.
11. R Development Core Team, R: A Language and Environment for Statistical Computing. `http://www.R-project.org/`, 2011.
12. Ramsay, J. and Silverman, B. *Functional Data Analysis.* Springer, 2005.
13. Shkolnikov, V., Methodology Note on the Human Life-Table Database (HLD). Unpublished Manuscript, `http://www.lifetable.de`
14. Slavtchova-Bojkova, M. and Yanev, N. M., *Branching Processes.* St. Kliment Ohridski University press, Sofia, 2007.
15. Thatcher, R., Kannisto, V. and Andreev, K., The survivor ratio method for estimating numbers at high ages. *Demographic Research*, 6(1), 2-15. 2002.
16. Trayanov, P., Crump-Mode-Jagers Branching Process: Modelling and Application for Human Population, *Pliska Stud. Math. Bulgar.*, 22, 207-224, 2013.
17. Trayanov, P. and Slavtchova-Bojkova, M., Crump-Mode-Jagers Branching Processes: Application in Population Projections, *Annual of The Sofia University St. Kliment Ohridski, Faculty of Mathematics and Informatics*, 2013.
18. Wilmoth, J. R., Andreev, K., Jdanov, D. and Glei, D. A., Methods Protocol for the Human Mortality Database. Unpublished Manuscript, `http://www.mortality.org`, 2007

Modeling the relationship between temperature and daily mortality in Cyprus

Haritini Tsangari[1], Zoi Konsoula[2], Stephanie Christou[3], Kyriakos Georgiou[4], and Edna Yamasaki[5]

[1] University of Nicosia Research Foundation, University of Nicosia, Nicosia, Cyprus
(E-mail: tsangari.h@unic.ac.cy)
[2] University of Nicosia Research Foundation, University of Nicosia, Nicosia, Cyprus
(E-mail: konsoula.z@unic.ac.cy)
[3] University of Nicosia Research Foundation, Nicosia, Cyprus
(E-mail: christou.st@unic.ac.cy)
[4] Cyprus Center for European and International Affairs, University of Nicosia, Nicosia, Cyprus
(E-mail: georgiou.k@unic.ac.cy)
[5] University of Nicosia Research Foundation, University of Nicosia, Nicosia, Cyprus
(E-mail: yamasaki.e@unic.ac.cy)

Abstract. Climatic changes, such as large temperature fluctuations and increase in the occurrence of heat waves, have been evidenced to affect mortality worldwide. In this paper we examine the effect of high temperatures on mortality in Cyprus, an island which is characterized by a Mediterranean climate. The modeling approach is described. First, the temperature function is created within the newly-developed framework of distributed lag non-linear models, to simultaneously capture non-linearities and delayed effects. The temperature function is, then, incorporated in a Generalized Linear Model with a quasi-Poisson distribution to allow for overdispersion, together with possible confounders such as meteorological indicators, trends and seasonality. Comparisons are additionally made, regarding the effect of temperature on mortality, between inland and coastal areas. All the results are presented in a tabular or graphical form and the conclusions are discussed.
Keywords: heat waves, mortality, distributed lag non-linear model, strata constraints, hot threshold, GLM, quasi Poisson, harvesting effect.

1 Introduction

Global climate change is projected to further increase the frequency, intensity and duration of heat waves. Exposure to high temperatures can result in a variety of adverse health effects including deaths due to heat-related causes such as heat stroke, but also exacerbating many preexisting health conditions (Rainham and Smoyer-Tomic[32]; Kovats and Hajat[25]; Gosling et al.[16]). Many studies conducted worldwide, have, in fact, indicated a consistent strong

association between elevated temperature and all-cause (excluding external causes) mortality, despite any variation observed amongst diseases (Armstrong[3]; Baccini et al.[5]; Michelozzi et al.[27]; Zanobetti and Schwartz[40]; Biggeri and Baccini[7]; Hajat et al.[22]).

The association between temperature and mortality has been evidenced to be non-linear, following a J-, U-, or V-shaped curve, where minimum mortality is detected at moderate temperatures, while an excess health risk is observed at temperatures above a certain threshold, with higher mortality at temperature extremes (Armstrong[3]; Armstrong et al.[4]; Baccini et al.[5]; Curriero et al.[9]; Hajat and Kosatsky[19]).

In addition, many studies have shown evidence of the so-called "delayed effect". They have indicated that temperature can affect not only deaths occurring on the same day, but on several subsequent days, where the converse is also true: deaths on each day depend on the effect of the same day's temperature as well as the lag effects of the previous days' temperatures (Anderson and Bell[2]; Braga et al.[8]; Gasparrini et al.[15]). The estimate of the effect depends on the appropriate specification of the lag dimension of the dependency, defining models flexible enough to represent simultaneously the exposure-response relationship and its temporal structure (Gasparrini et al.[15]).

The island of Cyprus has a typical Mediterranean climate characterized by hot dry summers and rainy changeable winters, separated by short autumn and spring seasons of rapid change. During summertime, it is mainly under the influence of a shallow trough of low pressure extending from the great continental depression centered over Southwest Asia, which results in high temperatures with almost cloudless skies and negligible rainfall (Price et al.[31]). In Cyprus climate change has been observed, with an increase in the average annual temperature by 0.8°C in the last thirty-year period and a drop in precipitation by 17% from the second half of the century. Climate change is expected to act in many ways as a multiplier of existing environment and health problems (Symeou[36]).

The current study is the first to provide evidence on the effect of extreme weather on mortality in a country with a Mediterranean climate, and the first that examines this issue for the island of Cyprus. The study, additionally, implements a new methodological approach.

2 The GLM modeling framework

A Generalized Linear Model (GLM) framework will be used in our analysis. A general form of the model for the mortality counts, , t=1,….n, is given by:

$$g(\mu_t) = \alpha + \sum_{j=1}^{J} s_j(x_{tj}; \boldsymbol{\beta}_j) + \sum_{k=1}^{K} \gamma_k u_{tk} \ , \qquad (1)$$

where $\mu = E(Y)$, g is a monotonic link function and $\mathbf{Y}$ has a distribution from an exponential family (McCullagh and Nelder[26]). In epidemiological

studies of the impact of extreme weather on human health, where the response variable is a non-negative daily count (e.g., mortality), overdispersion is often observed, where the variance of the outcome is greater than its mean ($\mathbf{V(Y)} = \phi\mu, \quad \phi > 1$). GLM models with quasi-Poisson regression have been shown to capture overdispersion well, by extending the Poisson distribution with the estimation of an additional dispersion parameter (Armstrong et al.[4]; Guo et al.[17]; Everitt and Hothorn[12]; Hajat et al.[21]; Schwartz et al.[35]; Zeger[42]). The functions s_j in equation (1) denote smoothed relationships between the variables x_j and the linear predictor, defined by the (unknown) parameter vectors β_j. The variables u_k include other predictors with linear effects specified by the related coefficients γ_k.

2.1 The temperature function in GLM

First, we consider the function $s_1(x_{t1}; \boldsymbol{\beta})$ for temperature, x, that will be included in the GLM framework of equation (1), hereafter called the "temperature function". As mentioned in section 1, the relation between temperature and mortality has been evidenced to have two main characteristics: non-linearity and delayed effect. Many methods have been proposed to deal with non-linearity, depending on the shape of the relationship, the degree of approximation required and interpretational issues. Among the most commonly used methods are smooth curves, such as polynomials, quadratic B-splines or natural cubic splines (Dominici et al.[10]) or linear-threshold parameterizations (e.g., "hockey-stick model"), which assume a high temperature threshold, k, and can by represented by a truncated linear function (x−k)$_+$ which equals (x−k) when x>k and 0 otherwise (Armstrong[3]; Hajat et al.[21]; Pattenden et al.[29]; Baccini et al.[5]).

Among the methods that have been proposed to deal with delayed effects, a major role is played by distributed lag models (DLM) (Schwartz[34]; Zanobetti et al.[41]; Braga et al.[8]). When a linear relation is assumed, this methodology allows the effect of a single exposure event to be distributed over a specific period of time, using several parameters to explain the contributions at different lags, thus providing an estimate of the overall effect. The simplest formulation is an unconstrained DLM. However, each individual coefficient at specific lags is often imprecisely estimated and highly correlated with estimates of other coefficients, resulting in collinearity between exposures in adjacent days. To gain more precision in the estimate of the distributed lag curve, some constraints can be imposed, where an effective choice includes strata constraints (Welty and Zeger[38]; Armstrong[3]; Pattenden et al.[29]; Gasparrini et al.[15]; Gasparrini and Armstrong[14]). In such a "lag-stratified distributed lag model" several days are averaged as the effects of temperature over a period of time rather than from the contribution of one day, assuming a constant effect (equal coefficients) within lag intervals (strata).

Although there exist well-developed methods for dealing with non-linearity or time latency in the temperature-mortality association, these two components are rarely modeled simultaneously. We will use a methodology that unifies many of the previous methods to deal with delayed effects and at the same time provide more flexible alternatives regarding the shape of the relationships, relaxing the assumption of linearity. More specifically, the temperature function will be modeled using the newly-developed framework of Distributed Lag Non-Linear Models (DLNM) (Armstrong[3], Gasparrini et al.[15]; Gasparrini and Armstrong[14]). DLNM can describe non-linear relationships by choosing a "cross-basis", which is a bi-dimensional space of functions describing on the same time the shape of the relationship along the predictor, x, (temperature) and the distributed lag effects. Choosing a cross-basis amounts to specifying two independent sets of "basis" functions, which will be combined (Gasparrini et al.[15]). A DLNM can be specified by

$$s(x_t; \boldsymbol{\eta}) = \sum_{j=1}^{v_x} \sum_{k=1}^{v_l} \mathbf{r}_{tj.}^T c_{.k} \eta_{jk} = \mathbf{w}_t^T \boldsymbol{\eta},$$

where $\mathbf{r}_{tj.}$ is the vector of lagged exposures for the time t transformed through the basis function, the vector $\mathbf{w}_{t.}$ is the tth row of the cross-basis matrix $\mathbf{W}$, $\mathbf{C}$ is an $(L+1) \times v_l$ matrix of basis variables for the lag vector $\mathbf{l}$, and $\boldsymbol{\eta}$ is a vector of unknown parameters. More details regarding the algebraic notation and estimation of DLNMs can be found in Gasparrini et al.[15].

In our study, the choice of the non-linearity dimension of the cross-basis of DLNM will be led by visual inspection of the shape of the temperature-mortality relation, assuming a high threshold temperature (see section 4). Regarding the lag dimension of the cross-basis, we will we assess the effect of temperature on mortality with lags up to 10 days before the day of death, using a constrained distributed lag model, with strata constraints on the coefficients ("lag-stratified distributed lag model"), to avoid collinearity and improve the precision of the estimates. We will define 3 strata intervals with dummy parameterization, assuming constant distributed lag effects along the strata of lags 0-1, 2-5 and 6-10.

2.2 Confounding factors in the temperature-mortality relation

The relationship between temperature and mortality may be confounded by measured or unmeasured covariates, which need to be controlled for properly in the GLM model (Peng et al.[30]; Touloumi et al.[37]; Dominici et al.[11]). The meteorological variable relative humidity has been shown to be a confounder of the mortality-temperature relation and natural cubic splines have been used as a smoothed function (Armstrong et al.[4]; Guo et al.[7]; Braga et al.[8]; Curriero et al.[9]; Anderson and Bell[2]; Armstrong[3]). We will similarly use natural cubic splines to control for the non-linear effect of relative humidity (function s_2 in equation (1)). Our GLM model will also control for secular trends and seasonality, by using smooth functions of time (day of the year) (function s_3 in equation (1)). Natural cubic splines are most commonly used in this context,

where the degree of smoothness is very important, since it determines the amount of residual temporal variation in mortality available to estimate the temperature effect (Armstrong et al.[4]). The relation between temperature and mortality has also been evidenced to be affected by calendar days, where, for example, on weekends the number of hospital admissions can be lower than on weekdays and can also be lower during public holidays (Armstrong et al.[4]; Guo, et al.[17]; Michelozzi et al.[28]; Peng et al.[30]). Thus, any additional confounding by seasonally varying factors which vary on shorter timescales will be controlled by adding categorical/dummy variables for day of the week and public holidays ($\gamma_k u_k$ in equation (1)).

Since our interest is on the heat effect on mortality, the analysis will concentrate on the warm periods of each year, where a warm period is defined as the months from April to September. The same definition was chosen by many previous studies (e.g., Baccini et al.[5]; Michelozzi et al.[28]; Almeida et al.[1]; Pattenden et al.[29]), in order to ensure reasonable statistical power, given the small number of events (mortality), and based on the evidence that heat waves occurring at times other than summer may have just as strong a health impact (Hajat et al.[20]; Michelozzi et al.[27]). Therefore, the data are composed by multiple equally-spaced and ordered series of the same seasons for each year, and do not represent a single continuous time series. We will use the methodology suggested by Gasparrini and Armstrong[14], especially for seasonal analysis, in order to define this multiple series.

The results will be obtained using R statistical software (The R Foundation for Statistical Computing).

3 Data

Daily mortality data were provided by the Ministry of Health of the Republic of Cyprus, for each of the five districts in Cyprus (Nicosia, Limassol, Larnaca, Paphos, Ammochostos) for the period between the years 2004 and 2009. The data included total (all-cause) mortality excluding external causes, as classified in the Eurostat Shortlist of 65 causes of death.

Daily meteorological data were collected by the Cyprus Meteorological Service in the five main urban centers of the island. The meteorological parameters that were used for the purpose of this study included measures of temperature and relative humidity. No temperature measure has been shown to be consistently better at predicting mortality and thus there is no standard indicator of heat stress (Barnett et al.[6]; Michelozzi et al.[28]). We considered the daily surface maximum temperature (in °C), which was used in many related studies (e.g., Armstrong et al.[4]; Filleu et al.[13]; Guo et al.[17]; Rocklöv and Forsberg[33]). Daily values of relative humidity at 8:00 LST and 13:00 LST (in %) were obtained for each district, where the mean of the two values was calculated. We avoided unequal spacing of the observations by imputing missing values as the moving average of surrounding observations (e.g. Rocklöv and Forsberg[33]).

Cyprus was considered as a total area, using the combined data from all the stations, but separate analyses were also performed for Nicosia (urban area) and Limassol (coastal area) for comparative purposes.

4 Analysis and results

Table 1 presents descriptive statistics for the main variables of the study, all-cause (total) mortality counts, maximum temperature and relative humidity, by district, for the warm periods (April to September) of the years 2004-2009.

District	Total Mortality		Maximum Temperature (°C)		Relative Humidity (%)	
	Mean	SD	Mean	SD	Mean	SD
Nicosia	4.56	2.19	32.84	5.48	43.02	13.66
Limassol	3.33	1.91	30.41	4.25	63.22	10.30
Larnaca	1.75	1.38	29.81	4.28	55.11	11.89
Paphos	1.10	1.08	27.55	3.79	67.50	9.19
Ammochostos	0.54	0.74	30.39	4.91	54.31	14.14

Table 1. Descriptive statistics of the mortality and meteorological variables, per district, for the warm periods (April to September), 2004-2009.

Figure 1 shows the relation between daily all-cause mortality and maximum temperature in Cyprus.
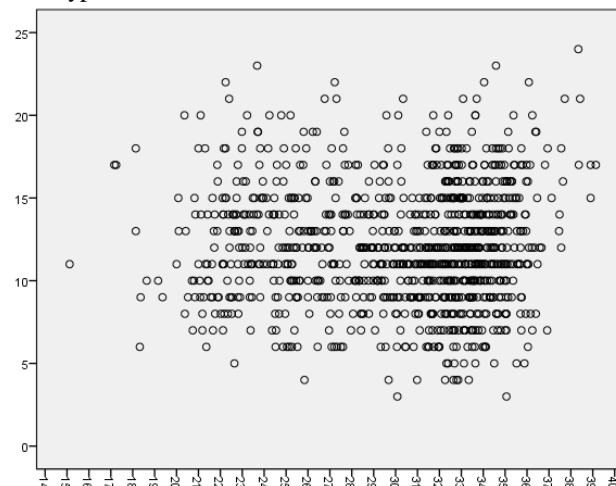
Fig. 1. Mortality vs. maximum temperature: Cyprus, warm periods, 2004-2009.

Examination of figure 1 indicates a non-linear effect of temperature. More specifically, it appears to be constant up to one point (zero slope up to temperatures around 29°C) and then we have a V-shaped relation with a hot threshold, the common point where two linear terms are constrained to join, which corresponds to a change in the effect estimate and the temperature associated with the minimum mortality rate. Therefore, led by visual inspection, the non-linearity component of the temperature function in DLNM will be captured for our data by the "linear-thresholds" model ("hockey-stick" model), with a high threshold parameterization (see section 2.1). Similar plots were found for Nicosia (urban area) and Limassol (coastal area), when the respective data were examined separately.

Based on figure 1, we tested a grid of temperatures from 31°C to 35°C, in 0.1°C increments, to identify the threshold temperature that satisfied our criteria for model choice (e.g., minimizing residual deviance and Akaike Information Criterion (AIC)) (Armstrong[3]; Guo et al.[17]). The hot threshold temperature for Cyprus was found to be 33.7°C. Using similar procedures, the threshold temperatures for Nicosia and Limassol were found to be 32.5°C and 38°C respectively.

The GLM model was then fit to the data, including the temperature function and the potential confounders of the temperature-mortality relation. The final estimated GLM model could be described by the following equation:

$$\log(E(Y_t)) = \boldsymbol{\alpha} + \boldsymbol{\beta}\mathbf{T_{t,l}} + S_2(RH_t,3) + S_3(d_t,4) + \boldsymbol{\gamma}_1 DOW_t + \gamma_2 Holiday_t$$

where t is the day of observation (days 151 up to 273 of each year, restricted to the periods from April to September), Yt is the observed daily death counts on day t, α is the intercept, $T_{t,l}$ is the temperature function (a matrix obtained by applying DLNM to temperature), l corresponds to lags of temperature, β is the vector of coefficients for $T_{t,l}$, $S_2(RH_t,3)$ is a natural cubic spline with 3 degrees of freedom to smooth relative humidity, $S_3(d_t,4)$ is a natural cubic spline with 4 degrees of freedom for long-term trends (day of the year), as a smooth function to capture the variation within the warm period, DOW_t is the indicator variable for "day of the week" effect (1=Sunday) on day t (γ1 is the corresponding coefficient), and $Holiday_t$ is a dummy variable for the holiday effect (1=Public Holiday; γ2 is the corresponding coefficient). All the components of the model were significant (p-values<5%), except the Holiday effect. The model had a good fit, with model criteria and diagnostics tools indicating that all patterns (autocorrelation and trends) were captured effectively. The corresponding GLM models were also fit for the separate analyses for Nicosia and Limassol. The significance of the components was similar, although relative humidity was not found to be a significant confounder for the urban area of Nicosia.

Table 2 shows the relative risk increment per degree of heat sustained per day (effect of lags in the same strata interval is equal), for Cyprus as a total area as well as for Nicosia and Limassol considered separately.

Lags	Relative risk: % per ^{0}C above threshold-per lag (95% CI): Cyprus (threshold=33.7^{0}C)	Relative risk: % per ^{0}C above threshold-per lag (95% CI): Nicosia (threshold=32.5^{0}C)	Relative risk: % per ^{0}C above threshold-per lag (95% CI): Limassol (threshold=38^{0}C)
0-1	4.24 (2.03 to 5.81)	1.47 (0.41 to 2.54)	21.18 (6.18 to 38.30)
2-5	0.50 (-0.39 to 1.41)	0.49 (-0.09 to 1.08)	15.47 (5.79 to 26.03)
6-10	0.41 (-0.29 to 1.11)	0.30 (-0.15 to 0.76)	-7.79 (-17.04 to 2.48)
0-10	**13.17 (8.50 to 18.05)**	**6.59 (3.49 to 9.79)**	**73.99 (-6.54, 223.91)**

Table 2. Results for relative risk (increase in mortality) from the Lag-stratified distributed lag linear threshold model - Cyprus, Nicosia, Limassol (2004-2009)

The results in Table 2 show that the effect of heat in Cyprus is much more pronounced for lags 0-1 (4.2% in each of lags 0 and 1, compared to 0.5% in each of higher lags, more than 8 times higher). In other words, during the same and next day of a heat event, a 1 degree increase in maximum temperature above the threshold of 33.7^{0}C is associated with an estimated increase of around 8.5% in all-cause mortality in Cyprus. Table 2 also provides the estimated overall effect of temperature over all 10 lags, which is the total effect from the lag-specific contributions, computed by summing the log relative risks of each lag and it is largely insensitive to constraints (Armstrong[3]; Gasparrini et al.[15]). Looking at the results for Cyprus, the total risk over the 10 lags is around 13% higher for every degree above 33.7^{0}C.
Figure 2 presents the overall effect of temperature on all-cause mortality in Cyprus, over lags 0-10.
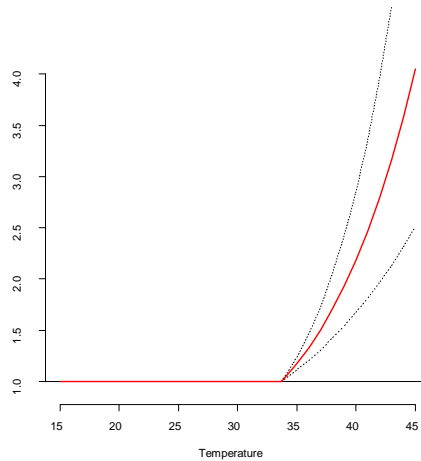
Fig. 2. Overall effect (relative risk) over all 10 lags: Cyprus (2004-2009).

As figure 2 indicates, the effect has zero slope up to the threshold temperature and increases after the threshold, with a significant increase in mortality risk at very high temperatures: at temperatures around 40^0C the risk of dying is around 3 times higher compared to temperatures close to the threshold.

Figure 3 shows a three-dimensional graph of the exposure-response relationship along temperature and lags, with reference at 33.7^0C, the threshold temperature and provides a general picture of the results. Slices of the 3D plot, for specific temperatures (35^0C, 37^0C, 40^0C and 42^0C), appear in the bottom part of the figure.
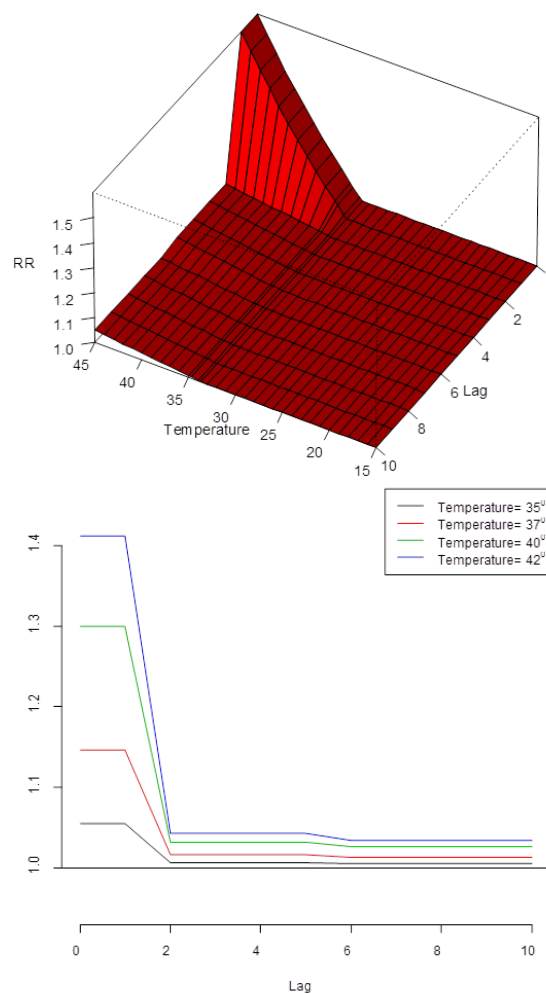
Fig. 3. 3-D plot of relative risk along temperature and lags (upper) and slices of the 3-D plot (lag-specific effects) for various temperatures (bottom): Cyprus

Figure 3 shows that heat (i.e. temperatures above the threshold of 33.7^{0}C) has a much stronger effect at lags 0 and 1, compared to lags 2-5 and 6-10, and the effect is much stronger at higher temperatures. For example, it is 40% higher at 42^{0}C compared to 35^{0}C, where at the temperature of 35^{0}C the risk is negligible at lags higher than 2. In addition, the effect at lower temperatures (e.g., 35^{0}C and 37^{0}C) has a smoother shape, compared to the sudden drop for temperatures above 40^{0}C, as we move further away from the event (e.g., a week away).

Focusing on the results obtained from the separate analysis of the data from Nicosia (urban area), showed that, similar to the results for Cyprus, the effect of heat is much more pronounced for lags 0-1, however, the effect in Nicosia is much lower compared to considering Cyprus as a total area (Table 2). A comparison of the 3D plot of Nicosia (not shown) with the plot for Cyprus, showed that the change in effect from lags 0-1 to lags 2-5 is much smoother in Nicosia compared to Cyprus, with the effects in the two strata being very close. In addition, the effect on mortality is stronger at higher temperatures (e.g. 40^{0}C and 42^{0}C), around 10% higher compared to temperatures around 35^{0}C, where the increase in mortality is actually close to zero compared to the threshold temperature of 32.5^{0}C and it has an overall smoother shape, with a smaller decrease from lags 0-1 to higher lags. The results regarding Limassol (coastal area) shown in Table 2 similarly show that significant effects occurred within 0-1 lags, which are much higher compared to the total area of Cyprus and the urban area of Nicosia for lags 0-1 and also quite high for lags 2-5 as well. The accumulated effect for Limassol is as high as 74%, but it is associated with a wide confidence interval that ranges from a negative effect to a highly positive effect, reflecting high variability/overdispersion within lags. The most noticeable result is that the relative risk for Limassol for lags 6-10 is highly negative, indicating a deficit of deaths in lags 6-10.

5 Discussion

The current study is the first to examine and quantify the effect of high temperatures on all-cause mortality in a Mediterranean island, Cyprus, using a methodology that captures simultaneously any non-linearities and lag effects, based on the general framework of distributed lag non-linear models, while also adjusting for the effect of potential confounders.

The results showed that high temperatures have a significantly adverse effect on public health in Cyprus, irrespective of living in the inner part of the island or the coastal area. In addition, temperature had an effect on all-cause mortality, independent of the effect of relative humidity or seasonal factors, like day of the year (e.g. middle of July or August) or shorter-term effects, like the day of the week (e.g., after a prolonged exposure to the sun during the weekend). An immediate or direct health effect of heat was found, with higher risk within the current and next day of a severe heat event, as opposed to a lower effect in longer lags, as we move further from the event, where the risk drops significantly after two days. The delayed effect of heat could also be seen vice

versa: a death due to high temperatures is not due only to the thermal stress of the same day, but also of the previous couple of days. The results of a pronounced direct effect of heat (lags 0-1) on all-cause mortality agree with previous studies that have shown that the heat effect is immediate (Armstrong[3]; Braga et al.[8]; Guo et al.[17]; Pattenden et al.[29]).

In addition to the immediate effect of heat, the results showed that the effect on public health is much more pronounced for higher temperatures, as opposed to temperatures close to the threshold, where the effect is smoother, with a sharp drop from lag 1 to lag 2.

Focusing on the two areas, Nicosia and Limassol, provided similar results of an immediate short-term effect within the first two days, which is reduced in longer lags and for lower temperatures. However, the threshold temperatures corresponding to the lowest observed mortality varied. This variation by latitude and topographical features appeared in other studies (e.g., Baccini et al.[5]) and could reflect population differences in acclimatization or adaptation to high temperatures between coastal and inner-country areas. The meteorological indicator relative humidity should also be considered, since it appeared to play a significant role in the effect of high temperatures on mortality: the mean levels of relative humidity were, as expected, higher in coastal areas, compared to Nicosia, while it was not a significant confounder in the temperature-mortality relation for Nicosia, as opposed to Limassol (and Cyprus as a total area).

In addition, differences in the level of the temperature effect between areas were observed in the study: the effect observed for Nicosia was less pronounced, much smaller and smoother, almost negligible at lags 2-10, indicating a lower risk of mortality in this urban area. The model for the coastal area of Limassol showed a deficit in deaths at longer lags (6-10), with negative relative risk. This reduction in mortality, one week or so after the event, suggests that the heat wave affected especially frail individuals whose health was already so compromised that would have died in the short term anyway (e.g., 2 or 3 weeks later) and whose events were only accelerated by a brief period of time by the effect of exposure. This so called "harvesting effect" or "mortality displacement", has been observed in previous studies, where following heat waves there is a decrease in overall mortality in subsequent weeks, thus representing a short-term forward shift in mortality (Armstrong[3]; Guo et al.[17]; Braga et al.[8]; Hajat et al.[18]; Kinney et al.[24]).

Although the effect of heat appeared to be strong during the first two days and disappeared gradually after this, the choice of including up to 10 lags in our model has led to capturing this harvesting phenomenon for Limassol. In fact, studies of the effect of high temperatures using short lags (up to 2 or 3 lags only) may overestimate the hot effect, as the harvesting effect could only be captured by using longer lags (Anderson and Bell[2]; Guo et al.[17]). To explore better the number of lags for the model, and ensure that any shorter or longer-term effects were captured, sensitivity analysis was additionally performed for the number of total lags, up to 27 lags. The results were very similar to the results for 10 lags, therefore no need for a change in the models was deemed necessary.

6 Conclusion

The adverse health effects of heat waves are largely preventable, especially if appropriate measures are implemented, which include, among others, the setting up of early warning systems (Hayhoe et al.[23]; WHO[39]). As a result, a number of cities across Europe have already begun to develop and implement hot-weather response plans (Rainham & Smoyer-Tomic[32]). The results of the current study can thus be used for the development of early Heat-Health warning systems for the population in Cyprus, targeting climatic variables. Overall the heat effect appears to increase the risk of mortality and requires special attention. The corresponding Governmental departments must shift their focus from surveillance and response to prediction and prevention, to link accurate forecasts of extreme events with effective public health measures and interventions, taking at the same time into consideration the special characteristics of urban and coastal areas.

References

1. S. P. Almeida, E. Casimiro and J. Calheiros. Effects of apparent temperature on daily mortality in Lisbon and Oporto, Portugal, Environmental Health, 9, 1-7, 2010.
2. B.G. Anderson and M.L. Bell. Weather-Related Mortality: How Heat, Cold, and Heat Waves Affect Mortality in the United States, Epidemiology, 20, 205-213, 2009.
3. B. Armstrong. Models for the relationship between ambient temperature and daily mortality, Epidemiology, 17, 624-631, 2006.
4. B.G. Armstrong, Z. Chalabi, B. Fenn, S. Hajat, S. Kovats, A. Milojevic and P. Wilkinson. Association of mortality with high temperatures in a temperate climate: England and Wales, J. Epidemiol. Commun. H., 65, 340-345, 2011.
5. M. Baccini, A. Biggeri, G. Accetta, T. Kosatsky, K. Katsouyanni, A. Analitis, H.R. Anderson, L. Bisanti, D. D'Ippoliti, J. Danova, B. Forsberg, S. Medina, A. Paldy, D. Rabczenko, C. Schindler and P. Michelozzi. Heat effects on mortality in 15 European cities, Epidemiology, 19, 711-719, 2008.
6. A.G. Barnett, A.C.A. Tong and S. Clements. What measure of temperature is the best predictor of mortality?, Environmental Research, 110, 604–611, 2010.
7. A. Biggeri and M. Baccini. Modelling Short-Term Effects of Meteorological Variables on Mortality, http://www.sis-statistica.it/files/pdf/atti/CIMe0905p121-130.pdf, 2012.
8. A.L. Braga, A. Zanobetti and J. Schwartz. The time course of weather-related deaths, Epidemiology, 12, 662–667, 2001.
9. F.C. Curriero, K.S. Heiner, J.M Samet,, S.L. Zeger, L. Strug and J.A. Patz. Temperature and mortality in 11 cities of the Eastern United States, Am. J. Epidemiol., 155, 80-87, 2002.

10. F. Dominici, M. Daniels, S. L. Zeger and J.M. Samet. Air pollution and mortality: estimating regional and national dose–response relationships, Journal of the American Statistical Association, 97, 100-111, 2002.
11. F. Dominici, L. Sheppard and M. Clyde. Health Effects of Air Pollution: A Statistical Review, International Statistical Review, 71, 243–276, 2003.
12. B. S. Everitt and T. A. Hothorn. Handbook of Statistical Analyses Using R, 2nd Edition, Boca Raton, FL.: Chapman & Hall, 2009.
13. L. Filleu, L. Cassadou, S. Médina, P. Fabres, A. Lefranc, D. Eilstein, A. Le Tertre, L. Pascal, B. Chardon, M. Blanchard, C. Declercq, J-F. Jusot, H. Prouvost and M. Ledrans. The Relation Between Temperature, Ozone, and Mortality in Nine French Cities During the Heat Wave of 2003, Environmental Health Perspectives, 114, 1344–1347, 2006.
14. A. Gasparrini and B. Armstrong. Distributed lag non-linear models in R: the package dlnm, dlnm version 1.6.3, 2012 ftp://ftp.cn.debian.org/CRAN/web/packages/dlnm/vignettes/dlnmOverview.pdf
15. A. Gasparrini, B. Armstrong and M.G. Kenward. Distributed lag non-linear models, Statistics in Medicine, 29, 2224–2234, 2010.
16. S.N. Gosling, J.A. Lowe, G.R. McGregor, M. Pelling and B.D. Malamud. Associations between elevated atmospheric temperature and human mortality: a critical review of the literature, Climatic Change, 92, 299–341, 2009.
17. Y. Guo, A.G. Barnett, X. Pan, W. Yu and S. Tong. The Impact of Temperature on Mortality in Tianjin, China: A Case-Crossover Design with a Distributed Lag Nonlinear Model, Environmental Health Perspectives, 119, 1719–1725, 2011.
18. S. Hajat, B.G. Armstrong, N. Gouveia and P. Wilkinson. Mortality Displacement of Heat-Related Deaths: A Comparison of Delhi, Sao Paulo, and London, Epidemiology, 16, 613-620, 2005.
19. S. Hajat and T. Kosatky. Heat-related mortality: a review and exploration of heterogeneity, J. Epidemiol. Commun. H., 64, 753-760, 2010.
20. S. Hajat, R.S. Kovats, R.W. Atkinson and A. Haines. Impact of hot temperatures on death in London: a time series approach, Journal of Epidemiology and Community Health, 56, 367-372, 2002.
21. S. Hajat, R.S. Kovats and K. Lachowycz, Heat-related and cold-related deaths in England and Wales: who is at risk?, Occupational and Environmental Medicine, 64, 93-100, 2007 .
22. S. Hajat, S. Vardoulakis, C. Heaviside and B. Eggen, B. Climate change effects on human health: projections of temperature-related mortality for the UK during the 2020s, 2050s, and 2080s., J Epidemiol. Commun. H., (forthcoming), 2014 doi:10.1136/jech-2013-202449.
23. K. Hayhoe, S. Sheridan, L. Kalkstein and S. Greene. Climate change, heat waves, and mortality projections for Chicago, Journal of Great Lakes Research, 36, 65–73, 2010.
24. P.L. Kinney, M.S. O'Neill, M.L. Bell and J. Schwartz. Approaches for estimating effects of climate change on heat-related deaths: challenges and opportunities, Environ. Sci. Policy, 11, 87–96, 2008.
25. R.S. Kovats and S. Hajat. Heat Stress and Public Health: A Critical Review, Ann. Review of Public Health, 29, 41-55, 2008.
26. P. McCullagh and J.A. Nelder. Generalized Linear Models, 2nd Edition, Boca Raton, FL.: Chapman & Hall/CRC Interdisciplinary Statistics Series, 1989.
27. P. Michelozzi, F.K. De' Donato, A.M. Bargagli, D. D'Ippoliti, M. De Sario, C. Marino, P. Schifano, G. Cappai, M. Leone, U. Kirchmayer, M. Ventura, M. Di Gennaro, M. Leonardi, F. Oleari, A. De Martino and C.A. Perucci. Surveillance of

Summer Mortality and Preparedness to Reduce the Health Impact of Heat Waves in Italy, Int. J. Environ. Res. Publ. Health, 7, 2256-2273, 2010.

28. P. Michelozzi, U. Kirchmayer, K. Katsouyanni, A. Biggeri, G. McGregor, B. Menne, P. Kassomenos, H.R. Anderson, M. Baccini, G. Accetta, A. Analytis and T. Kosatsky. Assessment and prevention of acute health effects of weather conditions in Europe, the PHEWE project: background, objectives, design, Environmental Health, 6, 1-10, 2007.

29. S. Pattenden, B. Nikiforov and B.G. Armstrong. Mortality and temperature in Sofia and London, Journal of Epidemiology and Community Health, 57, 628-633, 2003.

30. R.D. Peng, F. Dominici and T.A. Louis. Model choice in time series studies of air pollution and mortality, Journal of the Royal Statistical Society: Series A (Statistics in Society), 169, 179–203, 2006.

31. C. Price, S. Michaelides, S. Pashiardis and P. Alpert. Long term changes in diurnal temperature range in Cyprus, Atmos. Res., 51, 85-98, 1999.

32. D.G.C. Rainham and K.E. Smoyer-Tomic. The role of air pollution in the relationship between a heat stress index and human mortality in Toronto, Environmental Research, 93, 9-19, 2003.

33. J. Rocklöv and B. Forsberg. The Effect of High Ambient Temperature on the Elderly Population in Three Regions of Sweden, International Journal of Environmental Research and Public Health, 7, 2607-2619, 2010.

34. J. Schwartz. The Distributed Lag between Air Pollution and Daily Deaths, Epidemiology, 11, 320-326, 2000.

35. J. Schwartz, C. Spix, G. Touloumi, L. Bachárová, T. Barumamdzadeh, A. Le Tertre, T. Piekarksi, A.P. De Leon, A. Pönkä, G. Rossi, M. Saez and J.P. Schouten. Methodological issues in studies of air pollution and daily counts of deaths or hospital admissions, Journal of Epidemiology and Community Health, 50, S3–11, 1996.

36. C. Symeou. Impacts of climate change on human health in Cyprus, 2009. http://cyprus-institute.us/2009/Symeou_Christina_Global_Climate_Change_project.pdf.

37. G. Touloumi, R. Atkinson, A. Le Tertre, E. Samoli, J. Schwartz, C. Schindler, J.M. Vonk, G. Rossi, M. Saez, D. Rabszenko and K. Katsouyanni. Analysis of health outcome time series data in epidemiological studies, Environmetrics, 15, 101–117, 2004.

38. L.J. Welty and S.L. Zeger. Are the acute effects of particulate matter on mortality in the national morbidity, mortality, and air pollution study the result of inadequate control for weather and season? A sensitivity analysis using flexible Distributed Lag Model, American Journal of Epidemiology, 162, 80-88, 2005.

39. World Health Organization (WHO). Improving public health responses to extreme weather/heat-waves – EuroHEAT. Technical summary, 2009. http://ccsl.iccip.net/e92474.pdf.

40. A. Zanobetti and J. Schwartz. Temperature and mortality in nine US cities, Epidemiology, 19, 563-570, 2008.

41. A. Zanobetti, M.P. Wand, J. Schwartz and L.M. Ryan. Generalized additive distributed lag models: quantifying mortality displacement, Biostatistics, 1, 279-292, 2000.

42. S.L Zeger. A regression model for time series of counts, Biometrika, 75, 621-629, 1988.